NATIONAL AERONAUTICS AND SPACE ADMINISTRATION

Technical Report 32-1177

Surveyor III Mission Report

Part II. Scientific Results

Prepared by:

The Surveyor Investigator Teams, Scientific Evaluation Advisory Team, and Working Groups

JET PROPULSION LABORATORY
CALIFORNIA INSTITUTE OF TECHNOLOGY
PASADENA, CALIFORNIA

June 1, 1967

NATIONAL AERONAUTICS AND SPACE ADMINISTRATION

Technical Report 32-1177

Surveyor III Mission Report

Part II. Scientific Results

Prepared by:

The Surveyor Investigator Teams, Scientific Evaluation Advisory Team, and Working Groups

JET PROPULSION LABORATORY
CALIFORNIA INSTITUTE OF TECHNOLOGY
PASADENA, CALIFORNIA

June 1, 1967

TECHNICAL REPORT 32-1177

Prepared Under Contract No. NAS 7-100
National Aeronautics & Space Administration

Preface

This three-part document constitutes the Project Mission Report on *Surveyor III*, the third in a series of unmanned lunar soft-landing missions.

Part I of this Technical Report consists of a technical description and an evaluation of engineering results of the systems used in the *Surveyor III* mission. Part II presents the scientific data derived from the mission, and the scientific analysis conducted by the members of the *Surveyor* Investigator Teams, *Surveyor* Scientific Evaluation Advisory Team, and the five associated working groups. Part III consists of selected pictures from *Surveyor III* and appropriate explanatory material.

Results given in this report are based on data evaluation prior to June 1, 1967. It is expected that future evaluation and analysis of the *Surveyor III* data will provide additional scientific results.

(Blank Page)

Contents

Contents (contd)

Contents (contd)

Contents (contd)

I. Introduction

T. Vrebalovich, L. D. Jaffe, and S. E. Dwornik

Surveyor III was launched from Cape Kennedy, Florida, at 07:05:01 GMT on April 17, 1967. An *Atlas/Centaur* launch vehicle placed the *Surveyor* into a parking orbit at a 165-km altitude and, after a coast of 22 min, 7 s, injected it into a trajectory intersecting the moon. The spacecraft mass at injection was 1040 kg; after final touchdown, 302 kg. A midcourse maneuver was performed on April 18. The center of the aiming ellipse chosen for this maneuver was selenographic latitude 2.92°S, longitude 23.25°W. *Surveyor III* landed at 2.94°S, 23.34°W, within 2.8 km of the aiming point, at 00:04:53 GMT on April 20, 1967. Data obtained from the successful mission have significantly increased knowledge of the moon.

The landing site is the southeast part of Oceanus Procellarum, about 370 km south of the crater Copernicus. The spacecraft rests in a subdued, rounded crater about 200 m in diameter and is inclined from 12 to 15 deg to the horizontal on the eastern slope of the crater. The crater's identity and the location of *Surveyor III* within it were determined by comparing features visible from the *Surveyor* with those found in high-resolution *Lunar Orbiter III* photographs.

The *Surveyor III* spacecraft is similar to *Surveyor I* (Refs. I-1 and I-2); the only major change in scientific instrumentation was the addition of a soil mechanics surface sampler (SMSS). This device replaced an approach television camera, which was carried by *Surveyor I* but not used. The SMSS is essentially the instrument described by Scott in Ref. I-3, but without strain gages, an accelerometer, or position potentiometers. Primarily, it consists of a scoop, about 12 cm long and 5 cm wide, mounted on a pantograph arm that can be extended about 1.5 m, or retracted close to the spacecraft, by a motor drive. The arm can also be moved in azimuth and elevation by motor drives, or dropped onto the lunar surface, under force provided by gravity and a spring. A door on the scoop can be opened and closed by a motor. The SMSS can manipulate the lunar surface material in a number of ways, and the results can be observed by the *Surveyor* television camera.

A minor difference between *Surveyors I* and *III* was that *Surveyor III* carried two auxiliary mirrors, attached to the spaceframe, to permit a better survey of selected areas below the spacecraft in its landed position – where interaction between lunar surface and spacecraft could have occurred. Small modifications were made in the television survey camera itself. Television was treated as a scientific experiment on *Surveyor III*.

As in the *Surveyor I* landing, strain gages recorded the loads in each shock absorber during the landing events. Interpretation of these records and other data received

from the spacecraft showed that, because the vernier engines did not shut down at the planned height of 4 m above the surface prior to initial touchdown, three separate touchdowns occurred on the lunar surface. Because the spacecraft had a lateral velocity of about 1 m/s, the distance between the first and second touchdown events was about 20 m, and about 11 m between the second and third touchdowns. A final translational movement of about 30 cm occurred following the third touchdown. The vernier engines, which had maintained a stable spacecraft during all of the landing events, shut down prior to the third touchdown.

The marks of the footpads on the lunar surface in the second touchdown, though not in the first, have been identified in the post-landing pictures. The position of these marks correlated with the interpretation of the landing dynamics. There may have been a small amount of soil erosion by the vernier engines during the second touchdown.

Lunar material disturbed by the vernier engines during the unique landing apparently coated part of the mirror of the television camera or abraded it, causing the glare evidenced in parts of many television pictures. Temperature measurements indicate no dust layer on *Surveyor's* thermal compartments.

The television camera could not view the lunar surface outside the crater within which *Surveyor III* landed, but the sloping walls of the crater allowed the camera to view nearby features more clearly than would have been possible on a flat terrain. The spacecraft took 6315 pictures from April 20 to May 3, 1967.

Data on the mechanical properties of the lunar surface material were obtained from examination of the depth of the footpad imprints, the strain gage records, and computer simulation of the landing, as well as by the SMSS. The SMSS made eight bearing tests and fourteen impact tests on the lunar surface, and dug four trenches. The SMSS also picked up three objects from the lunar surface.

In addition to lunar observations, color pictures of the earth were taken during a solar eclipse and some time after the eclipse. A picture of Venus was also obtained.

Section II of this document, prepared by the *Surveyor III* Scientific Evaluation Advisory Team, briefly presents the principal scientific results of the *Surveyor III* mission. The subsequent sections, prepared by *Surveyor III* investigators and working groups, give more detail concerning the results. These sections have been written independently of one another; some differences in interpretation may exist among them.

Individual pictures taken by *Surveyor* are best identified by the day of the year and GMT at which they were taken. April 20, 1967, was Day 110; May 3 was Day 123. Mosaics are best identified by catalog numbers.

References

I-1. Surveyor Scientific Evaluation Advisory Team, "Surveyor I: Preliminary Results," *Science*, Vol. 152, pp. 1737–1750, 1966.

I-2. Jaffe, L. D., "Lunar Surface Exploration by Surveyor Spacecraft: Introduction," *J. Geophys. Res.*, Vol. 72, pp. 773–778, 1966.

I-3. Scott, R. F., "Soil Mechanics Surface Sampler Experiment for Surveyor," *J. Geophys. Res.*, Vol. 72, pp. 827–830, 1967.

Acknowledgment

Special appreciation is extended to Robert Steinbacher, JPL, for valuable assistance in organizing and carrying out the scientific effort for *Surveyor III*; and to Stephen Gunter, JPL, for responsibility in video data handling for the scientific groups associated with *Surveyor III*, and providing pictures in the various forms needed for analysis.

II. Principal Scientific Results of the *Surveyor III* Mission

L. D. Jaffe, S. A. Batterson, W. E. Brown, Jr., E. M. Christensen, D. E. Gault, J. W. Lucas, R. H. Norton, R. F. Scott, E. M. Shoemaker, G. H. Sutton, and A. L. Turkevich

Data returned by *Surveyor III*, during and after landing on the lunar surface, provided significant additional knowledge of the moon. Of particular interest are the results on mechanical properties of the lunar surface and the comparisons of terrain and microfeatures inside and outside a crater, made possible by observations from *Surveyors I* and *III*.

This section outlines the major scientific findings derived from *Surveyor III* data, and is based on information obtained by varied methods. The methods are described in more detail in the following sections of this report.

A. Mechanical Properties of Lunar Surface Material

During the *Surveyor III* landing events, the footpads formed craters and imprints on the lunar surface. Associated with the footpad craters were patterns of ejected material, indicative of the direction of spacecraft motion. The craters, imprints, and ejecta have been used in analyses of lunar soil properties. Several other methods were also used to derive the mechanical properties of the lunar soil: analyses and simulations of the landing dynamics, analyses of the soil mechanics surface sampler (SMSS) experiment, and slopes of small natural craters. Considering all methods, it would seem that the following ranges of soil properties are compatible with the observations and represent the differences in techniques of analysis and, possibly, variation in the lunar soil properties from place to place. The ranges are as follows:

(1) Cohesion range: 1.5×10^3 to 7×10^3 dynes/cm^2.

(2) Angle of internal friction range: 35 to 40 deg.

(3) Static bearing capacity range: 2×10^5 to 6×10^5 dynes/cm^2.

Note that static bearing capacity increases with bearing size.

The SMSS picked up a clod, or aggregate of lunar soil grains, which was crushed when the scoop door was closed, and a rock fragment that was not crushed. It is estimated that a pressure of approximately 2×10^7 dynes/cm^2 was applied to the rock when the scoop was closed. The rock did not break under this stress.

Lunar soil was observed to remain in the SMSS scoop, with the door fully open, until jarred free by the SMSS motions or impact. It is possible that the soil adhered to the scoop (see Section IV) or it may be that moldable, slightly cohesive soil adapted itself to the inside shape of the scoop and was jammed in place by a trenching operation, without adhesion (see Section VIII).

Vibrations of the spacecraft following the third touchdown have been analyzed to give an indication of the elastic shear or rigidity modulus of the surface soil (see Section V).

B. Macroscopic Features of Local Terrain

Surveyor III landed in a subdued crater with a low, rounded rim. The crater is slightly more than 200 m in diameter and about 15 m deep. The spacecraft is situated on the inner east wall of the crater, about halfway between the center of the crater and the rim crest; it is inclined 14.7 $\pm$0.1 deg toward the west. The selenographic coordinates of the landed spacecraft are 2.94°S lat, 23.34°W lon, relative to selenodetic control adopted by the Aeronautical Chart and Information Center.

The small craters observed in the *Surveyor III* pictures range in diameter from about 10 cm to more than 20 m. Most craters smaller than 3 m in diameter are relatively shallow and nearly rimless or have very subdued rims. Approximately 25% of the craters that range from 3 to about 13 m in diameter have distinctly raised rims and relatively steep walls. The other craters in this size range have subdued forms. The rims of most craters are composed of material similar in texture to parts of the surface between the craters. Most craters have a normal cup shape, with walls and floors concave upward. However, one prominent crater more than 20 m across, located near the center of the main crater, is dimple-shaped. Most of the craters appear to be irregularly or nearly randomly distributed over the rim, walls, and bottom of the main crater, but some of the very shallow rimless craters are aligned approximately in the north-south direction. The size/frequency distribution of the craters at the *Surveyor III* landing site is closely similar to the mean distribution observed on the lunar plains by *Rangers VII* through *IX*.

Bright pieces of fragmental debris are scattered irregularly over most of the visible parts of the lunar surface. Most of the observed fragments are relatively angular, but some well-rounded fragments, which generally appear to be deeply buried in the lunar surface, are also present. Generally, the fragments are equant in shape, but some are distinctly tabular and a few have the form of sharp, narrow wedges. Two prominent strewn fields of blocky debris were observed around two craters, 13 and 15 m across, at the *Surveyor III* site. One of these craters has a sharp, raised rim and the other a more subdued, round rim.

Fragments close to the spacecraft have a peculiar grainy, knobby, or pitted texture. Some fragments, notably pieces associated with a strewn field of blocks to the northeast of the spacecraft, have smooth, nearly planar, faces – as though they were broken along preexisting joints or fractures. Some large blocks, most of which are tabular in form, appear to be laminated or to contain planes of weakness parallel to the long dimensions of the blocks. Most of the fragments at the surface of the *Surveyor III* landing site are evidently part of a layer of particulate material of low cohesion. The layer is at least 1 m thick along the upper parts of the wall of the main crater in which *Surveyor III* landed and may be much thicker near the center of the crater. The presence of coarse, blocky ejecta from superposed craters on the northeast rim and high on the southwest wall indicates that coarser fragments or more coherent material are present at depths of a few meters on or near the rim of the main crater. No strewn fields of blocks or blocky crater rims are found near the bottom of the main crater. This may indicate that the base of the relatively fine-grained debris layer is deeper than any of the craters present there.

Lunar surface brightness temperatures sensed by *Surveyor III* during the lunar day correspond to a thermal parameter, γ, greater than 400 in centimeter-gram-second units; this is in agreement with earth-based data. Also during the day, lunar surface directional thermal emission was sensed and later found to be consistent with earth-based data. Temperature measurements taken during the eclipse permit a more accurate determination of the thermal parameter and indicate a value of approximately 400; this is not in agreement with the value of 1420 obtained by earth-based eclipse measurements for the landing site region. The *Surveyor III* temperature data lag earth-based measurements during the eclipse.

The average radar cross section of the moon, as measured from the earth, closely approximates the values measured by *Surveyor* radars over small areas (250-m radius).

C. Characteristics of Local Microstructure

From the strain gage data, it is concluded (see Section V) that the undisturbed lunar surface density to a depth of 0.5 cm is not greater than about 1.2 g/cm^3, and that the material to this depth compressed during the impact to a density of 1.7 to 1.8 g/cm^3. Analysis of both SMSS and the touchdown measurements, from a soil mechanics viewpoint, led to a density estimate of about 1.5 g/cm^3 for the top few centimeters of lunar soil (see Section IV). In penetrations to this depth, it was observed that the material appeared to be relatively incompressible. It would appear that the two computed ranges of density can be reconciled if a lunar soil profile of increasing density is postulated. The increase must be fairly rapid to explain the observations, with a density of 1 g/cm^3 or less in the top few millimeters, increasing to about 1.5 g/cm^3 by a depth of a few centimeters, and to an asymptotic value of perhaps 1.8 to 2.0 g/cm^3 at a depth of perhaps 5 to 10 cm, based on limiting lower-porosity considerations and an assumed solid-component density of 3 g/cm^3. The corresponding porosity range is from about 0.7 at the surface to 0.35 at depths greater than 10 cm.

The SMSS experiments indicated an increase in the strength of the lunar soil with depth, an effect which became apparent at depths of 4 or 5 cm. At 5- to 10-cm depths, considerable difficulty was encountered in deepening the trenches with the SMSS, although the deeper material was visually identical to the soil at shallower depths. The soil mechanical properties are not independent of one another nor of density. Thus, it should be observed that an increase in density of the soil with depth will imply both an increased friction angle of the soil and an increase in the cohesion resulting from a greater number of contacts between particles. In addition, the cohesion may also differ with depth because of physicochemical reasons.

Individual particles of undisturbed surface material, visible to the *Surveyor III* camera, ranged in size from blocks 4 m long down to the limit of resolution. One to ten particles/cm^2, larger than 1 mm in diameter, were noted. The observed cumulative frequency was an exponential function of particle diameter, with an exponent of about -2.5. Laboratory tests suggest that some fine particles were probably missed in counting, and the exponent for cumulative frequency per unit volume probably is higher. In the two strewn fields, around craters of from 13 to 15 m in diameter, 10-cm to 1-m blocks were much more frequent than elsewhere. Less than 15% of the surface is covered with particles larger than 1 mm in diameter. The surface retained a good imprint of footpad ridges about 60 μm high. This observation (together with laboratory simulations, the appearance of disturbed lunar surface, mechanical property measurements, and photometric observations of the footpad imprint and of the undisturbed surface) suggests that a substantial fraction of the surface material consists of particles smaller than 60 μm in diameter and an appreciable fraction ($>10\%$) probably consists of particles smaller than 10 μm.

A preliminary search for color differences (by color reconstitution methods) revealed no determinable differences in color among various coarse blocks, the fine-grained matrix of the surface, or fine-grained material disturbed by the surface sampler. All of the materials observed on the lunar surface are gray.

The estimated normal luminance factor (normal albedo) of an undisturbed part of the lunar surface next to footpad 2 of the *Surveyor III* spacecraft is 8.5 $\pm 2\%$. The smooth walls and bottom of the footpad imprints are different photometrically from the undisturbed lunar surface and from material ejected by the footpads. Observations of the imprint of footpad 2 (next to the spacecraft) indicate that this smooth surface is more like a Lambertian surface than is the undisturbed lunar surface. About 30% more light is emitted toward the eastward-facing camera from the smooth imprint surface than from nearby undisturbed parts of the moon at phase angles of 40 to 60 deg in the lunar morning; but, in the lunar afternoon, the imprint is not significantly brighter than the undisturbed surface. This indicates that the very small irregularities between the grains have been partially smoothed out or filled in by pressure of the smooth footpad.

Other disturbances of the lunar surface by *Surveyor III* exposed darker material at depths of a few centimeters or less. The fine-grained particulate debris of the lunar surface is probably 20 to 30% lower in albedo at depths of only a fraction of a millimeter beneath the optically observed surface. Coarse particles protruding above the general level of the surface have a higher albedo than the fine-grained matrix of the surface.

Although some of the observations (e.g., mechanical properties, radar reflectivity) made by *Surveyor III* set limits on possible terrestrial materials that could explain

the results, no firm conclusion can be made at present about the chemical composition of the lunar surface.

D. Effects of Engine Exhaust

The vernier engines continued to operate throughout the first and second landings and until shortly before the touchdown of the third landing. This produced no noticeable effect on the spacecraft, other than on the television camera mirror. Glare was produced on part of the mirror when the sun, or large amounts of reflected sunlight, illuminated it. It is suspected that this part of the mirror was contaminated during the landing by the deposition of lunar material, by pitting, or by the deposition of exhaust gas. A lunar surface feature visible at the second landing site possibly could have been caused by vernier engine exhaust erosion. Good correspondence between the outer-face temperatures of electronic compartments of *Surveyor III* and *Surveyor I*, for a given sun incidence angle, indicates that there was no thermally significant layer of dust on the faces. Pictures of the top of one compartment show a few specks of material, but no significant coverage. Thus, contamination of the spacecraft, induced by vernier engines, is not expected to be a major problem in future missions.

E. Nonstatic Nature of Lunar Surface

Many of the observations made during the *Surveyor III* mission can be interpreted as exhibiting lunar phenomena at different stages of their life histories. The observations provide evidence of the nonstatic nature of the lunar surface, even though the changes are occurring over a long period of time.

For example, one of the craters has a sharp, raised rim and is associated with rocks of large angularity perched on top of the local landscape. It is interpreted as young, relative to another crater nearby that has a rounded rim and less prominent debris. Similarly, examination of rocks in the vicinity of *Surveyor III* leads to a classification in terms of increasing roundness (or lack of angularity), which is interpreted as a measure of the time of exposure to abrading influences. The blocks associated with the subdued (older) crater are significantly rounder than those associated with the raised-rim crater. Finally, the relation of rocks to the lunar surface in their immediate vicinity suggests a chronology in which freshly produced rocks are perched on top of the surface, and older rocks are more or less buried. This correlates well with the roundness of the rocks and the nature of the neighboring craters. In addition, the fortunate landing of *Surveyor III* on a slope provided pictures showing that this burying process proceeds faster on the uphill side of a rock than on the downhill side.

Evidence for a different type of process that occurs on the moon is the observation that disturbed lunar surface material is darker than that of the undisturbed surface. However, coarse fragments protruding above the surface, as well as the one excavated rock, have a higher albedo than the fine-grained matrix of the surface. Because the surface material is continually being churned up by meteorite impacts, some process (confined in action to the surface) must be continually changing the photometric properties of the exposed particles.

F. Relation of Properties at *Surveyor I* and *Surveyor III* Landing Sites

The *Surveyor I* landing site was a relatively flat, smooth mare surface encircled by hills and low mountains, whereas the *Surveyor III* landing site was in a subdued crater greater than 200 m in diameter. Comparisons of the pictures obtained at these two different sites indicate that the smaller craters and the fragmental debris are similar in distribution of shape and size. The majority of the craters at both sites are inferred to be of impact origin. One difference between the two sites is in the deposition of the granular material around the more rounded rocks, which are, in general, believed to be buried deeper in the lunar surface than are the more angular rocks. At the *Surveyor I* site, the contact line between the more rounded rocks and the surface is about in the same plane as the lunar surface, although a fillet of fine material can be observed. This indicates that processes are at work which generally result in a smooth deposition. At the *Surveyor III* site, however, the fillet of material around some of the more rounded rocks tends to be higher on the uphill end than on the downhill end, indicating a downhill movement of the fine material, as mentioned previously.

Apparent soil similarities for the top few centimeters at the *Surveyor I* and *Surveyor III* landing sites are:

(1) Static bearing capability is within the range of from 2×10^5 to 6×10^5 dynes/cm^2 for a footpad penetration of 2.5 to 5 cm. This is derived from computer simulation of shock absorber force histories and footpad penetrations during landing.

(2) Material disturbed by the footpads consists of clumps or clods formed of particulate material smaller than the resolution of the camera, a fine spray thrown a meter or more, and smoothed areas that retain the compressed contact area.

(3) Noncompressed disturbed material is darker than the undisturbed surface.

(4) The material has little compressibility.

(5) There is general homogeneity at the positions of the second and third landings of *Surveyor III* and at that of *Surveyor I*.

(6) Cohesion and angle of internal friction at the two sites probably are comparable.

Lunar surface brightness temperatures sensed during the day by *Surveyors I* and *III* were essentially identical. A thermal parameter value of approximately 800 from *Surveyor I* post-sunset data was significantly different from the approximately 400 from *Surveyor III* eclipse data.

The variation in radar cross section between *Surveyor I* and *III* tracks, about 5 km long, is relatively small (within $\pm 20\%$), except for a few anomalies related to surface features.

G. Astronomical Observations

Surveyor III pictures of the eclipse of the sun by the earth reveal a bright region in the refraction halo surrounding the earth, which was correlated with the position of the sun, and a series of bright beads over regions of the earth largely clear of clouds. Clouds usually occult the refracted rays of the sun, most of which pass through the low atmosphere at the limb; the beads occur in the depressions in the optical silhouette of the earth. Preliminary reduction of the color of the refracted light showed that the brightest region, near the position of the sun, exhibits a correlated color temperature close to 4800°K. The color temperature generally tends to be lower for light that follows paths of greater atmospheric absorption.

Preliminary analysis of *Surveyor III* pictures of the partially illuminated earth revealed colors similar to those recorded from orbit by the *Mercury* and *Gemini* astronauts.

(Blank Page)

III. Television Observations From *Surveyor III*

E. M. Shoemaker, R. M. Batson, H. E. Holt, E. C. Morris, J. J. Rennilson, and E. A. Whitaker

Surveyor III landed on the lunar surface at 00:04 GMT, on Day 110 (April 20), 1967, approximately 23 h after local sunrise on the moon. The television camera was turned on about 1 h after touchdown, and 6315 pictures were taken during the remainder of the lunar day. The camera was operated extensively for the first period of lunar visibility from the Goldstone Tracking Station of the Deep Space Network (DSN) and, except on Day 115 (April 25), on each successive Goldstone pass of the moon. During this period, the sun rose from an elevation angle of 11 deg in the east to within 3 deg of the zenith and then sank almost due west of the spacecraft. Many pictures were obtained of the illuminated eastern horizon in the period immediately preceding sunset. In addition to those received at the Goldstone station, some were obtained at the Canberra, Australia, station of the DSN.

A. Television Camera

1. Description

The television camera on *Surveyor III* is closely similar to the survey camera carried on *Surveyor I* (Ref. III-1). In the *Surveyor* survey camera, images are reflected from a rotatable mirror through a zoom lens onto the active element of a vidicon tube. The mirror can be rotated in azimuth and elevation relative to a line through the center of the vidicon tube and the zoom lens axis, which remain fixed in attitude. This rotation provides the capability of scanning the lunar scene and sky over a vertical angular range of 100 deg and a horizontal range of nearly 360 deg. The axis of the camera is inclined 16 deg to the nominal vertical axis of the spacecraft, which causes the horizon to vary in camera elevation angle as a function of the azimuth angle, when the spacecraft lands in an approximately level attitude. The variation of the horizon for a flat surface is very nearly a sine function of the azimuthal angular position and has a half amplitude of 16 deg.

The camera normally is operated with the zoom lens positioned for focal lengths at either the extreme long (100-mm) or short (25-mm) focal lengths. At the long focal length, or narrow-angle mode of operation, the field of view is 6.4 deg; at the short focal length, or wide-angle mode, the field of view is 25.3 deg. The lens is capable of being set at varying focal positions, which are required to obtain focused pictures of parts of the lunar surface near the spacecraft in the narrow-angle mode. In this mode, the camera has a calibrated angular resolution of 0.5 mrad at 15% relative response. This resolution permits discrimination of objects on the lunar surface slightly less than 1 mm in diameter at the distance of the spacecraft footpads from the camera (1.6 m).

A filter wheel, located between the zoom lens and the rotatable mirror, may be positioned in four discrete positions. In one position, the optical path is intercepted by a clear piece of glass; in the other three positions, there are three color filters.

Within the zoom lens is a variable iris aperture that provides nominal focal ratios ranging from *f*/4 to *f*/22. The iris can be operated by command to six distinct calibrated positions. It can also be operated in an automatic mode in which the iris position is controlled by the integrated scene luminance detected by a photocell in the lens.

A focal plane shutter between the zoom lens and the faceplate of the vidicon tube provides exposures of 150 ms and 0.5 s to many minutes. The camera is normally operated at the 150-ms exposure, which is calibrated for each camera and which is reproducible within about 2%. Long exposures are obtained by commanding the shutter open and later commanding it closed. This mode of operation is referred to as the integrating mode and was used to take pictures of faint objects, such as Venus and the spacecraft and lunar surface illuminated by refracted sunlight during an eclipse.

With a given aperture and filter position and 150-ms exposure, the dynamic range of the camera is approximately 25 to 1. The linear part of the function of the logarithm of video voltage vs logarithm of lunar scene luminance is less for the *Surveyor III* camera than for the *Surveyor I* camera. By combined use of various filters, apertures, and exposure times, the total range of response of the *Surveyor III* camera, like that of the *Surveyor I* camera, is about 1,000,000 to 1.

The image on the vidicon target can be scanned in two different modes: one produces a 200-line picture; the other produces a 600-line picture. The 200-line scan mode is employed when the video signal must be broadcast over the omnidirectional antenna and must be accommodated to the low bandwidth achievable during transmission from the omnidirectional antenna. The 600-line picture is transmitted over the planar array (high-gain) antenna after this antenna has been oriented so that the main beam from the antenna is intercepted at tracking stations on the earth. The 200-line pictures are, therefore, usually taken shortly after landing, before the planar array antenna has been oriented. For the remainder of the mission, the television pictures are normally taken and transmitted in the 600-line mode.

The principal differences between the *Surveyor III* camera and the *Surveyor I* camera are in the use of different colored filters, the different response of the vidicon tube, and the addition of a small visor attached to the hood of the camera. New color filters were used in the *Surveyor III* camera to obtain a closer match of the camera-filter spectral response functions to the standard CIE color-matching functions than was achieved with the filters used on *Surveyor I*. As shown in Fig. III-1, a close match was achieved.

Because of technical difficulties involved in manufacture, each vidicon tube of the type employed in the *Surveyor* camera differs slightly from the others in sensitivity, dynamic range, erasure characteristics or retentivity of the image, shading, resolution, and imperfections that produce minute bright spots on the image. In addition, it is possible for dust to settle on the faceplate of the vidicon tube. The dust particles produce dark spots

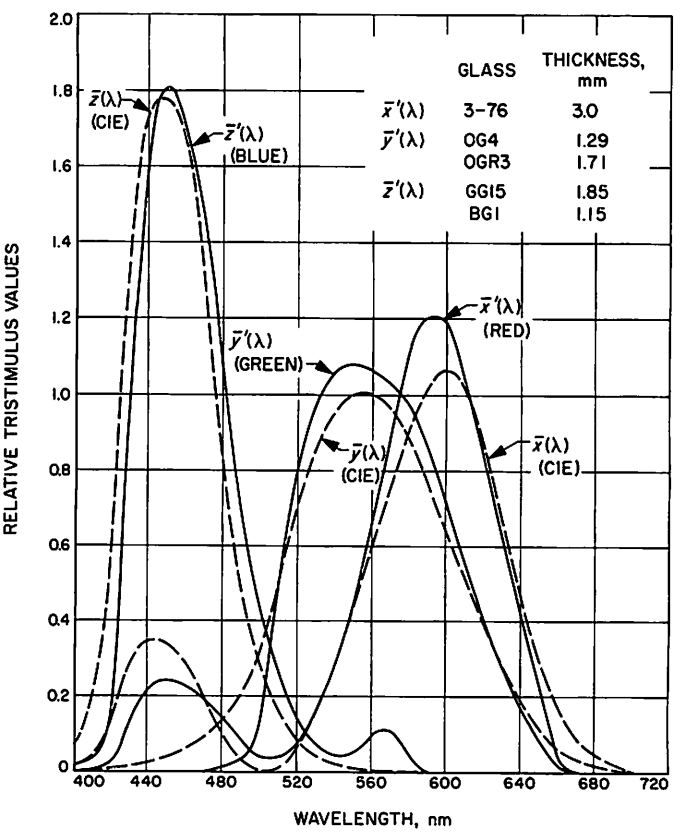

Fig. III-1. Camera-filter response functions of *Surveyor III* camera compared with CIE (Commission Internationale l'Eclarage 1931) color-matching functions. Camera-filter spectral response functions are shown with solid line; CIE color-matching functions are shown with dashed line

in the image. The vidicon tube employed in the *Surveyor III* camera displayed a higher retentivity of the image than that employed in *Surveyor I* and had a higher number of imperfections that produced small bright spots. Slightly less dust appeared to be present on the vidicon faceplate of the *Surveyor III* camera after landing on the lunar surface than in the case of *Surveyor I*.

To reduce veiling glare, a visor was added to the hood of the camera to reduce the amount of sunlight falling directly on the mirror and inner parts of the camera optical train. The hood carries the mirror and is an integral part of the mirror rotation system, so that the visor maintains a fixed position in azimuth relative to the mirror. Degradation of the surface of the mirror during lunar landing increased the veiling glare so much, however, that the addition of the visor was of relatively little value.

2. Operating Characteristics

During operation of the *Surveyor III* camera after touchdown, problems were encountered that may be attributed to the unusual circumstances of landing. Normally, the camera mirror is capable of being rotated in elevation to a position that essentially closes or seals the hood. The torque required to rotate the mirror to an open position after closure was close to the torque generated by the mirror elevation stepping motor on the *Surveyor III* camera, however. For this reason, the camera was flown to the moon with the mirror open. The spacecraft touched down three times during its landing on the lunar surface. During the first two touchdowns, the vernier engines, which control the descent of the spacecraft, continued to fire. After the first series of pictures was received from the television camera, it was found that many were partially or completely obscured by strong veiling glare. Evidently, the mirror and possibly other parts of the optical train of the camera were either partially coated with particles or rocket effluent or pitted by impact of particles entrained by the rocket effluent. Between one-half and two-thirds of the area of the mirror was degraded significantly. The particles or pits responsible for degradation of the mirror surface were too small to be detected by direct observation of the mirror at the 25-mm focal length (smaller than 0.5 mm).

Because of the glare, usable pictures could be obtained only in limited ranges of azimuth during the early lunar morning and late lunar afternoon. Whenever sunlight fell directly on the mirror, the image of the lunar surface was completely obscured when the image was reflected through the directly illuminated part of the mirror. In addition, considerable glare is present in other pictures taken when the mirror is averted from the sun, owing to light re-emitted from the lunar surface.

Because of operational difficulties in rotating the mirror, the camera was operated over an azimuth range extending only to one side of the +3-deg azimuth position during most of the lunar day. Because of the time requirements for the SMSS and other experiments, insufficient time was available for systematic lunar surveys during each Goldstone pass. Much more time would have been required for the completion of systematic surveys than in the case for normal operation, and only a fraction of the planned operation of the camera was executed during each Goldstone pass.

The camera operated best during high sun angles, but under high sun the photometric conditions are less favorable for detecting relief features on the lunar surface. Craters and subtle relief features were almost impossible to observe at high sun, although blocky fragments could be observed because they differ in albedo from the rest of the lunar surface material. Most of the details of the topography and geology of the *Surveyor III* landing site are extractable from the pictures only with considerable difficulty.

3. Categories of Pictures Taken

Of the 6315 pictures taken with the television camera, about 45% of the pictures were taken in the narrow-angle mode at sequential camera azimuth and elevation settings to provide high-resolution coverage of the entire area visible to the camera. The wide-angle mode was used to take 8% of the total number of pictures, providing panoramas of the landing site at lower resolution than that of the narrow-angle pictures, but with one-tenth the number of frames. Immediately after touchdown, before the high-gain antenna had been oriented, 55 wide-angle pictures were taken in the 200-line, low-resolution television mode.

Special sequences of pictures were taken for a variety of purposes. Pictures were taken in wide- and narrow-angle modes, and with color filters of photometric and color target areas as well as other areas of special interest for photometric or color studies. Surveys were made along certain azimuths in which pictures were taken at several different focal settings at each

elevation step. These pictures will be used to determine distance to points on the surface, from optimum focus, and will be used to construct focus ranging profiles out to about 10 m from the spacecraft. Other special surveys were obtained at varying sun angles of the areas close to the visible footpads of the spacecraft and of areas directly beneath the crushable blocks of the spacecraft. In addition, special surveys were made of parts of the spacecraft in order to search for particles and possible structural damage.

A unique sequence of pictures was obtained of the earth during an eclipse on Day 114 (April 24). During the eclipse, a picture was also obtained of Venus, and an attempt was made to photograph stars to gain precise information on the orientation of the camera and the spacecraft. All attempts to obtain pictures of stars both during the eclipse and later were unsuccessful, however, because of difficulties in commanding the camera mirror to rotate and because of the high background of veiling glare produced by scattering of light from the lunar surface onto the mirror.

The special surveys account for about 25% of the total number of pictures taken during the first lunar day; the remainder were taken in support of operations of the surface sampler experiment.

4. Categories of New Information Provided by Television Pictures

The television pictures have provided new information on the location of the landing site on the lunar surface, on the lunar surface itself, and on the appearance of the earth as seen from the moon, during eclipse and partial direct illumination by the sun. Calculation of the trajectory of the spacecraft by the Flight Performance and Analysis Group, from information obtained by tracking the spacecraft on its translunar trajectory, led to a determination of the location of the spacecraft on the lunar surface, with an uncertainty of a few kilometers. By close comparison of the detailed features of the surface observed by the television camera on *Surveyor III* with features observed from lunar orbit in photographs acquired by *Lunar Orbiter III*, it was possible to determine the precise location of the *Surveyor III* spacecraft with respect to the features shown in the *Lunar Orbiter* photographs. The evidence by which the location of *Surveyor III* has been determined and its relation to the larger features of the lunar surface are described by Whitaker.

Many kinds of new information on the small details of the lunar surface and the specific topographic and geologic features of the landing site are contained in the television pictures, as discussed in the sections on topography and geology by Shoemaker, Morris, Batson, and Holt. Some of the photometric observations of the lunar surface at the *Surveyor III* landing site have been reduced and are described in this report by Holt and Rennilson. In addition, preliminary evaluation of the color of various features on the lunar surface at the *Surveyor III* landing site is presented by Rennilson.

Observations of earth during the eclipse of the sun by the earth have provided the first direct observations of the distribution of refracted sunlight that weakly illuminates the lunar disk during this type of eclipse. The distribution and color of light in the refraction halo surrounding the earth during the eclipse are described by Rennilson, Shoemaker, and Whitaker. Finally, the observations of the crescent earth illuminated directly by the sun are described by Whitaker and Rennilson. The pictures obtained from *Surveyor III* are the first that have been taken of the earth from the distance of the moon by methods permitting reproduction of pictures of the earth in color.

B. Location of *Surveyor III* on Moon

The nominal target for *Surveyor III* was 3°S latitude, 23°W longitude, which is in a small but relatively crater-free part of the Oceanus Procellarum about 120 km (75 mi) southeast of the crater Lansberg and due north of the center of Mare Cognitum (Fig. III-2). The area is crossed by the weak south end of a ray from Copernicus, and contains two very low segments of mare ridges (Figs. III-3 and III-4). The whole region is well covered by *Lunar Orbiter III* photographs, which reveal a fairly low density of subtelescopic craters, closely resembling those observed around the *Surveyor I* landing site.

The best estimate of the position of the landing site obtained from pre-landing tracking data was 2.99°S, 23.37°W. This position was plotted on ACIC lunar chart AIC 76A, and the point transferred to *Lunar Orbiter III* medium-resolution photograph M154 (Fig. III-5), from which it was further transferred to high-resolution photograph H154. Because *Surveyor I* and *Rangers VII* through *IX* landed to the east and three times to the north of the positions derived from tracking data, it was considered that *Surveyor III* would probably be located in the central third of H154.

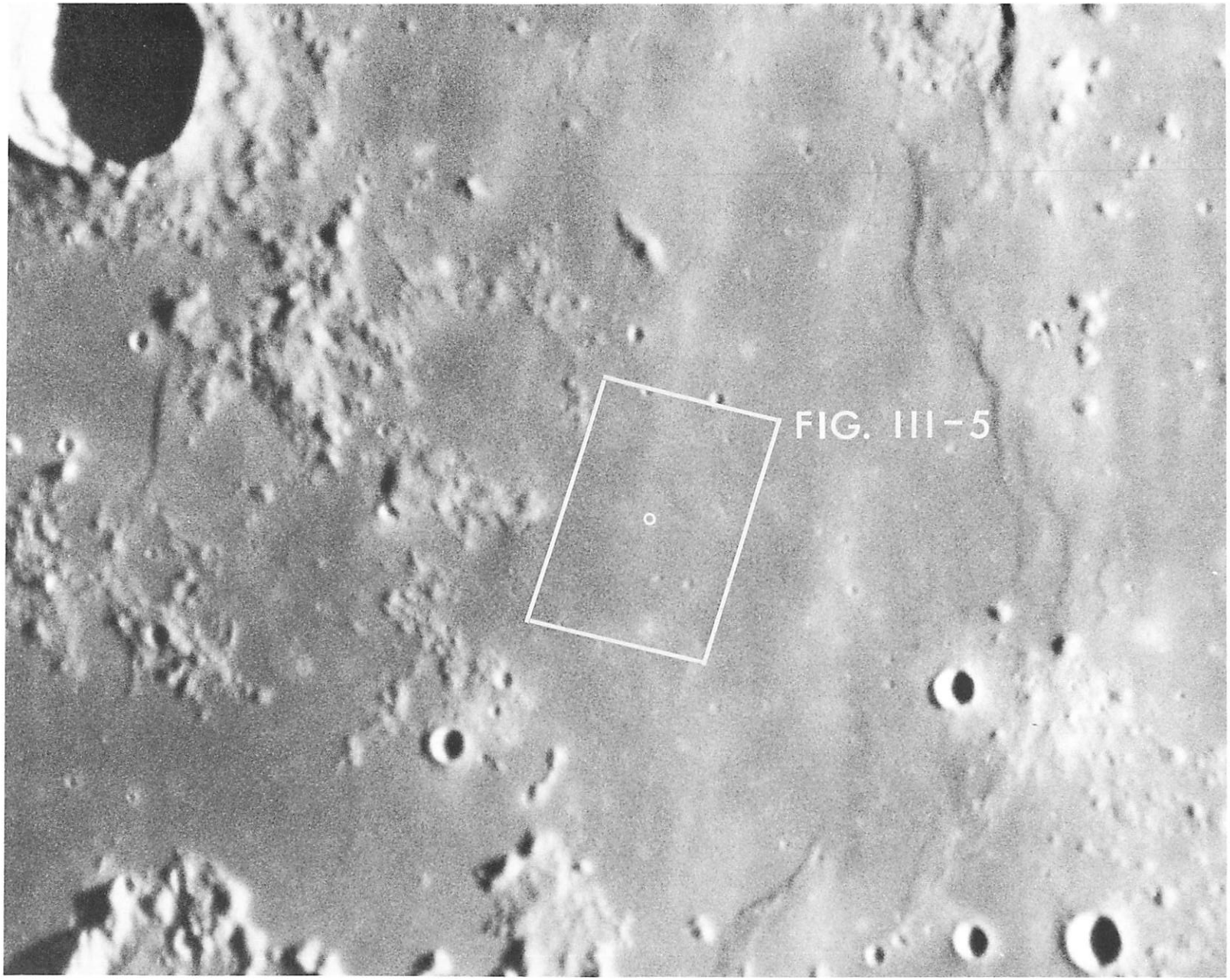

Fig. III-2. Crater Lansberg and region to southeast showing *Surveyor III* location (small circle) and outline of *Lunar Orbiter III* photograph M154 (University of Arizona Lunar and Planetary Laboratory 61-in. reflector photograph)

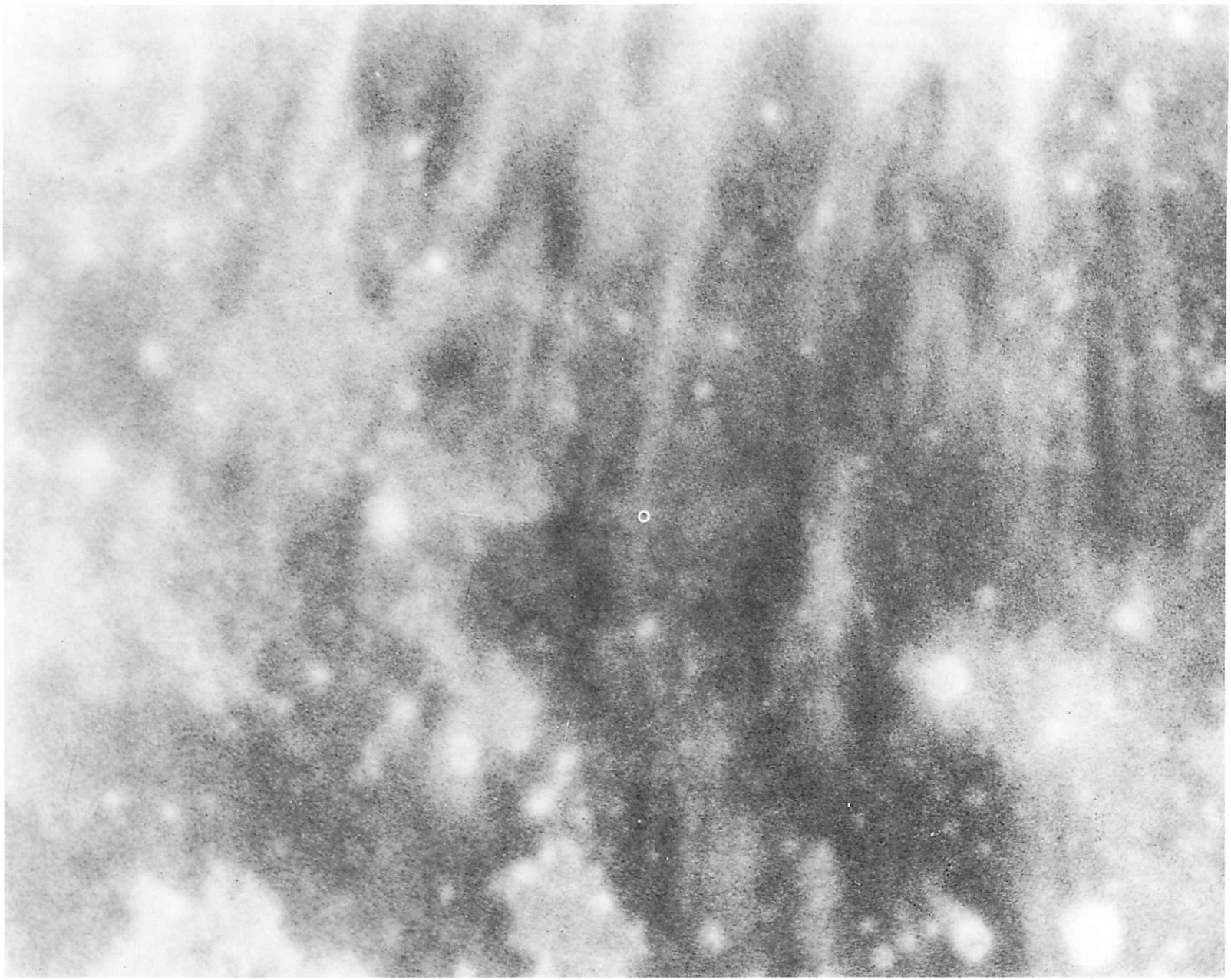

Fig. III-3. Same region as Fig. III-2 with full-moon illumination, showing relationship between *Surveyor III* location (small circle) and Copernicus rays (Yerkes Observatory 40-in. refractor photograph)

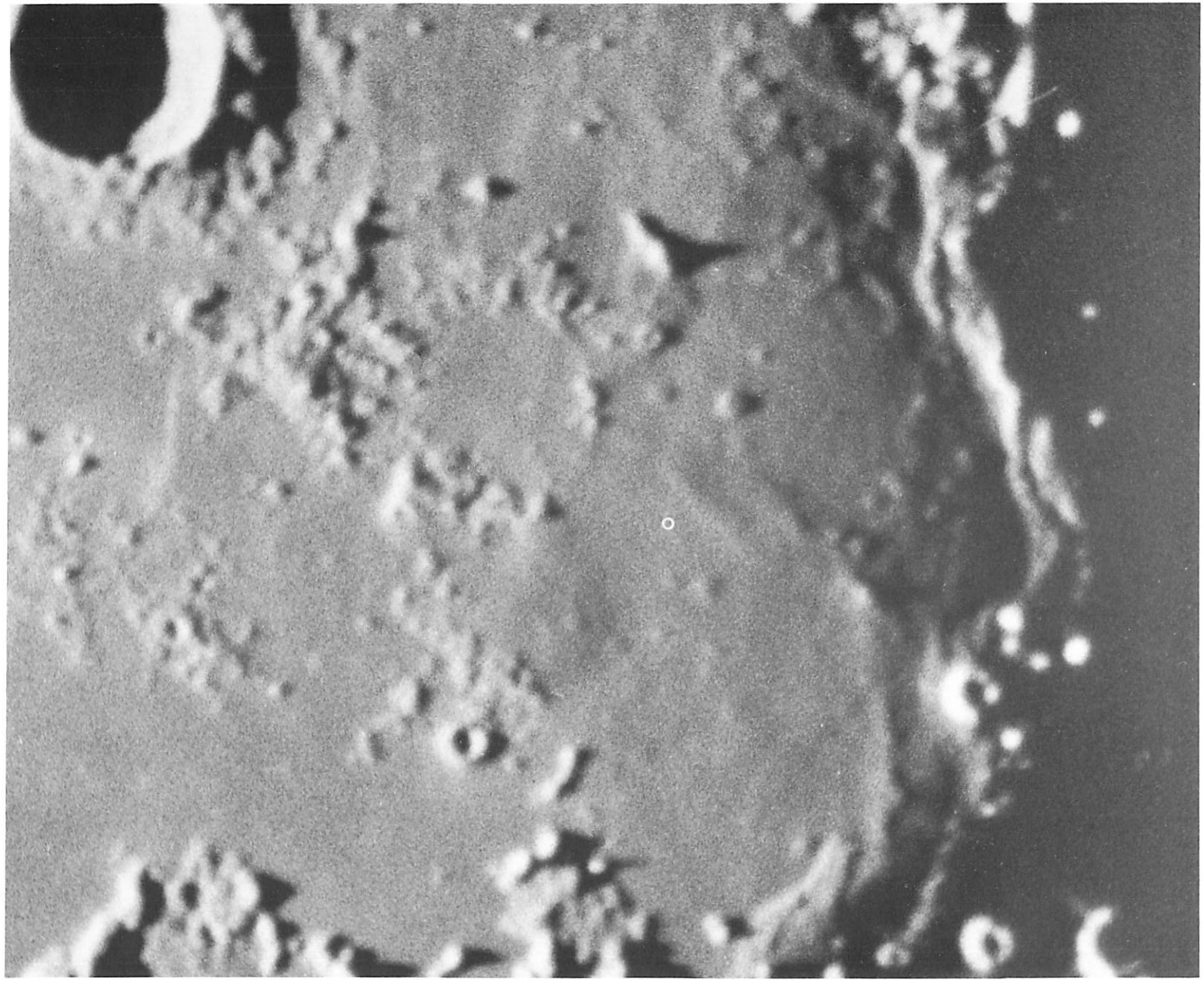

Fig. III-4. Same region as Figs. III-2 and III-3 with low evening illumination, showing low mare ridge segments northeast of *Surveyor III* (McDonald Observatory 82-in. reflector photograph)

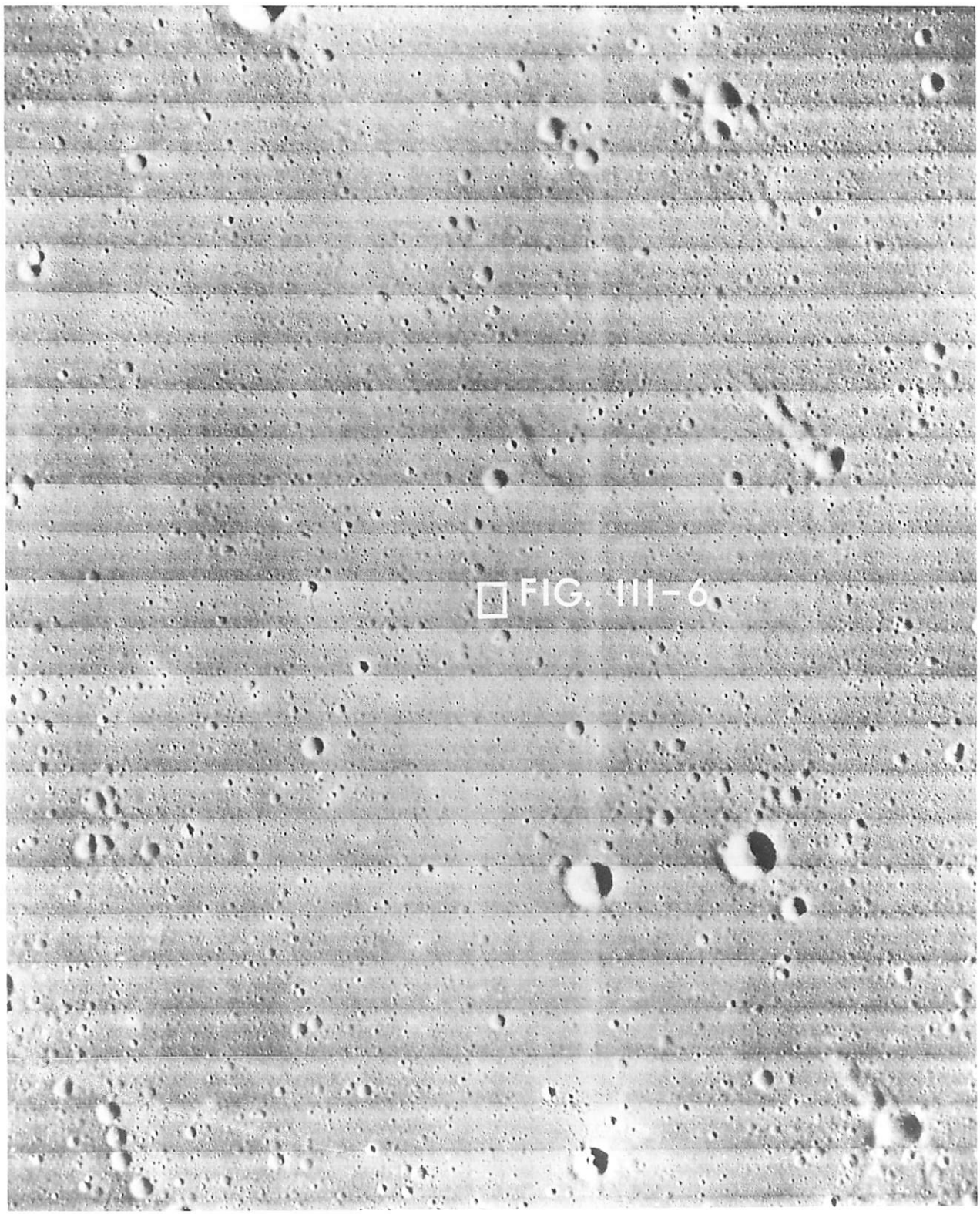

Fig. III-5. *Lunar Orbiter III* medium-resolution photograph M154 showing outline of Fig. III-6

A study of preliminary mosaics of wide-angle *Surveyor III* pictures showed that the spacecraft had landed on a west-facing surface sloping about 10 deg to the horizontal; the average level of the horizon was about 5 deg higher than nominal for a flat surface. These data implied that the spacecraft was situated on the inner east wall of a shallow crater.

A comparison with *Surveyor I* panoramas of narrow-angle surveys of areas to the north and south of the spacecraft suggested that the horizon lay at least 50 m away, indicating the crater in which the spacecraft landed had a diameter of 100 m or more. These surveys also showed several small, but distinct, craters and a number of blocks, estimated to be large enough to be visible on *Lunar Orbiter III* photograph H154. A rough plan of the crater and its details was drawn and memorized, and the general pattern searched for in all craters 50 to 250 m in diameter in the central third of H154.

A crater was found that seemed to have the correct disposition of small craters and rocks; measurements of azimuths of these features confirmed the identification. Figure III-6, an enlargement of a part of H154, shows this crater and its immediate surroundings. The crater has a diameter of approximately 200 m, and a depth of about 15 m. The selenographic coordinates of *Surveyor III* determined from the *Lunar Orbiter III* photograph and the ACIC map are 2.94°S latitude, 23.34°W longitude.

C. Topography of *Surveyor III* Landing Site and Attitude of Spacecraft

The crater in which *Surveyor III* landed is one of a family of craters of subdued topographic form that occupies more than 50% of the surface of this part of the Oceanus Procellarum. The rim of the crater is low and gently convex upward; the position of its precise crest is difficult to define. Slopes within the crater range between about 10 and 15 deg on the steepest parts of the crater wall, exclusive of the walls of smaller superposed craters. The floor of the crater is gently concave upward and merges imperceptibly with the sloping walls. A profile across the center of the crater shows a reversal of curvature approximately halfway between the center of the crater and the rim crest, both in vertical and radial positions (Fig. III-7).

About 100 small craters, resolved in photographs from *Lunar Orbiter III*, are scattered over the floor, inner slopes, and rim of the larger crater in which the spacecraft is located. These small craters range from 1 to 25 m in diameter. Many of them are subdued in form, with gentle interior slopes and rounded rims. A few, however, have sharp, raised rims and steep inner walls. In addition, the inner surface of the main crater is strewn sparsely with coarse blocks, most of which are spatially associated with three of the largest superposed small craters.

1. Topographic Maps

Topographic maps of the *Surveyor III* landing site have been prepared by two independent methods. One method utilizes the photometric information contained in a single high-resolution *Lunar Orbiter III* photograph of the site. The technique by which photometric data from a lunar picture are reduced to topographic profiles and maps is called photoclinometry. The other method utilizes information on the angular position of objects identified both in a high-resolution *Lunar Orbiter III* photograph and in the *Surveyor III* pictures. This method is an application of analytical photogrammetry. The photoclinometric technique provides extensive information about the over-all shape of the main crater in which *Surveyor III* is located, whereas the photogrammetric method provides accurate information on the three-dimensional position of a limited number of points on the lunar surface relative to the spacecraft.

The photometric method of deriving a surface profile utilizes measurements of scene luminance and an adopted mean photometric function of the lunar maria for determining slope of the surface in the phase plane. Luminance of a small area of the lunar surface has been found from telescopic observations and from *Surveyor I* measurements to depend only on the normal luminance factor or albedo, the phase angle, and the slope of the surface in the phase plane. The phase angle is defined as the angle between the vector to the observer and the vector to the sun from a given point, and the plane containing these two vectors is the phase plane. At any image point in a picture of the lunar surface, where the albedo, the vector to the observer, and the vector to the sun are known, the orientation of the trace of the surface in the phase plane can be determined from a measurement of the surface luminance.

The luminance of elements of the lunar surface can be estimated from measurements of film density in pictures such as those acquired by *Lunar Orbiter III*. To estimate luminance from film density, the transfer characteristic function of the system by which the picture is produced

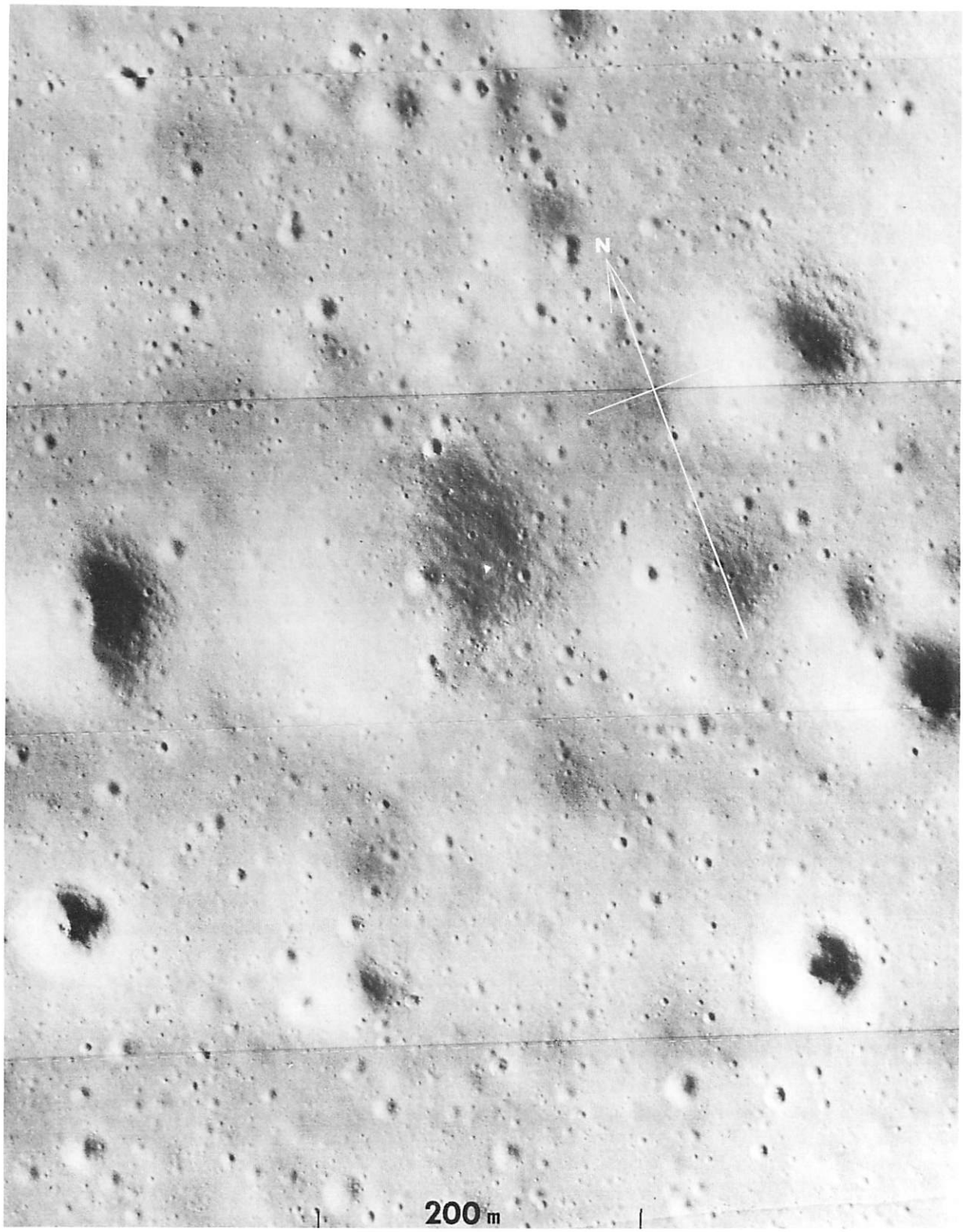

Fig. III-6. Small part of *Lunar Orbiter III* high-resolution photograph H154, showing location of *Surveyor III* in 200-m-diameter crater. The small triangle represents the true size and orientation of the spacecraft

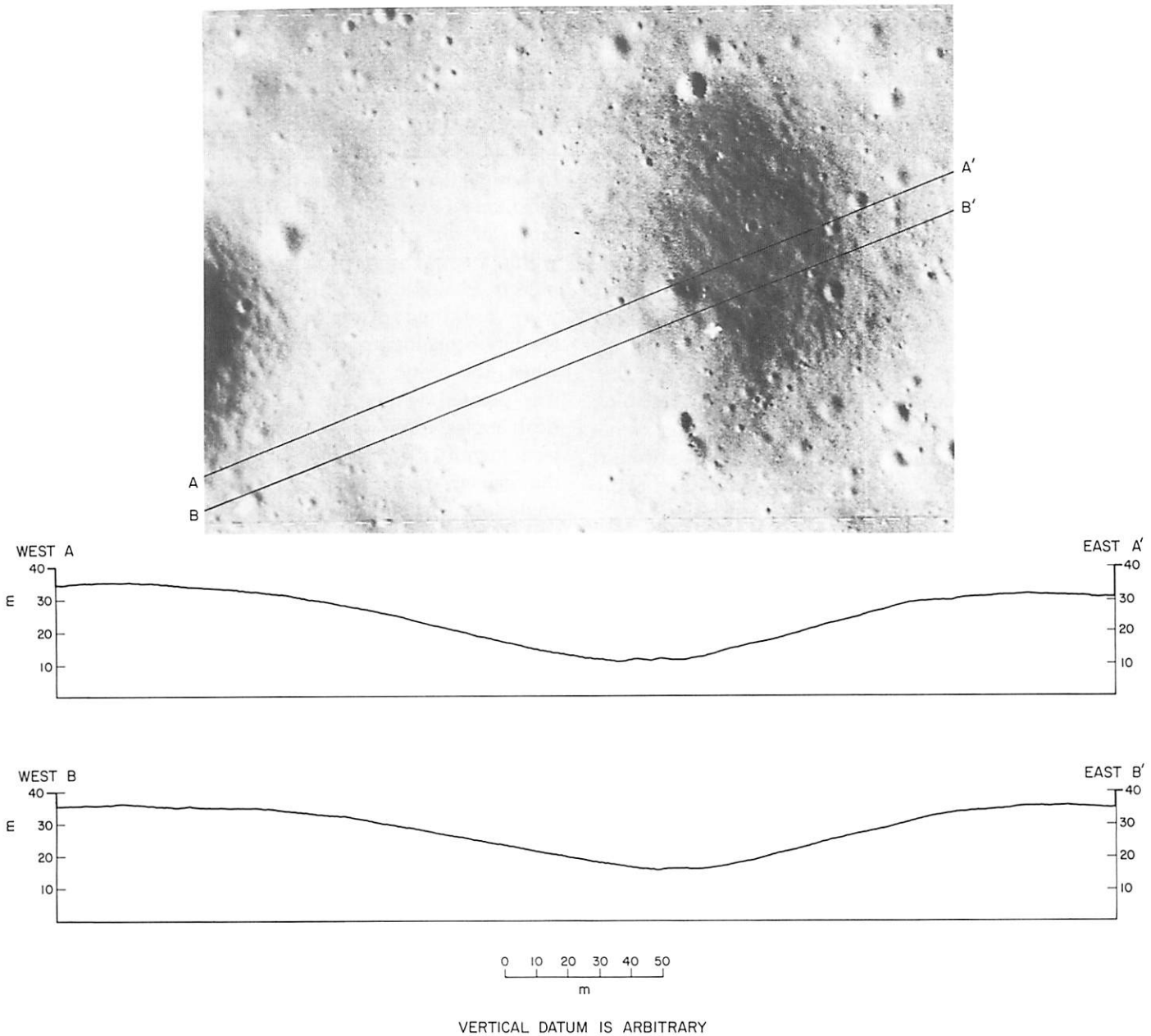

Fig. III-7. Photoclinometric profiles of the *Surveyor III* landing site. Profiles were calculated from photometric measurements of *Lunar Orbiter III* photograph H154, framelet 27, along lines AA′ and BB′ (photoclinometry by H. E. Holt and S. G. Priebe)

must be known from preflight or internal calibration, or some other method of estimating this transfer characteristic function must be found.

Variations in density across the negative of the photograph, *Lunar Orbiter III*, P-9C, H154, framelet 027, were measured along 54 phase plane traces with a microdensitometer. From about 110 to 150 digitized measurements were obtained along each trace; each measurement represented about 6 m^2 on the lunar surface. The density measurements were converted to estimated luminance by multiplication by a luminance factor. The luminance factor is derived from comparison of computed luminances to the measured densities of several areas whose orientation was determined by means of subjective photointerpretation. Thus, the system transfer characteristic function was assumed to be linear. This form of the function was adopted for simplicity of calculation, inasmuch as accurate calibration for the *Lunar Orbiter III* imaging system was not available. Any difference between the actual system transfer characteristic function and the assumed linear function would have led to errors in the computed topographic relief.

The slope in the phase plane of each surface element along each phase plane trace was computed from the estimated luminance for each image element, using the terrestrially measured mean lunar photometric function for the lunar maria. These slopes were connected to form profiles of the lunar surface along each phase plane trace. The profiles, which are nearly vertically oriented, were placed side-by-side in relative positions, according to the locations of their starting points. Relative elevations between adjacent profiles were derived from the assumption that the rim crest of the crater in which *Surveyor III* landed is approximately level, an assumption that appears to be justified from stereoscopic examination of *Lunar Orbiter III* photographs H154 and H137.

The general outline of the crater rim crest, obtained from adjustment of the phase plane profiles, and the relative elevation of more than 300 points taken from the profiles were plotted on a map. Contour lines were drawn, on the basis of these points at vertical intervals of 2 m. The resulting contour map (Fig. III-8) shows that the crater ranges from 220 to 240 m in diameter. The depth of the crater derived by photoclinometry is 18 m, and the average slope from the center of the crater to the rim crest is 10.5 deg. Near the vicinity of the *Surveyor* spacecraft the slope of the crater wall derived by photoclinometry is about 14 deg.

By close comparison of the *Surveyor III* pictures with the *Lunar Orbiter III* photograph of the *Surveyor III* landing site, it is possible to identify more than 100 craters and large blocks. Because the number of these features is so large, it is possible to use the information obtained from the two sets of pictures to produce a topographic map of the crater by methods analogous to ordinary field surveying, after a solution was obtained of the orientation of the *Surveyor III* camera. The planimetric position of the camera was located by resection within the main crater (in which the spacecraft landed) to within 0.5 m, relative to the objects identifiable in the *Lunar Orbiter III* photographs; the azimuthal orientation of the camera and the spacecraft was found to within 1 deg. Distances from the *Surveyor III* camera to objects identifiable in the *Lunar Orbiter* photographs were obtained directly from *Lunar Orbiter* high-resolution photograph H154. This photograph was taken when the optic axis of the high-resolution camera was pointed within about 2 deg of the vertical. Vertical angles from the *Surveyor III* camera to the objects identified in the field of view were obtained from the camera mirror azimuth angle and the elevation angle telemetry and from positions of objects within the *Surveyor* pictures. These data were used to obtain elevations of points on the lunar surface relative to the *Surveyor* camera by elementary trigonometry. A preliminary contour map prepared by this method is shown in Fig. III-9.

Comparison of Figs. III-8 and III-9 shows that the slopes estimated by the photoclinometric technique are slightly steep and the depth of the main crater obtained by this method is, therefore, too great. Adjustment of the slopes derived from the photoclinometric technique to fit the slopes measured with the aid of the *Surveyor III* pictures will provide an improved solution for the functional relationship between densities measured from the *Lunar Orbiter III* negative and the lunar surface luminance. The map prepared by photoclinometry, however, provides a much better definition of the position and shape of the rim crest of the main crater than can be obtained using the *Surveyor III* pictures.

2. Attitude of the Spacecraft

Surveyor III landed on the west-facing east wall of the main crater, southeast of the center of the crater. It lies almost halfway between the center of the crater and the rim crest; the mean elevation of the footpads is about 7 m below the mean elevation of the rim crest.

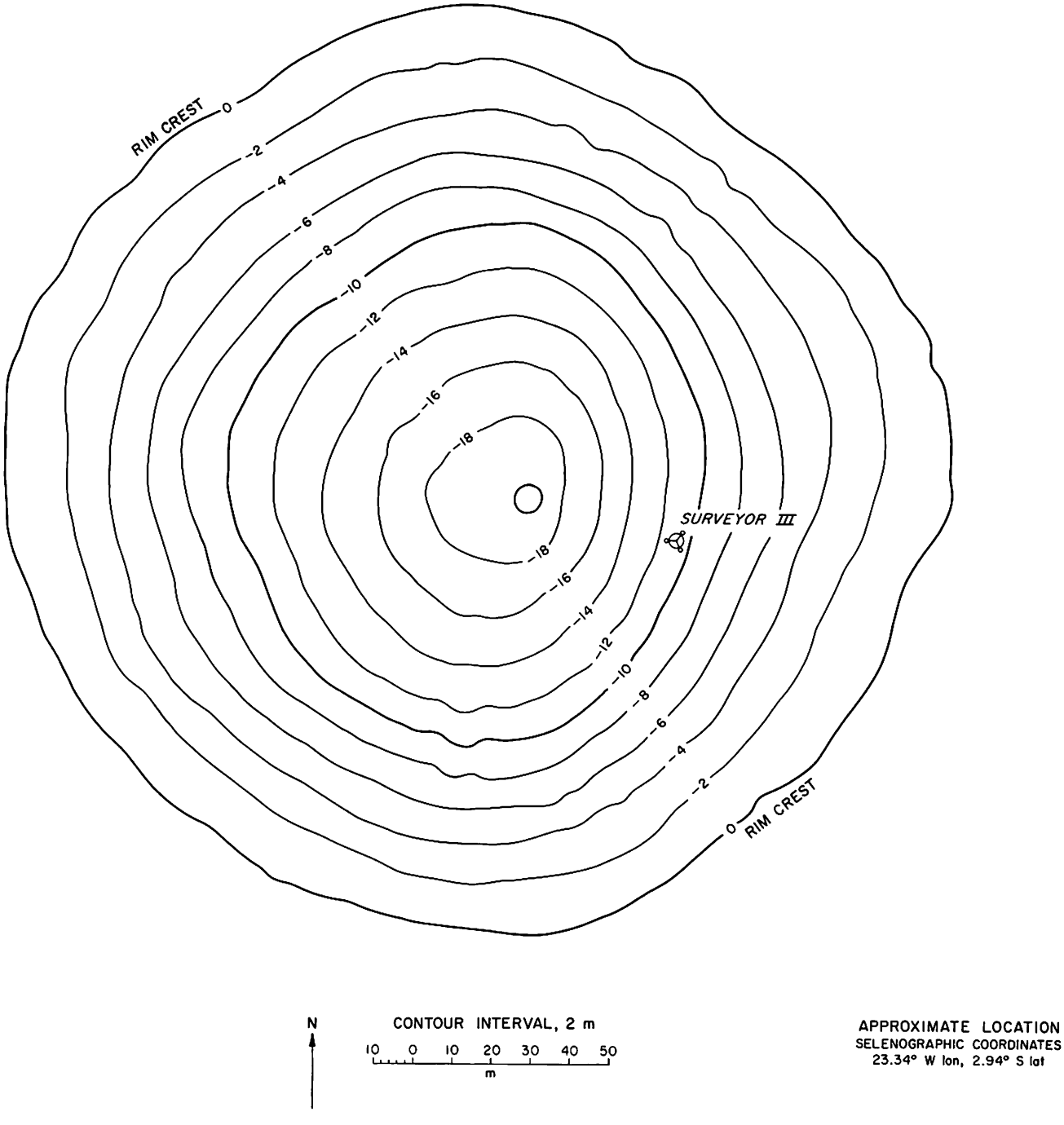

Fig. III-8. Contour map of *Surveyor III* landing site prepared from photoclinometric profiles derived from *Lunar Orbiter III* photograph H154, framelet 27 (photoclinometry by H. E. Holt and S. G. Priebe)

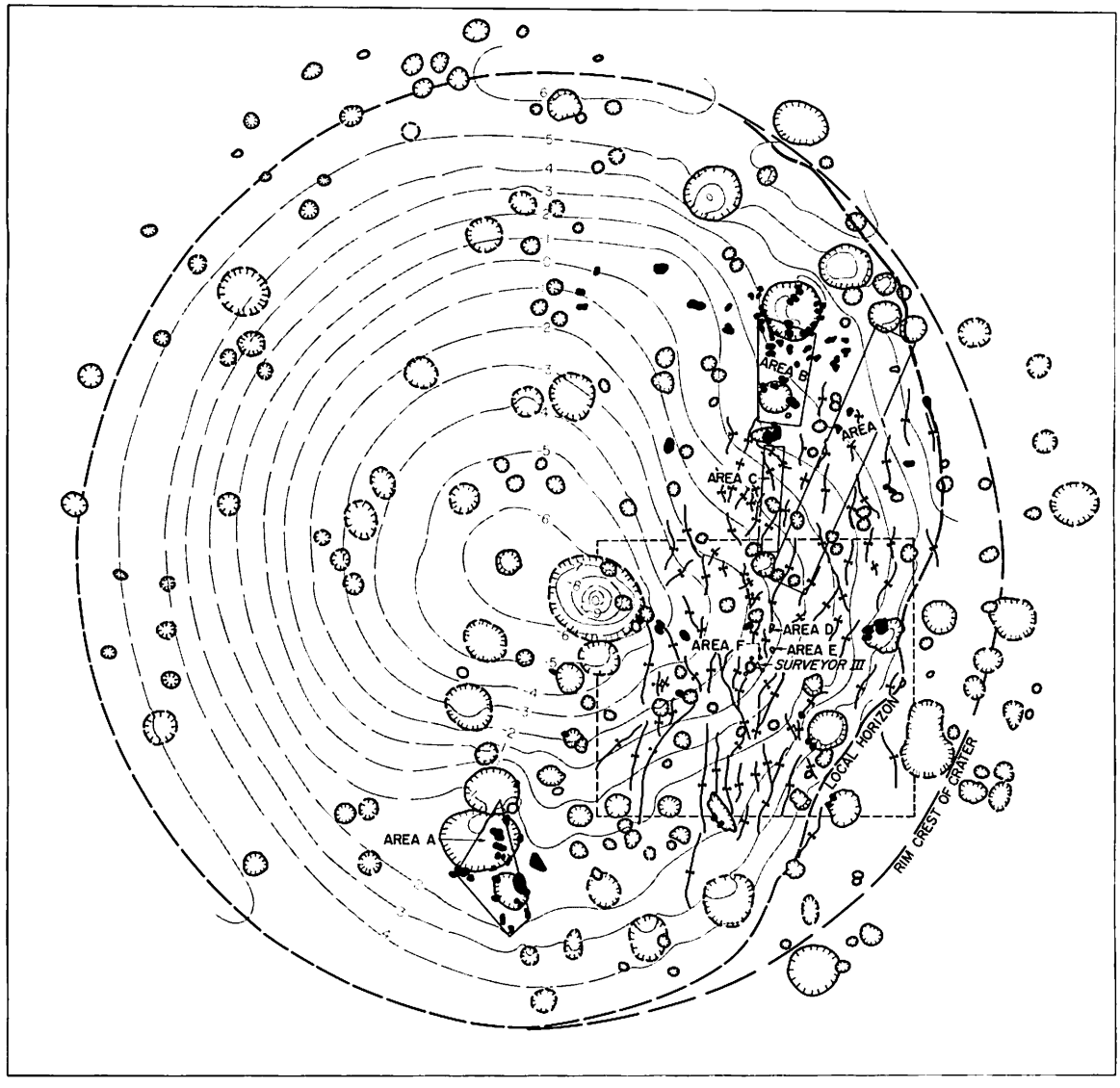

Fig. III-9. Contour map of *Surveyor III* landing site, showing craters and blocks resolved in *Lunar Orbiter III* photographs, the local horizon, as observed from the *Surveyor III* camera, the rim crest of the main crater, and areas studied in detail with the *Surveyor III* pictures. Contours were plotted using information obtained from *Lunar Orbiter III photographs* and from *Surveyor III* pictures (topography by R. M. Batson and Raymond Jordan; geology by E. C. Morris and E. M. Shoemaker)

The attitude of the spacecraft has been estimated by the three following independent methods:

(1) Adjustment of the position of the planar array antenna of the spacecraft so that it provides the maximum signal transmitted to the earth and the solar panel so that maximum rate of charge is obtained. The attitude of the spacecraft can be estimated with the aid of the known radiation pattern of the antenna. The antenna was adjusted slightly on occasion to compensate for libration of the moon, and the solar panel was adjusted to track the sun. Several estimates of position were obtained. Observational data on fine adjustment or tuning of the antenna and the solar panel indicate that the spacecraft is tilted 12.5 ±2 deg in a direction 6.6° north of west.[1]

(2) Observations of the earth and Venus. Preliminary reduction of the observations of the position of the earth and Venus in the television pictures by Rennilson indicates the spacecraft is tilted 13 ±1.5 deg in a direction 6° north of west.

(3) Assumption that the rim crest of the crater in which the spacecraft is located is, on the average, horizontal. Observations of the lunar horizon as seen from the *Surveyor III* camera can be reduced to an attitude for the spacecraft, after corrections have been made for the departure of the horizon from the rim crest. These observations, as reduced by Shoemaker, indicate the spacecraft is tilted 14.8 deg in a direction 6° north of west.

The azimuth of tilt by all methods is found to be very nearly west. Observations of the position of the shadow of the western rim of the crater on the spacecraft and on the eastern wall of the crater, near the time of lunar sunset, provide a very sensitive test of the orientation of the spacecraft. Predictions of the times at which the shadow would be seen at various positions on the spacecraft, derived from observations of the horizon and the attitude derived by Shoemaker, were found to be accurate within about 10 to 15 min. The western component of tilt of the spacecraft was found to be 14.7 ±0.1 deg from observations of the shadow of the western rim. Thus, the spacecraft is tilted very nearly toward the center of the crater at an angle somewhat steeper than the mean local slope of the crater wall, which is 10 deg. The legs of the spacecraft appear to straddle a shallow crater about 2 m in diameter, tentatively identified in the *Lunar Orbiter III* photographs of the site (Fig. III-10); footpad 1, on the downhill side of the spacecraft, lies in a shallow north-trending trough.

Because of the convexity of the crater rim, only the western half of the crest of the rim of the crater in which the spacecraft is located is visible from the camera. The eastern horizon, as seen from the camera, lies 35 m from the camera and is about 1 m below the eastern rim crest. The trace of the horizon is approximately an ellipse tilted to the east; the horizon rises from a point nearest the camera on the eastern crater wall, both to the north and to the south, and approximately coincides with the rim crest west of the camera. The camera is inclined 23.5 deg in a direction 47° north of west; the horizon varies in angular elevation 24 deg above and 20 deg below the plane normal to the camera axis. When plotted on a cylindrical projection about the camera axis, the trace of the horizon in camera coordinates is very nearly a smooth sine wave of 44-deg amplitude and 360-deg wavelength (Fig. III-11). The maximum of the sine wave lies approximately in the direction of maximum tilt of the camera.

D. Geology of *Surveyor III* Landing Site

Small morphologic elements of the landing site include small craters, linear ridges and troughs, and fragmental debris. Small craters account for the irregularities of largest relief on the inner surface of the main crater in which *Surveyor III* landed; they are, however, difficult to observe in the pictures because of glare and because the best pictures were obtained under conditions of high sun. A well-developed system of low-amplitude ridges and troughs was found on the walls of the main crater and is well portrayed in the *Lunar Orbiter III* photographs of the landing site. These ridges and troughs are part of the patterned ground characteristic of this part of the Oceanus Procellarum and are probably related to a set of subsurface fractures. The relief of the ridges and troughs is so small, however, that they have not been detected in the *Surveyor III* pictures.

Fragmental debris is readily observed on both the *Lunar Orbiter III* photographs and the *Surveyor* pictures of the landing site. Blocks ranging from 0.5 m to several meters across are detectable in the *Lunar Orbiter III* photographs, and grains and lumps as small as 1 mm are observable close to the spacecraft in the *Surveyor III*

[1]Computation of the attitude of spacecraft from orientations of the planar array antenna was carried out by Robert Lackman at the Hughes Aircraft Company.

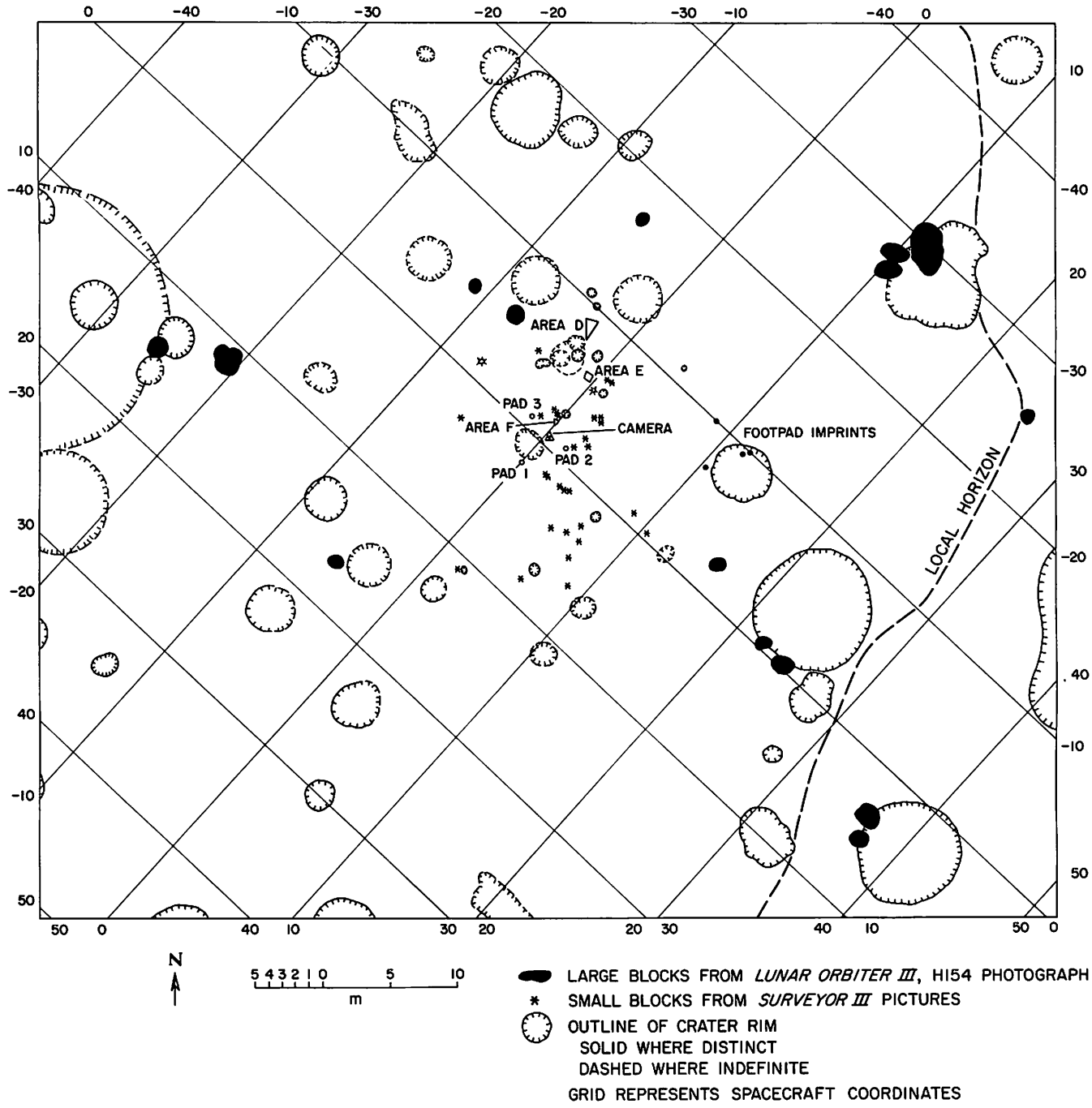

Fig. III-10. Detailed planimetric map of area around *Surveyor III* spacecraft, showing craters and blocks, the local horizon, areas studied for size distribution of fragmental debris, the present position of the footpads and camera of *Surveyor III*, and the position of footpad imprints made during the second touchdown of the spacecraft. The position of the spacecraft is known to within about 0.5 m relative to craters and blocks resolved on the *Lunar Orbiter III* photographs

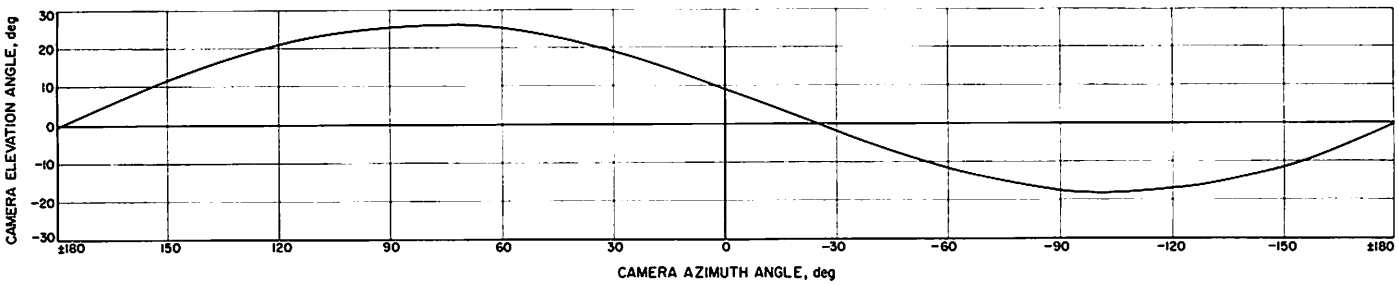

Fig. III-11. Running average trace of the horizon seen from *Surveyor III* camera, plotted on cylindrical projection in camera coordinates

pictures. The most easily extracted information about the geology of the landing site in the *Surveyor III* pictures is related to the distribution and characteristics of the fragmental debris and of the layer of this debris, or regolith, which is inferred to underlie the observed surface.

1. Small Craters

The craters observed in the *Surveyor III* pictures range in diameter from about 10 cm to about 16 m. Most of the craters smaller than 3 m in diameter are relatively shallow and nearly rimless or have very subdued raised rims. Approximately 25% of the craters that range from 3 m to approximately 13 m in diameter have distinctly raised rims and relatively steep walls; the other craters in this size range are of subdued form. The rims of most craters are composed of material similar in texture to parts of the surface between the craters. It may be inferred that most of the small craters have been excavated in fragmental material similar to that exposed at the surface.

Most craters have a normal cup shape, with walls and floors concave upward; however, one prominent crater over 20 m across, located near the center of the main crater, is dimple-shaped. Most of the craters appear to be irregularly or nearly randomly distributed over the rim, walls, and bottom of the main crater, but some of the very shallow rimless craters are aligned approximately in the north-south direction, parallel to one of the major lineation directions of the patterned ground. These aligned craters are probably related in origin to the patterned ground; they may have been formed by subsidence or by drainage of fragmental debris into fractures or fissures. A few irregular, elongated depressions up to 5 m long are present on the east wall of the main crater, where the small craters are most easily observed. These irregular depressions are not parallel with the major lineation directions and are inferred to be of secondary impact origin.

The size/frequency distribution of craters on the rim and within the main crater in which *Surveyor III* landed has been estimated by combining data obtained from the *Surveyor III* pictures and from the *Lunar Orbiter III* photographs. The frequency distribution of craters ranging in size from 25 cm to 4 m was estimated from one sample area (area 1, Fig. III-12) on the northeast wall of the main crater, for which usable *Surveyor* pictures were obtained in the early lunar morning. In an area of 450 m^2, 79 craters were counted. From the *Lunar Orbiter* photograph, 95 craters ranging in diameter from 4 to 25 m were counted in an area of 49,000 m^2. The combined distribution is compared in Fig. III-13 with the mean crater frequency distribution obtained from *Ranger VII* through *IX* pictures and a revised crater distribution obtained from *Surveyor I* pictures. It can be seen that the crater size/frequency distribution of the *Surveyor III* landing site is closely similar to the mean distribution observed on lunar plains by *Rangers VII* through *IX* in the size range of 1 to 16 m. A low frequency observed for the *Surveyor III* site, in the size range of 25 cm to 1 m, probably is due to incompleteness of the observational data rather than to an actual crater deficiency at the *Surveyor III* landing site. The revised crater frequency distribution obtained for the *Surveyor I* site for craters smaller than 1 m closely approximates the projected mean crater frequency distribution obtained from *Ranger VII* through *IX* pictures. Very shallow craters smaller than 1 m were easier to recognize in the *Surveyor I* pictures, as compared with *Ranger* and *Surveyor III* pictures.

2. Patterned Ground

Lunar patterned ground consists of one or more sets of parallel ridges and troughs, which generally have amplitudes of a few tens of centimeters and wavelengths

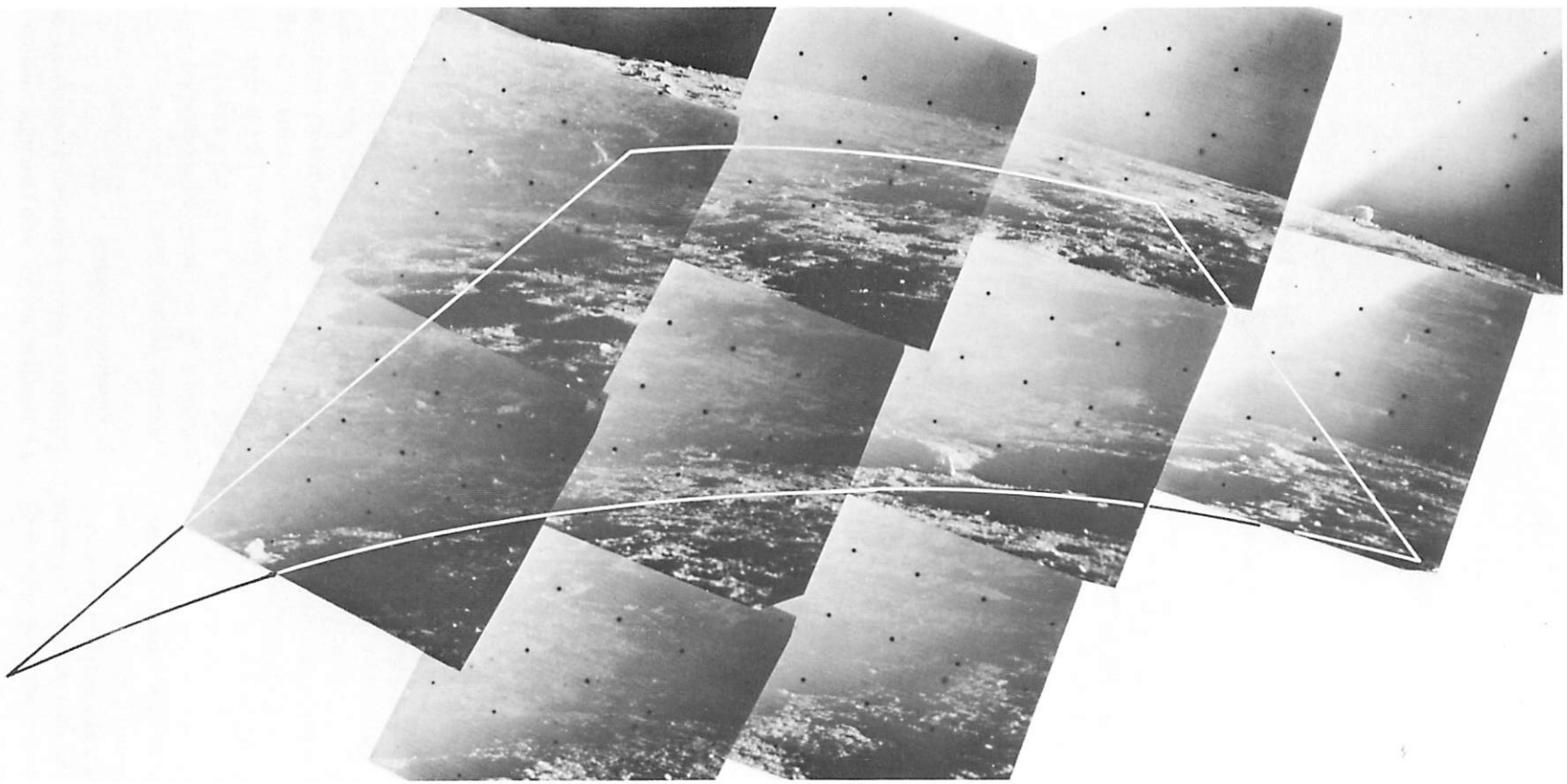

Fig. III-12. Mosaic of narrow-angle *Surveyor III* pictures, showing part of northeast wall of crater in which the spacecraft is located. The crater wall is illuminated by the glancing rays of the early morning sun, which reveals a large number of small craters and many angular fragments of debris strewn across the wall of the main crater. Outline shows boundary of area 1, which was studied for the size/frequency distribution of small craters (Day 110, 09:37:21 to 09:37:56 GMT)

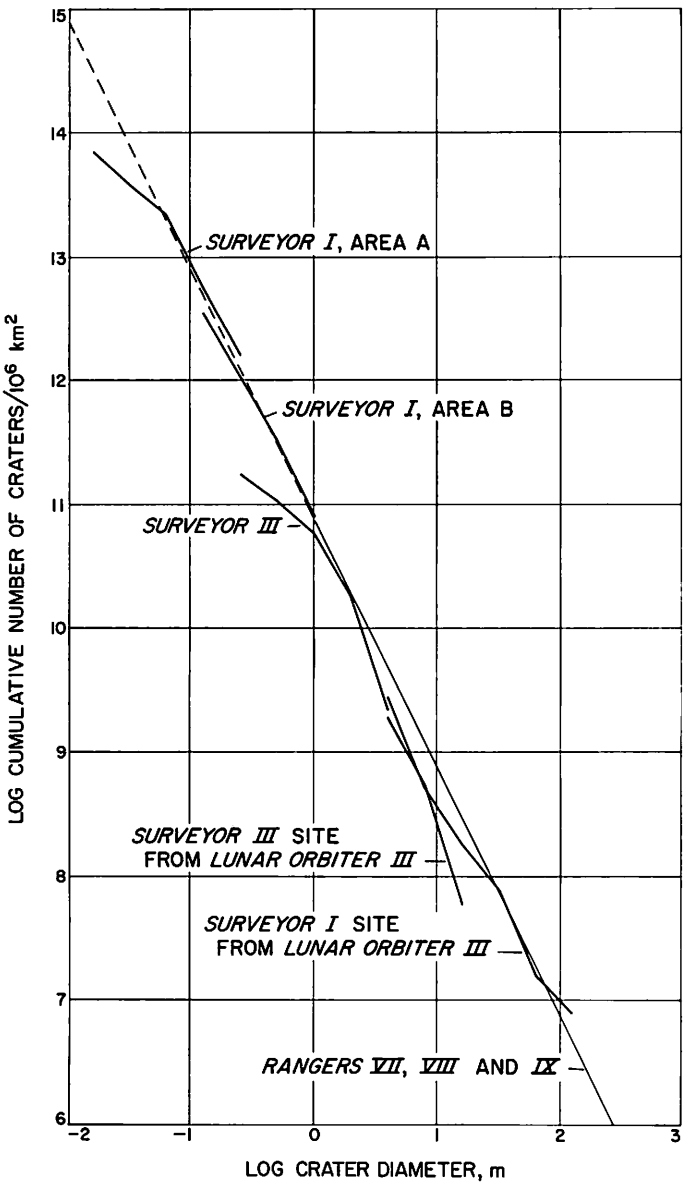

Fig. III-13. Size/frequency distribution of small craters at *Surveyor III* landing site compared with the size/frequency distribution of craters estimated for the *Surveyor I* landing site and the mean size/frequency distribution of small craters on lunar plains determined from *Ranger VII, VIII,* and *IX* pictures. The size/frequency distribution of craters at *Surveyor III* landing site was measured from *Surveyor III* and *Lunar Orbiter III* photographs

on the order of from 5 to 10 m. This pattern is well developed at the *Surveyor III* landing site, where the long axes of the ridges and troughs trend in two dominant directions, one slightly west of north and the other about 30° east of north. The intersection of the two ridge and trough sets gives a corrugated appearance to the surface when it is illuminated at very low angles by the sun. The east wall of the main crater was illuminated in such a manner at the time that *Lunar Orbiter III* photographs were taken; only in this part of the crater is the pattern detectable.

Certain rows of subdued craters and more pronounced troughs are oriented parallel with the north-trending element of the patterned ground at the *Surveyor* landing site. The pattern is inferred to be controlled by underlying fractures or joints; it may have been developed and sustained by mass movement of fragmental material on the surface, perhaps during seismic agitation, and by drainage of surficial fragmental debris into open joints. A majority of craters aligned in rows parallel with the pattern are inferred to have developed either by subsidence of joint blocks, or like the troughs in the patterned ground, by drainage of surficial debris into fissures that are opened and closed by shaking from nearby impact events.

3. Fragmental Debris

Bright angular-to-rounded pieces of fragmental debris are the most conspicuous features in the *Surveyor III* pictures. The observed fragments, which range in size from about 1 mm to 4 m in longest dimensions, are scattered somewhat irregularly and, in most places, sparsely over most of the visible parts of the lunar surface. Except in two prominent strewn fields of coarse blocks, the resolvable fragments occupy no more than about 14% of the surface.

Most of the observed fragments are relatively angular, but some well-rounded fragments are also present which, in most places, appear to be buried deeply in the lunar surface. On the whole, the fragments tend to be equant in shape, but some are distinctly tabular and a few have the form of sharp, narrow wedges. In a few cases, the edge of a wedge-shaped fragment protrudes from the lunar surface in such a way as to resemble a spike or hatchet blade (Fig. III-14).

All of the recognizable fragments are conspicuously brighter at high sun than the rest of the lunar surface. Although the brightness, in part, depends on the orientation of the surfaces of the fragments, it is clear that the fragments have a higher albedo, in some cases perhaps as much as 30% higher than the average albedo of the rest of the surface.

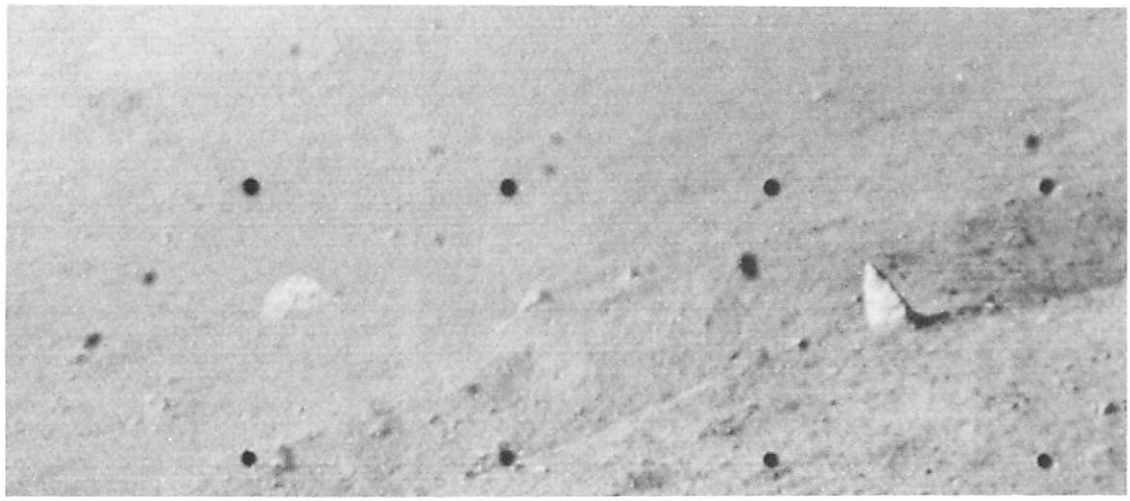

Fig. III-14. Part of narrow-angle *Surveyor III* picture, showing area on northeast wall of crater in which the spacecraft is located. Two craters, about 1.5 and 2 m in diameter, and a wedge-shaped fragment protruding 20 cm above the surface are shown in the picture (Day 120, 14:37:00 GMT)

Over much of the surface, the distribution of fragments appears to be nearly random; locally, however, strewn fields of blocks are present, and at least two examples were found of aligned rows of fragments. In one of these rows lying northeast of the camera, a conspicuously rounded group of fragments runs approximately east-west. These aligned groups of fragments may represent small elements of rays of nearby or distant craters.

The fragments exhibit all variations of apparent position with respect to the surface, from pieces that appear to rest almost entirely on top of the surface (Fig. III-15) to pieces that appear to be almost completely buried, with only a small part showing. From qualitative examination of the pictures, the impression is gained that, in the average case, about half of the fragment is buried beneath the surface and half protrudes above it. Rounded fragments, in most instances, seem to be more deeply buried than average.

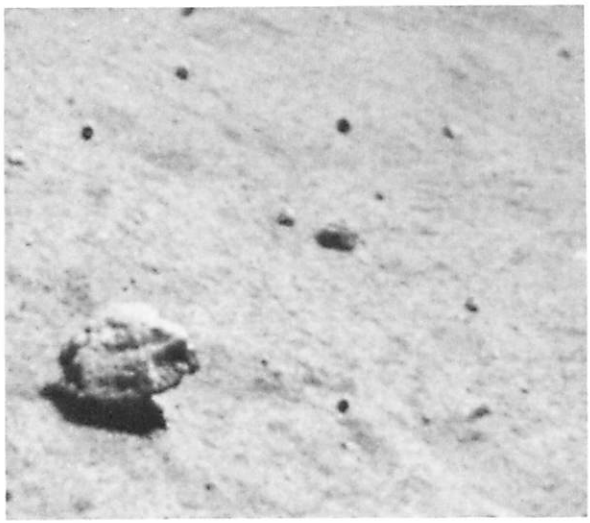

Fig. III-15. Part of wide-angle *Surveyor III* picture, showing rounded fragment 20 cm across lying on top of fragmental debris (Day 116, 09:07:06 GMT)

As in *Surveyor I*, no examples were found in which a fragment seemed to be perched on a pedestal, as reported from the *Luna IX* pictures by Lebedinskiy (Ref. III-2). It is believed that the pedestals reportedly observed in the *Luna IX* pictures are an illusion that is, in part, a result of the lower resolution of the *Luna IX* pictures and of the particular conditions of illumination under which they were taken. This illusion can be experienced in observing some fragments in the *Surveyor III* pictures by viewing the pictures at certain angles and under poor conditions of lighting.

Most of the fragments close to the spacecraft have a peculiar grainy, knobby, or pitted texture. The resolvable pits are generally shallow, but on at least one fragment close to the spacecraft (Fig. III-16) they are nearly as deep as those observed in rock B at the *Surveyor I* landing site. On this fragment, the pits may indicate the presence of vesicles in the fragment. Some fragments, notably pieces associated with a strewn field of blocks to the northeast of the spacecraft, have smooth, nearly planar, faces as though they were broken along preexisting joints or fractures. A number of large blocks,

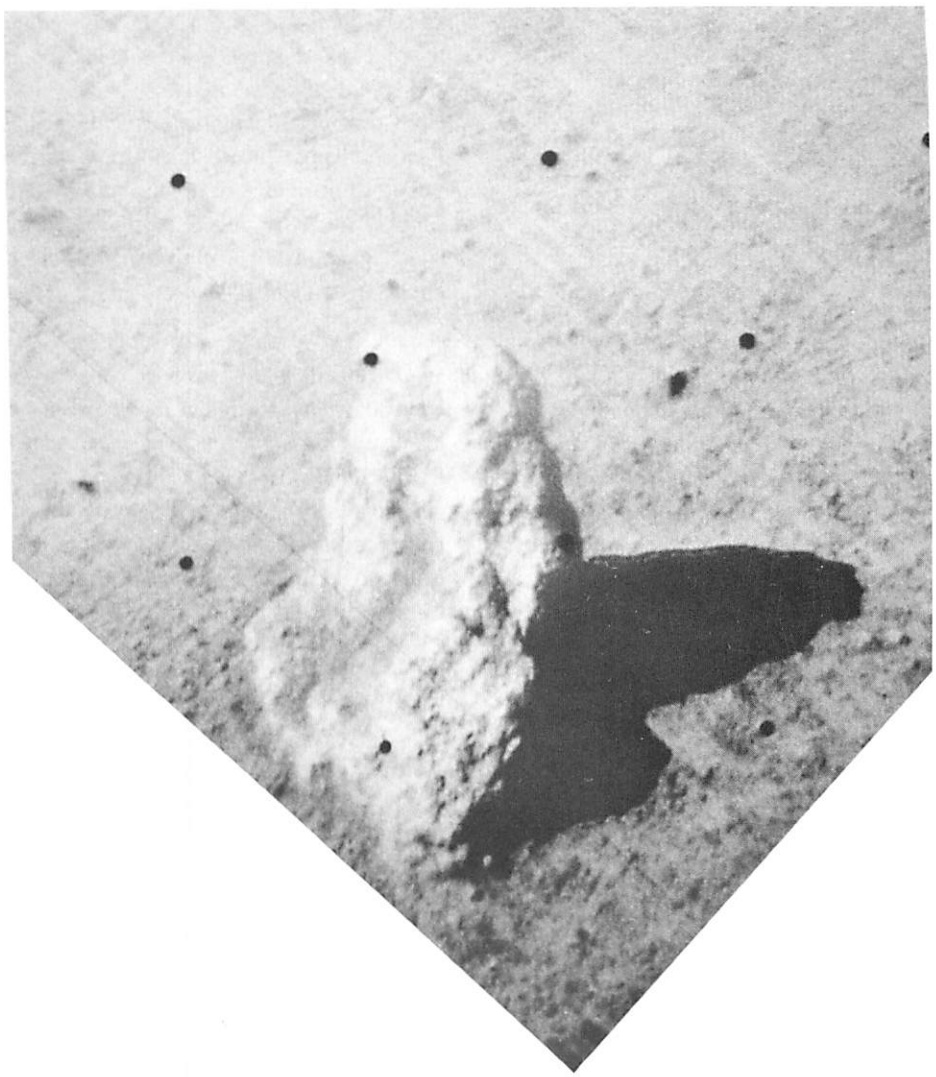

Fig. III-16. Part of narrow-angle *Surveyor III* picture, showing rounded fragment lying close to the spacecraft. Fragment is 13 cm high and has small deep pits on the surface. This fragment, like rock B seen at the *Surveyor I* landing site, may be vesicular (Day 120, 14:51:59 GMT)

most of which are tabular in form, appear to be laminated or contain planes of weakness parallel to the long dimensions of the blocks. The apparent lamination is expressed as grooves and ridges along the narrow sides of the blocks (Fig. III-17).

The coarsest blocks scattered about the surface of the *Surveyor III* landing site occur mainly in two distinct strewn fields. One field (area B, Fig. III-18) is associated with a sharp raised rim crater about 13 m across on the northeast rim of the main crater and the other field (area A, Fig. III-19) with two adjacent subdued craters high on the southwest wall of the main crater. In the case of the strewn field associated with the crater to the northeast (area B), the majority of the blocks are clearly related to the crater, as there is a rapid increase in spatial density of blocks toward the crater. The crater is also occupied by blocks. The blocks outside are inferred to have been ejected from this crater and to have been derived from material that underlies the rim of the main crater at depths only 2 or 3 m below the surface. The observed blocks are strikingly angular and range from a few centimeters (the limit of resolution) to more than 2 m across. Blocks associated with the more subdued craters to the southwest (area A) show a similar range in size, but are more rounded in appearance. The largest of the two southwesterly craters with which these blocks are associated is about 15 m in diameter; it is inferred that most of the blocks were ejected primarily from the larger crater.

In the northeastern and southwestern strewn fields, the size/frequency distribution of the blocks per unit area lies well above the size/frequency distribution for the more typical surface (Fig. III-20). Because of the relatively large size and number of blocks in each strewn field that could be studied in the *Surveyor III* pictures, it has been possible to conduct a preliminary statistical investigation of the roundness and degree of burial of these blocks, and the relationship of roundness and burial to the characteristics of the principal crater associated with each strewn field.

To obtain a measure of roundness that could be used for statistical studies, a descriptive parameter, here called the *roundness factor*, was devised that may be obtained from the pictures as follows: Circles are fitted to all of the corners or curved parts of the outline of each block that occult the more distant lunar scene (Fig. III-21). The geometric mean of the radii of curvature of these corners is divided by the radius of that circle which encloses

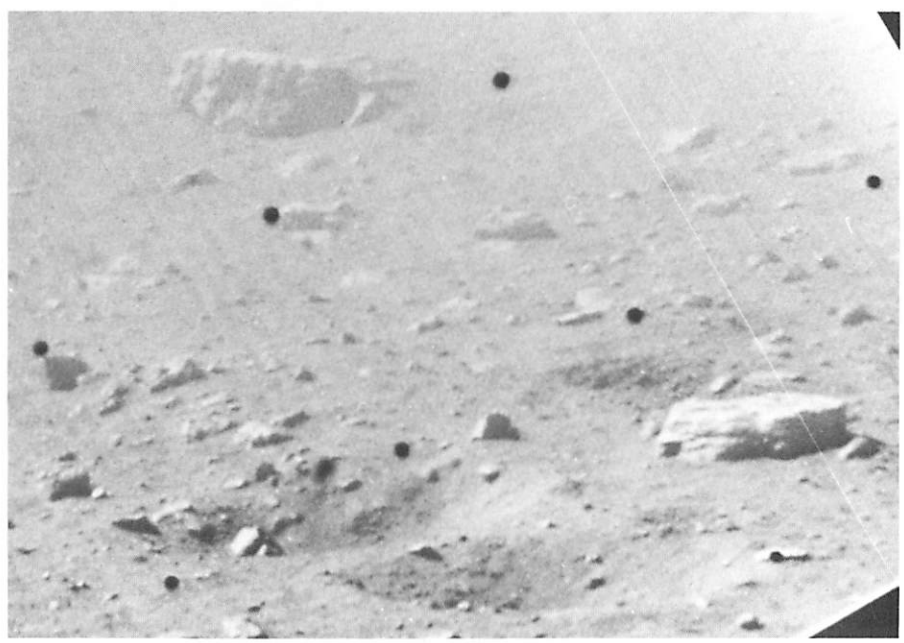

Fig. III-17. Part of narrow-angle *Surveyor III* picture, showing abundant blocky fragments on north wall of crater in which the spacecraft is located. Some of the largest blocks shown are tabular in shape and appear to be laminated (Day 120, 14:52:35 GMT)

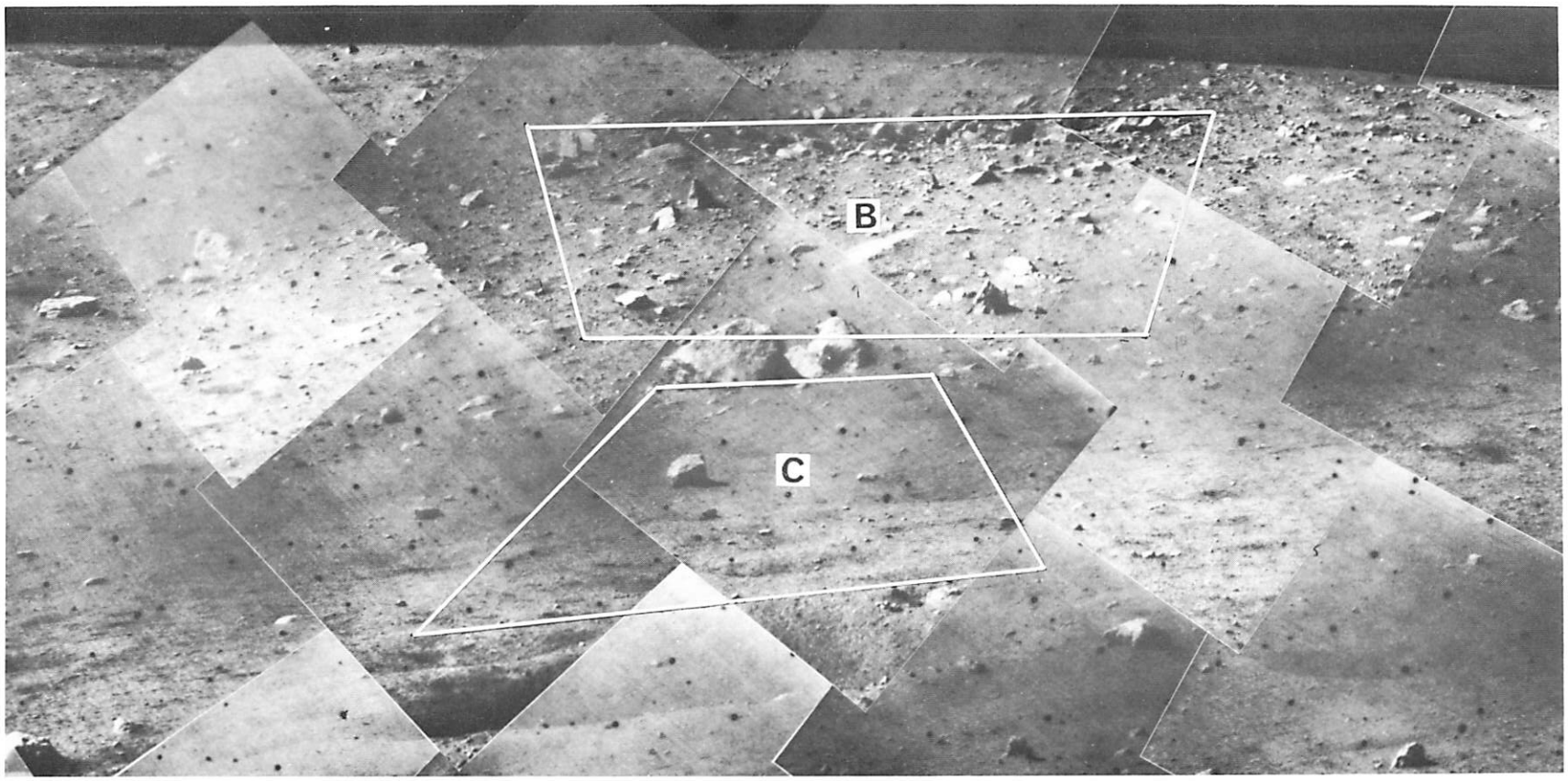

Fig. III-18. Mosaic of narrow-angle *Surveyor III* pictures, showing crater 13 m across and associated strewn field of blocks on northeast wall of main crater in which the spacecraft is located. Outlines show boundary of area B, in which roundness factor and burial factor of blocks were measured, and boundary of area C, in which size/frequency distribution of fragments was measured (Catalog No. 8851)

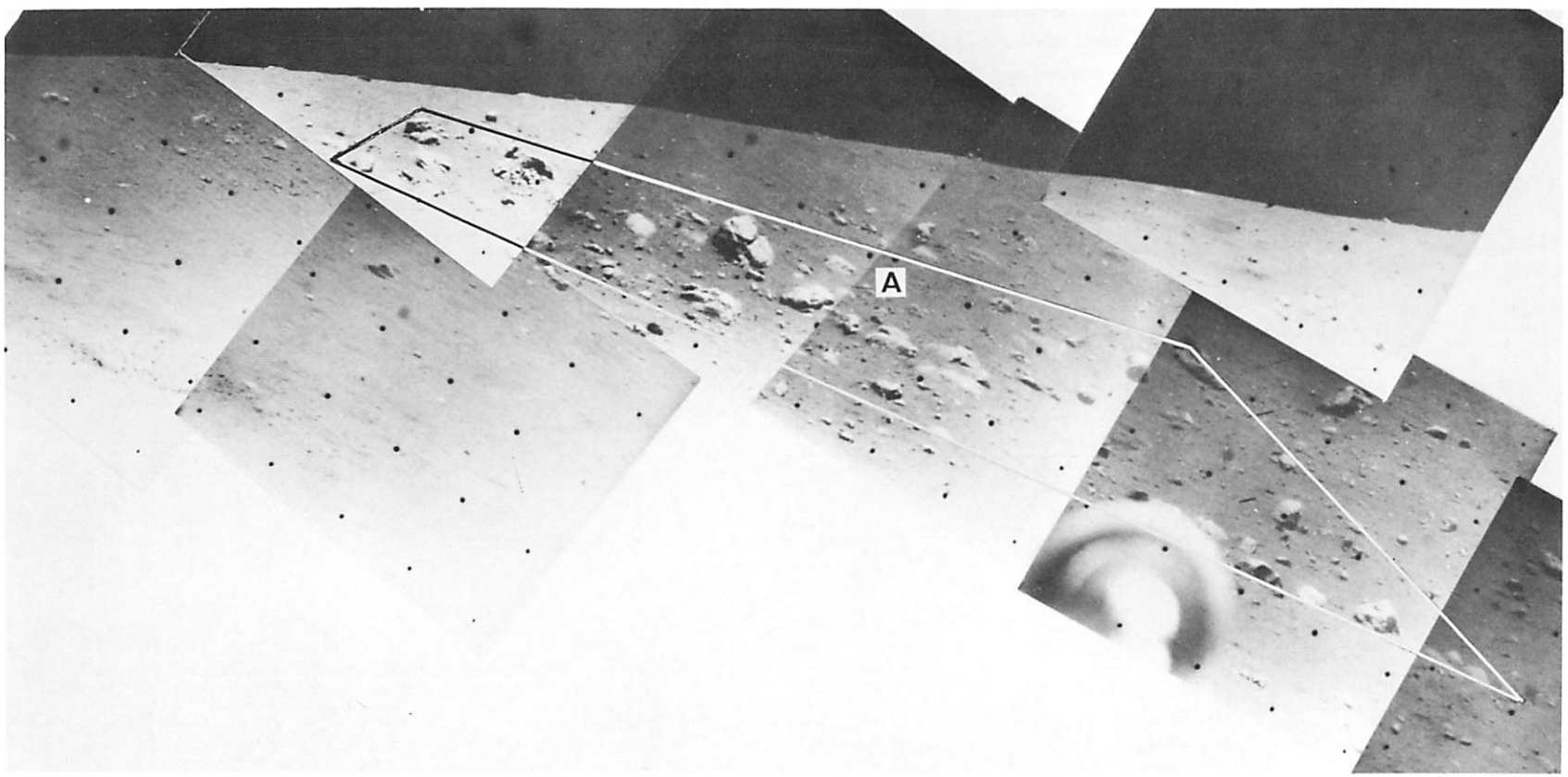

Fig. III-19. Mosaic of narrow-angle *Surveyor III* pictures, showing part of southwest wall of main crater and strewn field of blocks. Outline shows boundary of area A, in which roundness factor and burial factor of blocks were measured. Two subdued rim craters with which the blocks are associated are present, but difficult to discern in these pictures because of high sun illumination
(Catalog No. 87SI, Day 117, 12:49:25 to 13:01:21 GMT)

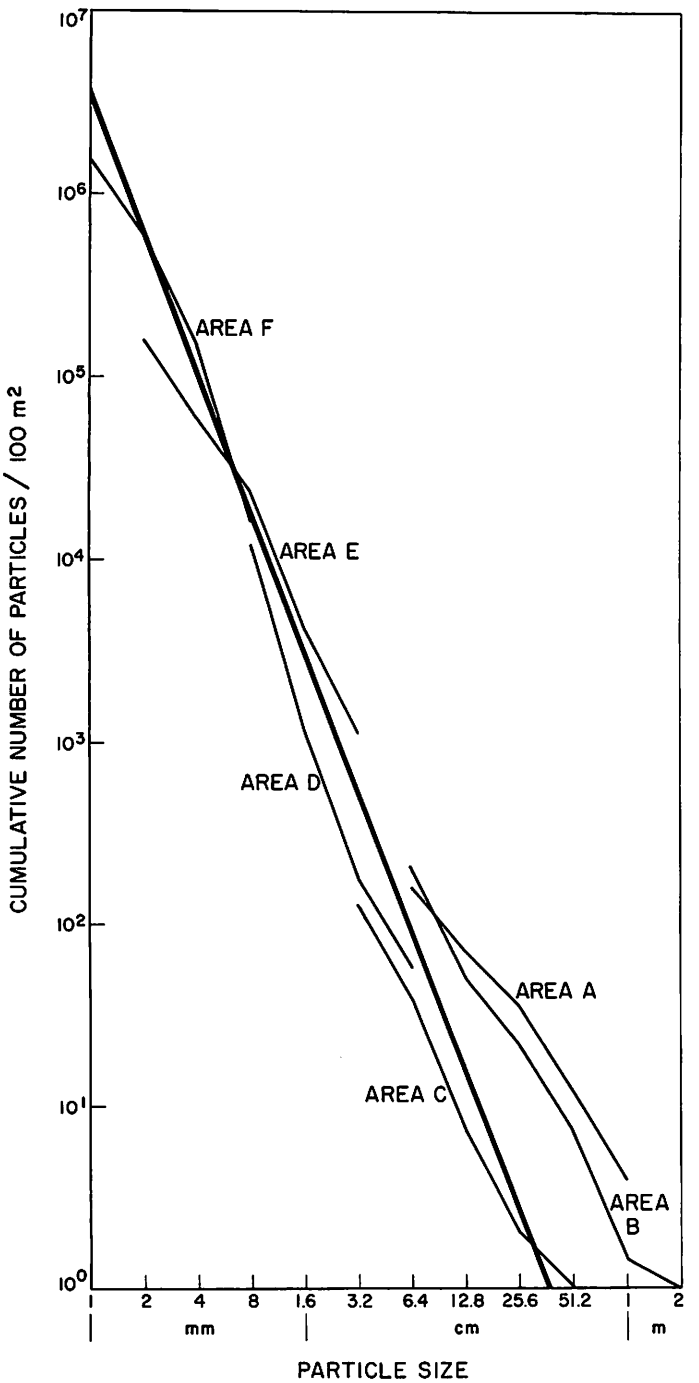

Fig. III-20. Size/frequency distribution of fragments at the *Surveyor III* landing site. Locations of areas A, B, C, D, E, and F, in which the size/frequency distribution of fragments was measured, are shown in Figs. III-9 and III-10. Mean cumulative size/frequency distribution of fragments on characteristic parts of lunar surface at *Surveyor III* landing site is shown with heavy line. This line is the plot of the equation $N = 3 \times 10^6 y^{-2.6}$, where N is the cumulative number of fragments and y is the diameter of fragments in millimeters. Fragments in strewn fields of areas A and B are larger than those observed in the more characteristic parts of the lunar surface

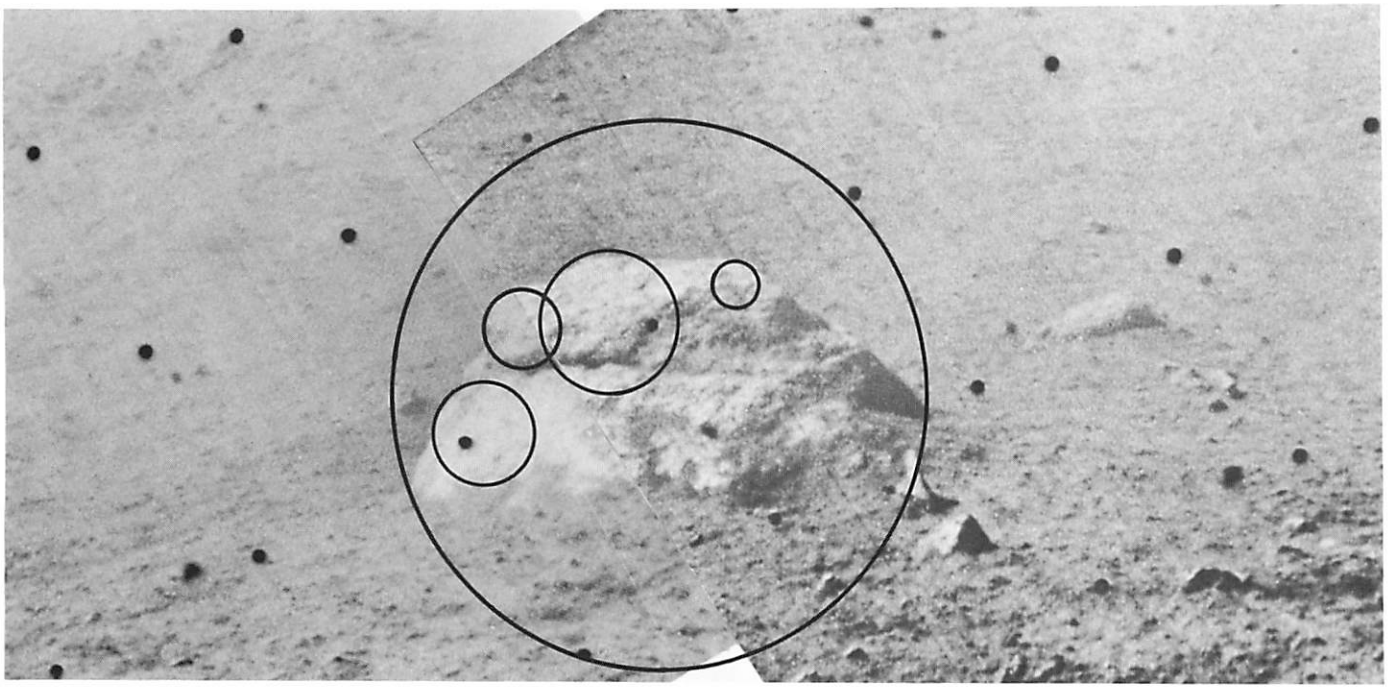

Fig. III-21. Mosaic of two narrow-angle *Surveyor III* pictures, showing block about 0.5 m across close to spacecraft and position and size of circles used in measuring roundness factor. Largest circle encompasses entire block. Smaller circles are fitted to corners and rounded parts of the outline of block that occults the distant lunar scene. The geometric mean of the radii of the small circles divided by the radius of the large circle is defined as the roundness factor (Day 120, 14:54:23 and 14:52:22 GMT)

the outline of the block. This ratio is the roundness factor, and, for blocks that are not deeply buried in the surface, it will vary between the limits of 0 and 1. For very round fragments whose tops are just exposed above the surface, it is possible to obtain values of the roundness factor larger than 1, although no values this high were observed for the blocks measured in the strewn fields.

The roundness factor was measured for 25 blocks located within a confined area in each strewn field (Fig. III-22). Blocks associated with the sharply formed crater to the northeast exhibit a mean roundness of 0.17 with a standard deviation of roundness of 0.11. The blocks associated with the more subdued, rounded rim crater to the southwest exhibit a mean roundness of 0.33 and a standard deviation of roundness of 0.17. The difference in roundness between these two samples of blocks is significant, by Student's t test, at the 0.999-probability level.

A measurement of degree of burial of blocks in the lunar surface was obtained by the following method. The angle between a line parallel with the horizon that meets the block, where its outline against the more distant lunar scene comes to the surface, and the tangent to the outline of the block at this point was measured on each side of each block (Fig. III-23). The sum of these two angles for each block divided by 2π rad, here defined as the *burial factor*, can vary between 0 and 1. Rounded fragments whose tops just barely show above the surface have burial factors that approach 1, whereas rocks that sit up on the surface and exhibit overhanging sides have burial factors that approach 0.

Measurement of the burial factor for the same 25 blocks in each strewn field that were studied for roundness gave the following results: The mean burial factor of blocks associated with the sharply formed crater to the northeast is 0.62 with a standard deviation of burial factor of 0.09 (Fig. III-24). The blocks associated with the more subdued, rounded-rim crater to the southwest have a mean burial factor of 0.69 with a standard deviation of burial factor of 0.07 (Fig. III-24). The difference between these means is significant at the 0.995-probability level, by Student's t test.

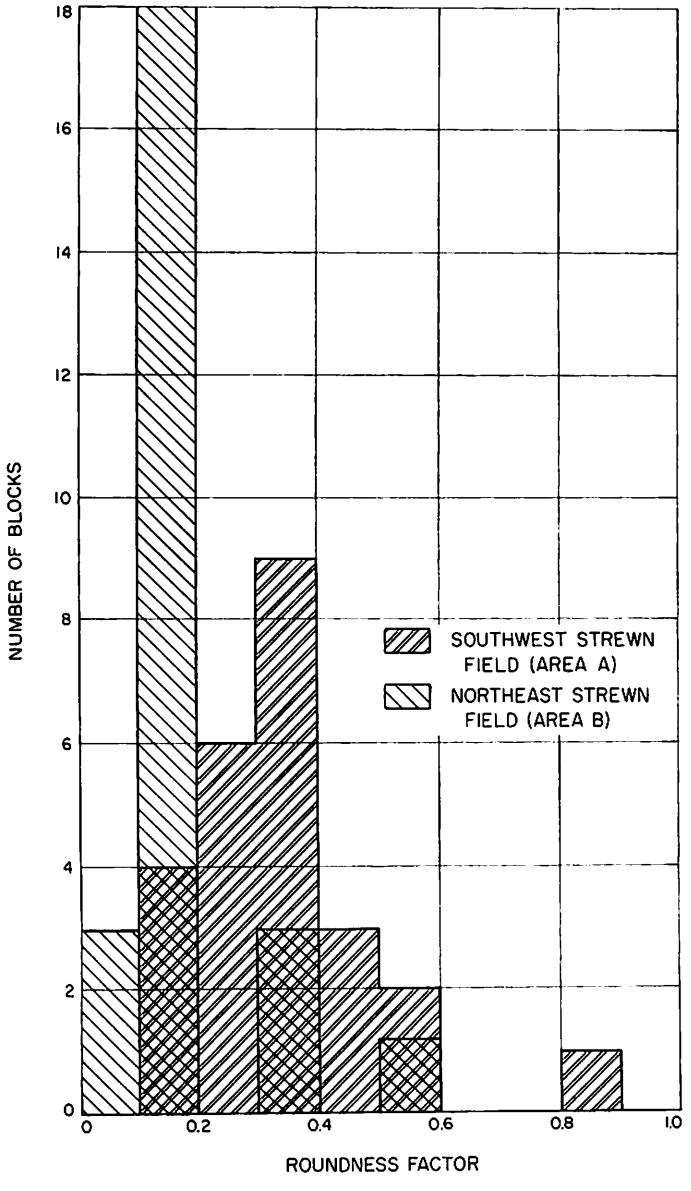

Fig. III-22. Histograms showing frequency distribution of roundness factors for 25 blocks in area A and 25 blocks in area B. Blocks in area A, associated with subdued rim craters, are significantly more rounded than blocks in area B, associated with a sharp rim crater

No significant correlation was found between roundness and burial of individual blocks within each strewn field. The linear correlation coefficient between the roundness factor and burial factor for the blocks in the strewn field around the northwest crater is −0.07 and for the blocks in the strewn field associated with the southwest crater −0.16. Both of these coefficients are well below the 95% confidence level. If the blocks in both the strewn fields are examined as a single sample, the linear correlation coefficient between roundness factor and burial factor is +0.13, which is also below the level of significance. Examination of the scatter diagram (Fig. III-25) of burial factor versus roundness factor shows that, while there is no significant linear correlation, there are relatively few blocks in the strewn fields that tend to have high roundness but a low burial factor.

While there is no significant linear correlation between roundness and burial for blocks in a given strewn field of presumably one age, it may be expected that, as individual fresh pieces are added to the regolith of the lunar surface, they start out with relatively low roundness and usually are perched on top. In time, the fragments usually become more rounded and will show varying degrees of burial. Thus, for fragments generally mixed together in the debris layer or regolith, there should be a correlation between the roundness and degree of burial. Further studies of the *Surveyor* pictures will be required to confirm this hypothesis.

In summary, the blocks associated with the more subdued craters have twice as high a mean roundness factor as those associated with the crater with a sharp raised rim, and the blocks around the subdued crater are significantly more buried in the lunar surface than those around the crater with the sharp raised rim. These results suggest that blocks freshly exposed on the lunar surface tend to be rounded off in the course of time by solid particle bombardment and possibly by evaporation of material by the solar wind or other high-energy radiation. Initially, the ejected blocks tend to be shallowly embedded in the lunar surface, but, in time, may become partly or completely covered up by ejecta arriving from other parts of the surface. Progressive burial of blocks may take place also as a result of downhill movement of the debris layer by creep.

The size/frequency distribution of fragmental debris at the *Surveyor III* landing site was studied both in the strewn fields of blocks just described and in four sample areas that lie closer to the spacecraft (area C, Fig. III-18; area D, Fig. III-26a; area E, Fig. III-26b; and area F, Fig. III-26c). These sample areas were chosen so that the resolution and area covered would provide particle counts spanning different, but overlapping, parts of the particle size range. All sharply formed bright fragments recognizable in the relatively high sun pictures in each sample area were measured and counted. A total of 2205 grains and fragments ranging in diameter from 1 mm to more than 1 m were measured.

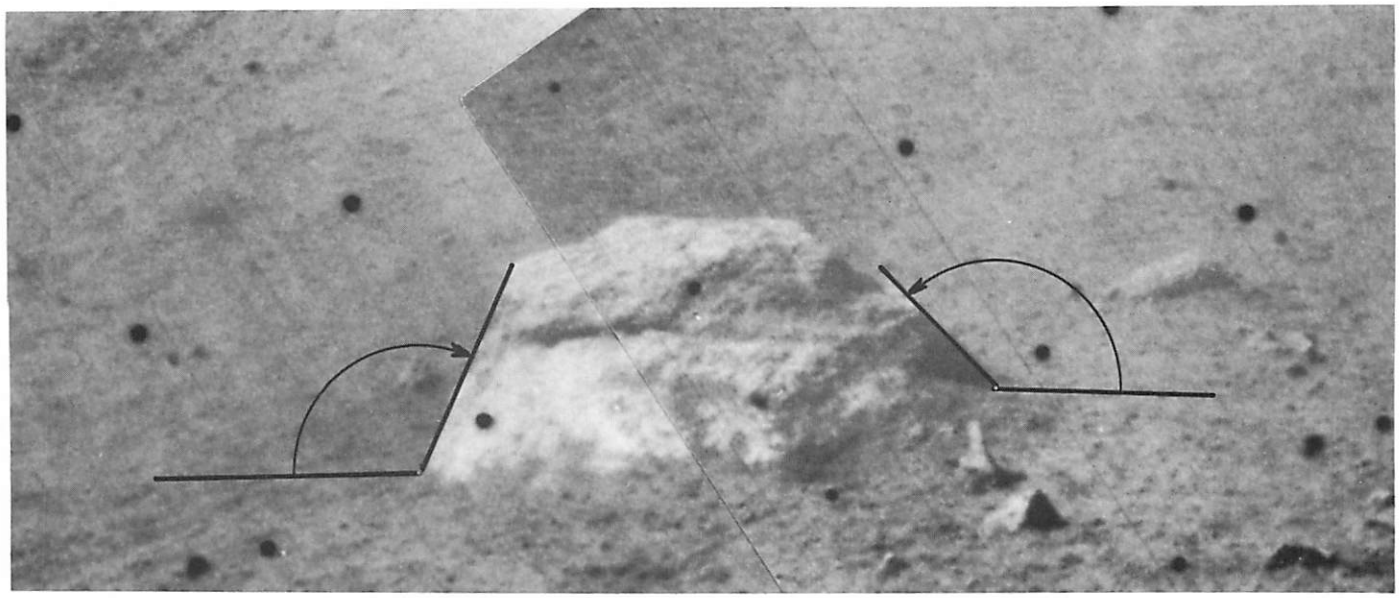

Fig. III-23. Mosaic of two narrow-angle *Surveyor III* pictures, showing block about 0.5 m across close to spacecraft and angles measured to determine burial factor. Angles are measured between lines parallel with the horizon and the tangents to the outline of the block, where the outline of the block against the more distant lunar scene meets the surface. The sum of the two angles divided by 2π rad is defined as the burial factor (Day 120, 14:54:23 and 14:52:22 GMT)

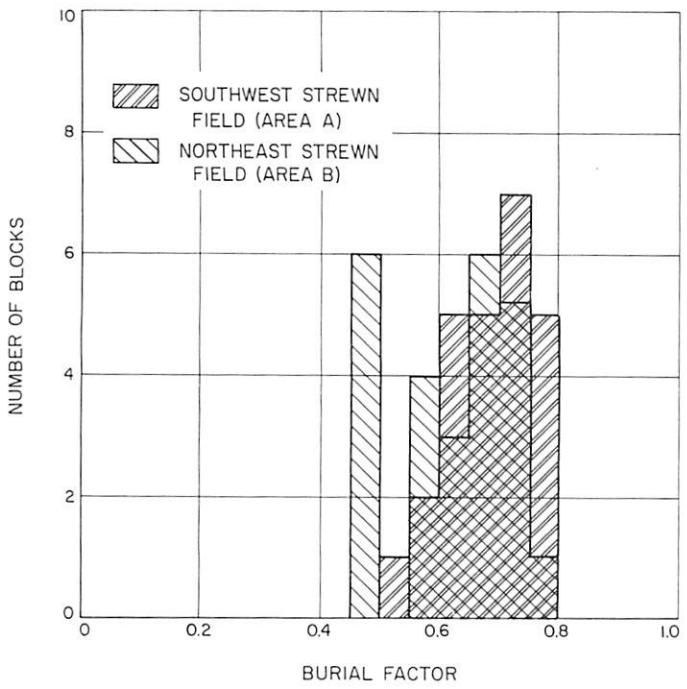

Fig. III-24. Histograms showing frequency distribution of burial factors for 25 blocks in area A and 25 blocks in area B. Blocks in area A, associated with subdued rim craters, are significantly more deeply buried in the surface than the blocks in area B, associated with a sharp rim crater

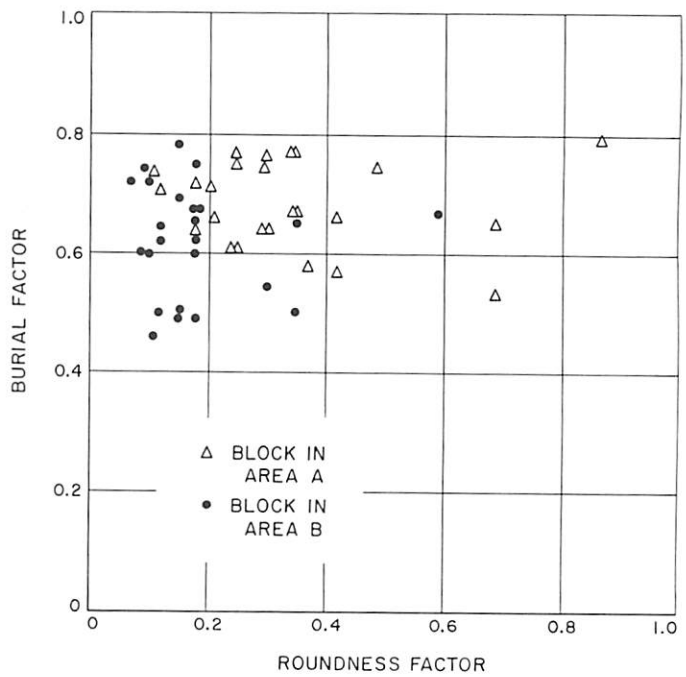

Fig. III-25. Scatter diagram of roundness factor vs burial factor for 50 blocks in areas A and B. The roundness factor and burial factor have no significant linear correlation; relatively few blocks, however, exhibit both high roundness and low burial

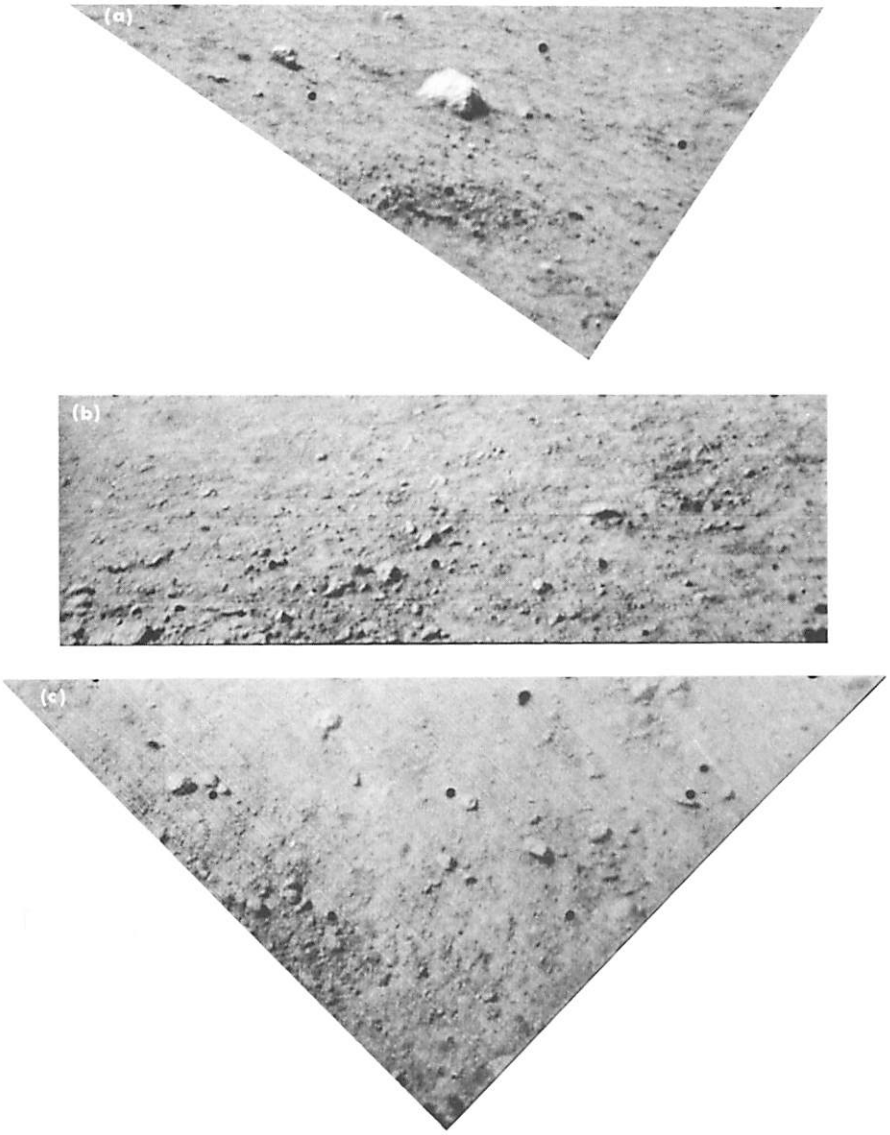

Fig. III-26. Parts of narrow-angle *Surveyor III* pictures, showing small areas on the lunar surface close to the spacecraft in which the size/frequency distribution of fragments was measured; (a) area D: smallest fragments resolved in this picture are about 8 mm across; largest fragments present are 6 to 12 cm across (Day 120, 14:38:45 GMT). (b) area E: smallest fragments resolved in this picture are about 2 mm across; largest fragments present are 3 to 4 cm across (Day 120, 14:32:01 GMT). (c) area F: smallest fragments resolved in this picture are about 1 mm across; largest fragments present are 8 mm across (Day 120, 14:38:08 GMT)

The integral size/frequency distribution of measured fragments, normalized to an area 100 m^2 for each of the sample areas, is shown in Fig. III-20. Fragments in the strewn fields associated with the northeast and southwest craters are, on the whole, an order of magnitude coarser than the fragments observed on the more characteristic parts of the landing site. The size/frequency distribution function for the fragments in each strewn field resembles the size/frequency distribution function for fragments ejected from impact craters formed in strong rock, such as at Meteor Crater, Arizona (Figs. III-27 and III-28).

The integral frequency of fragments for the average surface, outside of the strewn fields of blocks, is approximately a simple power function of the grain size with an exponent of about −2.6. This distribution may be compared with a revised size/frequency distribution of fragments observed in the *Surveyor I* landing site (Figs. III-29 and III-30). The power function used to approximate the observational results for *Surveyor III* has a slightly lower exponent than that obtained for the particles studied at the *Surveyor I* landing site, which is −2.2. The observed difference between the size/frequency distribution of fragments in the two areas may be within the error of measurement.

Experimental studies were made of the relationship between the size/frequency distribution of particles obtained by measuring and counting fragments from a photograph of the surface of a fragmental debris layer and the distribution found by mechanically sieving the

Fig. III-27. Sample of ejected fragmental debris collected from the rim of Meteor Crater, Arizona. Area of floor of box in which sample has been placed is 1 m^2. Fragments are sandy dolomite from the Kaibab formation of Permian age. Coarsest piece is 12 cm across, and finest grains identifiable in the picture are about 1 mm across. Spacing between coarser fragments resembles that observed for blocks in strewn fields around small craters at the *Surveyor III* landing site

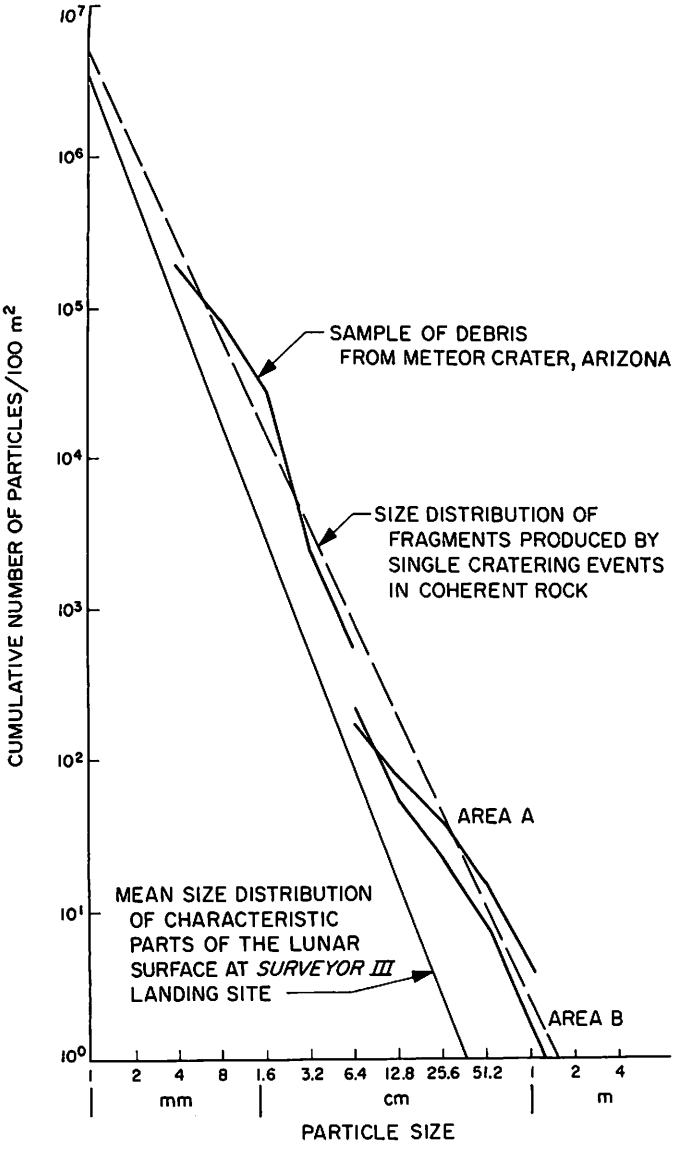

Fig. III-28. Size/frequency distribution of fragments in areas A and B of *Surveyor III* landing site compared with size/frequency distribution of debris from Meteor Crater, Arizona. Fragments in strewn field of area A are associated with a 15-m-diameter crater, and fragments in area B are associated with a 13-m-diameter crater. Size/frequency distribution of debris from Meteor Crater, Arizona, measured from Fig. III-27. Dashed line represents the mean size/frequency distribution of fragments produced by single cratering events in coherent rock. Mean fragment size/frequency distribution of characteristic parts of the lunar surface at the *Surveyor III* landing site are shown for comparison

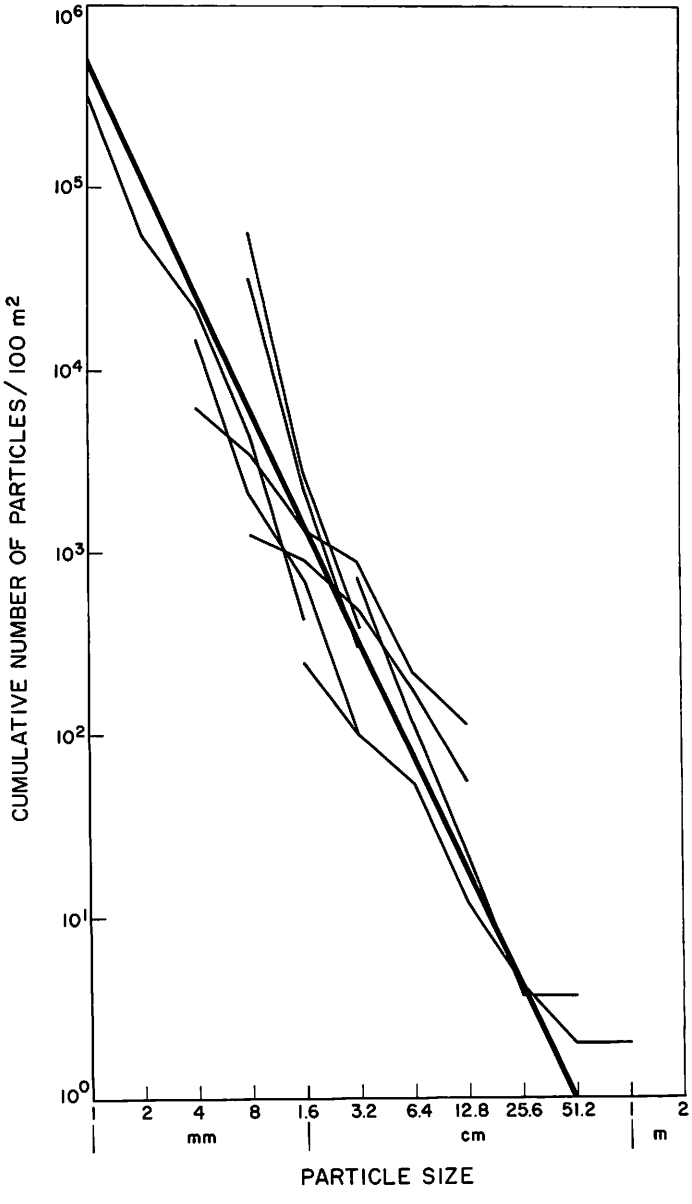

Fig. III-29. Mean cumulative size/frequency distribution of fragments on characteristic parts of lunar surface at *Surveyor I* landing site (revised). Heavy solid line represents the general size/frequency distribution determined from eight sample areas. This line is the plot of the equation $N = 5 \times 10^5 y^{-2.2}$, where N is the cumulative number of fragments and y is the diameter of fragments in millimeters

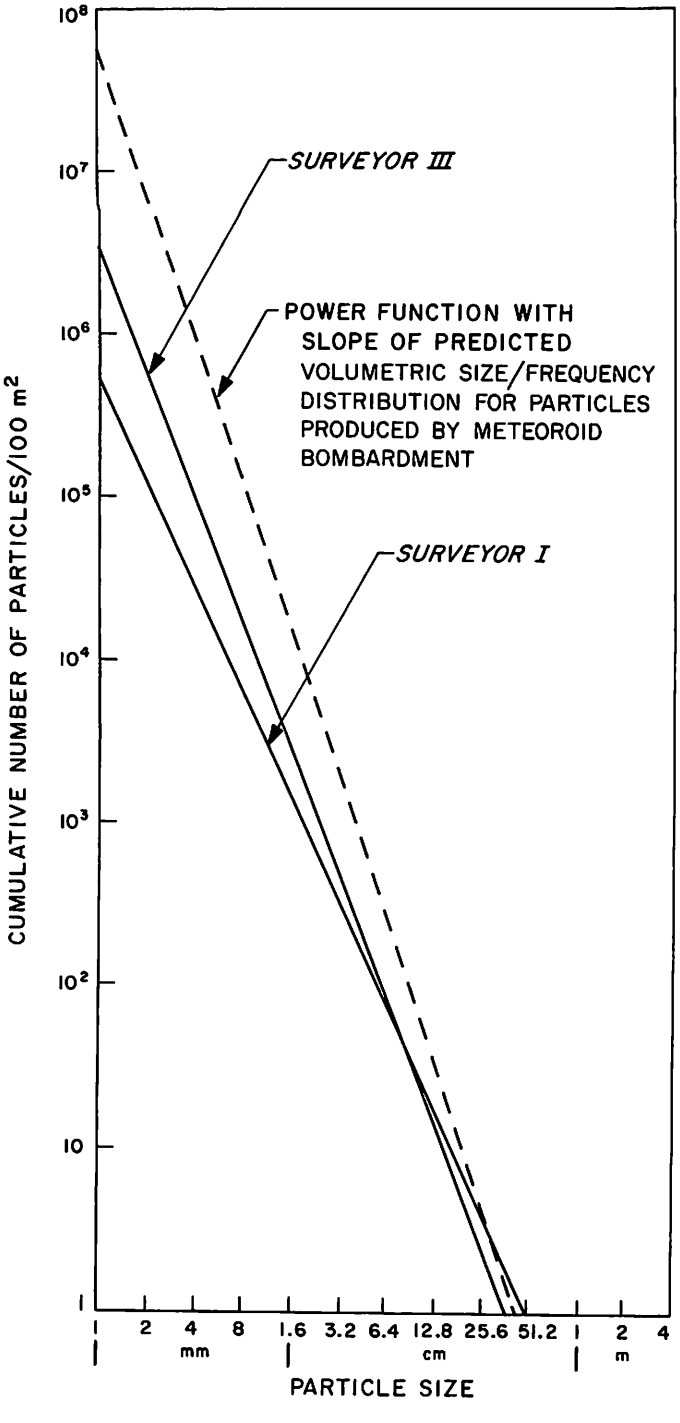

Fig. III-30. Mean cumulative size/frequency distribution of fragments on characteristic parts of the lunar surface at *Surveyor III* landing site compared with mean cumulative size/frequency distribution of fragments observed at *Surveyor I* landing site. The volumetric size/frequency distribution of fragments expected to be produced by incident flux of meteoroids on the lunar surface is shown with dashed line. The volumetric fragment size/frequency distribution represents the distribution expected in each area of 100 m^2 to a depth equal to one-half the diameter of the coarsest fragment. The volumetric fragment size/frequency distribution at both *Surveyor I* and *Surveyor III* landing sites probably is close to this predicted distribution

entire layer. Among the different materials studied were samples of ash and pumice from the volcanic ash flow deposited in the Valley of 10,000 Smokes in Alaska during the eruption of 1912 (Fig. III-31). The difference between the particle distribution obtained by measurement and counting of grains from pictures and by mechanical sieving for this sample is shown in Fig. III-32. It may be seen that the number of small particles counted in pictures of the surface layer of fragments tends to be much lower than the number of small particles found by sieving the entire layer. A similar difference was observed in the study of fragment size distribution of dolomite ejecta from Meteor Crater, Arizona. Theoretically, for each decrease by a factor of ten in size, the number of small fragments per unit volume should increase ten times as rapidly as the number of recognizable small fragments per unit area exposed at the surface. On this basis, the volumetric size/frequency distribution of fragments in the debris layer of the lunar surface is inferred to be represented by a power function with an exponent of approximately -3.1 to -3.6.

Present evidence on the mass/frequency distribution of interplanetary solid particles in the size range capable of producing by impact the observed fragments on the lunar surface at the *Surveyor I* and *III* landing sites indicates that it is very close to a simple inverse function. The volumetric size/frequency distribution of particles that would be expected to be produced by an incident flux upon the moon of meteoroids with this mass/frequency distribution would be a simple power function with an exponent close to -3. Thus, the inferred volumetric size/frequency distribution of fragments at the *Surveyor I* and *Surveyor III* landing sites is close to that predicted for fragmental debris produced by meteoroid bombardment.

Fig. III-31. Sample of ash and pumice from volcanic ash flow deposited in the Valley of 10,000 Smokes, Alaska, during the eruption of 1912. Area of floor of box in which sample has been placed is 1 square meter. Coarsest fragments of pumice in sample are 4 to 5 cm across; finest grains identifiable in the picture are about 1 mm across

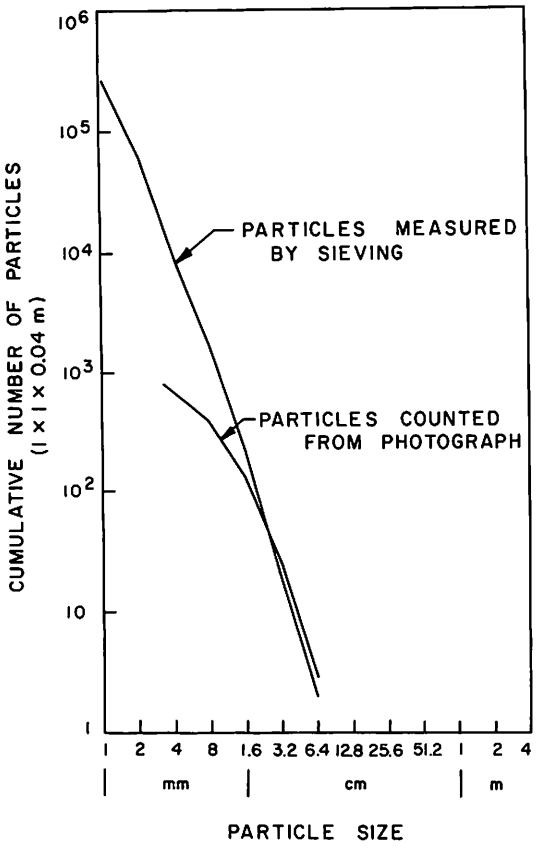

Fig. III-32. Size/frequency distribution of particles in sample of ash and pumice from the volcanic ash flow deposited in the Valley of 10,000 Smokes, Alaska, during the eruption of 1912. Upper curve shows size/frequency distribution obtained by sieving the entire sample shown in Fig. III-31. Lower curve shows size/frequency distribution of particles identifiable in Fig. III-31. The difference in these two curves illustrates the difference between the volumetric size/frequency distribution of fragmental debris and the size/frequency distribution of identifiable fragments on the surface of the debris layer

The fine-grained matrix of the lunar surface material at the *Surveyor III* landing site shows a peculiar patchiness of albedo like that observed at the *Surveyor I* landing site (Ref. III-1). Dark rubbly patches commonly occupy small shallow craters. These patches resemble, in some respects, the dark lumpy rims surrounding the imprints of the spacecraft footpads and the material disturbed by the surface sampler. We believe that these patches have probably been formed by breakup of fresh clots of fine-grained material that have been ejected from nearby small impact craters, and that the shallow craters they occupy are very young secondary craters produced by the low-speed impact of these relatively soft clots.

In places, fine-grained material appears to be banked up slightly against the sides of some of the larger blocks protruding above the lunar surface, both in the strewn fields of blocks and around blocks elsewhere within the main crater (Fig. III-33). Similar banking up of fine material and partial covering of blocks by fine material were observed around blocks at the *Surveyor I* landing site. The steep faces of coarse blocks can be considered ballistic traps for small particles sprayed out from nearby parts of the lunar surface, and it is inferred that the banks of fine-grained material have been deposited particle by particle from the particle spray from numerous small nearby impact events.

4. Lunar Surface Areas Disturbed by *Surveyor III*

Imprints in the lunar surface material produced at several of the touchdown points of the spacecraft footpads are visible to the east of the camera (Fig. III-34) and are of interest to compare with the natural disturbances of the surface, such as secondary impact craters. These disturbances also provide clues about the size distribution of fragments beneath the surface. Well-developed imprints in the lunar surface lie just upslope from the present position of footpads 2 and 3. There are three other well-defined marks left at the site of the second touchdown of the spacecraft (Fig. III-35) at 12, 14.5, and 15 m upslope from the camera. The mark at 12 m was formed by footpad 1 and the two marks at 14.5 and 15 m by footpad 2, which evidently touched the surface twice before the spacecraft lifted clear of the surface on its second ascent under power. The imprint of footpad 3 is not clearly distinguishable at the site of second touchdown, although its position can be fairly accurately predicted; the position of this imprint is in a shallow crater, and only a small part of the imprint appears to be visible. The imprints left by the first touchdown do not appear to be visible from the present position of the camera. They lie either beyond the eastern horizon or on a part of the crater wall that is observed only at a grazing angle, where the imprints would be difficult to detect.

We have searched for marks produced by the vernier engine effluents at the second touchdown site of the spacecraft. One such mark may be present near the imprint at 15 m, which we believe was produced by footpad 2. It is possible that this disturbance of the surface was produced by the combined effects of the effluent from vernier engine 2 and the dragging of footpad 2.

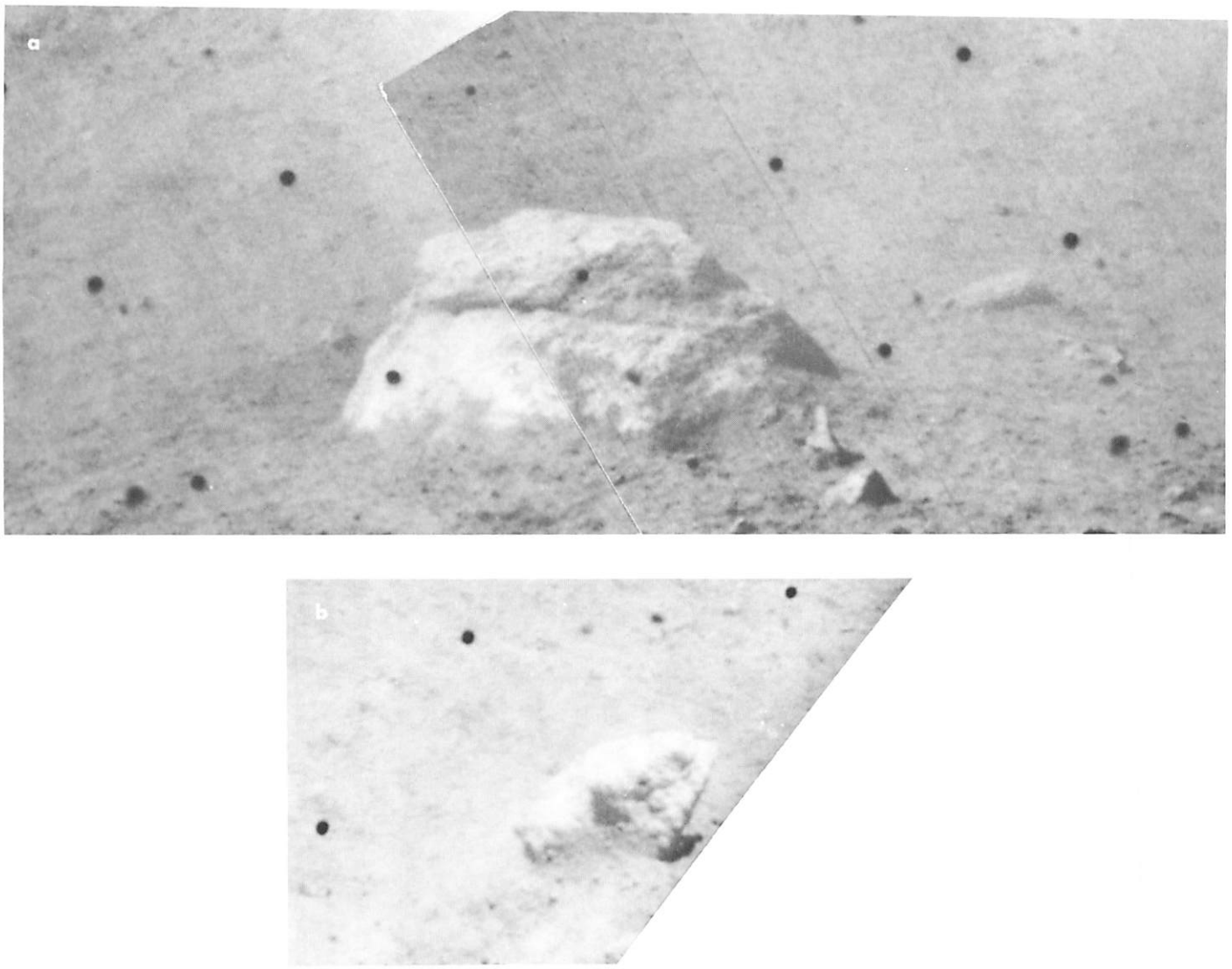

Fig. III-33. (a) Mosaic of two narrow-angle *Surveyor III* pictures, showing block about 0.5 m across close to spacecraft, and fine-grained material banked up against side of block. Note nearly horizontal groove in side of block facing camera. This groove may have been produced by differential erosion of the surface of the block along a bedding plane or a comparatively easily eroded layer (Day 120, 14:54:23 and 14:52:22 GMT). (b) Narrow-angle *Surveyor III* picture, showing angular block close to spacecraft and fine-grained material banked up against the side of the block facing the camera. Block is 7 cm across. Note small particles 1 to 5 mm in diameter that can be resolved in the fine-grained debris (Day 118, 14:30:51 GMT)

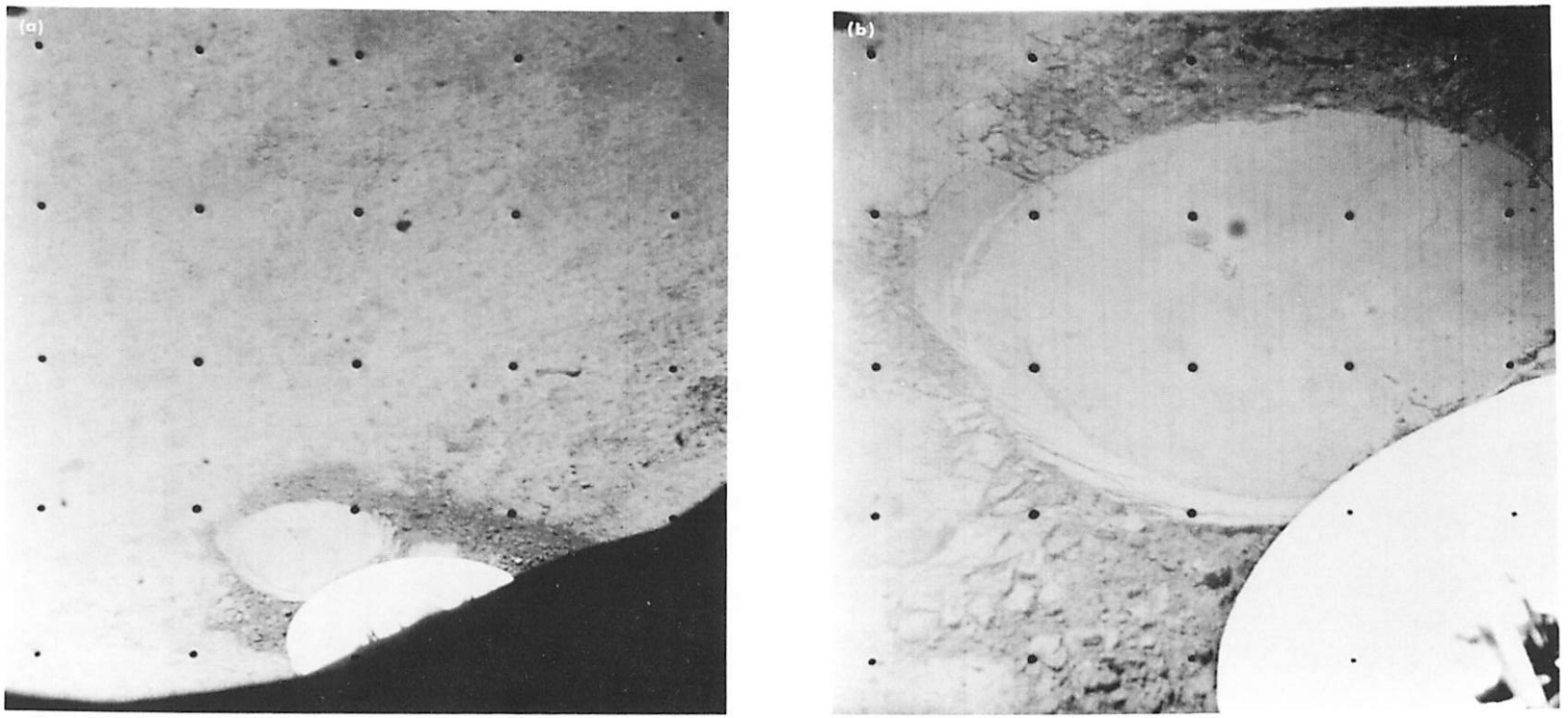

Fig. III-34. (a) Wide-angle *Surveyor III* picture, showing imprint in lunar surface produced by footpad 2 of the spacecraft. Part of the top of footpad 2 may be seen next to the imprint. Note the smooth bottom and sloping walls of the imprint and the dark raised rim of lumpy material around the imprint (Day 116, 05:54:53 GMT). (b) Narrow-angle *Surveyor III* picture, showing imprint in lunar surface produced by footpad 2. Part of the top of footpad 2 is visible in the lower right-hand corner of the picture. Note breaks in smooth wall of imprint resembling chatter marks. Rim of dark lumpy material is absent near upper left-hand corner of the picture. The dark lumpy material appears to have collapsed or slumped across the sector of the imprint wall near the top of the picture and extends down to the floor of the imprint (Day 116, 06:05:55 GMT)

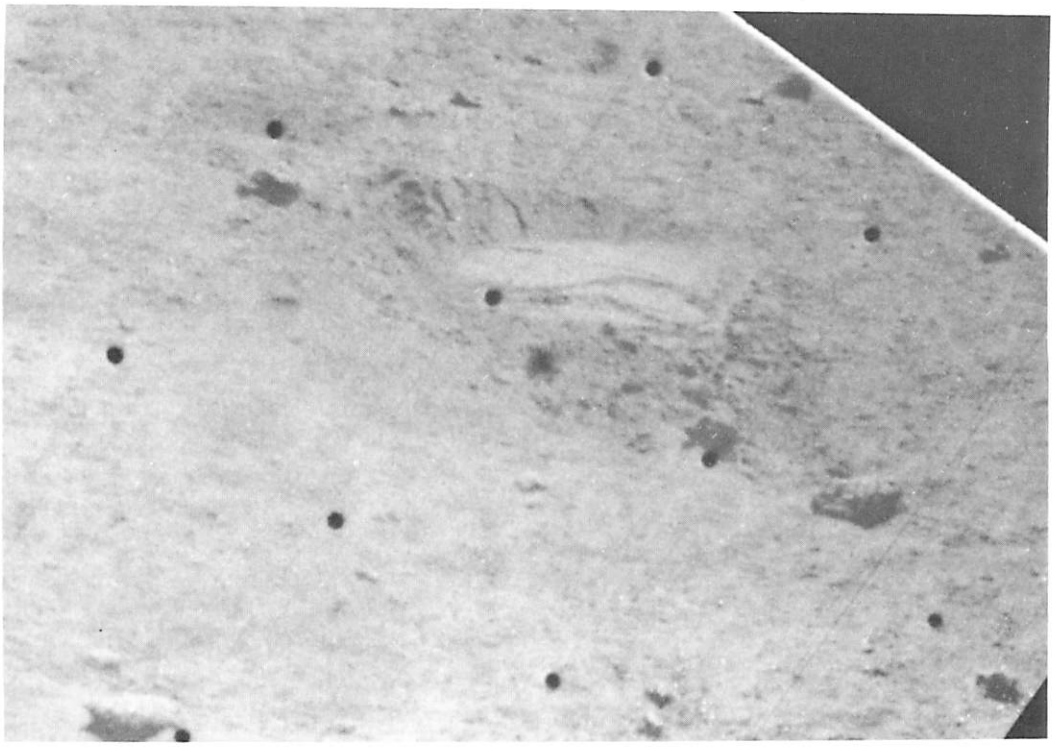

Fig. III-35. Narrow-angle *Surveyor III* picture, showing imprint in lunar surface produced by footpad 1 of the spacecraft during the second touchdown of the landing sequence. The imprint occurs on a small crater wall facing the camera, and the imprint is stepped down along several breaks toward the camera and toward the center of the small crater. The crater in which the imprint is formed is about 1 m across (Day 116, 08:37:36 GMT)

The imprints just upslope from footpads 2 and 3 are nearly flat-bottomed depressions, the floors of which lie a few centimeters deeper than the adjacent undisturbed parts of the lunar surface. Most of the observable parts of the walls of these two depressions are smooth conical surfaces that conform approximately in shape to the tapered or chamfered part of the underside of each footpad. The wall of the imprint left by footpad 2 is not complete, however, and it is offset, in places along short distinctive breaks.

The imprint of footpad 2 is nearly encompassed by a raised rim of lumpy material with an albedo significantly lower than that of the undisturbed surface. The raised rim and dark material are absent along a short sector of the edge of the imprint on the upslope side, the side from which the footpad approached the surface. On the downslope side, dark lumpy debris is spread out for an observable distance of at least 0.5 m. Along the east-southeast sector of the imprint, a smooth wall is not present, and dark lumpy material extends from the rim of the depression to the floor. Presumably, a smooth, sloping surface was produced during penetration of the footpad and later either collapsed or was covered over by dark material slumping down across it.

The dark lumpy rim of the imprint next to footpad 2 resembles the ejected dark rim material around footpads 2 and 3 at the *Surveyor I* landing site. Apparently, the lumps are mostly aggregates of finer particles formed by breakup of the slightly cohesive lunar surface debris. The observed lumps range from 1 mm to 5 cm across and have a mean diameter of about 1 cm.

The floor of the imprint near footpad 2 exhibits a regular series of very low mounds arranged in a pattern similar to that of a waffle iron. This pattern must have been produced by the bottom of the footpad, the skin of which was evidently pressed slightly into the honeycomb structure of the pad interior. Two small bumps in the depression probably are either small fragments lying on the floor of the imprint or reflect dents in the bottom

of the footpad that may have been produced by a hard lunar fragment during the first, second, or third touchdown of the spacecraft. The breaks in the smooth wall are somewhat similar to chatter marks formed on glacial pavements and probably have been formed by downslope distortion of the wall as the spacecraft footpad pulled away in the downslope direction.

The smooth walls and floor of the imprint next to footpad 2 are different photometrically from the undisturbed lunar surface, as indicated in the following section on photometry. Observations of the imprint on several different days during the lunar morning and early afternoon indicate this smooth surface is more like a Lambertian surface than is the natural lunar surface. Much more light is scattered toward the eastward-facing camera from the smooth imprint surface than from nearby undisturbed parts of the moon in the early lunar morning, but in the lunar afternoon the imprint is not brighter than the undisturbed surface. This indicates that the very small irregularities between the grains have been partially smoothed out or filled in by pressure and by sliding of the smooth metallic footpad.

Only part of the imprint near footpad 3 is observable from the camera, but it appears to be smoother and more regular than the imprint next to footpad 2. Dark lumpy material also forms a partial rim around the imprint near footpad 3, and there are dark streaks in the walls of the depression, probably formed by collapse or drainage of particles down the upslope side of the depressions.

The three clearly visible imprints at the site of second touchdown are much less regular in form than those next to the spacecraft. All three are formed on the walls of small craters. Two imprints were left by footpad 2 low on the northeast wall of a crater about 4 m across. The uppermost, and presumably first formed imprint of these two, has a well-defined rim on its upslope side, but none is clearly observable on the downslope side. The lower imprint looks as though it had been formed by dragging of the footpad along the crater wall during the second ascent of the spacecraft from the lunar surface. The imprint formed by footpad 1 at the second touchdown site is on the upper part of the east wall of a crater about 1 m across. This imprint, too, has a well-defined wall on the upslope side, formed of dark lumpy material, whereas the downslope side is open toward the center of the crater. The floors of all three of these imprints are relatively smooth and appear to have anomalous photometric properties like those of the footpad 2 imprint near the spacecraft.

Each of the four well-formed imprints observed is generally similar. It may be inferred that the mechanical properties of the lunar surface are rather similar at the positions of all four imprints and that the mechanical properties of the fragmental material at the *Surveyor III* landing site are closely similar to those of the material at the *Surveyor I* landing site (Ref. III-3).

Disturbances produced in the lunar surface by the soil mechanics surface sampler (SMSS) are similar in several ways to the disturbances produced by the footpads of the spacecraft. The disturbed material tends to form lumps or clots a millimeter to a few centimeters across, like those formed on the raised rims of the footpad imprints, and the disturbed lumpy material has a significantly lower albedo than the undisturbed surface. Where the SMSS scoop was pressed into the surface in a bearing test, a raised ridge of lumpy material was formed around the depression, which has been interpreted (Section IV of this report) to indicate that the fine-grained material at the lunar surface is relatively incompressible or only very moderately compressible. Smooth parts of the scoop left smooth marks or a smooth surface where pressed firmly against the fine-grained fragmental debris. The photometric properties of these artificially smoothed surfaces are like the smooth surfaces in the footpad imprints.

No bright, angular hard fragments were uncovered in the trenching operations with the SMSS, but they would be extremely difficult to detect, if they are scattered through the subsurface material as they are on the surface. The fact that smooth metallic surfaces leave smooth imprints in the lunar fragmental debris does not mean that coarse particles are absent. They are probably sufficiently well dispersed through the finer-grained matrix that they tend to yield when pressed against and tend to be concealed by the matrix in an imprint area.

From the geological standpoint, the most important conclusions to be drawn from the footpad imprints and areas disturbed by the SMSS are that the lunar surface material is only moderately compressible and that it has relatively low cohesion. It is also important to note that all disturbances of the surface produced by *Surveyors I* and *III* exposed darker material at depths of a few centimeters or less. In all likelihood, the fine-grained fragmental debris of the lunar surface is 20 to 30% lower in albedo at depths of only a fraction of a millimeter beneath the optically observed surface.

E. Interpretation of Geologic Observations

Observations of the lunar surface obtained from the *Surveyor III* mission, when combined with results obtained from *Surveyor I*, *Ranger* and *Lunar Orbiter* Projects, and observations at the telescope, can be used to infer hypotheses or amplify previous hypotheses about the geologic processes taking place on the lunar surface. The processes of most immediate interest are those which have produced the observed craters and the fragmental debris and which control the observed distribution of craters and fragmental debris. In addition, some inferences may be drawn about processes leading to the observed variations of albedo of the lunar surface and subsurface material.

It should be noted that the small features of the *Surveyor III* landing site are closely similar, in detail, to the features of the *Surveyor I* landing site. The characteristics of the craters and fragmental debris and the processes by which these features have been formed and modified are probably closely similar. In short, the lunar surface on the interior of a broad shallow crater on the maria is much like the surface on a relatively level area between the craters.

1. Origin of Observed Craters

We infer that most craters observed at the *Surveyor III* landing site are of impact origin. The size/frequency distribution of the observed craters corresponds to that which would be produced by repetitive bombardment of the lunar surface by meteoroids, a bombardment sufficiently prolonged that the crater population has reached a steady state or equilibrium (Refs. III-4 to III-6). In a steady-state population, old craters of a given size are destroyed as rapidly as new ones are formed. From investigations of *Ranger* and *Lunar Orbiter* pictures, the upper size limit of the steady-state or equilibrium crater population was found (Refs. III-4 and III-7) to be several hundred meters, much larger than any of the craters observed at the *Surveyor III* landing site.

Some direct evidence for the impact origin of two of the larger craters seen from the *Surveyor III* camera is provided by the size/frequency distribution of the blocks in the strewn fields associated with these craters. These blocks exhibit the type of size/frequency distribution that is produced by a single impact or explosion cratering event in relatively hard rock.

Some of the craters observed at the *Surveyor III* landing site are inferred to be of secondary impact origin; some apparently are structurally controlled and probably have been formed either by subsidence or by drainage of fragmental debris into cracks or fissures in the subsurface. Most of the shallow craters that contain patches of dark rubble resemble craters of secondary impact origin, investigated by Moore at the White Sands Missile Range (Ref. III-8), which are produced by weakly cohesive clots ejected from primary craters. Some other irregular, elongated craters at the *Surveyor III* landing site may also be of secondary impact origin. Linear troughs and rows of shallow craters, aligned parallel with troughs in the lunar patterned ground, are probably produced by drainage or collapse. At the present time, we have not been able to determine with confidence the number of craters of each different type and presumed different origin.

2. Origin of Fragmental Debris

The observed fragmental debris is inferred to have been derived primarily by the same process of repetitive bombardment that has produced the majority of the craters. The fragments at the surface are evidently part of a layer of fragmental material of low cohesion that is at least as thick as 1 m along the upper parts of the wall of the main crater in which *Surveyor III* landed and may be much thicker near the center of the crater. This layer we refer to as the lunar regolith. The inferred volumetric size/frequency distribution of fragments, derived from the observed size distribution of fragments on the surface, is similar to that which would be produced by repetitive bombardment of coherent rock by meteoroids with a mass/frequency distribution like that found from observations of meteors and recovered meteorites on earth.

Observed fragments in the regolith exhibit some diversity of surface texture and structure and probably have been derived from diverse sources, some nearby and some relatively distant from the *Surveyor III* landing site. Most fragments are massive, but a few are strikingly tabular in shape and appear to be laminated. Many fragments are pitted, and some may be vesicular. We infer that the large majority of the fragments have been derived from pre-existing relatively strong rock, possibly volcanic flows or lithified volcanic ash flows.

3. Creep of Lunar Regolith

Evidence from the *Surveyor III* pictures suggests the regolith is subject to creep or mass movement down the slopes of the main crater. As observed in the pictures, blocks and finer fragments tend to ride at different levels with respect to the surface, or, to put it in different

terms, blocks seem to be "stuck into" the surface at varying depths. Regardless of apparent depth of burial, the surface is not appreciably deflected as the side of a block is approached. Because of this relationship, we were able to obtain relatively unambiguous measurements of the burial factor for the coarser blocks.

The observed relationship of the blocks to the surface is not that which would be expected if the blocks had been buried to varying depths simply by penetration of the surface on impact or by later covering by fine-grained ejecta from nearby craters. In the former case, because the fine-grained material of the region is relatively incompressible, a small crater usually would be formed around the blocks, and, in the latter case, material would be banked up around the blocks. Some banking of fine material against blocks is observed, but it is a relatively minor effect.

The varying degree of burial of the blocks is probably significantly influenced by slow or intermittent downhill creep or flow of the entire layer of debris. During the flow, blocks that are initially deposited on top of the regolith or buried at only slight depth usually will sink, if their density is greater than the bulk density of the fine-grained debris and if coarse fragments are not too closely spaced within the fine-grained matrix. The surface of the fine-grained matrix will become smooth during flow; small depressions usually will be filled in and ridges or banks of debris usually will be flattened out.

The regolith at the *Surveyor III* landing site can flow under relatively low stress because it has very low cohesion. This low cohesion is demonstrated by the three following independent lines of evidence:

(1) Deformation of the lunar surface by the spacecraft footpads, which is similar to the deformation produced by the *Surveyor I* footpads, is consistent with the behavior of a near-surface material that is only weakly cohesive. A material with a cohesion between 10^3 and 10^4 dynes/cm^2 has been suggested to give a behavior representative of the lunar surface deformed by the footpads of *Surveyor I* (Ref. III-9). Christensen and others (Ref. III-3) conclude that the cohesion of the lunar soil at the *Surveyor III* site cannot exceed 7×10^4 dynes/cm^2.

(2) Tests of lunar surface material by the SMSS show that the behavior of the fine-grained material near the spacecraft is consistent with a low cohesion, between 1×10^3 and 3×10^3 dynes/cm^2, according to Scott, Roberson, and Clary (Section IV of this report).

(3) Presence of raised rims consisting essentially of fine-grained debris around many of the small craters shows the cohesion is generally low at most places visible from the camera. Craters of the size observed with rims of this type can be formed experimentally only in material with a cohesion of about 10^4 dynes/cm^2 or less.

Because of this low cohesion, creep or flow will take place in the regolith on sloping surfaces, if it is shaken or agitated (Ref. III-10). Agitation or shaking must occur from time to time as a consequence of impact events. Seismic waves are propagated a considerable distance beyond each impact crater that is formed, whether it is large or small. From field observations, made by Shoemaker at the Atomic Energy Commission, Nevada Test Site, of mass movement induced by subsequent cratering experiments on the walls of experimental craters formed in alluvium, we estimate that significant creep of the lunar regolith may be induced on sloping surfaces at a distance at least as great as 10 times the crater radius for each impact cratering event. Most of the seismic shaking that causes creep is probably a result of relatively small nearby impact events; only rarely does a large distant impact take place that will induce creep at any given locality. The formation of each impact crater present at the *Surveyor* landing site probably was accompanied by some downhill creep of the regolith over a small area surrounding the crater. In addition to seismic waves produced by impact, seismic waves of sufficient amplitude to cause creep may be produced by internal tectonic activity of the moon.

Creep of a very thin layer at the top of the regolith may also take place as a result of the thermal expansion and contraction induced by insolation. During an insolation cycle, material has a tendency to expand in a direction normal to the surface and to contract down the gravitational gradient. Because the thermal wave is damped out rapidly with depth on the moon, significant expansion and contraction are limited to a layer at most a few centimeters thick. Thermally induced creep may have, however, a tendency to make fine debris near the surface flow around and past protruding blocks.

The main crater in which the spacecraft is located probably has been partially filled in by mass movement of the fragmental debris. The presence of coarse blocky ejecta from superposed craters on the northeast rim and high on the southwest wall show that the fine-grained debris layer is, at most, a few meters thick on or near the rim of the main crater. No fields of strewn blocks

or blocky crater rims occur near the floor of the main crater, which indicates the base of the debris layer is deeper than any of the craters present there. The main crater probably is an old impact crater and initially had a significantly higher rim and deeper floor. Bombardment and mass movement may have reduced the height of the rim by many meters and filled in the floor with a deposit of fragmental debris several tens of meters thick at the center of the crater. The blocks in the northeast and southwest strewn fields are probably derived from the eroded remnants of the original fragmental rim deposit of the main crater, which evidently lies at shallow depth along the rim crest and is exposed from time to time by superposed craters. It is of interest that a relatively large dimple crater is located near the center of the main crater where a thick deposit of fine-grained debris may be present, a deposit required for a large crater to be developed by drainage.

4. Processes Leading to Diversity of Albedo

On the basis of observations made from *Surveyors I* and *III*, it is possible to draw two tentative new generalizations about photometric properties of material on the lunar surface: (1) protruding blocks, in all observed cases, have a higher albedo than the fine-grained matrix of the surface, and (2) freshly exposed fine-grained material derived from just beneath the surface has a lower albedo than the undisturbed fine-grained material at the surface. We present here a simple working hypothesis, based on the general model of surface processes given above and on geologic observations given earlier, which accounts for these two general photometric relationships.

From the studies of roundness, it is concluded that some process or combination of processes leads to progressive rounding of blocks over the course of time. It was also noted that the angular blocks associated with a relatively sharply formed crater northeast of the spacecraft have smooth planar faces, whereas the surfaces of most other blocks are pitted. This suggests that most of the pits are produced by impact of small particles and that small particle bombardment may be a significant process leading to the rounding of blocks. Other processes may also contribute to rounding. Sputtering of material from the blocks by solar protons may lead to significant mass loss and rounding. Professor Charles H. Townes has suggested to Shoemaker that ultraviolet radiation may cause appreciable evaporation of atoms from silicates on the lunar surface. We have observed ribs on rounded rocks at the *Surveyor I* landing site that may have been left by selective or differential evaporation of the surfaces of these blocks. Whatever the processes contributing to rounding, it is probably significant that those surfaces from which material is evidently being worn or evaporated away are the brightest surfaces observed from *Surveyors I* and *III*.

The general photometric relationships can be explained if it is assumed that the surfaces of particles in the shallow lunar subsurface tend to become coated with a dark substance. This hypothetical substance we will call *lunar varnish*. On the surfaces of blocks or coarse fragments that have been exposed to space for some time, the lunar varnish is scrubbed off by the processes that produce rounding. Under this hypothesis, the observed albedo of a large block is essentially the same as the albedo that would be observed on a new surface cut through the interior of the block.

The exposed surfaces of the fine particles on the lunar surface also have a tendency to be scrubbed. Because they are mixed fairly rapidly with coated particles just beneath the surface by mass movement and small cratering events, however, the scrubbing is incomplete and the fine-grained material at the surface has a lower albedo than the coarse blocks. In order for the material just beneath the surface to remain dark and not have its albedo raised by mixing with scrubbed particles from above, deposition or coating of particles by lunar varnish must take place just beneath the surface. The process of coating may also take place at greater depths. Inasmuch as the particles on the lunar surface are turned over or mixed to depths on the order of 1 mm in a period of time on the order of 100 to 1000 yr by small meteoroid bombardment, the deposition of lunar varnish must take place rapidly.

The composition of the lunar varnish and the processes by which it might be deposited are problems that remain to be solved. Hapke (Ref. III-11) has suggested that oxygen-depleted material derived by sputtering may be deposited on the under sides of grains on the lunar surface and on grains just beneath the surface. It appears that the experiments on which this suggestion was based do not show that the effect can be produced by sputtering. Hapke's experiments did produce a coating on the grains at very shallow depths, however, as required by our hypothesis. The lunar varnish may be deposited from gases escaping from depth or generated in the fragmental debris layer itself by high-energy charged particle radiation, or it may be deposited by some process or processes that we do not yet have sufficient clues to discover.

F. Photometric Observations of Lunar Surface Material

Several special, as well as general, photometric studies of the local lunar surface have been undertaken by means of the *Surveyor III* pictures. Areas of special interest for photometric study were the footpad imprints and the material disturbed by the SMSS. As in *Surveyor I*, the landing site was near the lunar equator, and the sun passed almost directly overhead. The site was, therefore, suitable for a general study of the local photometric function of the surface.

For the purpose of photometric data collection, several observing programs were planned for the *Surveyor III* mission. The plan consisted of taking pictures at selected steps along the east-west line to obtain photometric measurements in the plane defined by the vectors from the camera to the sun. Other target areas for pictures were selected at azimuths of ±45, ±90, and ±135 deg from the east-west line. Pictures taken at lunar noon were of special interest for study of the symmetry of the local photometric function. An additional objective was to measure the variation of the normal luminance factor (normal albedo) of the lunar surface from pictures taken of areas adjacent to the camera's shadow as it progressed (in the lunar afternoon) toward the east. Because of operational constraints and severe scattering of light from the mirror surface, only a few pictures suitable for photometric reduction were obtained.

Measurement and reduction of photometric data have been carried out in a manner similar to that used in the photometric analysis of *Surveyor I* pictures (Ref. III-1). Film negatives from the television Ground Data Handling System of the Space Flight Operations Facility, Pasadena, California, were measured with a Macbeth spot densitometer. The transfer characteristics of the negatives used and the total television transfer characteristic function for *Surveyor III* are shown in Figs. III-36 and III-37. Measurements of the film density of each gray level in pictures of the photometric target on leg 2 of the spacecraft were used to determine the total television transfer characteristic function. This function was used to determine scene luminance of areas of interest from the measurements of film density. The photometric geometry was calculated in terms of the vector normal to the local surface, the vector to the camera, and the vector to the sun. For convenience, these vectors were referred to lunar coordinates.

Several problems were encountered in the reduction of photometric data from the *Surveyor III* pictures. The most important and the most difficult problem to evaluate is the large amount of space light that was scattered from the camera mirror into the television images. The pattern of this scattered light varied as a function of the mirror azimuth and elevation angles and of the sun's positions. Light scattered from the mirror was also present when the mirror was turned away from the sun; thus, a significant amount of scattered light was derived from the luminous flux re-emitted by the terrain. As a start

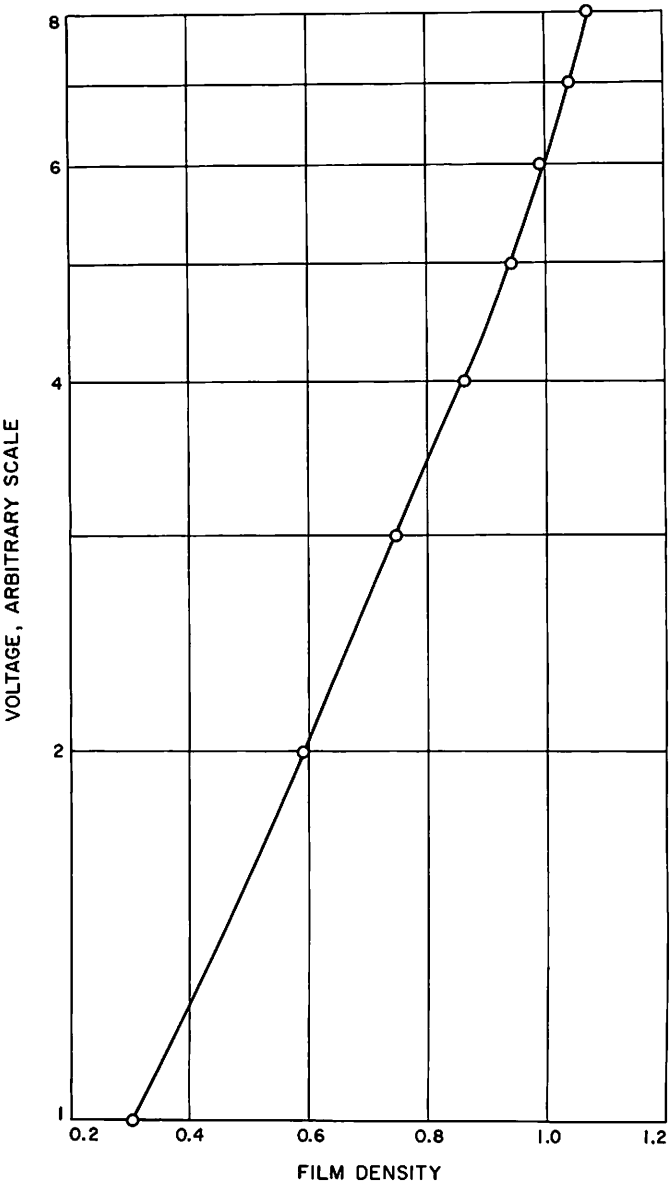

Fig. III-36. Typical plot of measured film density vs calibration voltage from electronic gray scale on negatives produced by Ground Data Handling System at the Space Flight Operations Facility. Electronic gray scale is added to each frame by the Ground Data Handling System to provide system photometric control

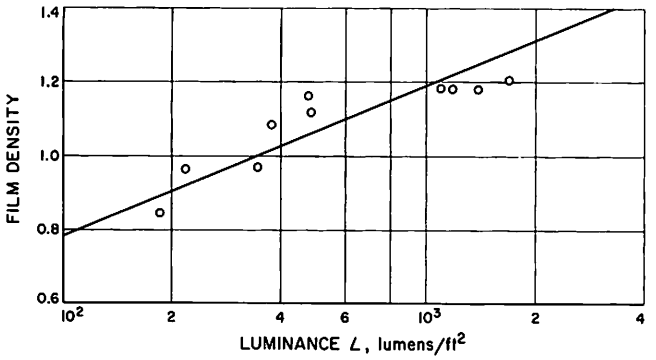

Fig. III-37. Total television system transfer characteristic function determined from observation of the photometric target on the spacecraft leg during lunar operations. This function is used to convert film density to scene luminance

toward evaluating the contribution of scattered light to television images, pictures were taken in wide angle of the photometric target on omnidirectional antenna B, after stepping the mirror in both azimuth and elevation to position the photometric target in various parts of the pictures. An estimate of the contrast attenuation resulting from scattered light can be made from these pictures, if it is assumed that the luminance of the objects in the pictures remains constant over the short period in which they were taken. This attenuation is illustrated in a narrow-angle picture of the photometric target on leg 2 of the spacecraft, shown in Fig. III-38. Measurements of the density of the spacecraft shadow observed in the lunar afternoon (Fig. III-39) can also be used to provide information on the pattern and intensity of the scattered light.

Several areas of special interest were chosen for a preliminary determination of the photometric properties of the lunar surface materials. These areas include the undisturbed surface in the vicinity of footpad 2, the footpad imprint next to footpad 2, an area disturbed by the SMSS, and the debris deposited on footpad 2 by the SMSS.

Examination of 14 measurements of the luminance of a small undisturbed area of the surface in the vicinity of footpad 2 indicates the photometric function of this area is similar to that observed at the *Surveyor I* landing site and that of other mare areas observed at the telescope. The estimated normal luminance factor (normal albedo) of this area is 8.5%. This calculated value has an estimated uncertainty of at least 25% because of uncertainty in the correction required for light scattered from the mirror.

Several times during the lunar day, pictures were taken of the floor of the imprint of footpad 2 next to the present position of the footpad; a few photometric measurements from these pictures have been reduced. The photometric function of the smoothed surface is conspicuously different from that of the undisturbed lunar surface, but the extent to which the function has been changed has not as yet been determined. The calculated luminance factor of the imprint floor is 30% greater than that of the adjacent undisturbed surface, at phase angles of approximately 40 to 60 deg in the lunar morning.

During operation of the SMSS, a sample of fine-grained material from the subsurface was placed on footpad 2. The measured part of the photometric function of this material does not differ appreciably in form from the function measured on the undisturbed areas; the normal luminance factor for this material is estimated to be about 7.6, about 10% less than that of the undisturbed surface. An area on the lunar surface disturbed by the SMSS, on the other hand, has an estimated normal luminance factor of 6.6, about 20% less than that of the undisturbed surface. It should be emphasized that these preliminary estimates have large possible errors because of uncertainties about the amount of light scattered from the mirror into the image formed on the vidicon target.

G. Colorimetric Observations of Lunar Surface

Color is commonly used in terrestrial geological studies as an aid in discriminating between rock types and in distinguishing the weathering state of rocks. Color filters were incorporated in the *Surveyor III* television camera, essentially for the same purposes. Because only a limited number of filters could be used in the television camera, three-color colorimetry was selected as the best method for measuring and describing the colors observed with the camera (Ref. III-12).

A technique suggested by Davies and Wyszecki (Ref. III-13) was used for selecting color filters to fit the response of the television camera approximately to the $\bar{x}(\lambda)$, $\bar{y}(\lambda)$, $\bar{z}(\lambda)$ color-matching functions of colorimetry. Two filters are used in series in the optical train of the camera. The filter glass components had to be 1 mm or more in thickness to withstand the vibration and rigors of space flight. Because of weight constraints, the filter pairs were limited to a total thickness of 3.0 mm. A special computer program was used for determining the ideal thicknesses and combinations of filters required to fit the *Surveyor III* camera system spectral response to the CIE color-matching functions; the fit obtained is

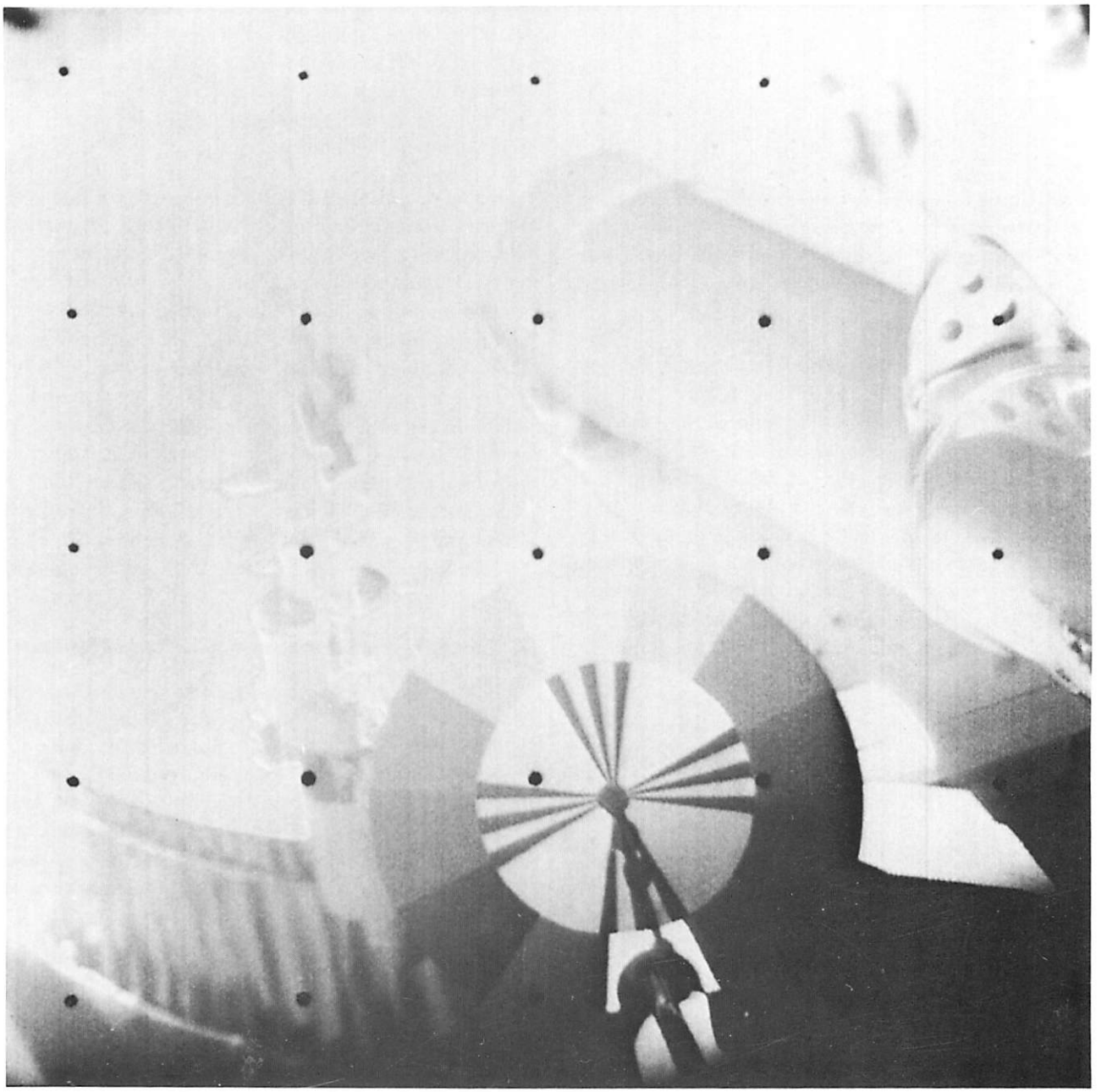

Fig. III-38. Narrow-angle *Surveyor III* picture of photometric target on leg 2. Note contrast attenuation and increase in light level toward the upper half of the picture (Day 116, 05:59:33 GMT)

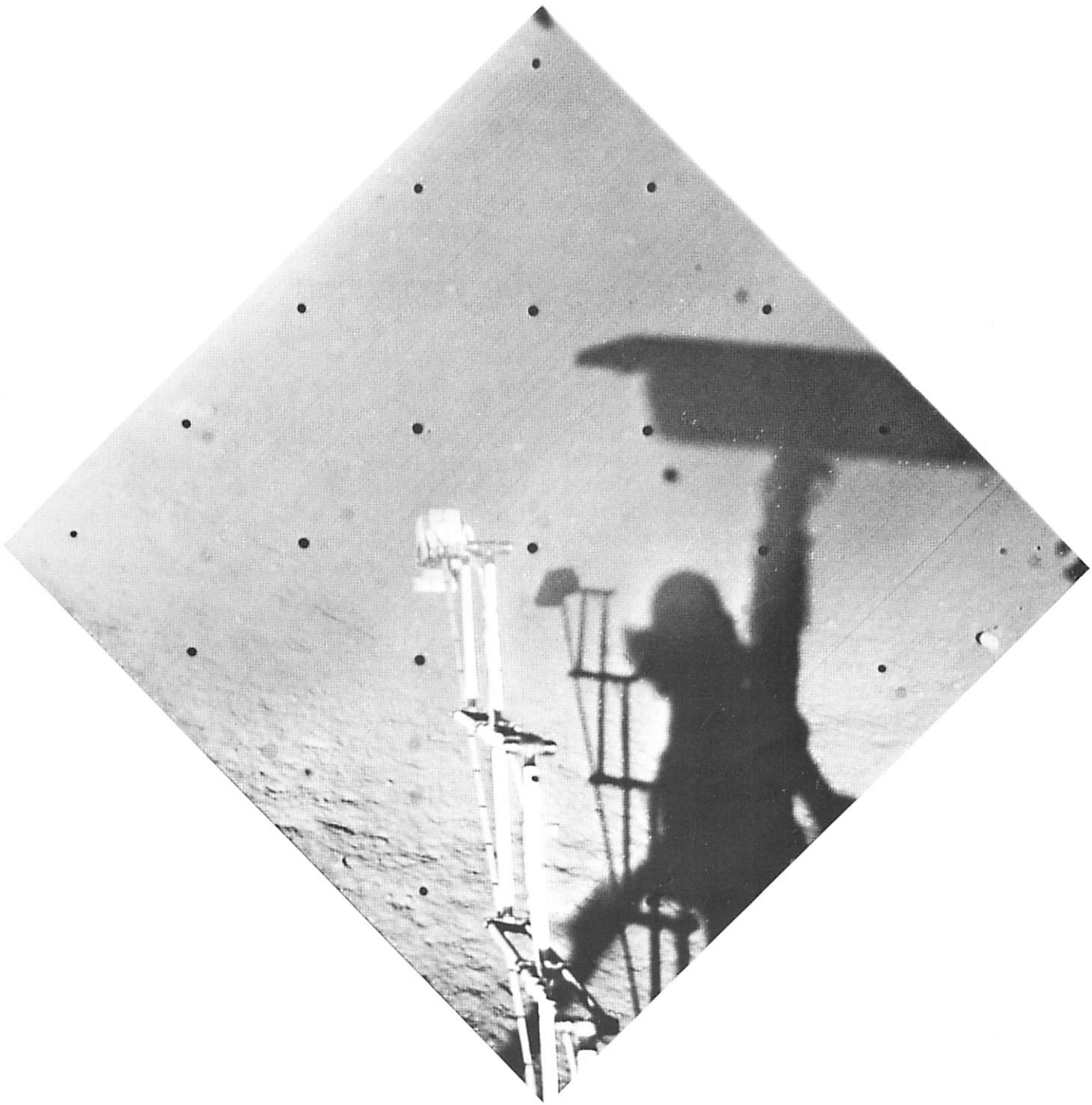

Fig. III-39. Wide-angle *Surveyor III* picture showing shadow of camera and solar panel. The shadows are washed out in the upper right half of the picture because of glare from camera mirror (Day 122, 14:37:01 GMT)

fairly good (Fig. III-1). The filters were coated with a neutral density deposit of Inconel so that, without varying the aperture, approximately equal video signals would be produced by exposure to a daylight source.

To measure color from the television pictures, it is necessary to determine the camera tristimulus values, which are proportional to the video voltage. The proportionality factors may be determined by measuring the video signal when the camera is exposed to object colors of known spectral radiance. Tristimulus values for the *Surveyor III* camera were determined by observing a 3×3 matrix of filter/source combinations prior to launch; the proportionality factors were obtained by least-squares solution. The chromaticity coordinates of these nine filter/source combinations were calibrated with a spectroradiometer.

The spectral response of the vidicon tubes used in the *Surveyor* television cameras is sensitive to temperature. Variation of the spectral response of the *Surveyor III* television camera with temperature was not calibrated prior to flight; thus, tristimulus values obtained from measurements of pictures of calibrated color targets, taken on the lunar surface at the operating temperature of the camera, must be used for accurate calculation of color. The color targets were provided as parts of the two photometric targets mounted on the spacecraft. Three colors are present on each target; they were calibrated with a spectroradiometer while irradiated by a known spectral source at various angles of incidence. Because of the contribution of scattered light to the *Surveyor III* pictures, the measurements of the photometric targets in the pictures must be analyzed carefully by computer techniques before a final interpretation of color is made.

Approximately 50 sets of pictures were obtained for colorimetric measurement during the *Surveyor III* television operations. Each set consists of multiple pictures taken through each of the three color filters. Experience from the *Surveyor I* pictures in reducing color measurements indicated there were significant variations between the video signals for pictures of the same scene taken in succession. The greatest difference occurred between the first and second pictures. After the third picture, the differences were negligible. Therefore, three pictures were taken through each color filter on *Surveyor III;* the first two are not used for color measurement. All of the pictures in a given set were taken by positioning the camera at one azimuth and elevation setting and rotating the filter wheel through the color sequence, to avoid incorrect picture registration. The neutral density coatings on the filters permitted all pictures in a set to be taken without change in iris, thereby eliminating errors in color measurement resulting from uncertainty in aperture.

Sets of pictures for colorimetric measurement were taken of various parts of the lunar surface. Some of the larger blocks and the material disturbed by the SMSS were of special interest. A first attempt to look for color differences has been made by preparing color pictures, by color reconstitution methods, using the preflight calibration for control. Figure III-40 shows three black and white pictures, taken through the $\bar{x}'$ (red), $\bar{y}'$ (green), and $\bar{z}'$ (blue) filters, that were used to prepare a color picture of the footpad, the photometric target, and the debris placed on the pad by the SMSS. The known colors on the photometric target, the white surface of the footpad, and the gold tip of the attitude control jet were reproduced fairly well in the reconstituted color picture; the debris is dark gray in color. Figure III-41 shows three pictures of a SMSS trench and the adjacent disturbed fine-grained material on the lunar surface taken through each of the color filters. The light blue color of the SMSS was reproduced well in a reconstituted color picture, although the color is somewhat washed out because the image of the sampler was nearly saturated in parts of the pictures; the disturbed material of the lunar surface is a relatively uniform dark gray. No demonstrable differences in color have been observed on any of the examined coarse blocks, which are all gray, but lighter than the fine-grained gray matrix of the surface. It will be necessary to digitize the television pictures and analyze the color by computer methods to determine whether subtle color differences are present among the materials observed.

H. Eclipse of Sun by Earth as Seen From *Surveyor III*

An unusual opportunity occurred late in the lunar morning to observe an eclipse of the sun by the earth, which took place on Day 114 during the Goldstone pass of the moon. Were it not for the fact that the spacecraft was tilted as much as 14.7 deg to the west and was oriented favorably with respect to azimuth, it would not have been possible to observe the earth from a landing site at 23°W longitude because of the limited range of elevation angles through which the mirror can be stepped. To observe the earth, the mirror was pointed upward, positioned at its highest permissible elevation step, and a wide-angle picture of the eclipse was obtained. The

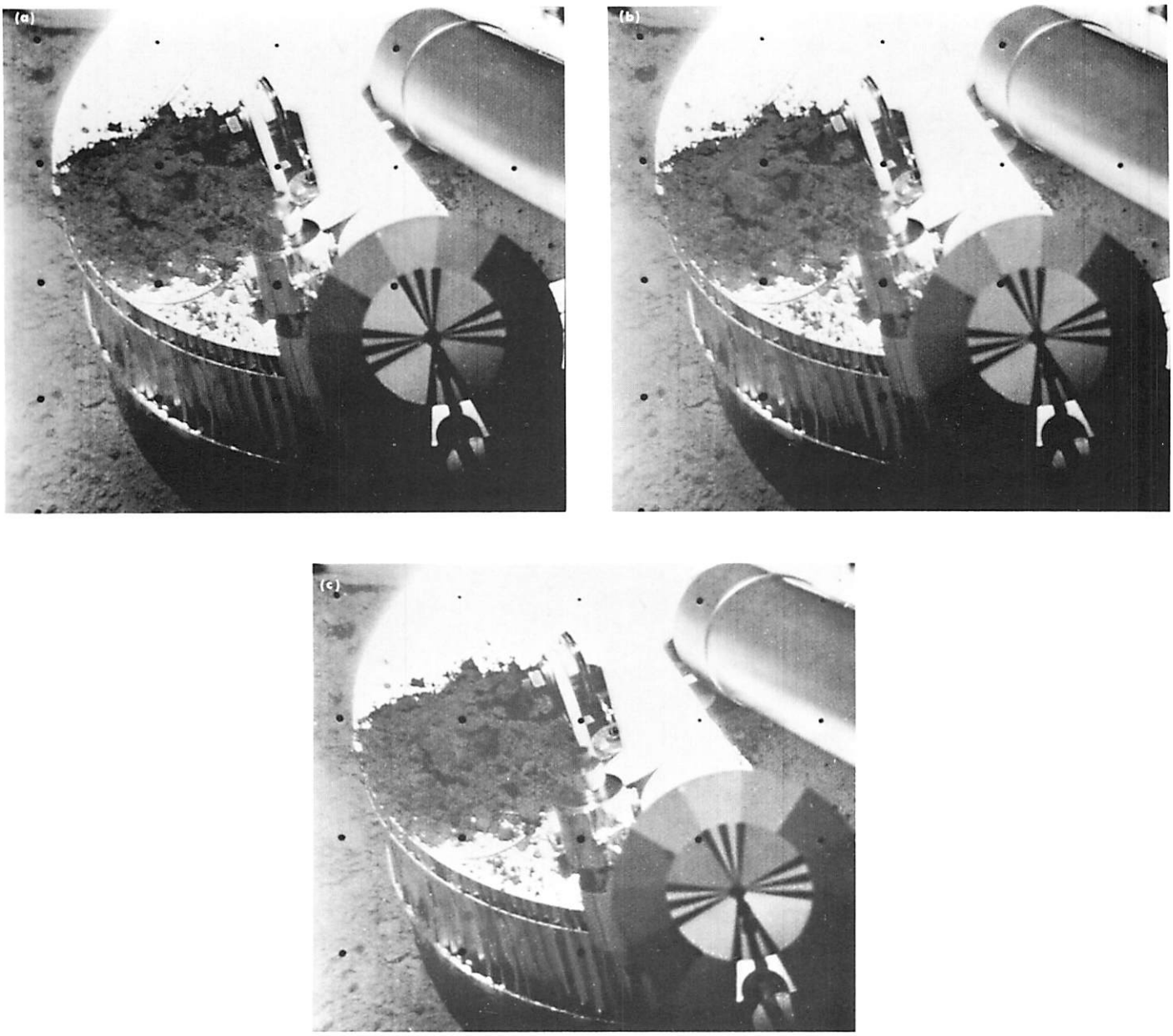

Fig. III-40. Narrow-angle *Surveyor III* pictures showing photometric target and debris on footpad 2. Pictures taken on Day 116: (a) through $\bar{x}'$ filter (red), 12:00:54 GMT; (b) through $\bar{y}'$ filter (green), 12:02:14 GMT; and (c) through $\bar{z}'$ filter (blue), 12:01:27 GMT

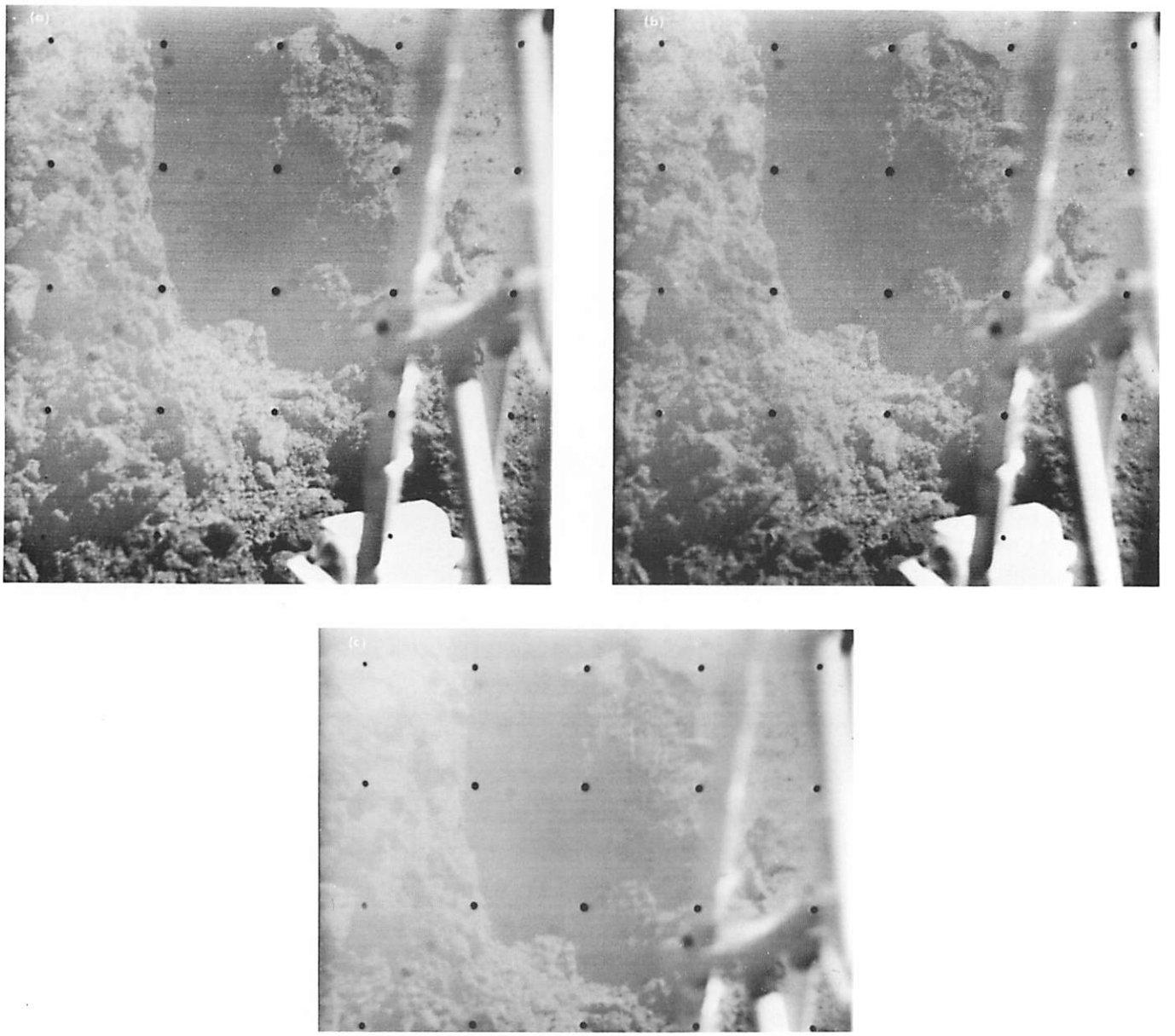

Fig. III-41. Narrow-angle *Surveyor III* pictures of SMSS trench observed on Day 114: (a) through $\bar{x}'$ filter (red), 05:19:23 GMT; (b) $\bar{y}'$ filter (green), 05:15:18 GMT; and (c) $\bar{z}'$ filter (blue), 05:20:20 GMT

image of the earth was reflected from a part of the mirror very close to its upper edge. During the eclipse, two series of pictures (a total of 20 pictures) were obtained through the color filters. The first series of pictures was obtained at approximately 11:24 GMT; the second set was obtained about 37 min later. The pictures were taken at two iris positions and multiple pictures were taken through each filter.

During the eclipse, the sun passed behind the earth along a path that brought the position of the center of the sun, as seen from the moon, to within 15 min of the sublunar point on the earth (Fig. III-42). At the time the sun was most nearly centered behind the earth, the projected center of the sun lay northeast of the sublunar point. The sublunar point was about 172°W longitude, 12.5°S latitude at the time the first series of pictures was taken, and at about 179°E longitude and 12.5°S latitude at the time the second series of pictures was taken. These positions are in the southwest Pacific. The limb of the earth lay along western North America, the eastern Pacific, eastern Antarctica, the central Indian Ocean,

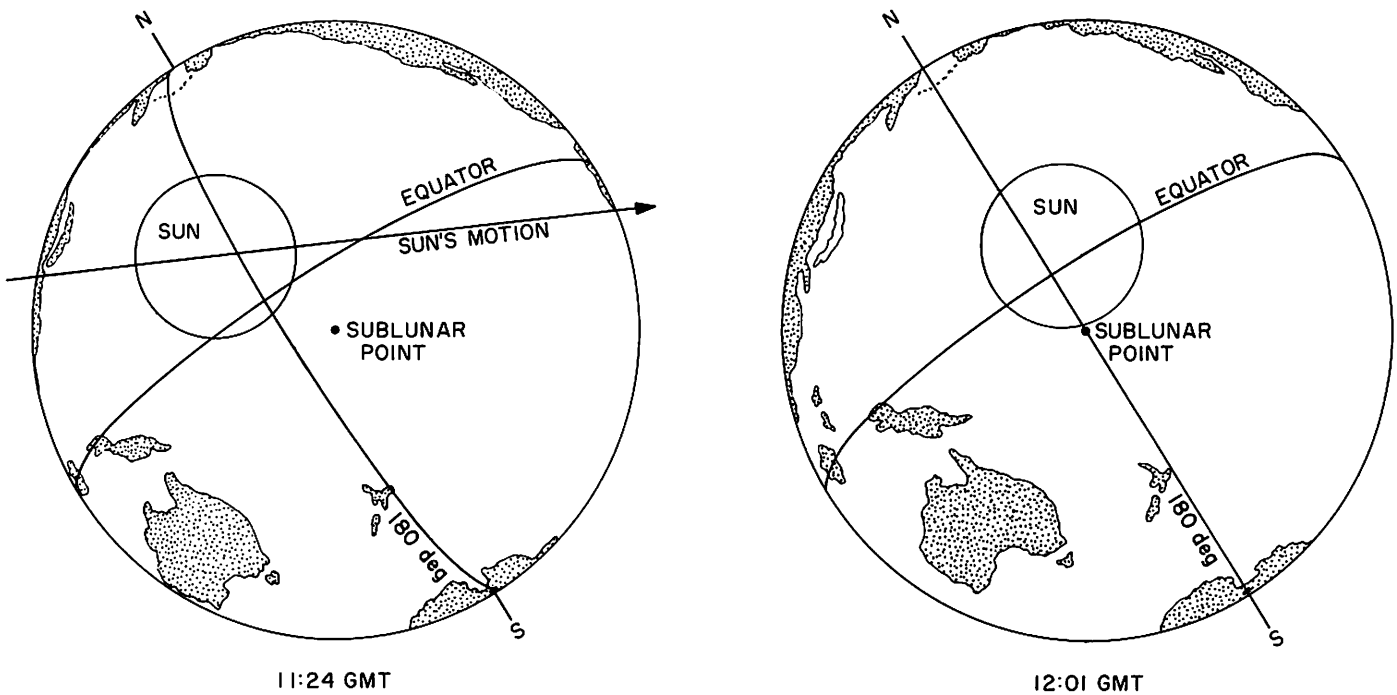

Fig. III-42. Diagrams showing orientation of earth and position of the sun, as seen from the moon on Day 116, at 11:24 GMT and 12:01 GMT. A series of pictures of the eclipse of the sun by the earth was taken with the *Surveyor III* television camera approximately at each of the times illustrated

southeast Asia, central China, eastern Siberia, and a short arc across the western Arctic Ocean.

In the first series of eclipse pictures, the earth is partially surrounded by a halo of refracted light that varies greatly in brightness from one position to another along the limb (Fig. III-43). A very bright region, approximately 60 deg in arc length, lies along the northern part of the limb, nearest the position of the sun. In the majority of pictures taken, parts of the image of the halo in this region are saturated. On either side of this bright region, the halo has a beaded appearance; small bright areas of short arc length are separated from other bright areas by sectors of the halo that are relatively faint. Most of these bright areas or beads are only a few degrees in length, but one relatively bright sector about 20 deg long is present that cannot be resolved into separate beads. At least 12 beads can be distinguished in the halo.

A gap ranging from about 50 deg to more than 90 deg is present in the images of the halo along the eastern limb of earth. Over most of the arc length of the gap, the halo was too faint to be detected with the exposures used, but over a short sector of the gap the image of the earth may have been cut off by the edge of the camera mirror.

In the second series of eclipse pictures, the very bright region in the halo shifted to the northeastern part of the limb, following the sun (Fig. III-43). More of the eastern limb was bright enough to be detected in the second series of television pictures than in the first series, and the gap was reduced to an arc length no greater than 40 deg. At least 18 beads can be distinguished in the halo in the best exposed pictures. Many of these beads occur at the same angular position, relative to the projection of the earth's axis, as the beads observed in the first series of pictures (Fig. III-43). The beads are clearly related to features in the earth's atmosphere, in contrast to the brightest region in the halo, which is related to the position of the sun.

To identify the atmospheric features controlling the distribution of the beads, each bead's position in the second series of pictures was measured relative to the projection of the earth's axis. These positions were plotted on the trace of the limb on stereographic projections of the northern and southern hemispheres of the earth. The

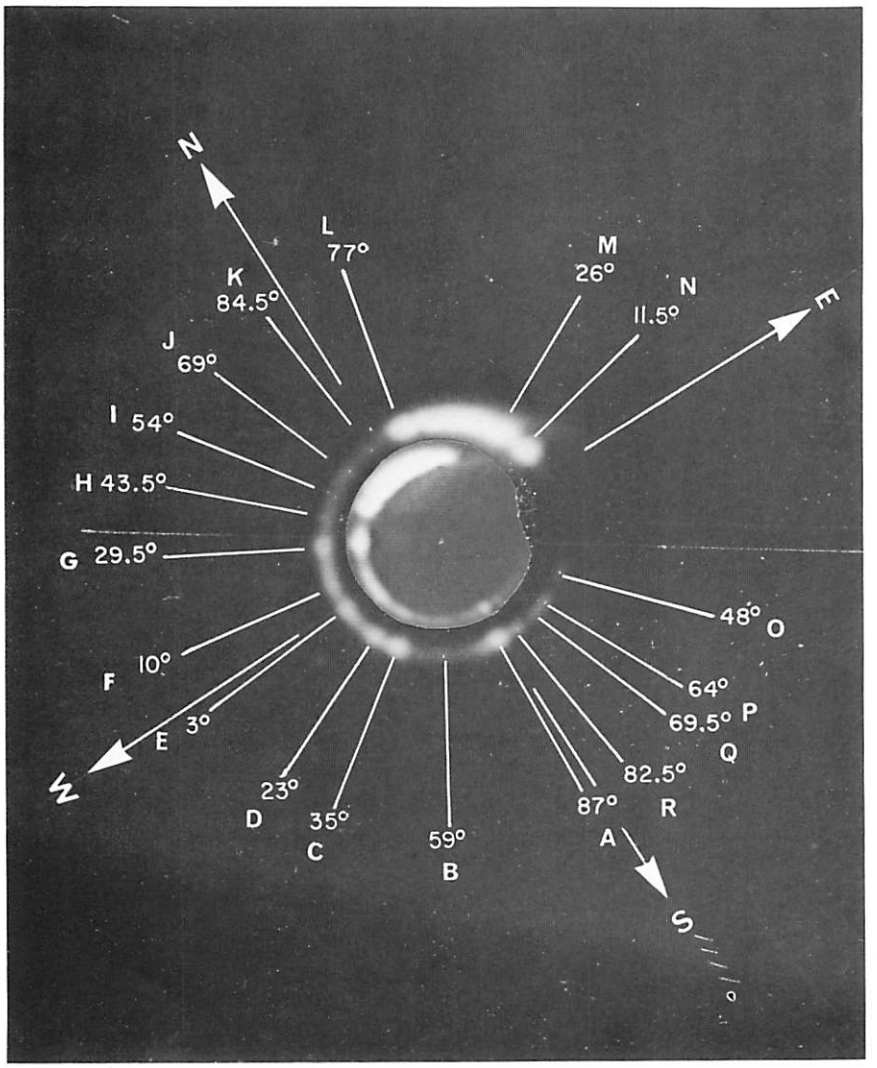

Fig. III-43. Superimposed *Surveyor III* pictures illustrating distribution of light in the refraction halo of the earth at the time the first series of eclipse pictures was taken and at the time the second series was taken. An eclipse image taken from the first series of pictures has been reduced in size and shown nested within an eclipse image taken from the second series of eclipse pictures. The angular orientation of both images is the same. Line marked N-S shows projection of earth's axis on plane of pictures. Eighteen beads, identified by letters, can be distinguished. Note the angular position of beads in the refraction halo tends to remain the same, but the bright region nearest the sun changes position between the time of the first series of pictures and the second series, following the sun

plotted positions of the beads were then compared directly with stereographic mosaics of ESSA 3 pictures of the earth taken on the day preceding the eclipse (Fig. III-44a and b). Even though there was some shift in cloud patterns between the time the ESSA 3 pictures were taken and the time of the eclipse, it can be seen that the beads occur predominantly over clear or largely clear regions between the clouds. Clouds tend to occult the refracted rays of the sun, most of which pass through the low atmosphere at the limb; the beads occur at depressions in the optical silhouette of the earth.

Preliminary reduction has been started on the colorimetric information contained in the pictures. Six pictures, one taken through each of the three color filters during each of the two periods of observation (Fig. III-45), were digitized using equipment at Jet Propulsion Laboratory, Pasadena, Calif. The video voltage recorded on magnetic tape was divided into 64 equally spaced levels. For calibration, the preflight recording of the 3 × 3 filter matrix was also digitized. Equations for computing tristimulus values were derived from the digital printout of the preflight calibration tape.

The digitization procedure adopted for the television pictures generates a larger number of digital picture elements along a scan line than there are scan lines in the picture; the digital picture is a rectangular matrix of 600 × 684 elements. In the first series of pictures, the image of the refraction halo is 54 lines high and 61 picture elements wide. The total number of picture elements yielding colorimetric data in each of the digitized pictures from this series was 644. Chromaticity coordinates for selected picture elements were calculated, by means of the tristimulus value equations, from the digital voltages of corresponding elements in pictures taken through each of the three color pictures. Because of present uncertainties about the preflight calibration tapes and because of possible jitter or other displacement of image points in corresponding pictures, the calculated chromaticity coordinates may have an error as much as 0.03 in x and y.

Chromaticity coordinates were calculated for 18 points on the images in the first series of eclipse pictures and were plotted on a chromaticity diagram (Fig. III-46). The location of these colorimetric measurements with respect to the eclipse images is shown in Fig. III-47. Also plotted on the chromaticity diagram are the locus of color temperatures for a body which obeys Planck's law (a blackbody) and the locus of color temperatures for natural daylight as far as 4800°K. Loci of correlated color temperature (Ref. III-14) are shown in Fig. III-46 crossing the Planckian locus.

Most of the colorimetric measurements were taken in the bright region of the halo controlled by the position of the sun. The majority of measurements in this region have a correlated color temperature close to 4800°K. Beads in the halo exhibit lower correlated color temperatures. The center of bead G, close to the bright region, has a correlated color temperature of about 4000°K, and the center of bead A, which lies over Anarctica, farthest from the projected position of the sun, has a correlated color temperature of approximately 2850°K. The correlated color temperature tends to decrease in directions away from the projected position of the sun and also tends to decrease toward the inner edge of the halo. As would be expected, the color temperature has a tendency to be lower for light that followed paths of greater atmospheric absorption. Most of the colors present in the images had purities less than 50%.

I. Partially Illuminated Earth as Seen from *Surveyor III*

During the period from 10:29 to 11:06 GMT on Day 120, 25 pictures of earth were taken with the *Surveyor III* camera in the wide-angle mode. The angle of elevation was too great for pictures of the earth to be taken in the narrow-angle mode. The images were obtained using the three color filters (red, blue, and green), and a color picture of the earth has been reconstituted from a selected set of three pictures. A diagram of the orientation of earth and the theoretical position of the sunrise line and corresponding series of pictures taken through each filter position are shown in Fig. III-48. The bright areas in the pictures are cloud covered; clouds can be seen to extend over most of the Atlantic Ocean and the northern coast of South America. Parts of the Caribbean Sea and southwestern Brazil appear to be free of clouds.

As the distance between centers of the television lines is about 2.5 min of arc, the details shown in the *Surveyor III* pictures of the earth are comparable to the details recorded in good quality telescopic photographs of Mars, near opposition, or observed visually with a telescope of about 20-cm aperture.

A preliminary analysis of the earth pictures by color reconstitution indicates the clouds are white, whereas the areas free of clouds vary in hue from greenish blue to purplish blue. The colors are similar to those recorded and seen by the *Mercury* and *Gemini* astronauts.

Fig. III-44. Stereographic mosaics of ESSA 3 pictures of (a) northern and (b) southern hemispheres of the earth. Pictures taken on the day preceding the eclipse. Bright areas are clouds and, in mountainous regions and the Arctic, snow fields; dark areas are clear. Note position of African continent, which may be seen in the clear areas on right-hand side of (a). Trace of limb of earth, as seen from the moon, and positions of beads and the bright region in the refraction halo of the earth observed in the second series of eclipse pictures taken by *Surveyor III* are shown by the white circles and lines that extend from 90° west to 90° east. Beads occur in areas that are largely clear. Letters beside symbols for beads correspond to letter identification of beads in Fig. III-43 (mosaic of ESSA 3 pictures provided through the courtesy of Dr. David S. Johnson, National Environmental Satellite Center, ESSA)

Fig. III-44 (contd)

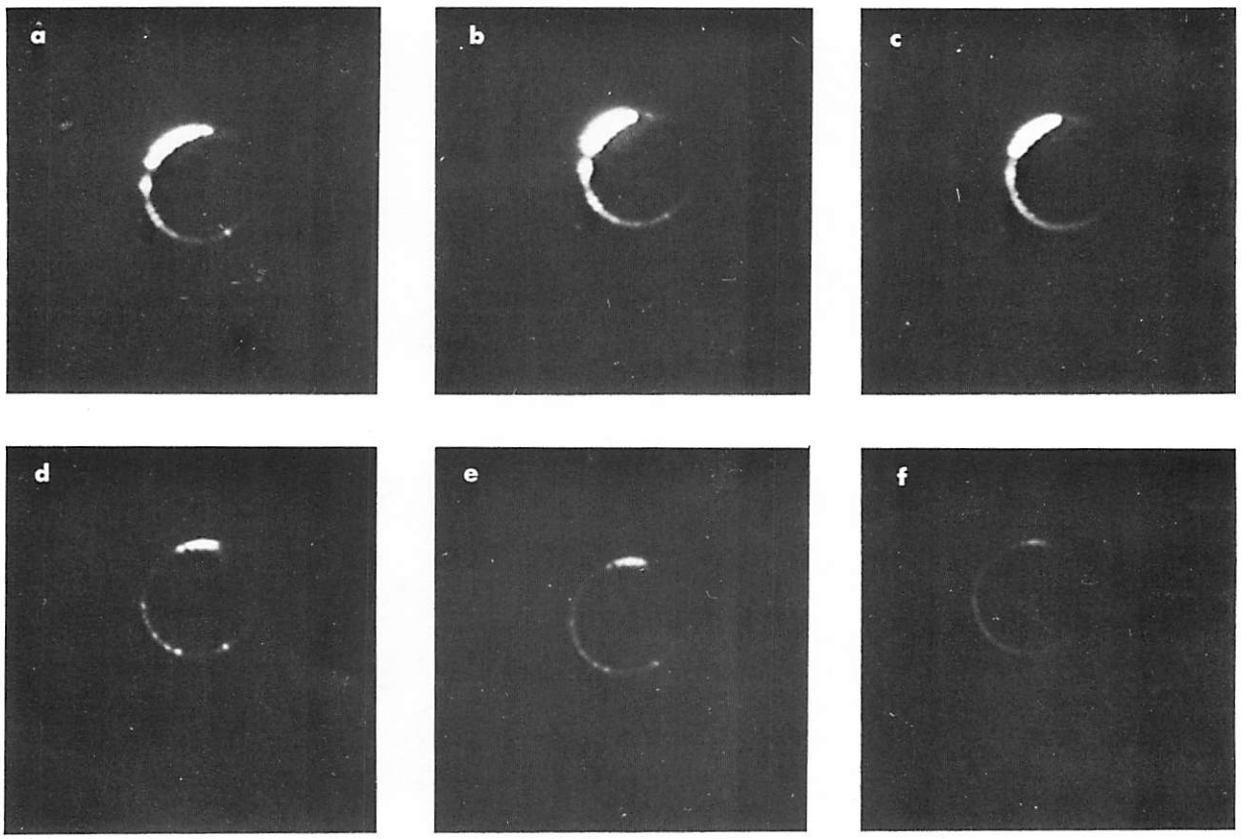

Fig. III-45. Wide-angle *Surveyor III* pictures showing eclipse of sun by earth as observed on Day 114 through the filters indicated: (a) $\bar{x}'$ (red), 11:31:40 GMT; (b) $\bar{y}'$ (green), 11:23:06 GMT; (c) $\bar{z}'$ (blue), 11:24:01 GMT; (d) $\bar{x}'$, 12:02:10 GMT; (e) $\bar{y}'$, 12:03:10 GMT; and (f) $\bar{z}'$, 12:02:44 GMT. (First set of figures includes a, b, and c; second set of figures includes d, e, and f)

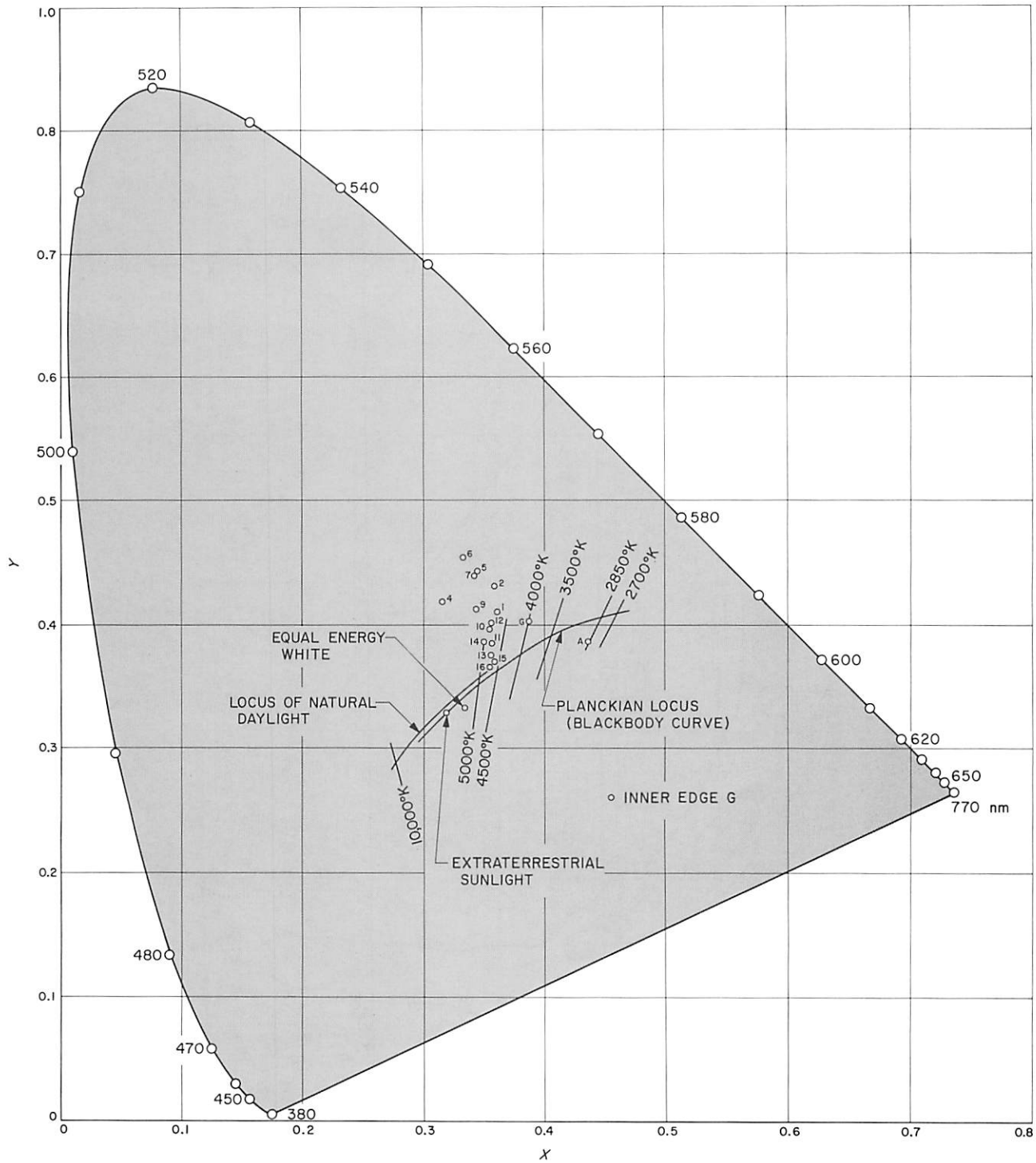

Fig. III-46. Chromaticity coordinates of selected points from the first series of *Surveyor* eclipse pictures. For purposes of comparison, the Planckian locus with correlated color temperature lines is shown together with the locus of natural daylight as measured by Y. Nayatani and G. Wyszecki (Ref. III-15)

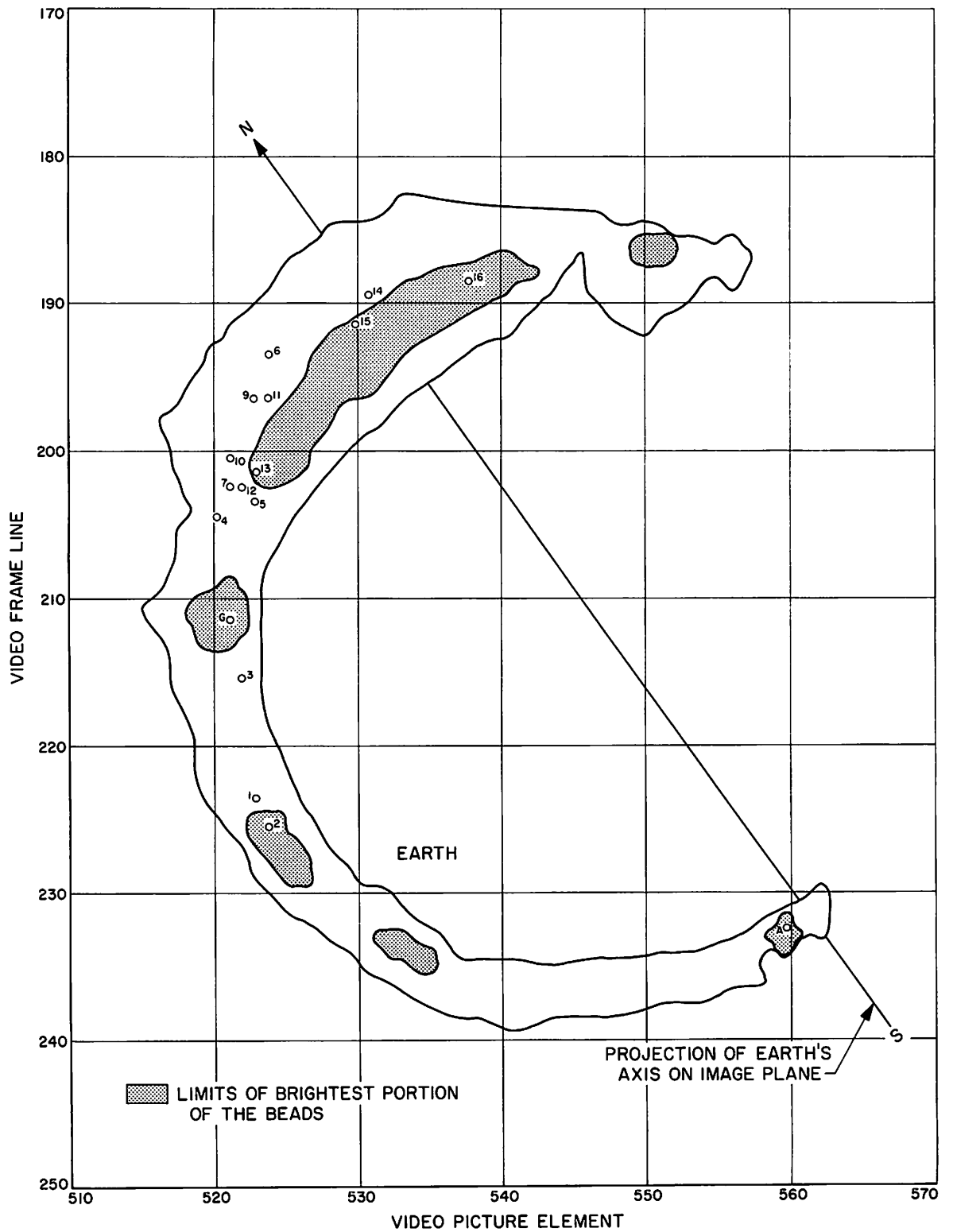

Fig. III-47. Diagram of the solar eclipse showing positions of points on the color composite image that were measured for color. The letters refer to the beads

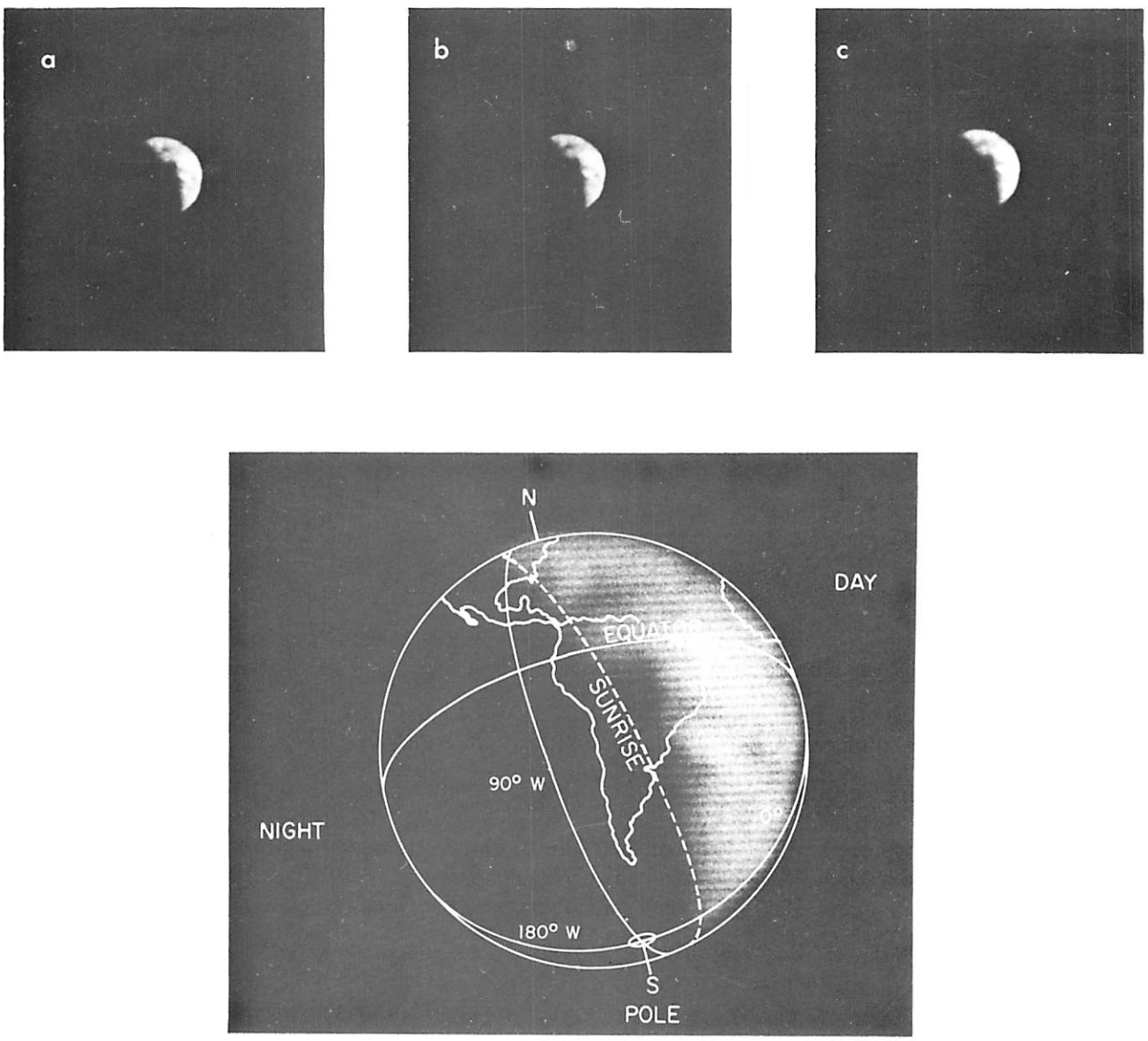

Fig. III-48. Wide-angle *Surveyor III* pictures of earth as observed on Day 120 through: (a) $\bar{x}'$ filter (red), 10:39:29 GMT; (b) $\bar{y}'$ filter (green), 10:37:18 GMT; and (c) $\bar{z}'$ filter (blue), 10:38:15 GMT. The lunar libration had caused a favorable movement of the earth's position giving an unobstructed view of earth from *Surveyor III*. Diagram shows orientation of earth when pictures were taken

References

III-1. Rennilson, J. J., et al., "Lunar Surface Topography," *Surveyor I Mission Report. Part II: Scientific Data and Results*, Technical Report 32-1023, pp. 1–44, Jet Propulsion Laboratory, Pasadena, Calif., Sept. 10, 1966.

III-2. Lebedinskiy, A. I., "Scientific Results of Processing of Panoramas From Photographs of the Lunar Surface Taken From Luna-9," from reprint of the USSR Academy of Sciences Izdatel'stvo NAUKA, National Aeronautics and Space Administration, Goddard Space Flight Center, Contract No. NAS 5-9299, ST-LPS-10493/Revision 1, 1966.

III-3. Christensen, E. M., et al., "Lunar Surface Mechanical Properties," *Surveyor III Preliminary Science Results*, Project Document 125, Jet Propulsion Laboratory, Pasadena, Calif., May 15, 1967.

III-4. Shoemaker, E. M., "Preliminary Analysis of the Fine Structure of the Lunar Surface in Mare Cognitum," *The Nature of the Lunar Surface*, Proceedings of the 1965 IAU-NASA Symposium, The Johns Hopkins Press (Hess, W. N., Menzel, D. H., O'Keefe, J. A., editors), pp. 23–78, 1966.

III-5. Trask, N. J., "Size and Spatial Distribution of Craters Estimated From the Ranger Photographs," in Shoemaker, E. M., *Progress in the Analysis of the Fine Structure and Geology of the Lunar Surface From the Ranger VIII and IX Photographs, Rangers VIII and IX. Part Two: Experimenters' Analyses and Interpretations*, Technical Report 32-800, pp. 252–267, Jet Propulsion Laboratory, Pasadena, Calif., March 15, 1966.

III-6. Marcus, A., "A Stochastic Model of the Formation and Survival of Lunar Craters. V. Approximate Diameter Distribution of Primary and Secondary Craters," *Icarus*, Vol. 5, No. 6, pp. 590–605, 1966.

III-7. Gault, D. E., et al., "Criteria for Equilibrium Crater Distribution on the Lunar Surface" (to be published as a NASA report).

III-8. Moore, H. J., and Lugn, R. V., "A Missile Impact in Water Saturated Sediments," in *Astrogeologic Studies Annual Progress Report, July 1964–July 1965, Part B: U. S. Geological Survey Open-File Report*, pp. 101–126, 1965.

III-9. Christensen, E. M., et al., "Lunar Surface Mechanical Properties," *Surveyor I Mission Report. Part II. Scientific Data and Results*, Technical Report 32-1023, Jet Propulsion Laboratory, Pasadena, Calif., Sept. 10, 1966.

III-10. Titley, S. R., "Seismic Energy as an Agent of Morphologic Modification on the Moon," in *Astrogeologic Studies Annual Progress Report, July 1965–July 1966, Part A: U. S. Geological Survey Open-File Report*, 1967.

III-11. Hapke, B. W., "Optical Properties of the Moon's Surface," *The Nature of the Lunar Surface*, Proceedings of the IAU-NASA Symposium, The Johns Hopkins Press, pp. 141–154, 1966.

III-12. Rennilson, J. J., "A Television Colorimeter for Lunar Exploration," Proceedings of the 8th International Colour Meeting, Lucerne, Switzerland, Centre d'Information de la Couleur, 23 Rue Notre-Dame-des-Victoire, Paris, France, June 1965.

References (contd)

III-13. Davies, W. E., and Wyszecki, G., "Physical Approximation of Color-Mixture-Functions," *J. Opt. Soc. Am.*, Vol. 52, No. 6, pp. 679–685, June 1962.

III-14. Judd, D. B., MacAdam, D. L., and Wyszecki, G., "Spectral Distribution of Typical Daylite as a Function of Correlated Color Temperature," *J. Opt. Soc. Am.*, Vol. 54, No. 8, pp. 1030–1040, 1964.

III-15. Nayatani, Y., and Wyszecki, G., "Color of Daylight From North Sky," *J. Opt. Soc. Am.*, Vol. 53, No. 5, pp. 626–629, 1963.

Acknowledgment

Special appreciation is extended to Raymond Jordan, Jo Anne Jordan, and S. G. Priebe, U. S. Geological Survey, and to Sayuri Harami and Patricia B. Fisher, JPL, for help in the reduction of the television data and in the preparation of this report.

(Blank Page)

IV. Soil Mechanics Surface Sampler: Lunar Surface Tests, Results, and Analyses

R. F. Scott and F. I. Roberson

After the success of *Surveyor I* in meeting the objectives of the engineering flight series, selection from among candidate experiments led to the inclusion of the soil mechanics surface sampler (SMSS) on the *Surveyor III* payload. Although originally planned for later *Surveyors*, the SMSS was modified to fit the reduced telemetry and commanding capability of *Surveyor III*. Specifically, the SMSS was adapted to the mounting location and the electronics interface of the approach television camera. This required a concentrated, short-term effort to modify, build, and test the SMSS to meet the demanding interface requirements.

Modifications to the SMSS included removal of the strain-, acceleration-, and position-measuring systems originally planned, and incorporation of a means for measuring current drawn by the motors during operation. A description of the modified device, its performance on *Surveyor III*, and some conclusions regarding the lunar surface material are presented in this section.

A. Subsystem Description

The SMSS subsystem consists of a mechanism, an electronics auxiliary, installation substructure, and wiring harnesses. The mechanism is an electromechanical device that can pick, dig, scrape, and trench the lunar surface, and transport lunar surface material. The electronics auxiliary provides command decoding, data buffering, power management, squib firing, and control of the mechanism, motors, and clutch. The installation substructure supports the mechanism and the auxiliary on the spacecraft. The wiring harnesses provide the electrical interconnections with the spacecraft and between units within the subsystem.

1. Extension/Retraction Mechanism

The extension/retraction mechanism is designed to support and position the scoop and to permit operations within the space envelope shown in Fig. IV-1. The mechanism rotates about azimuth and elevation pivot points to provide movement in spherical coordinates.

2. Drive System

Three electrical motors, operating through appropriate drive trains, furnish mechanical energy to manipulate the SMSS in extension and retraction, azimuth, and elevation. At command from earth, an electromechanical clutch disengages the elevation drive train, allowing the mechanism to be impelled downward by a pretensioned elevation torque spring, thus striking the lunar surface. A

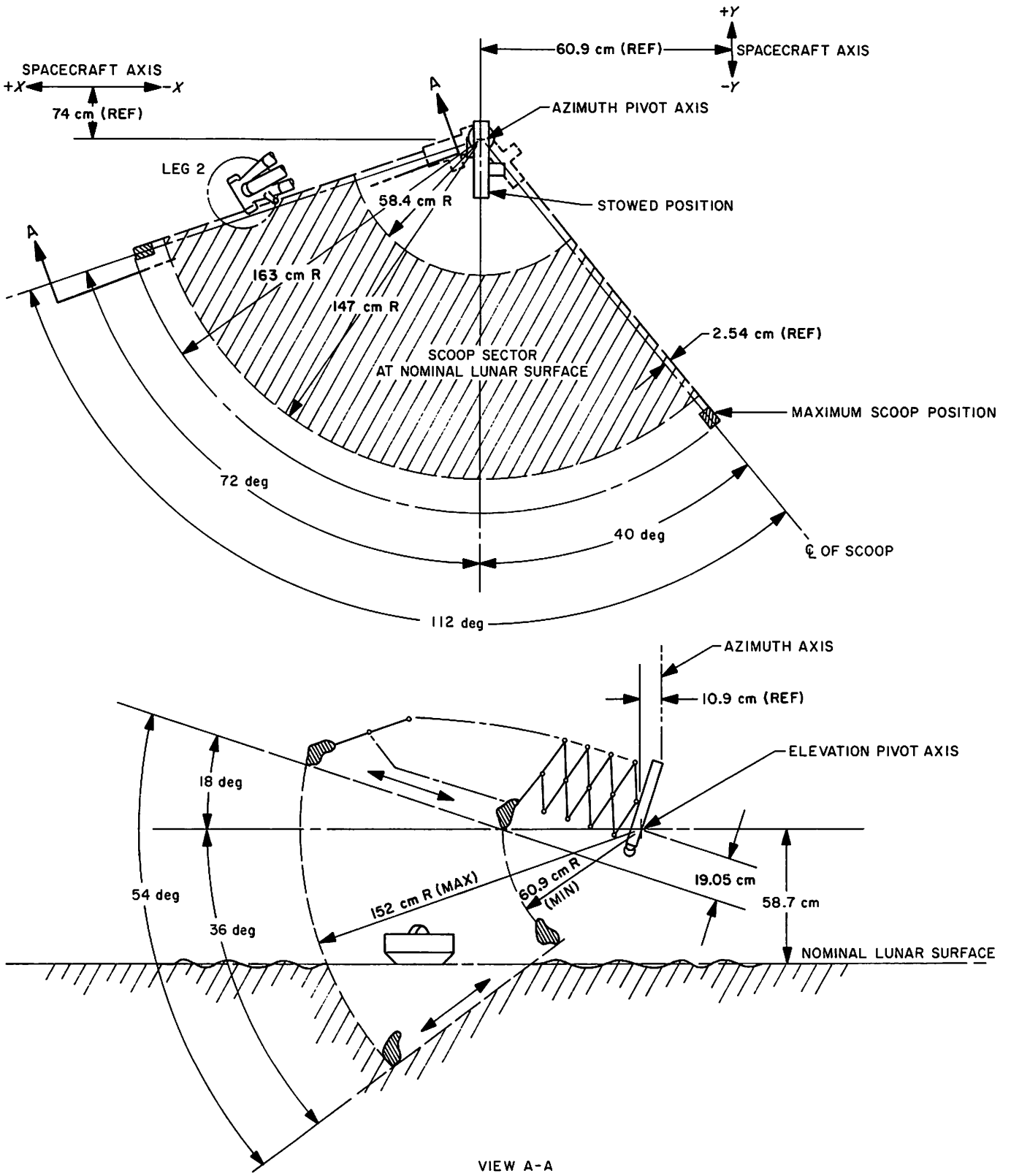

Fig. IV-1. Space envelope of operation, SMSS mechanism

fourth electric motor opens and closes the scoop. The motors and clutch draw electrical power from the spacecraft unregulated bus through the electronics auxiliary, which also provides switch control.

3. Scoop

The scoop consists of a container, a sharpened blade, and an electrical motor to open and close the container. A small footpad is attached to the scoop door to present a flat surface to the lunar surface. The scoop is capable of holding a maximum of approximately 3.2-cm diameter solid lunar material, and a maximum of 100 cm^3 of granular material.

Before the *Surveyor III* flight, a test of SMSS motor current vs force calibration was performed on the spacecraft at Cape Kennedy under ambient temperature conditions and at an unregulated voltage of 22 V. The purpose of this test was to acquire information about mechanical properties of the lunar surface.

4. Motor Control

Either a 2-s or a 0.1-s period of operation of any of the motors can be selected by earth command. The angle or distance through which the SMSS moves by these commands depends on the motor involved, its condition, temperature, voltage, and the working load.

B. Functional and Operational Description

The SMSS, as modified for *Surveyor III*, was mounted in the location formerly occupied by the approach television camera. This position lies below the survey television camera, between the auxiliary battery and leg 2, as shown in Fig. IV-2. The area of operation, for

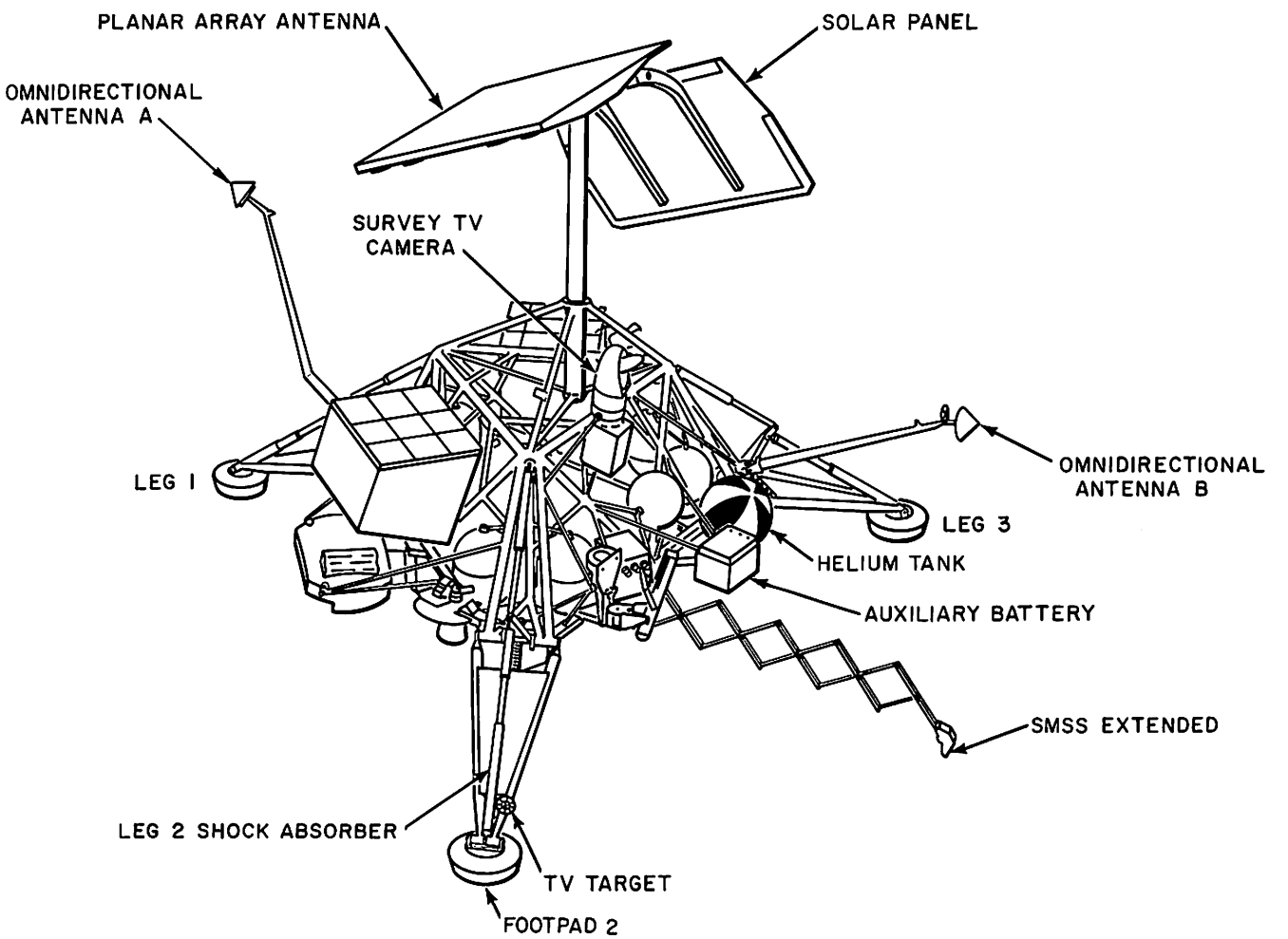

Fig. IV-2. *Surveyor* spacecraft, showing SMSS mounted at approach camera location

a nominal surface plane through the three footpads, is shown in Fig. IV-1. Because the azimuth axes of the SMSS and the camera are not collinear, the viewing angle, through the television system, of the scoop varies with the scoop's position. When the scoop is positioned near footpad 2, the camera looks directly down the extension arm, which largely obscures the scoop itself. When positioned near the auxiliary battery, a slight side view of the scoop is afforded.

As the SMSS is extended, the angle that the scoop makes with the test surface varies. The extension arm drawing in Fig. IV-1 shows the effect; the photographs of the scoop in contact with the surface (Fig. IV-3a and 3b) show the resulting angle for two extension positions on a nominal, flat surface. The flat surface of the scoop door is normal to the tangential elevation motion at maximum extension.

To make optimum use of operating time during a mission, a standard sequence of testing events has been established. Automatic, taped sequences of spacecraft commands have been prepared, which provide the correct motion, based on preflight tests, to accomplish the planned operations. Corrections for variations in motion sizes occurring on the moon are provided by manually commanding the mechanism after a given taped sequence is complete. Table IV-1 lists the size of each of the motions indicated by preflight calibration. These motion increments occurred at a motor voltage of 22.0 V and a motor temperature of 70°F. For comparison, the sizes of motion increments estimated during *Surveyor III* lunar operations also are listed. More precise calibrations will be made at a later time.

The originally planned initial standard sequence of tests included six static bearing tests and a single trench.

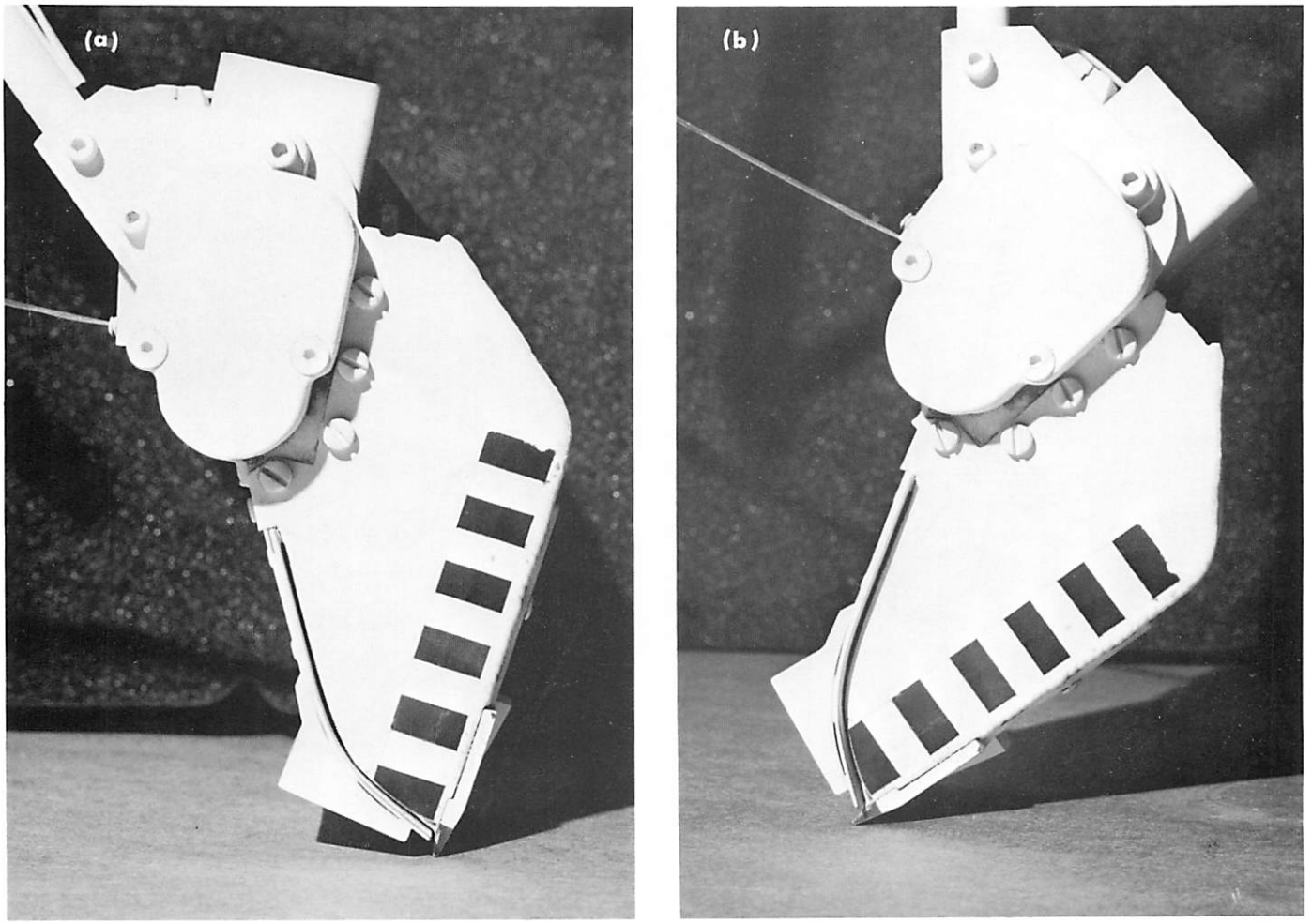

Fig. IV-3. Photographs showing angle that SMSS scoop door makes with a nominal surface at (a) maximum extension distance and (b) minimum extension distance at which surface can be reached

Table IV-1. SMSS motion increments (no load)

Motion, s	Test value[a]	Value on lunar[b] surface	Value on lunar[c] surface
2.0 (extend)	8.6 cm (3.4 in.)	4.4 cm (1.75 in.)	2.5 cm (1.0 in.)
2.0 (retract)	8.1 cm (3.2 in.)	3.8 cm (1.5 in.)	2.2 cm (0.9 in.)
0.1 (right azimuth)	1.5 deg	1.5 deg	2.3 deg
0.1 (left azimuth)	1.5 deg	1.5 deg	2.5 deg
2.0 (up)	6 deg	6 deg	12 deg
2.0 (down)	9 deg	9 deg	12 deg

[a]Nominal value, based on unit and system level tests at three extension distances.

[b]Preliminary estimate based on television observation.

[c]Based on SETL tests using full-scale model spacecraft and television system. Comparison made with Day 111 SMSS operations on lunar surface.

Provisions were made for performance of optional tests, based on decisions made during lunar operations. Such optional tests were to include: impact tests, picking up rocks, trenching deeper, and bearing tests on subsurface material.

A static bearing test is performed by exercising the extension and azimuth motions until the scoop is positioned above the desired surface point. Then, with the scoop door closed to provide the flat surface for contact, the scoop is driven downward with the elevation motor until the desired penetration is achieved, or until the motor is stalled. An open-scoop static test can also be conducted.

For an impact test, the scoop is again positioned above the desired surface point, and the elevation drive clutch is actuated, allowing the scoop to drop to the surface, accelerated by gravity and the torque spring attached at the elevation axis. An impact test can be performed with the scoop open or closed.

A trenching operation is performed by driving the scoop down into the surface with the door open, then drawing it toward the spacecraft with the retraction motor. Material can be removed from the trench by retracting the scoop until it is clear of the surface, forming a pile of soil at the foot of the trench, or by closing the scoop and lifting the material out of the trench.

Because position-indicating telemetry is not available, the operations of the SMSS experiment must be monitored closely by the survey television camera. Sequences and priorities for tests, therefore, depend on viewing conditions, spacecraft shadow patterns, and the performance of the television system.

C. Mission Description

1. Engineering Performance

During the flight phase of *Surveyor III*, a heater was employed in the SMSS electronics auxiliary. Despite the heater, the temperature of the auxiliary reached −33°F. The designed survival temperature for the unit was −67°F.

After touchdown and during the spacecraft assessment period, the heater remained off for 2.5 h, allowing the electronics auxiliary temperature to drop to an estimated −130°F. Thermal power was restored, and the temperature of the auxiliary remained within operating limits from initial turn-on (Day 111) until operations were concluded (Day 122).[1]

During the 18 h, 22 min of total on time for the SMSS auxiliary in the first lunar day, 5879 spacecraft commands were transmitted to it. All commands were correctly coded, and 1898 SMSS commands were generated. The SMSS and its electronics auxiliary responded correctly to each command throughout this period.

Following touchdown, it was found that some of the *Surveyor III* telemetry was not reliable so that no valid SMSS motor current data could be obtained.

2. Lunar Surface Operations

Late in the Goldstone view period of Day 111, it was determined that the temperature of the SMSS electronics auxiliary was high enough for operation. The decision

[1]All times of SMSS events are given in GMT. All SMSS experiments were performed during periods of lunar visibility from the Deep Space Station at Goldstone, Calif.

to turn on the SMSS power was followed by a short series of tests to assess the condition of the electronics and to attempt a solution of the spacecraft telemetry problems. This section will briefly describe SMSS operations on and after Day 111. The locations of all tests are shown in Fig. IV-4.

a. Day 111. Initial operations began according to the standard sequence, and included firing of the pyrotechnic locking device (to release the SMSS from its stored position) and transmission of four commands to extend in the 2-s timing mode. A television picture to verify operation of the extension motor showed that extension had occurred, but that the extended distance was less than expected.

The sequence of four commands was repeated, and television verified that the SMSS scoop had then reached the originally intended position. A standard sequence was next initiated and included commands to *extend*; *retract*; *move right*, *left*, *up*, and *down*. Completion of these motions showed that other SMSS motors had operated as specified. The scoop door motor and the clutch actuator were not tested at this time.

Glare in the television optical system, resulting from sun angle, had prevented a complete television survey of the area of SMSS operations. Because narrow-angle coverage was available only for the area near the auxiliary battery, it was decided to depart from the standard sequence. The scoop was extended and positioned above the surface near the auxiliary battery to prepare for the first static bearing test.

The Goldstone view period ended as the bearing test sequence was being initiated, with the result that the SMSS scoop did not contact the surface. The final position of the deployed mechanism on Day 111 is shown in Fig. IV-5.

b. Day 112. It had been intended, at the end of Day 111 operations, that the first bearing test would be performed on Day 112 at the final Day 111 position of the SMSS. Prior to further SMSS operations on Day 112, television surveys were conducted, including a narrow-angle survey of the SMSS operations area. However, during the television operations, problems occurred in azimuth stepping at a time when the camera was stepping clockwise, or to the right azimuth. Accordingly, it was decided to move the SMSS into the field of view of the television camera and to start testing the lunar surface. The SMSS was stepped right twelve 0.1-s steps, extended five 2-s steps, and down two 2-s steps to locate it at the surface. Another 2-s down command drove the closed scoop into the surface at bearing test 1, shown as point A in Fig. IV-4. After elevating the scoop clear of the surface, it was moved right and extended, in preparation for a trenching operation. The scoop was opened for the first time and driven down into the surface, using three 2-s lower commands. Sixteen 2-s retract commands, with television observation verifying performance, were used to drag the scoop in forming trench 1, located at point B in Fig. IV-4.

Because of the difficulty encountered in the camera stepping, it was positioned at +15-deg azimuth, and the SMSS was moved left to this position, near the auxiliary battery. There the camera could follow the retraction motion of the SMSS by stepping its mirror in elevation only. A trench was started by lowering the scoop (door open) into the surface, and retracting eighteen 2-s steps, allowing the camera to record the operation without use of the azimuth stepping drive.

At the completion of this trenching operation, which constituted the first pass through trench 2, shown at point C in Fig. IV-4, the SMSS was elevated, extended to the head of the trench, and driven down into the surface in preparation for the second pass through the trench. After eighteen retract commands, television observation revealed that the scoop had traveled only 10 cm, which indicated that it was stalled near the head of the trench.

A narrow-angle survey of trench 2 completed the activities for the Day 112 period. Figure IV-6 shows, in a wide-angle picture, the condition of the operation at the end of the pass, with bearing point 1 and trenches 1 and 2 visible.

c. Day 113. Objectives for this day's operation of the SMSS experiment were to continue in trench 2 to the maximum depth possible.

To clear the scoop of the stalled condition at the head of the trench, it was extended once and elevated twice, all in the 2-s timing mode. Then, two retraction and two down commands placed the scoop back in the trench, on the spacecraft side of the point of obstruction. Eighteen 2-s retract commands were transmitted; after a television survey, twelve additional transmissions completed the second pass through trench 2.

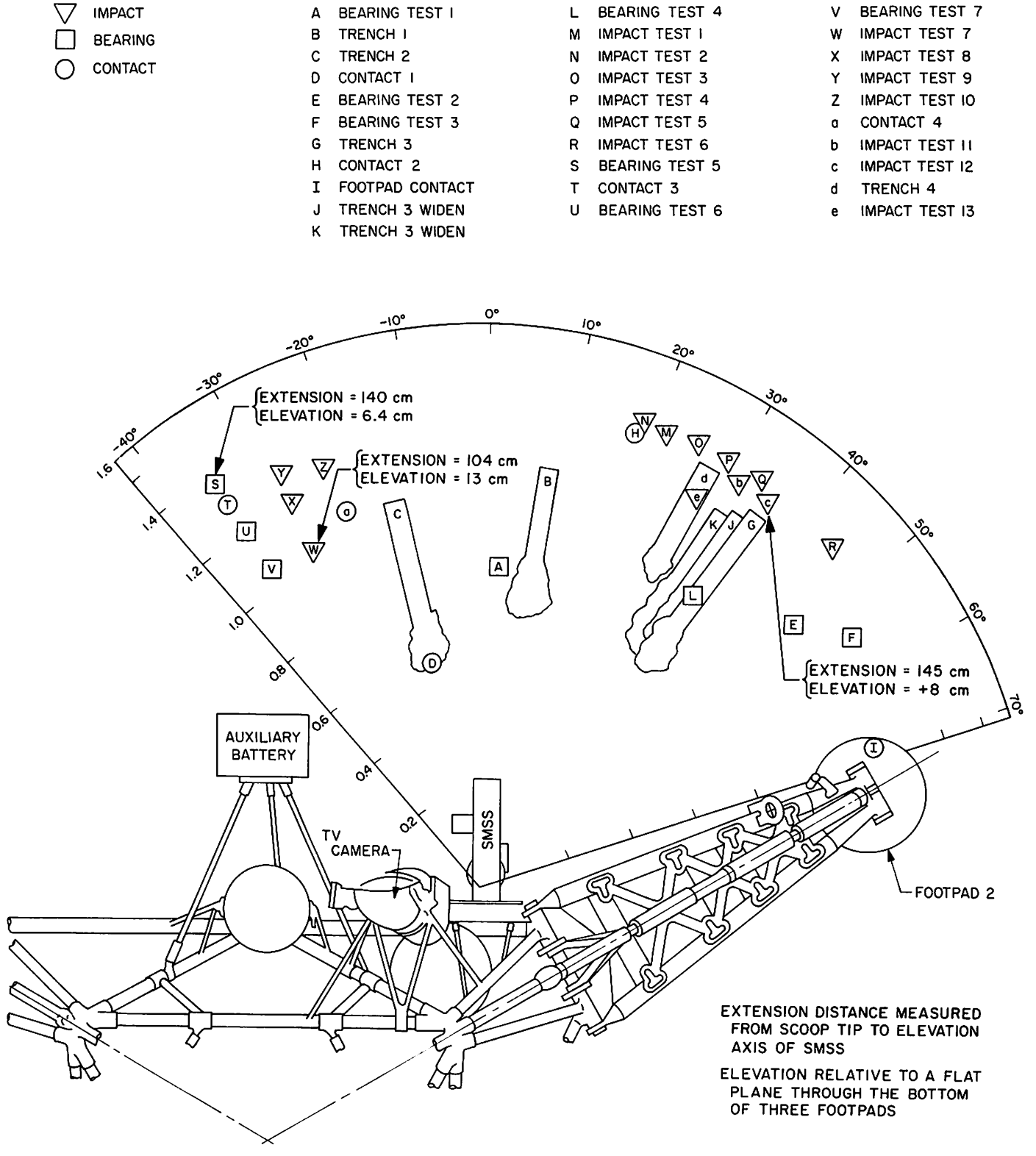

Fig. IV-4. Plan view of SMSS area of operations, showing location of all surface tests performed during first lunar day of *Surveyor III* mission. Angles are referenced to SMSS axis in stowed position

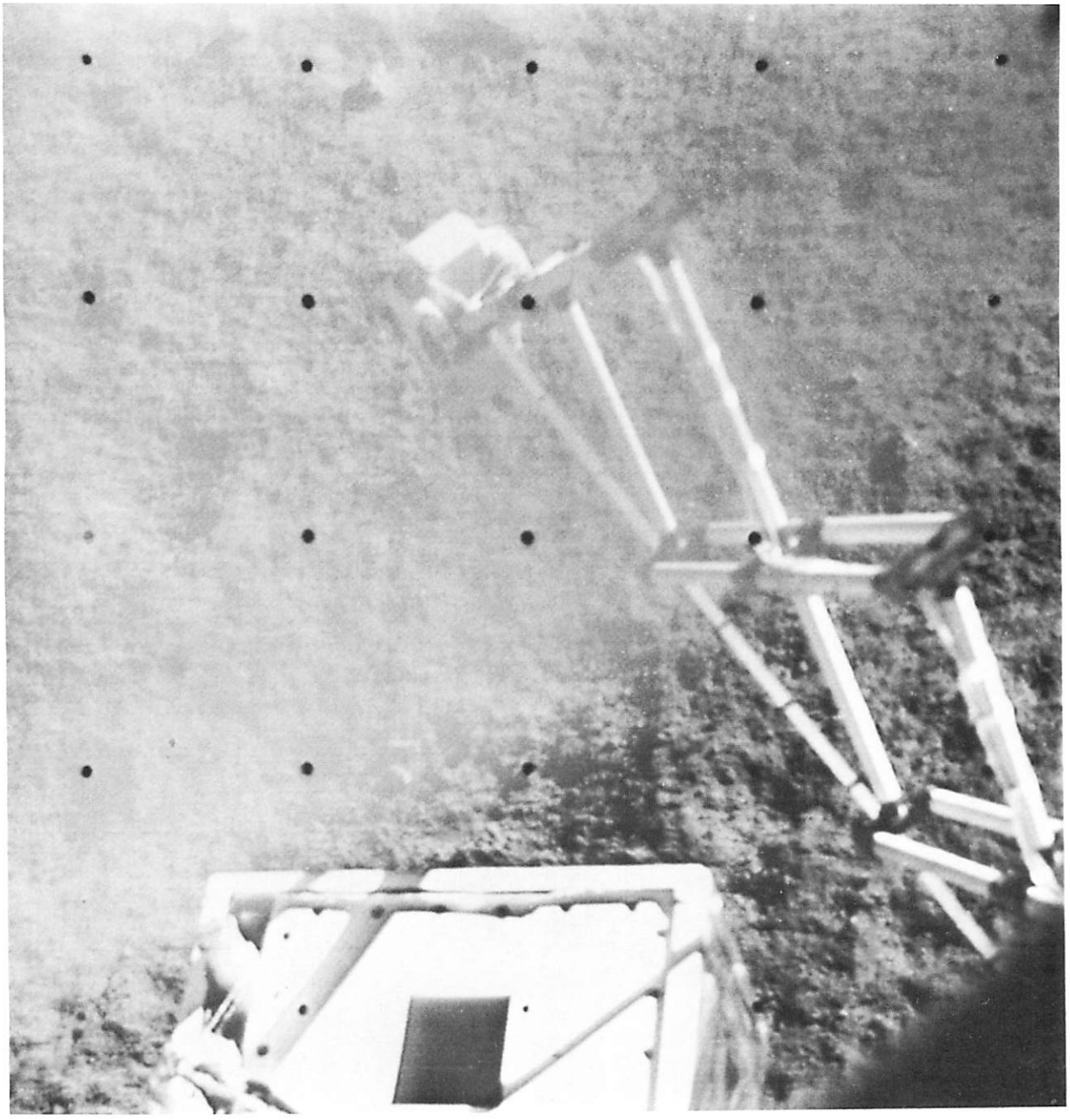

Fig. IV-5. SMSS deployed and ready for bearing test as Goldstone view ended on Day 111 (Day 111, 10:43:30 GMT)

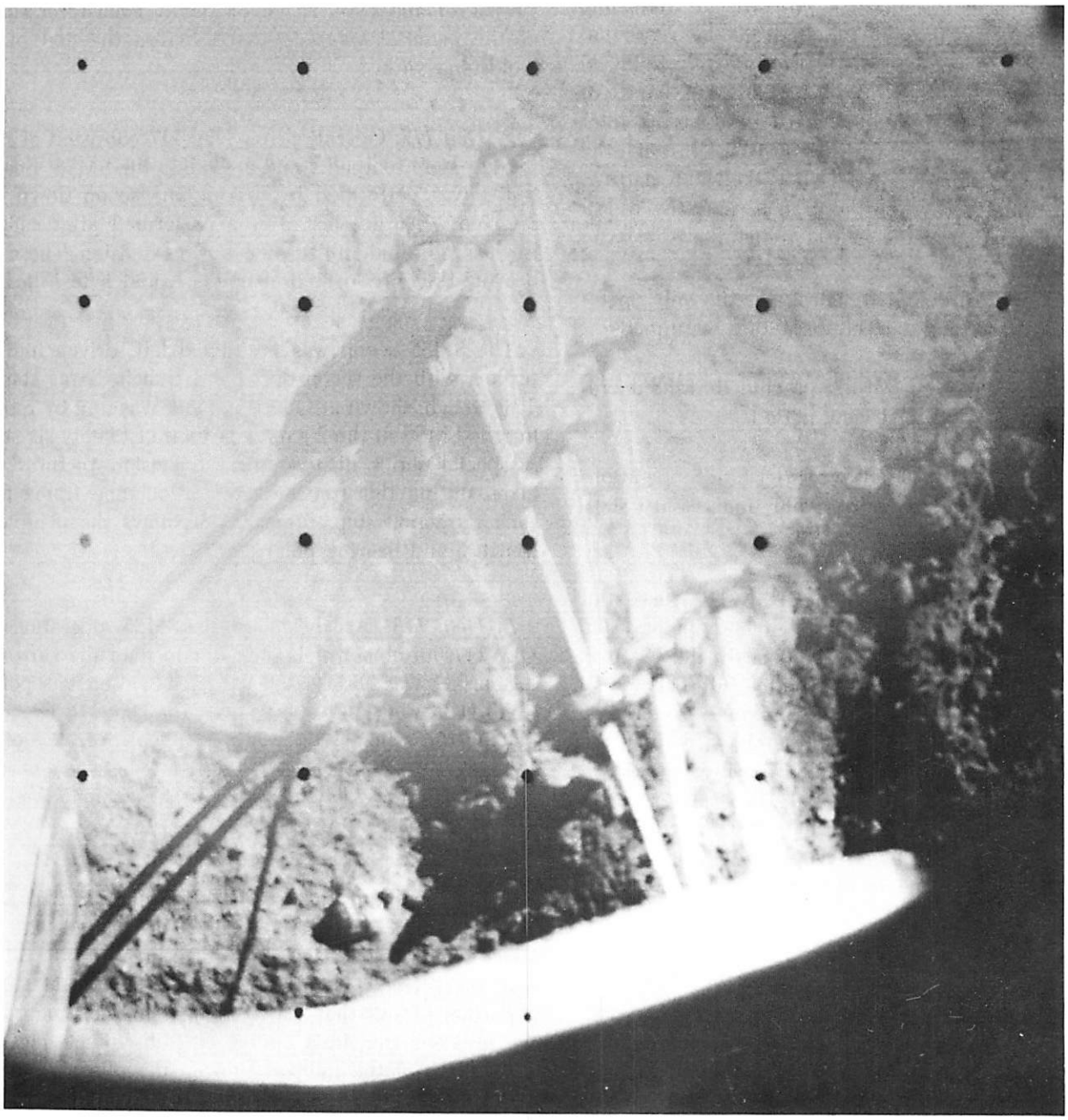

Fig. IV-6. Final picture of SMSS at completion of operations for Day 112. Trench 1 is visible at right edge of picture, and trench 2 is directly below SMSS mechanism (Day 112, 11:34:29 GMT)

A television survey of the trench preceded repositioning of the scoop to the head of the trench in preparation for the next drag. The scoop was driven down, again at the head of the trench, and a series of thirty 2-s retraction commands was given. Television observation showed the scoop traveled less than in the previous trenching pass, indicating loading at the limit of its retraction capacity. The thirty commands were repeated, followed by an extension step and three 0.1-s elevation steps. An additional fifteen 2-s retraction steps brought the total to 75 retraction commands for the third pass through the trench. The Goldstone view period ended with narrow-angle television surveys of the trench, and the SMSS remained in position at the foot of trench 2.

d. Day 114. A survey of trench 2 was the only operation related to SMSS. Solar eclipse studies were made.

e. Day 115. High temperatures precluded SMSS operations during this Goldstone view period.

f. Day 116. It was decided to restrict SMSS operations to the area near footpad 2 to avoid unnecessary stepping of the television camera mirror.

A study of pictures from the Day 113 survey of trench 2 revealed a solid object (contact 1, point D, in Fig. IV-4), possibly a rock, directly beneath the scoop in its last position. Some experiments with a full-scale model spacecraft with an SMSS attached provided a workable sequence of commands to pick up the object without the aid of television, because the camera position precluded narrow-angle viewing of the scoop. The scoop was visible in wide-angle television without violating the stepping constraint. Operations for Day 116 began with this sequence, which resulted in closing the scoop door on the object.

Elevation of the scoop revealed that the object had apparently been crushed in being retrieved. It was decided, however, to place the material in the scoop on the surface of footpad 2. The SMSS was extended eight 2-s steps, rotated right thirty-six 0.1-s steps, and viewed through the television system. Because of an uncertainty in the precise extension distance, the scoop was moved left, clear of the footpad, and lowered to the surface, to make a mark indicating its position. After elevating the scoop clear of the surface, study of the mark indicated further extension was required. The SMSS was extended two 2-s steps, moved against the right azimuth stop in five 0.1-s steps, and lowered to the surface of footpad 2. The scoop door was opened; the scoop was elevated and lowered to jar loose the material, and was moved up and to the left to clear the television view of the footpad. The position of the SMSS at the end of the operation and the surface material on the footpad are shown in Figs. IV-7 and IV-8. A narrow-angle, color-filter survey of the material was conducted before the end of the Goldstone view.

g. Day 117. Operations on Day 117 consisted of moving left from footpad 2 and extending the SMSS. Bearing test 2 was performed by driving the scoop down four 2-s steps. Bearing test 3 was performed after moving further right and still further out in extension. These two bearing tests are located at points E and F in Fig. IV-4.

The SMSS scoop was positioned left, driven into the surface with the scoop open, and trench 3 was started. This trench, shown at G in Fig. IV-4, was dug by retracting the SMSS in the 2-s mode a total of twenty-six steps. A special series of twenty-six television pictures was taken during this trenching operation, one frame after each retraction step. Figure IV-9 shows the completed trench 3 and bearing point 2.

h. Day 118. At the close of SMSS operations on Day 117, an object of higher albedo than the surrounding surface was observed near trench 3, at contact point 2 (item H in Fig. IV-4). Operations for Day 118 began by placing the scoop, with the door open, over the object (Fig. IV-10). With close coordination between narrow-angle television viewing and SMSS commanding, the object was picked up in the scoop.

After positioning the scoop over footpad 2, and opening the scoop door, a short series of 0.1-s elevate and lower commands was issued to ensure that the object had been freed from the scoop. This motion freed a portion of soil that had remained in the scoop since the previous trenching operation. Subsequent television observation of the footpad showed the pile of material, with the deposited object apparently covered.

Attempts were made to uncover the object by placing the scoop tip on the footpad and retracting it. This action succeeded in removing some material from the footpad and leaving an object exposed, which was tentatively identified as the one which had been picked up and deposited earlier.

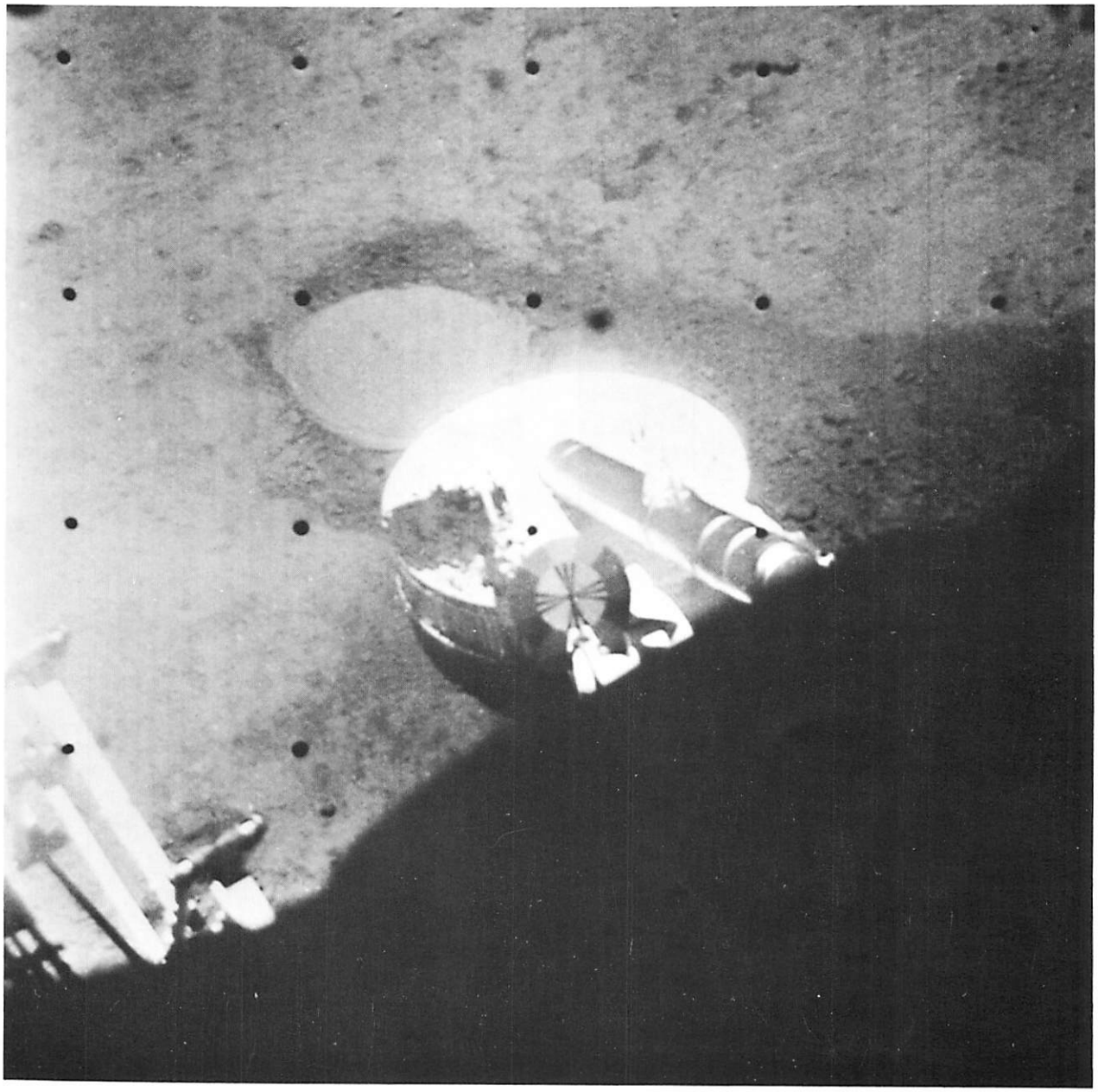

Fig. IV-7. Wide-angle view of SMSS and footpad 2. Note pile of lunar surface material on top of footpad (Day 116, 11:53:26 GMT)

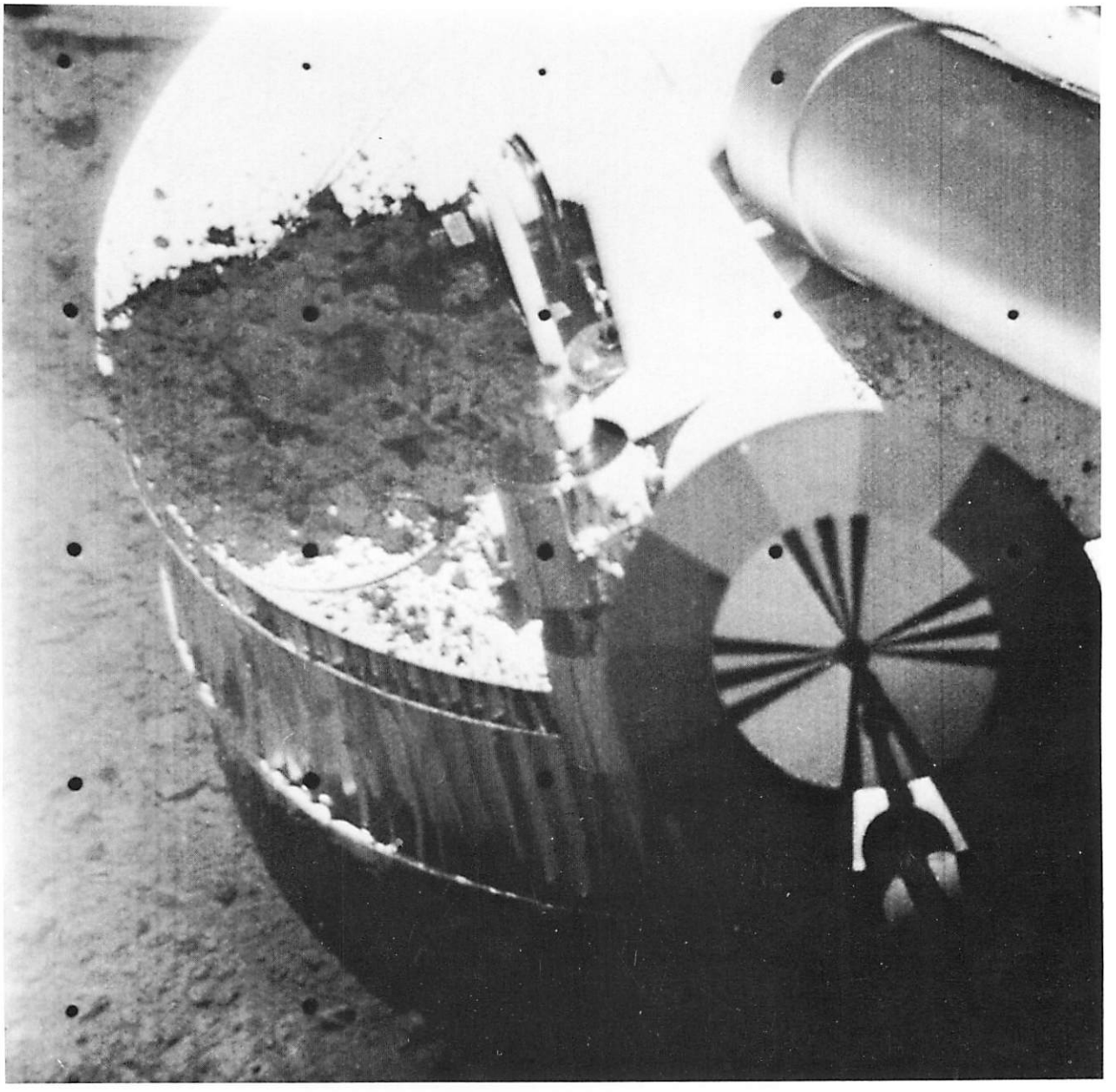

Fig. IV-8. Material dumped on footpad 2 by SMSS. The color calibration chart is in foreground (Day 116, 12:00:54 GMT)

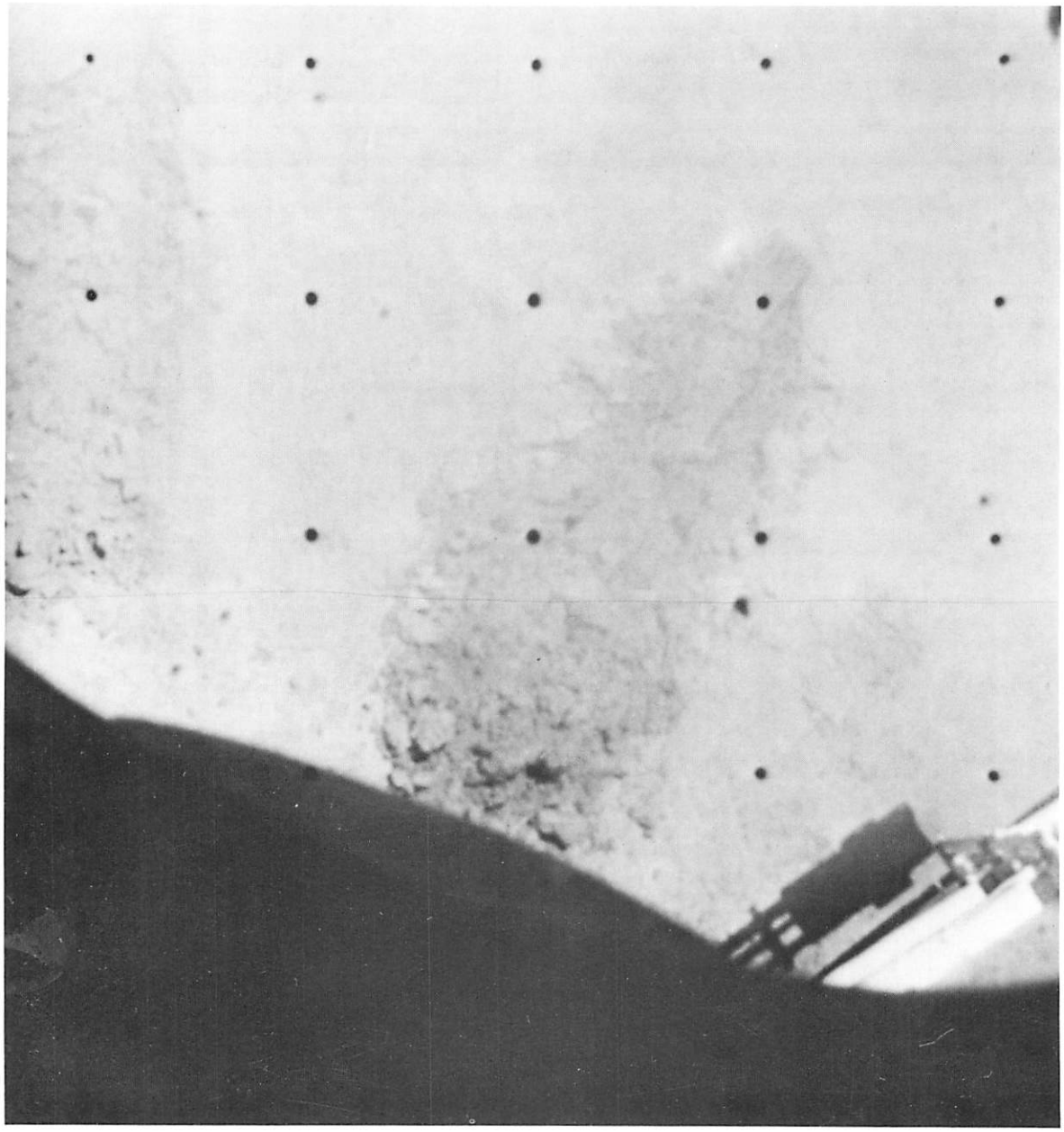

Fig. IV-9. Wide-angle view of SMSS at end of Day 117 operations. Trench 3 and bearing test 2 are visible on the surface (Day 117, 10:34:53 GMT)

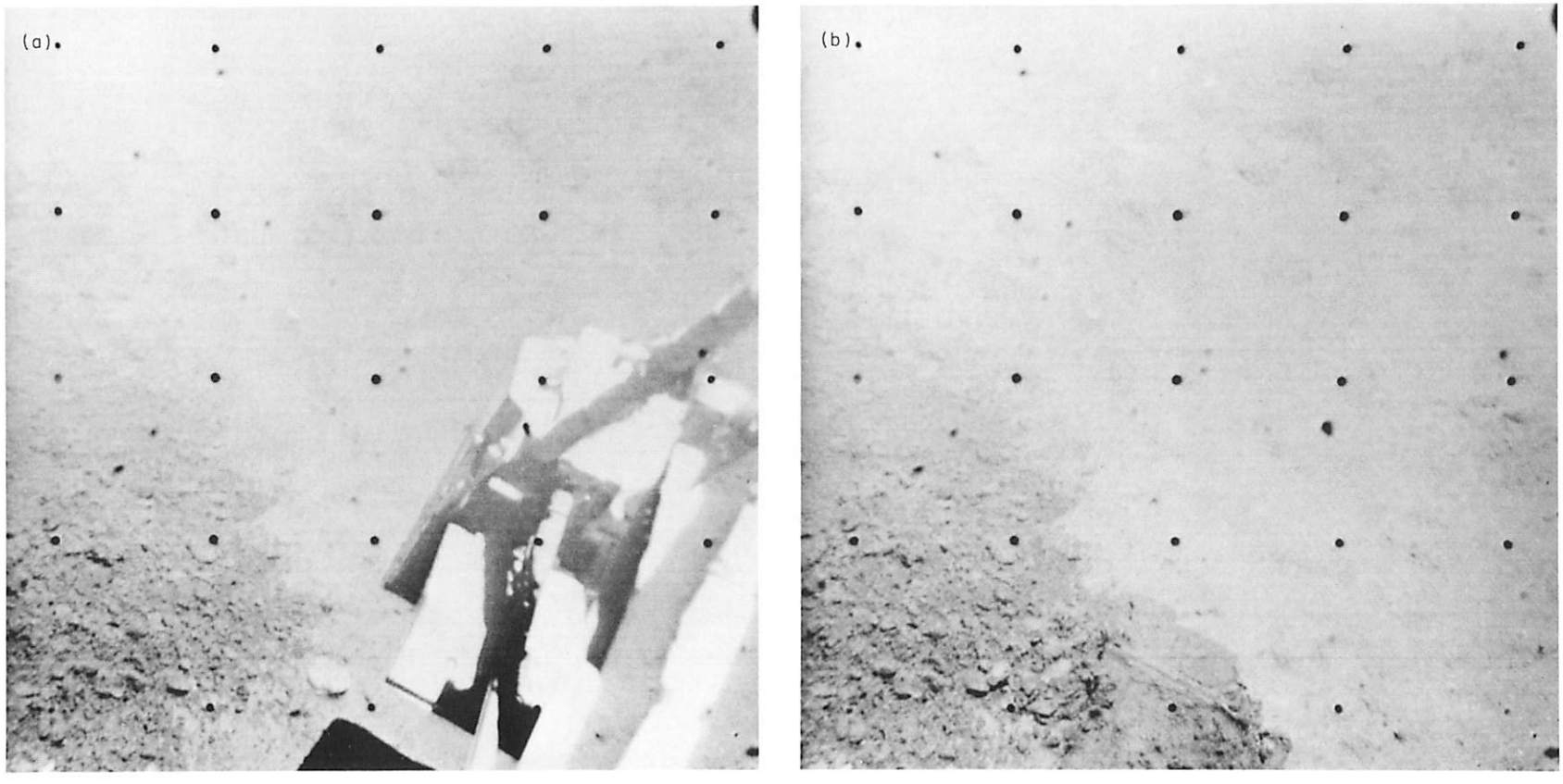

Fig. IV-10. (a) SMSS approaching to pick up lighter object. Darker material in bottom left corner fell out of scoop in previous movement (Day 118, 10:20:10 GMT). (b) Surface after removal of object in (a) (Day 118, 10:49:08 GMT). The work of the SMSS is clearly seen. Also note that the lighter shade of the surface is lost in the very small disturbance made by the SMSS

Items J and K in Fig. IV-4 represent further trenching operations at trench 3. The scoop was positioned near the head of the trench, to the left, and retracted, thus widening the trench to three scoop widths. Figure IV-11 shows the widened trench, prior to conducting bearing test 4 (item L in Fig. IV-4) in the bottom of the trench.

i. Day 119. A series of impact tests (items M through R in Fig. IV-4) was performed, starting with a drop from a single 2-s elevation above the surface at impact test 1. After assessing the impact result, the tests that followed were performed by releasing the scoop from higher positions. Impact tests 2 and 3 were performed by elevating the scoop two 2-s steps above the surface; impact tests 4, 5, and 6 were accomplished by elevating the scoop four 2-s steps.

At the conclusion of operations, the SMSS was exercised in several of its operating modes to record the size of motion increments provided by the motors, and to see whether any changes had occurred. There were no changes observed, on the basis of preliminary estimates.

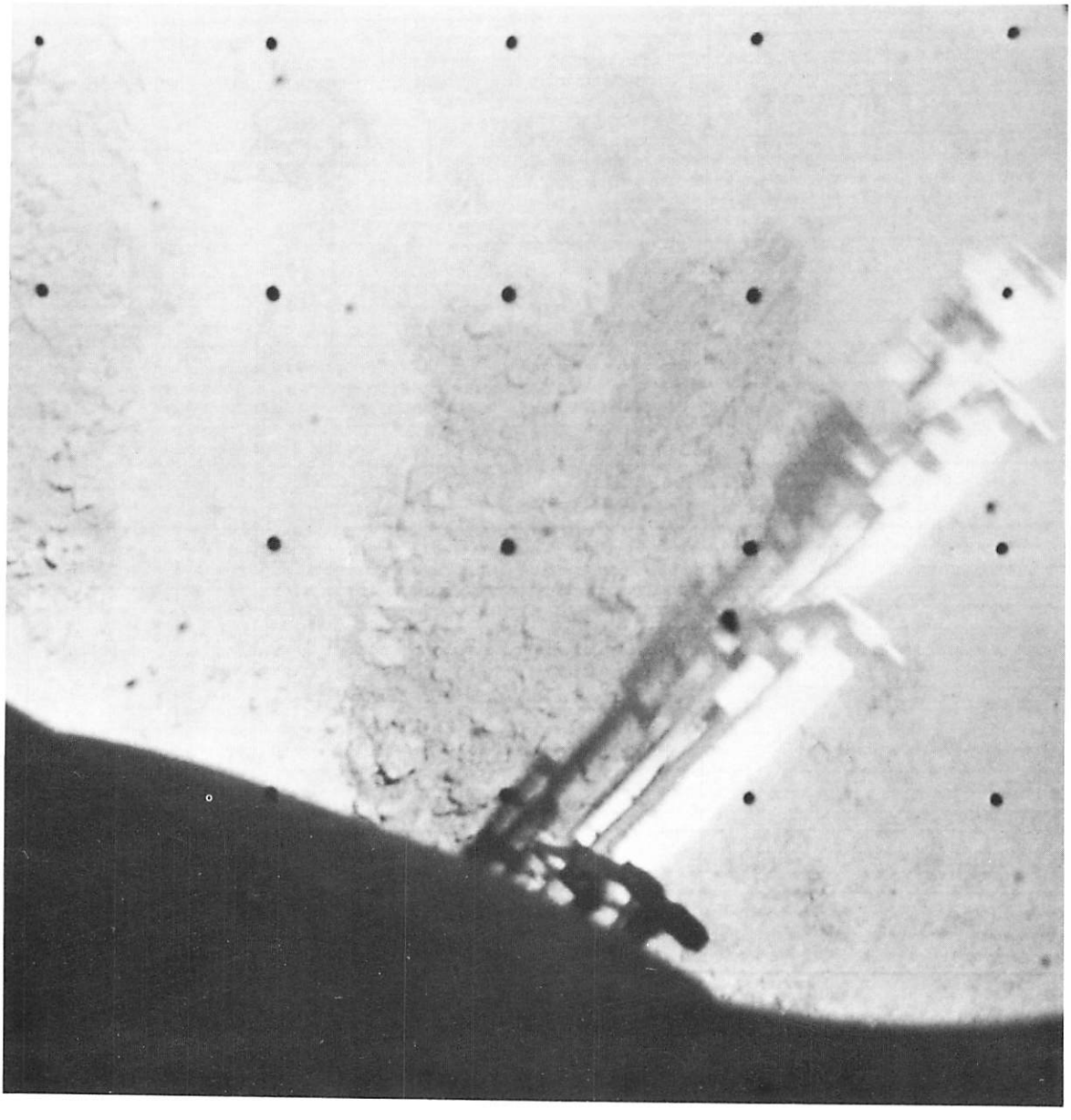

Fig. IV-11. Trench 3, widened, with SMSS scoop poised and ready for bearing test 4 in trench bottom. SMSS appears blurred due to motion when picture was taken (Day 118, 13:21:33 GMT)

j. Day 120. On Day 120, SMSS operations were again shifted to the area near the auxiliary battery. The SMSS was extended to near maximum extension, the scoop closed, and bearing tests 5, 6, and 7 were performed at a single azimuth position. The scoop was retracted between tests. During this test sequence, contact was made with a small surface object (item T in Fig. IV-4). The three tests are shown as items S, U, and V in Fig. IV-4.

By stepping the SMSS right two 2-s steps and performing impact tests 7, 8, and 9, with extension motions between, the three impact points (items W, X, and Y in Fig. IV-4) were placed on a line parallel to that of the bearing tests. Stepping right two more 0.1-s steps, impact test 10 was performed. Elevations of two 2-s steps for impact tests 7 and 8, and four 2-s steps for impact tests 9 and 10 were used.

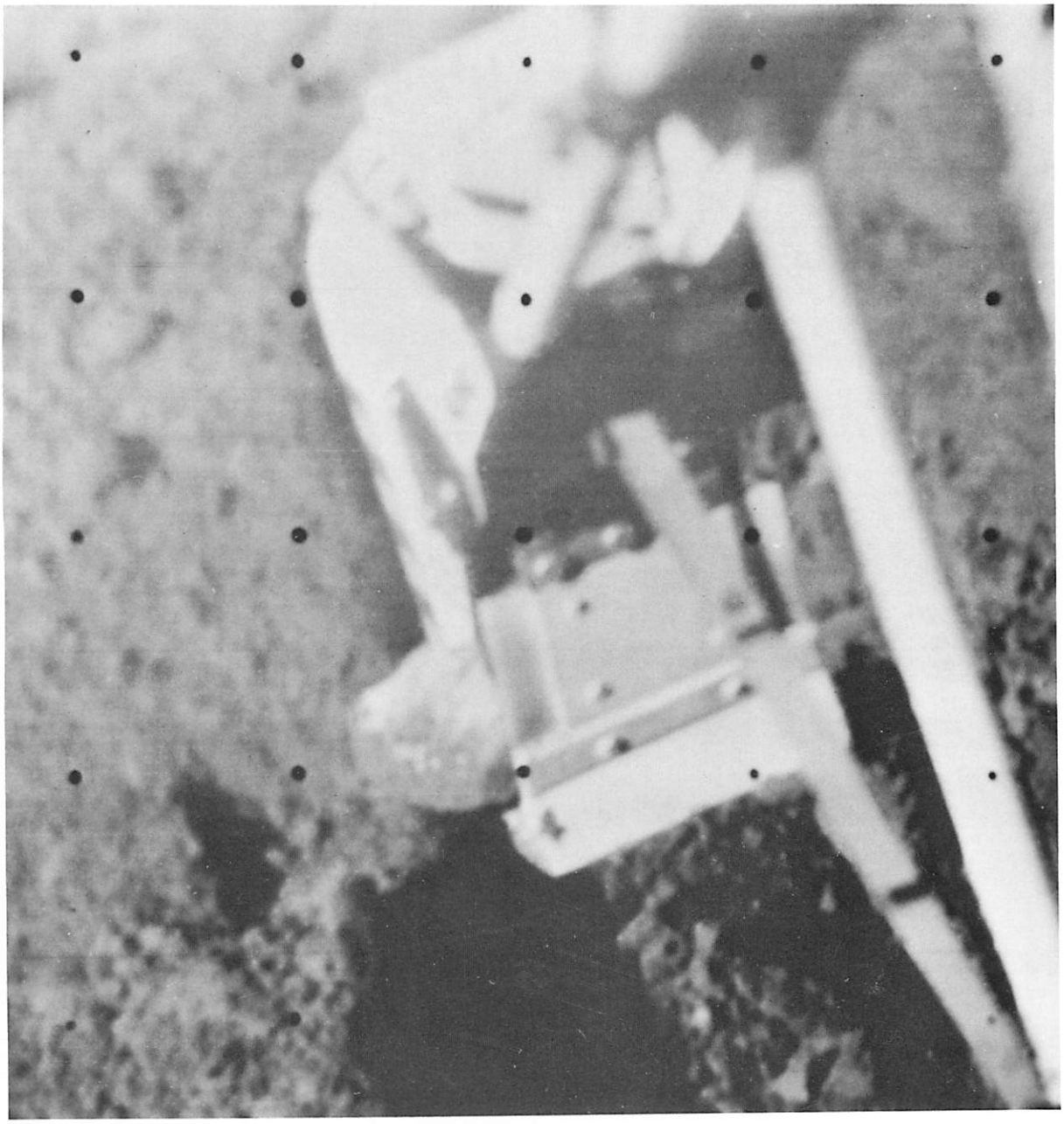

Fig. IV-12. Close-up picture of "rock" extracted from lunar surface and being held by SMSS (Day 121, 15:18:39 GMT)

k. Day 121. Initial activities involved coordinating the position of the scoop through narrow-angle television, and picking up an object (possibly a rock) turned up on the previous day. The object was gripped in the side of the scoop, which was repositioned to afford the best view of the rock (see Fig. IV-12), and a complete color-filter survey was performed. While positioning the scoop to place the object on the surface nearby (because the camera could not at this time be moved to view footpad 2), the object slipped out and was not seen again.

Three new trenching passes were made through trench 2, using twenty, thirty-three, and twenty-four 2-s retraction commands. Before the last pass, four impacts with the scoop open were performed in the trench bottom to loosen the material. Figure IV-13 shows the

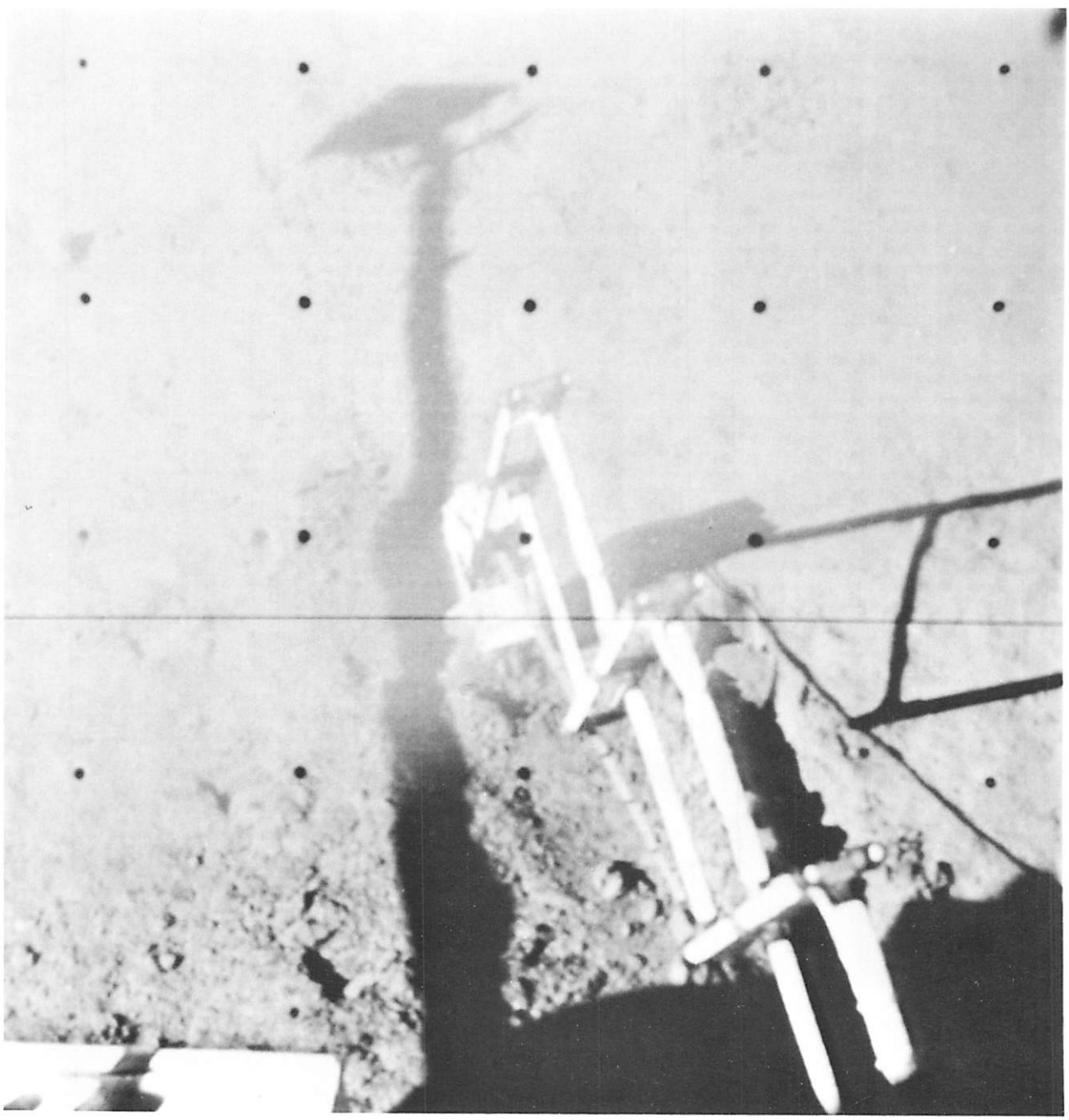

Fig. IV-13. SMSS with small "rock" in scoop. Rock was picked up on Day 121. On the surface below, several bearing test points are visible (Day 121, 14:56:38 GMT)

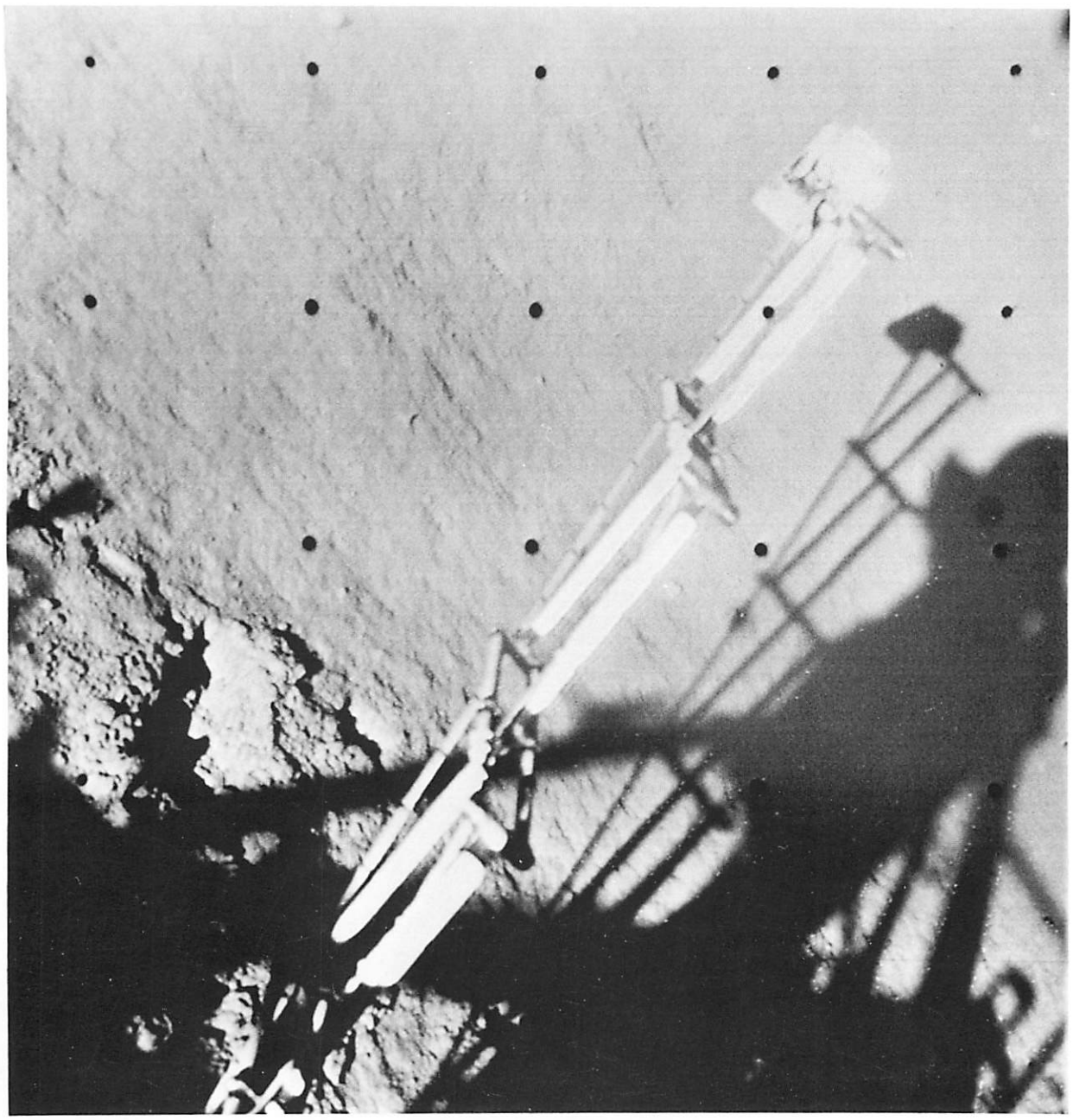

Fig. IV-14. Final position of SMSS at conclusion of lunar operations. Trench 4 and several impact points are visible on the lunar surface (Day 122, 14:20:11 GMT)

SMSS scoop with the rock in the door, as well as bearing tests 5, 6, and 7 from previous operations.

l. Day 122. Sun angles for Day 122 dictated moving of SMSS operations to the right, where available light permitted tests, and minimum camera stepping would be required to follow sunset shadows. The television camera was moved successfully.

Impact test 11, at position b in Fig. IV-4, was performed on the undisturbed surface with the scoop open, following a 2-s elevation movement. Another test from the same height, impact test 12, was repeated at position c because material deposited from the scoop on the surface in impact test 11 obscured the surface at point b. A short trench was dug at point d, followed by impact test 13 at location e in the trench bottom on subsurface lunar material. Final position of the SMSS, with trench 4 and several impact points visible on the surface below, is shown in Fig. IV-14.

Operations are summarized in Table IV-2. A television picture mosaic (Fig. IV-15) shows the area and results of operations in trench 1 (item B in Fig. IV-4).

The second trench, which was along an azimuth line that facilitated camera coverage, was worked on three separate Goldstone view periods (Table IV-2). The progress of trench formation is shown in television picture mosaics. Figure IV-16 shows the area before trenching operations began. The initial pass ended in the condition shown in Fig. IV-17.

Table IV-2. Summary of operations

Day	Operation performed	Item in Fig. IV-4
111	Deploy and check motors	
112	Bearing test, two trenches	A, B, C
113	Continue second trench	C
116	Place material on footpad 2	D
117	Two bearing tests, third trench	E, F, G
118	Pick up object, place on footpad, widen third trench, bearing test in trench	H, J, K, L
119	Six impact tests, calibrate motions	M, N, O, P, Q, R
120	Three bearing tests, four impact tests, move small rock	S, T, U, V, W, X, Y, Z, a
121	Pick up rock, continue second trench	a, C
122	Two impact tests, fourth trench, impact in trench	b, c, d, e

On the second pass, the SMSS scoop was extended slightly beyond the end of the first trench (Fig. IV-18), and the subsequent series of eighteen retract commands resulted in a short travel (Fig. IV-19).

During the Day 113 Goldstone view, the SMSS was removed from its position in the second trench (item C in Fig. IV-4) and a trench survey performed (Fig. IV-20). Two additional trench attempts resulted in the formation of the trench to the condition shown in Fig. IV-21, a survey performed during the Day 114 Goldstone view. Figure IV-22 is a general area survey, showing trench 2 under lighting conditions of Day 120. It should be noted that additional work was done in trench 2 on Day 121.

3. Performance

Reconstruction of the experiment sequences performed on the moon has started on a full-scale model of *Surveyor III* in the *Surveyor* Experiment Test Laboratory (SETL).

Through the use of a *Surveyor* television system on the model spacecraft, a picture of the SMSS from *Surveyor III* can be duplicated by manipulating the SMSS model until the picture matches. An example of this technique is shown in Fig. IV-23. Once the SMSS is aligned to match pictures, measurement of the extension, azimuth, and elevation can be made directly.

Motion increments of the SMSS on *Surveyor III* have been determined in this way for the initial checkout sequence. Results are compared with preliminary estimates in Table IV-1. Similarly, the position of surface points can be determined, and positions of three points are noted in Fig. IV-4. As additional points are measured, allowing cross checks, these positions will be refined.

D. Tests on Lunar Surface Material

Results of tests performed on the lunar surface by the SMSS and conclusions on the mechanical properties of the surface material, as deduced from the test results, are presented here.

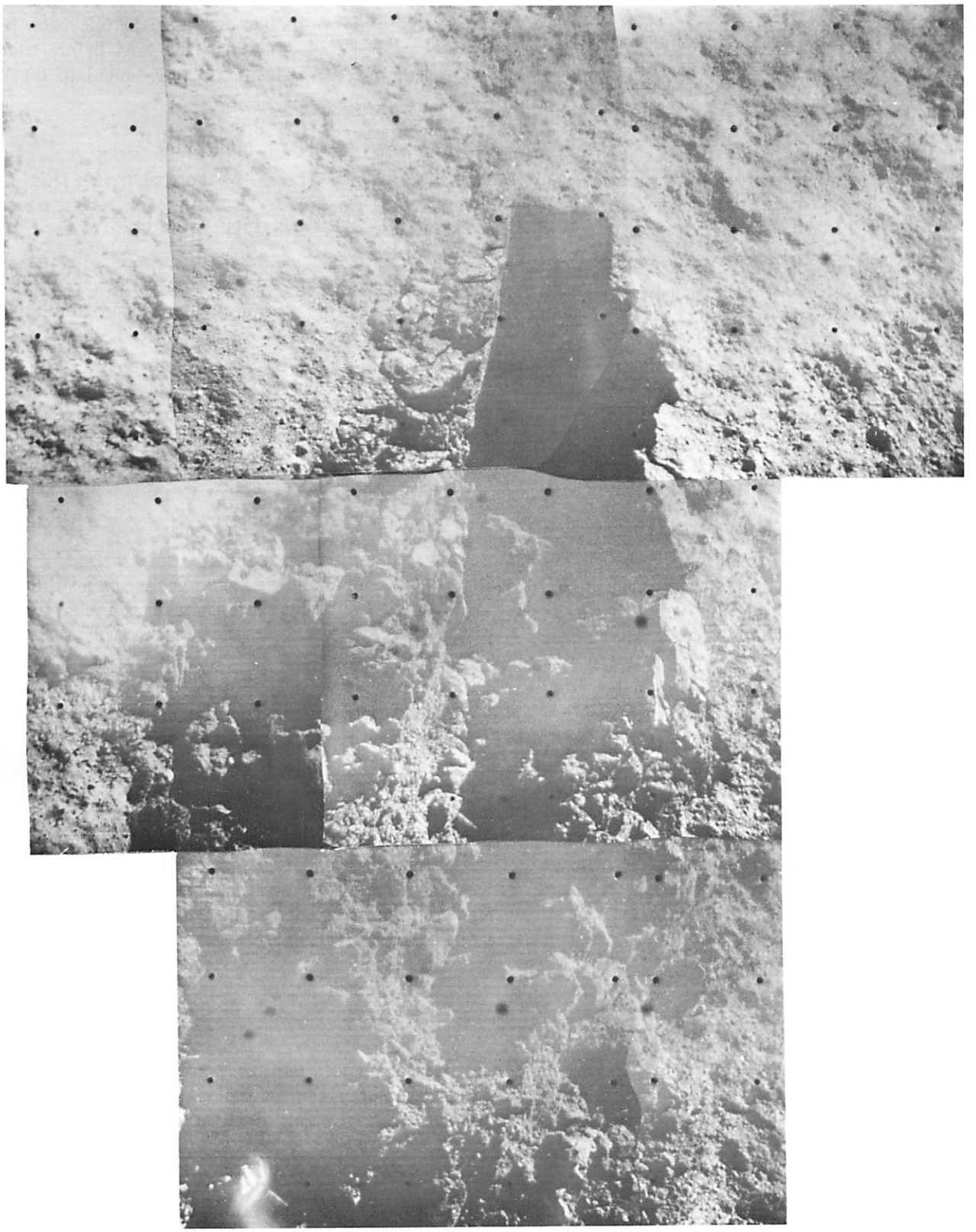

Fig. IV-15. Mosaic of first trench dug by SMSS (Catalog No. 95 SI, Day 112, 07:22:49 to 08:33:28)

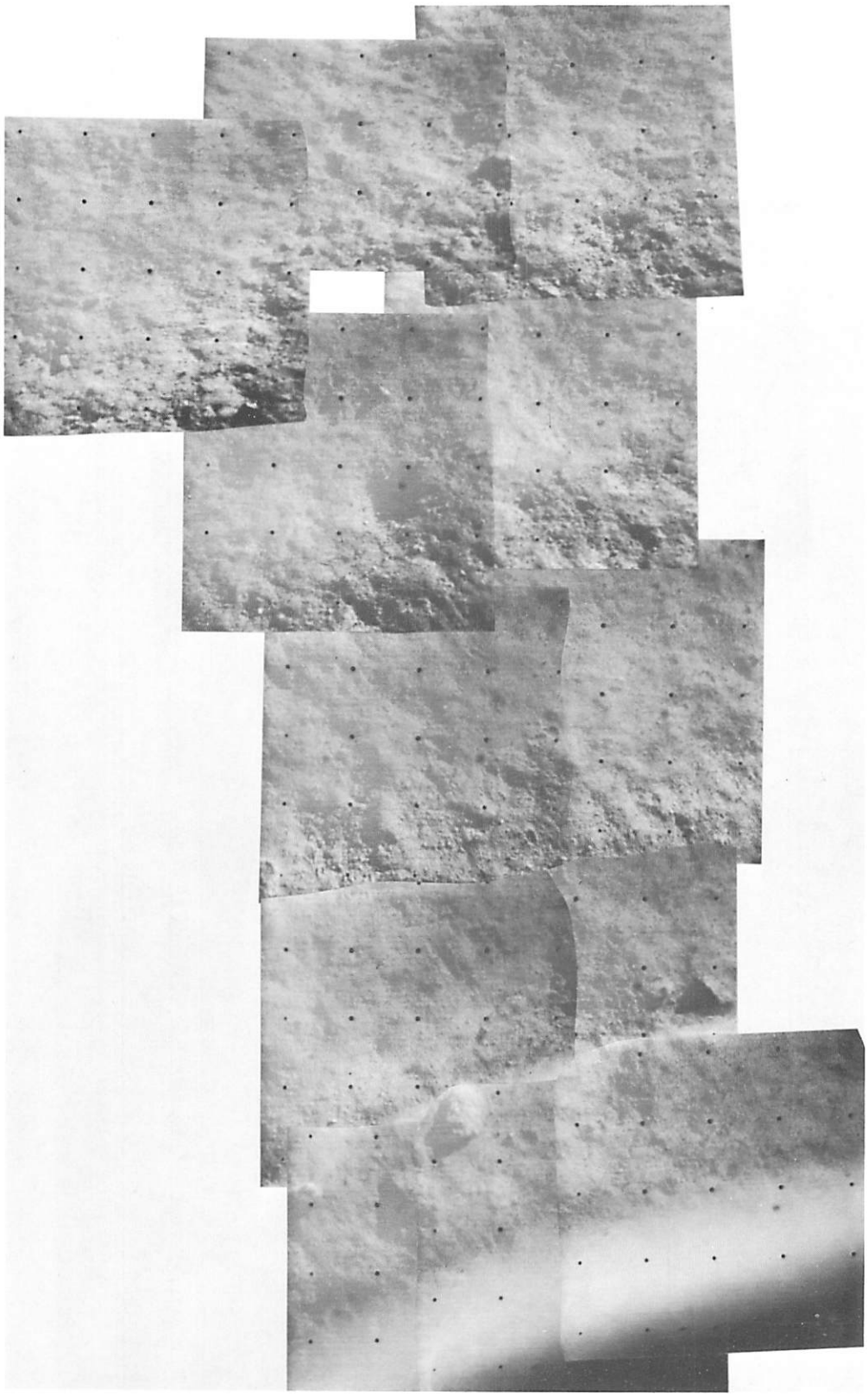

Fig. IV-16. Area where second trench was dug by SMSS, before disturbance (Catalog No. 96 SI, Day 111, 09:23:55 to 09:28:24)

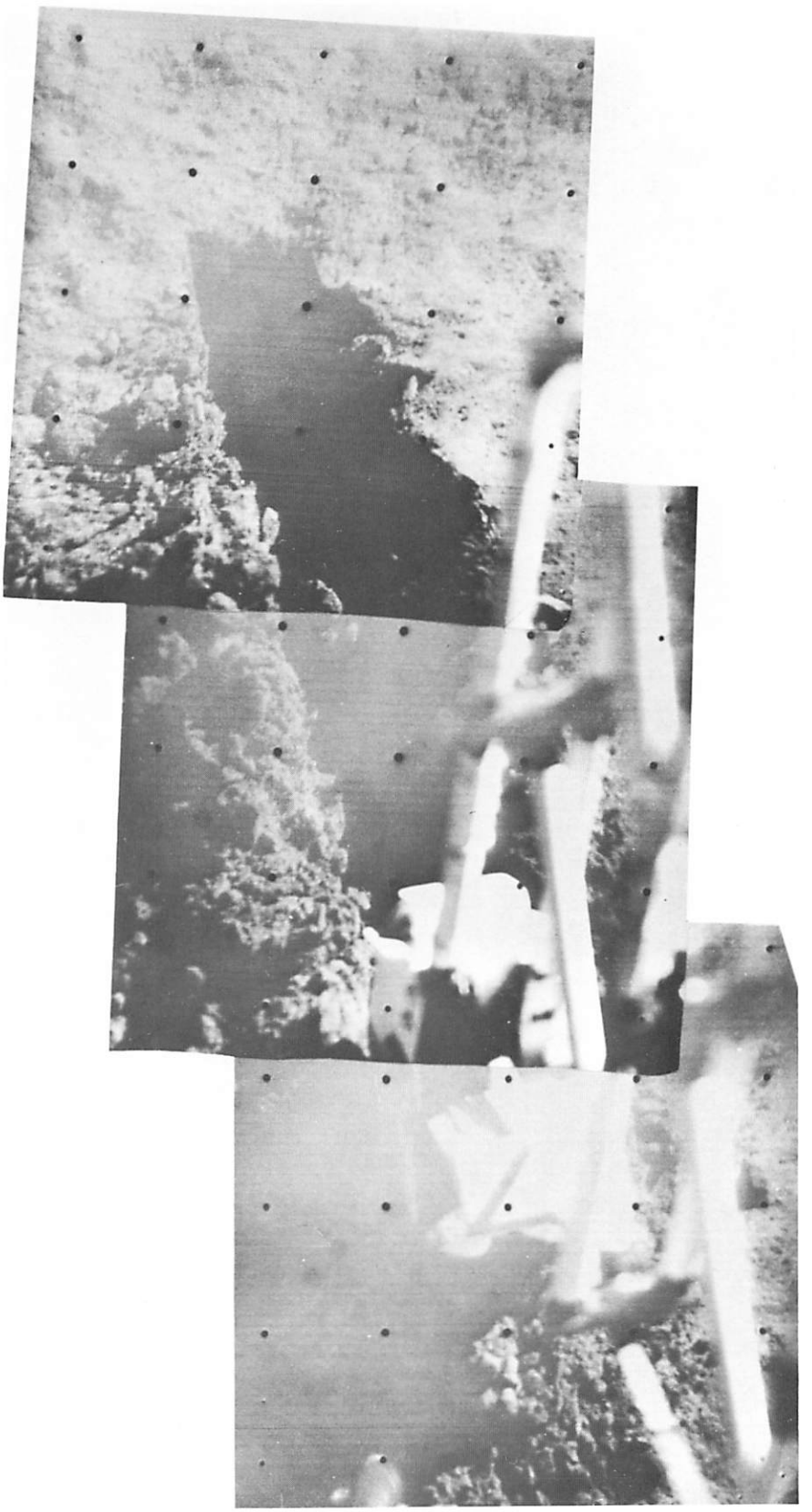

Fig. IV-17. Second SMSS trench mosaic with SMSS in position after first pass through trench (Catalog No. 97 SI, Day 112, 11:18:00, 11:18:52, and 11:19:33)

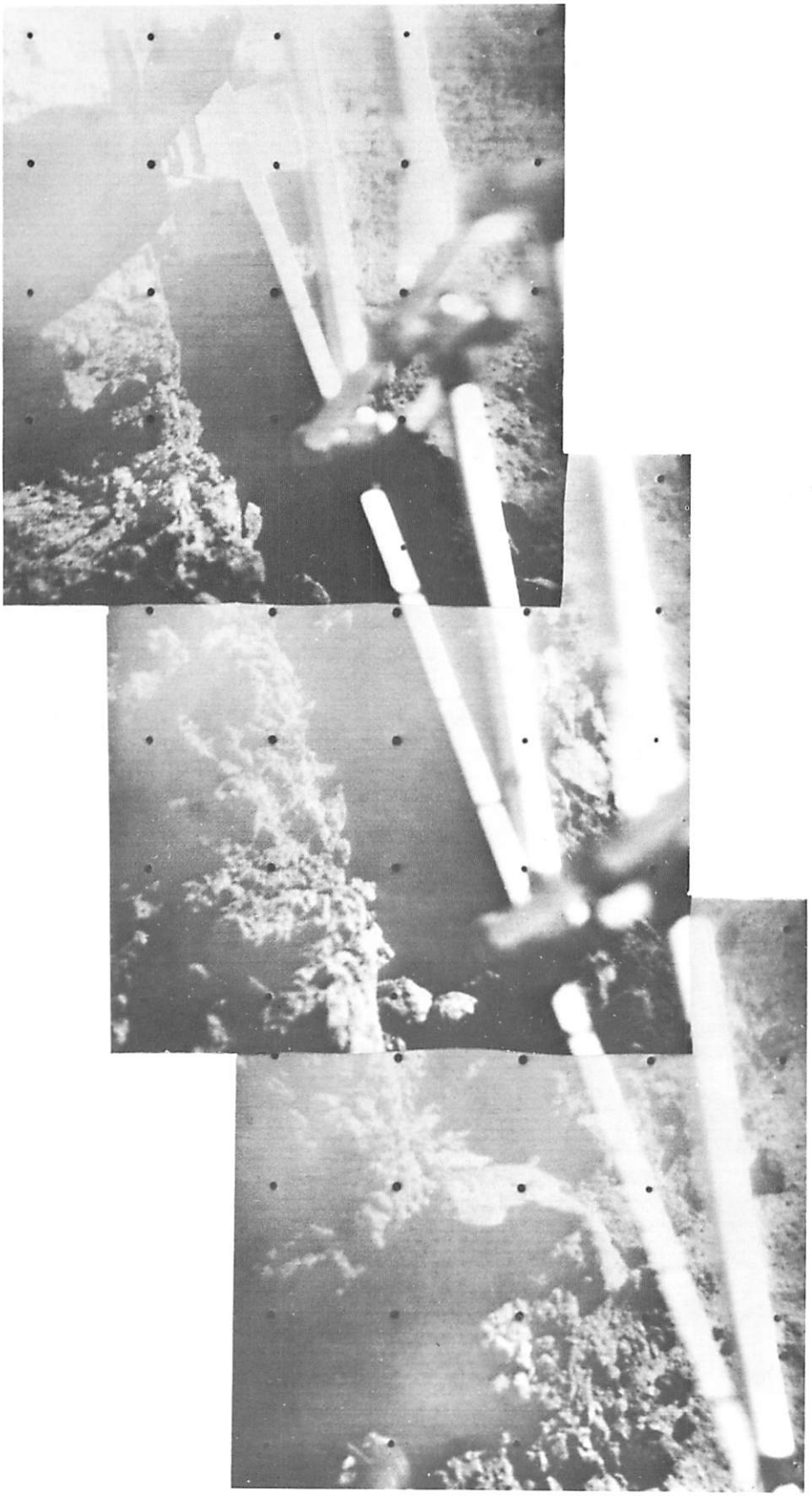

Fig. IV-18. SMSS positioned ready for second pass in trench 2 (Catalog No. 98 SI, Day 112, 11:24:42, 11:25:55, and 11:25:59)

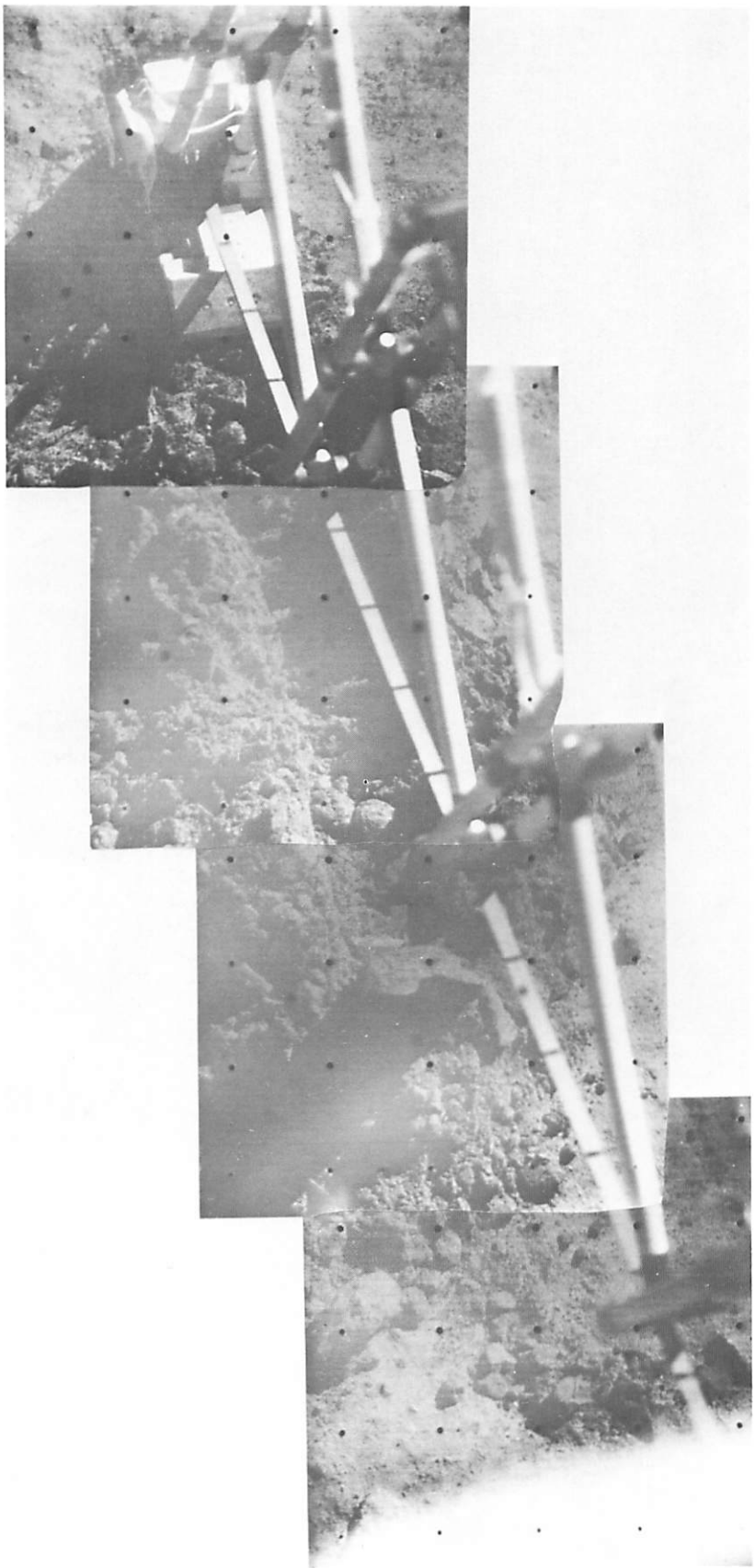

Fig. IV-19. Stalled position of SMSS in trench 2 after second attempt to trench (Catalog No. 99 SI, Day 113, 01:51:00, 01:51:43, 01:52:19, and 01:52:51)

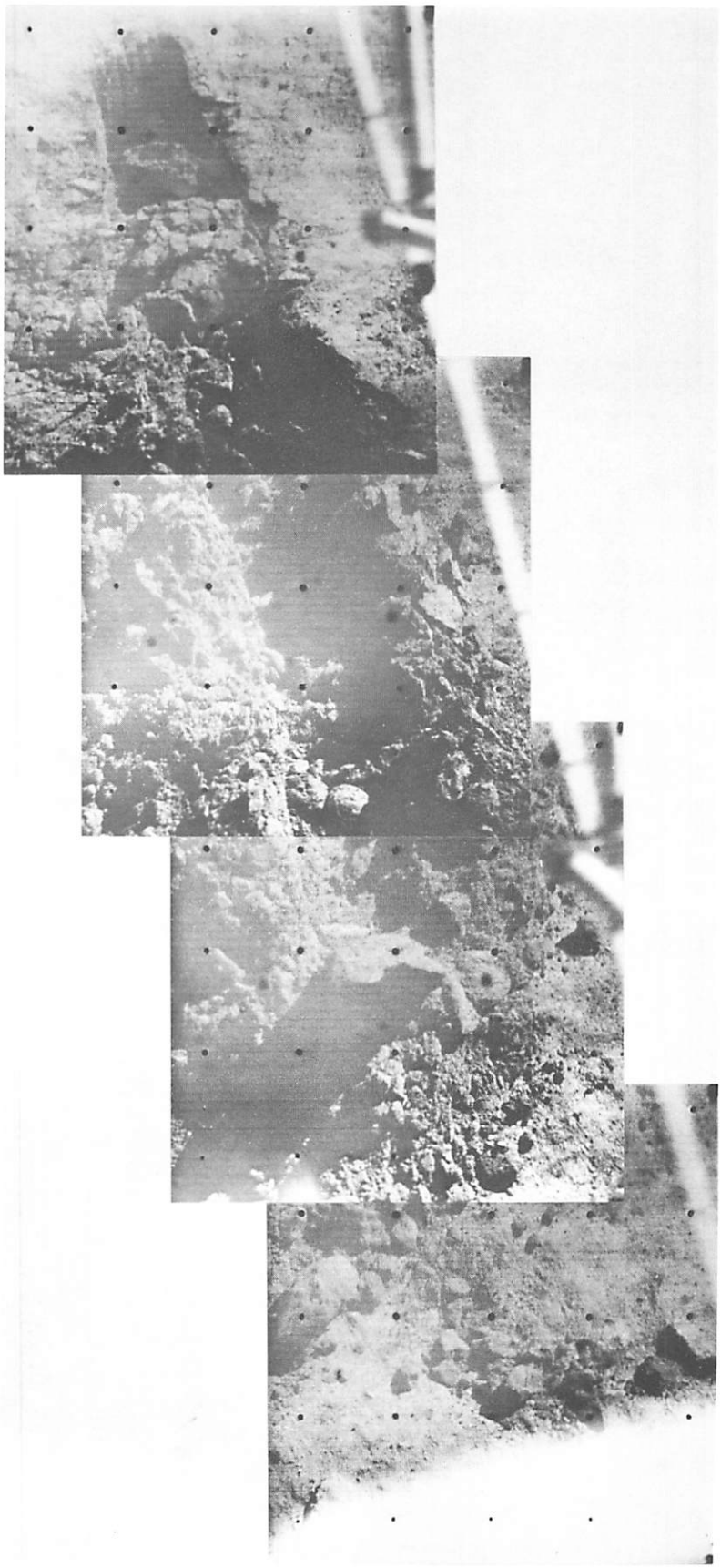

Fig. IV-20. Mosaic of trench 2 after SMSS has been removed following stalling at far end, where material from scoop has been dumped (Catalog No. 91 SI, Day 113, 06:39:01, 06:40:05, 06:40:38, and 06:41:08 GMT)

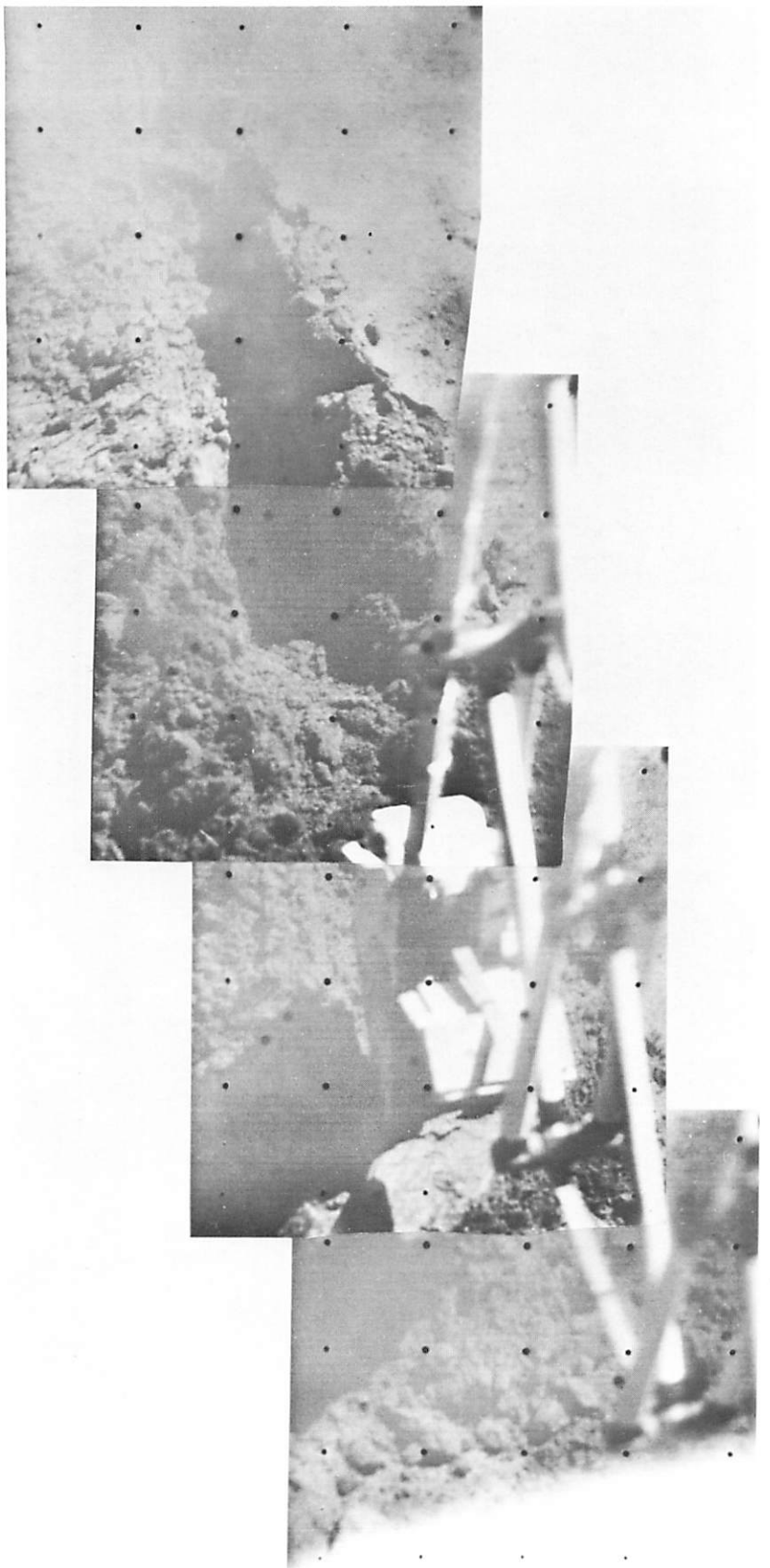

Fig. IV-21. Second trench after two additional drags through it (Catalog No. 100 SI, Day 114, 05:10:33, 05:20:09, 06:14:55, and 06:18:51)

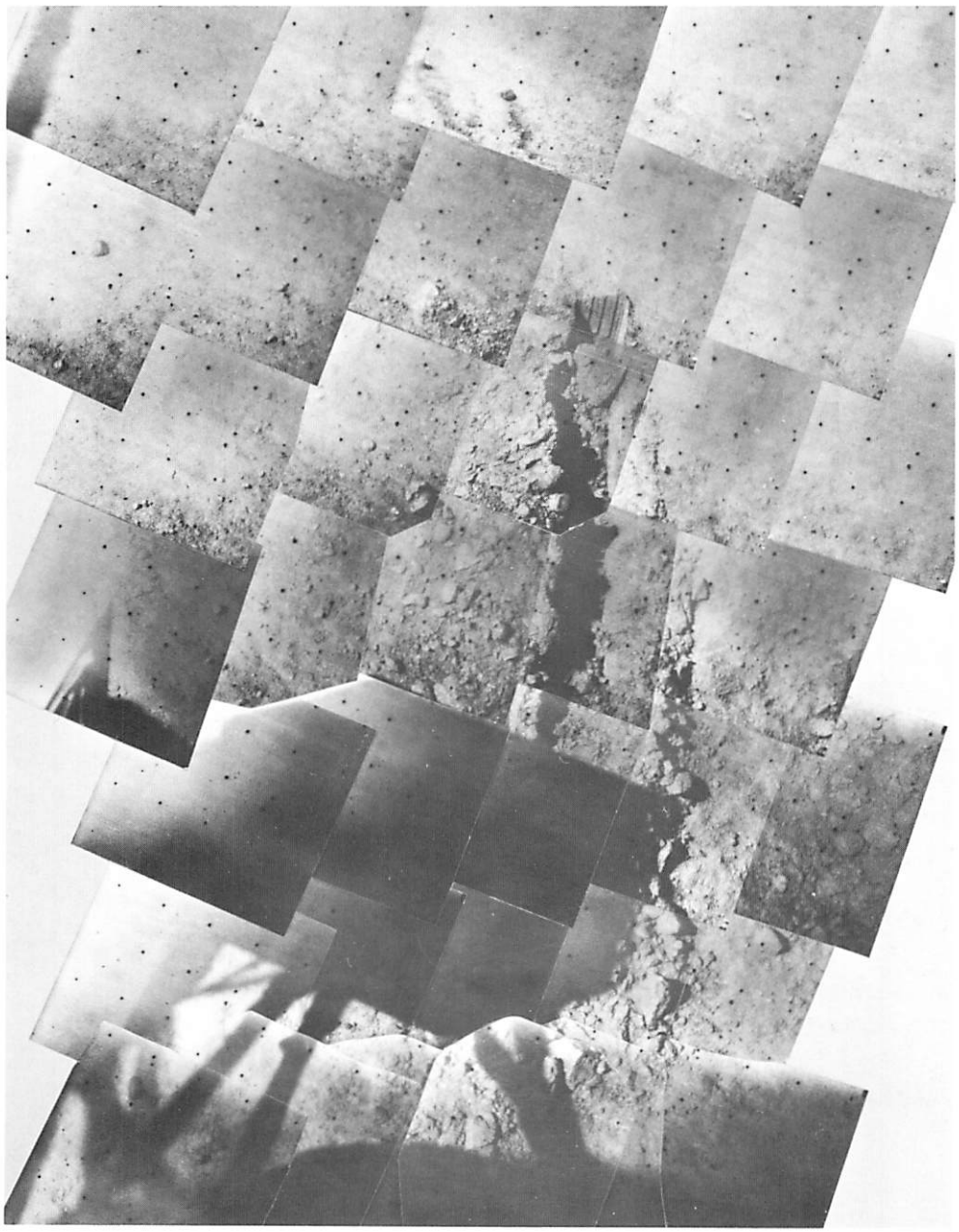

Fig. IV-22. General area survey of trench 2, improved mosaic

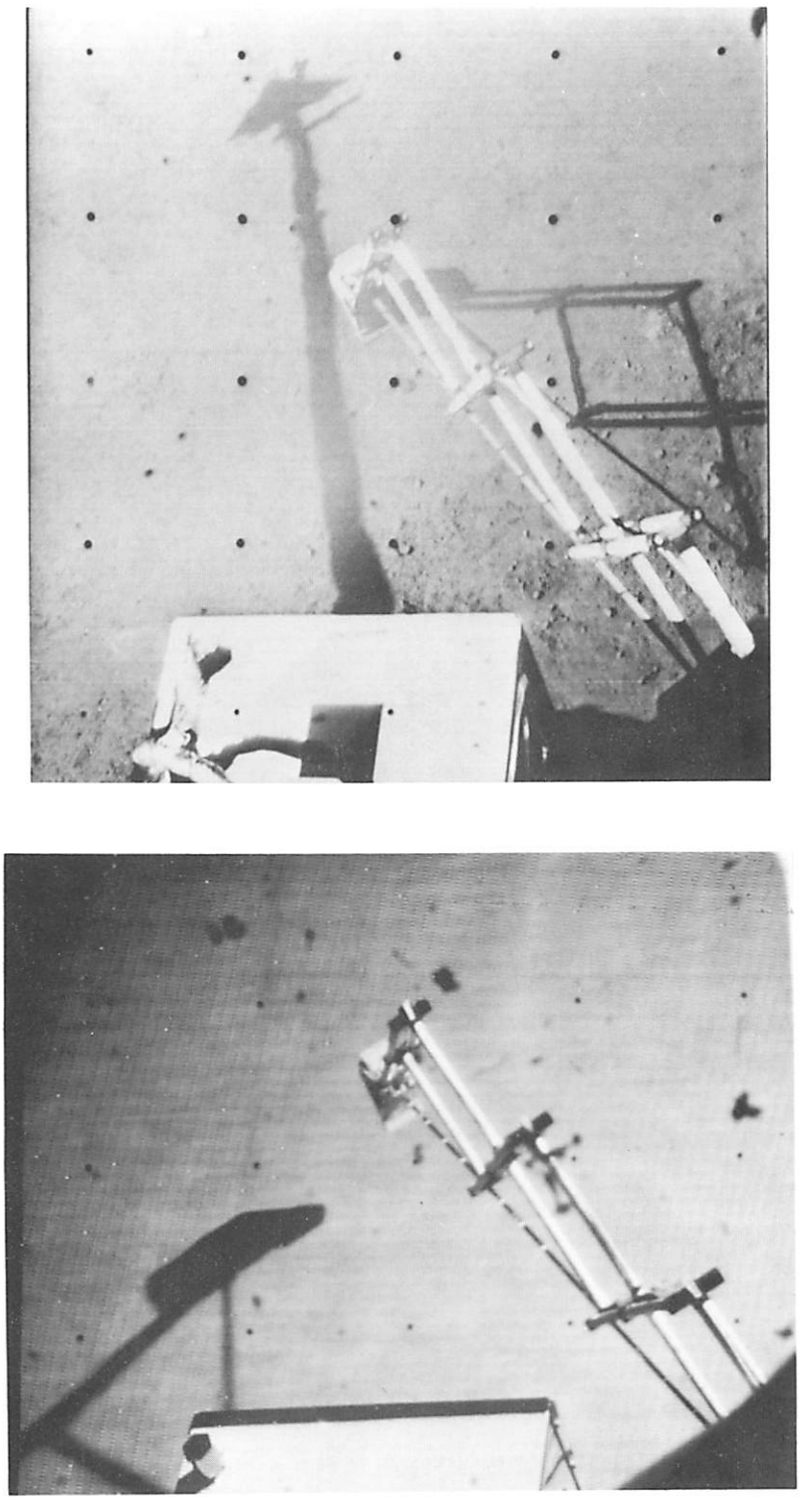

Fig. IV-23. Example of SETL position (bottom) matching picture from *Surveyor* (top). Auxiliary battery is at bottom of frame (Day 120, 15:30:32)

1. Tests Performed

Using the SMSS, many mechanical tests were performed from which calculations of varying degrees of refinement can be made. In this report, only preliminary estimates of material properties are given, based on a brief evaluation of the SMSS behavior and the photographic results. A summary of the tests from which mechanical properties can be derived is given in Table IV-3.

2. Bearing

There were eight bearing tests made with the SMSS door in the closed position so that an area 5 × 2.5 cm was presented to the lunar surface. As seen in Fig. IV-3a and 3b, the angle that the flat base of the scoop makes with the lunar surface varies with the extension distance of the SMSS. Only in the extreme extension position is the flat base aligned approximately parallel to the surface. Consequently, as the scoop is pushed into the surface in the bearing tests, the material under the scoop is forced down and the surface toward the spacecraft is observed to rise as the soil is displaced, as shown in Fig. IV-24.

When each trench was begun, the scoop was pushed into the lunar surface with the door wide open to enable a much smaller area to be presented to the surface. These tests have not been analyzed, and no results from them are shown in Table IV-3, although penetrations of 3.8 to 5 cm (1.5 to 2 in.) were obtained.

As a result of varying temperatures during the lunar day and different distances of extension of the SMSS, a range of forces can be applied to the lunar surface by

Table IV-3. Summary of SMSS bearing and impact tests

Test	GMT	Force, dynes × 10^5	Scoop closed, c, open, o	Penetration, cm	Drop height, cm
Bearing 1	Day 112, 05:07:01	49	c	2.5	
Bearing 2	Day 117, 08:45:20	27	c	2.5	
Bearing 3	Day 117, 09:21:55	22	c	1.9	
Bearing 4	Day 118, 13:32:44	27	c	0.6	(In trench bottom)
Bearing 5	Day 120, 15:35:31	27	c	2.2	
Bearing 6	Day 120, 15:45:42	4.5 to 9	c	Compressed clod	
Bearing 7	Day 120, 15:48:50	27	c	2.9	
Bearing 8	Day 120, 15:59:18	29	c	1.9	
Impact 1	Day 119, 09:27:02		c	1.3	15
Impact 2	Day 119, 09:42:02		c	3.3	30
Impact 3	Day 119, 09:49:04		c	2.5	30
Impact 4	Day 119, 10:08:29		c	3.8	60
Impact 5	Day 119, 10:16:45		c	4.3	60
Impact 6	Day 119, 10:26:40		c	3.8	60
Impact 7	Day 120, 16:17:06		c	1.3	30
Impact 8	Day 120, 16:24:57		c	1.6	30
Impact 9	Day 120, 16:32:45		c	1.6	60
Impact 10	Day 120, 16:41:30		c	1.6	60
Impact 11	Day 122, 12:38:33		o	6.3	15
Impact 12	Day 122, 13:03:40		o	6.3	15
Impact 13	Day 122, 13:30:37		o	1.3	15
Impact 14	Day 122, 14:07:29		c	5.1	78

Fig. IV-24. Picture showing SMSS on Day 112: (a) before (05:07:01 GMT) and (b) after completion of first lunar surface bearing test (05:17:27 GMT)

the tip of the scoop. It was originally intended that these forces be obtained directly by measuring the motor currents and using the preflight calibration data. However, the lack of usable telemetered information on spacecraft motor currents precluded this intention. The motors did not have temperature sensors, so it was necessary to estimate motor temperatures from those measured on the spacecraft and from temperature differences assumed from preflight tests. The information on forces in the bearing tests shown in Table IV-3 was obtained from such estimates of motor temperatures and from the known extension distances of the SMSS.

Television pictures were made after each test of the SMSS scoop in the lunar surface and of the disturbed surface after removal of the scoop. Other pictures were obtained of each surface disturbance at various sun angles on succeeding days. These pictures have been used to obtain the penetration distances given in Table IV-3 for bearing and impact tests.

Prior to some bearing and impact tests, the SMSS was lowered to the lunar surface by 0.1-s down commands to determine the surface location at the point. The commands were repeated until no further downward motion was detected. Although these operations imposed loads of 10^5 dynes on the surface, only a small amount of disturbance caused by the blade tip was observed.

3. Trenching

Three trenches were dug in the lunar surface with the SMSS. The first trench was excavated with only a single pass of the SMSS, whereas trenches 2 and 3 were subjected to repeated passes. A bearing test was made on the floor of trench 3. A fourth small trench was dug for the purpose of carrying out an impact test at a depth of from 5 to 7.5 cm.

The first trenching pass of the SMSS produced an excavation about 5 to 7.5 cm deep; the second pass deepened the trench to a depth of 10 to 12.5 cm (see Fig. IV-25), and a third pass produced a trench of from 15 to 17.5 cm deep. The motion increments produced by a 2-s retraction command of the SMSS vary with the load acting on the SMSS. When the force reaches a limit determined by temperature and spacecraft voltage, the retraction motor stalls and no retraction is obtained. It was found that the first pass in a trenching operation produced a trench of from 38 to 50 cm long with about twenty 2-s retraction commands. Motor stalling was observed in the second (see Fig. IV-20) and third pass in each trench, and as many as 75 commands were required to complete the third pass through trench 2. There are the two following explanations for this behavior:

(1) When a trenching operation is begun at the surface, the material is free to move sideways out of the way of the advancing scoop. When the trench has been excavated to a depth of several inches, the soil scraped from the trench floor accumulates and cannot get out of the way of the advancing, fully packed scoop (Fig. IV-25).

(2) There is a possibility that the lunar material becomes stronger or denser with depth.

Two tests were designed specifically to clarify the second explanation. In the first test, a bearing test was performed on the material at the bottom of trench 3, at a depth of from 5 to 7.5 cm below the surface (bearing test 4). In the second test, two open-scoop impact tests were performed on the undisturbed lunar surface adjacent to a trench (impact tests 11 and 12), and an open-scoop impact from the same drop height above the impact surface was made in the bottom of the trench, at a depth of from 5 to 7.5 cm below the lunar surface (impact test 13).

It is not possible, at this time, to make calculations from the trenching operations regarding the lunar material properties. Further evaluations of the lunar data must be conducted in combination with SMSS laboratory tests. The explanation for the small motion increments of the retraction motor observed under no load must be understood before the retraction forces can be estimated.

4. Impact

The bearing tests provide information on the static strength properties of the lunar soil. The tests primarily involve the soil's shearing strength, in which density plays a part. Impact tests were conducted to obtain further information on soil density in the absence of the motor current data, which would have enabled the weight of a scoopful of soil to be measured. In such tests, the penetration of the SMSS into the lunar soil is resisted by both the static strength and density of the soil. The contribution of the soil's density is greater as the impact velocity increases.

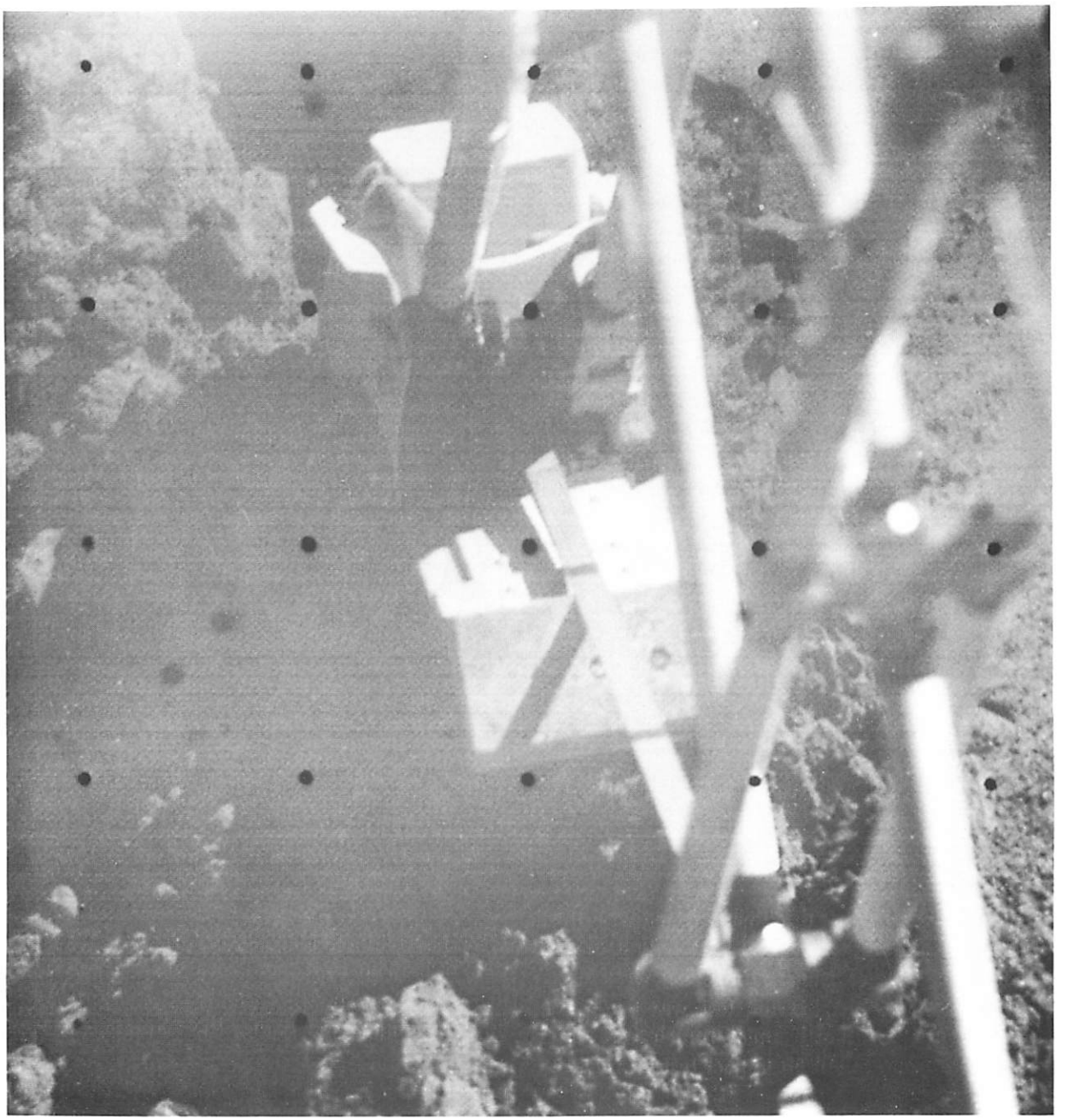

Fig. IV-25. Second pass of SMSS in trench 2. Note material ahead of scoop as it is drawn toward spacecraft (bottom of picture) (Day 113, 07:22:04 GMT)

The SMSS is a flexible arm on which vibrations are excited both by the release of the clutch, which initiates an impact test, and by the actual impact. Therefore, a complete analysis of the motion of the SMSS during impact is complicated. At this time, only approximate soil density comparisons can be made between terrestrial laboratory experiments and lunar impact tests. On the moon, fourteen impact tests, from a variety of drop heights, were conducted at different locations within the reach of the SMSS on and below the lunar surface. The results of those tests are presented in Table IV-3; their location is shown in Fig. IV-4. The drop height given in Table IV-3 is, at present, approximate. As an example, the result of impact test 3 is shown in Fig. IV-26.

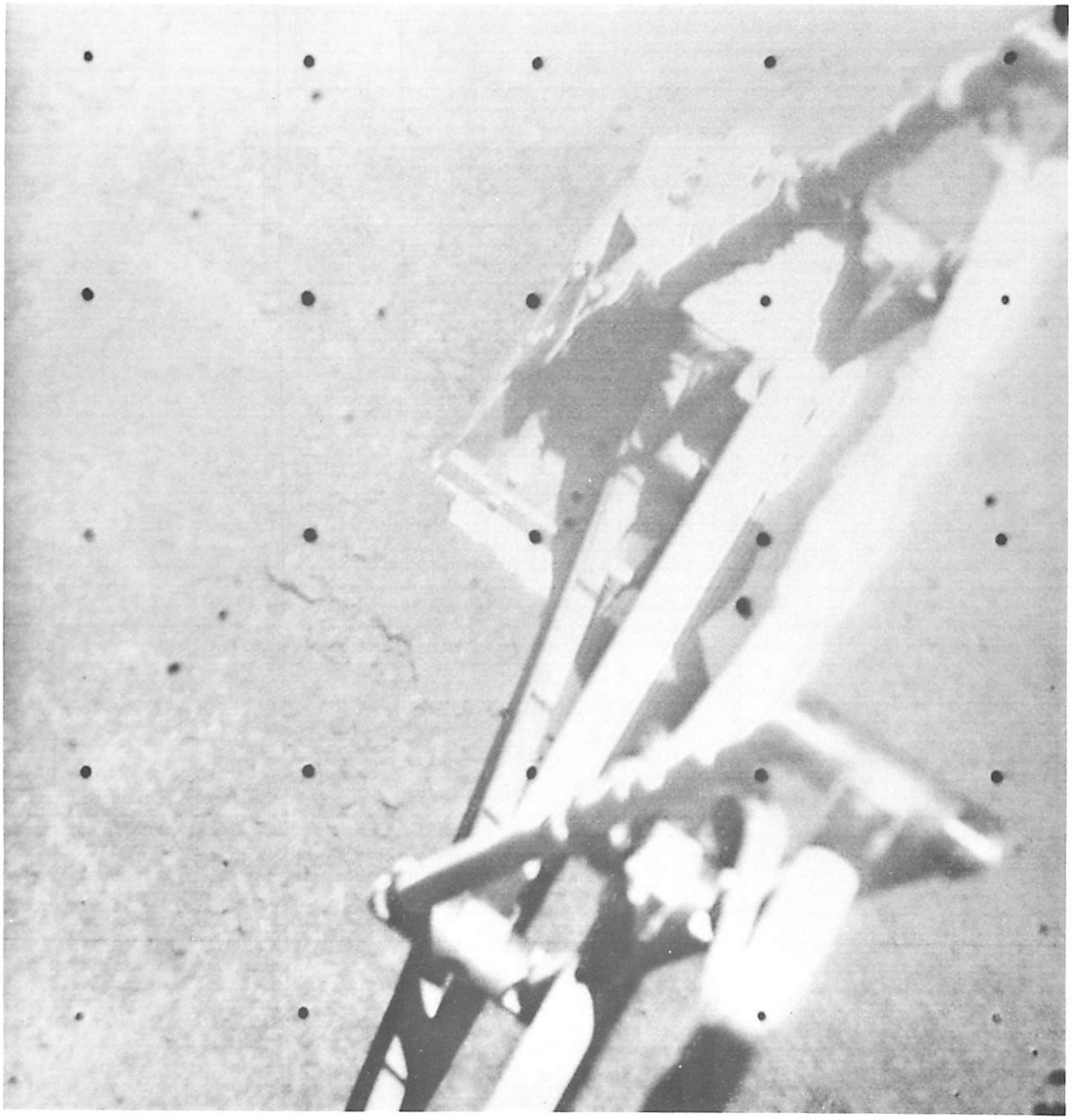

Fig. IV-26. SMSS scoop is shown embedded in the lunar soil following a drop from a height of about 30.5 cm in impact test 3. A previous SMSS impact impression is shown in top left corner of picture (Day 119, 09:49:45 GMT)

5. Material Handling and Dumping

Following a trenching operation, it was frequently found that some of the lunar soil adhered to the inside of the SMSS, even when the soil was disturbed considerably. On occasion, this material fell out on the undisturbed lunar surface, leaving patches or trails of excavated material, as seen in Fig. IV-27.

In the process of excavating the second trench, a lump of lunar material was found below the scoop. The door was closed on the lump to find out if the material was

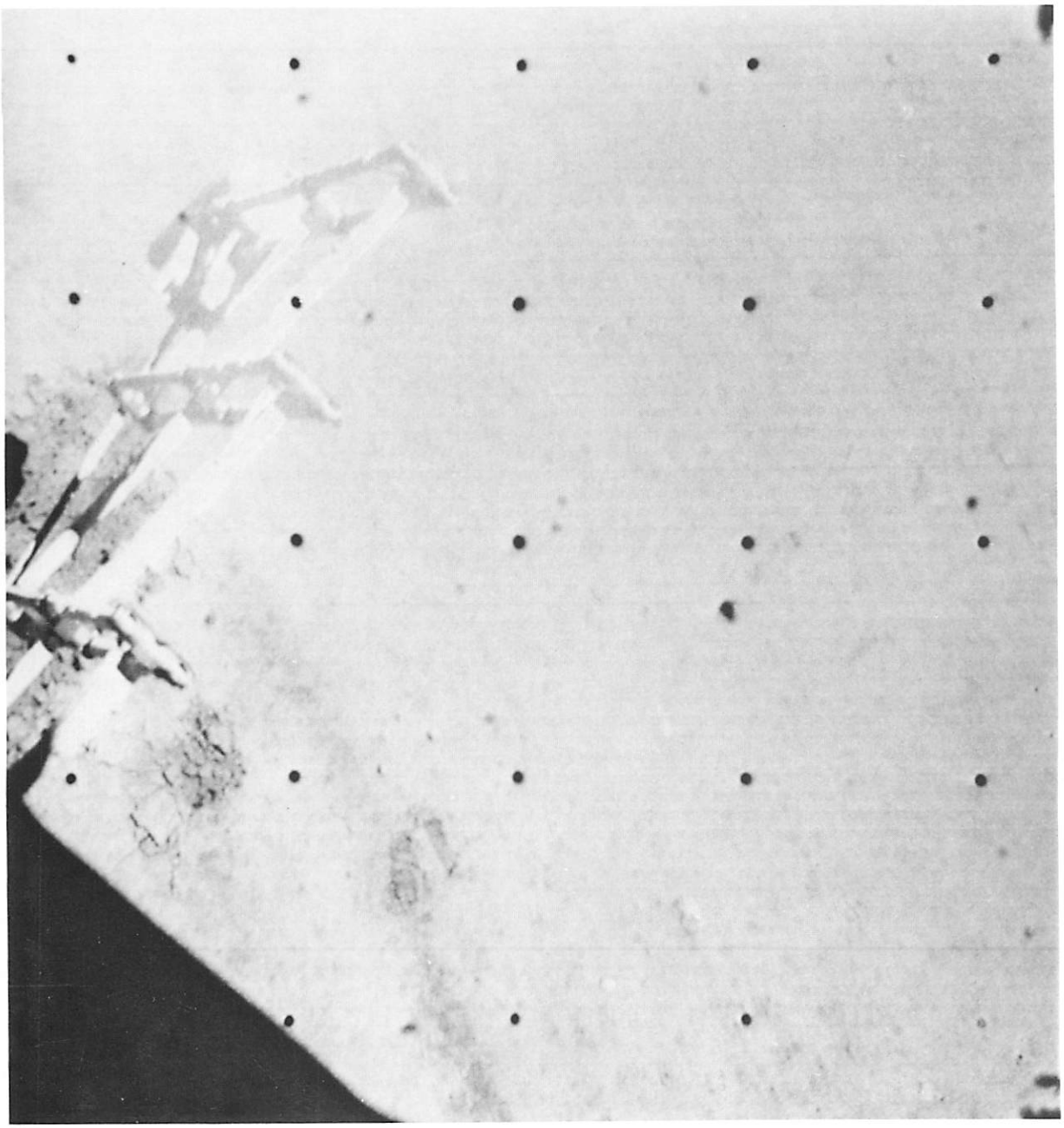

Fig. IV-27. SMSS in position to begin picking up object. In moving SMSS to this position, material from a trenching operation has fallen from scoop to leave a dark trail across the lunar surface. Bearing tests 2 and 3 are seen to the right of the SMSS; trench 3 is obscured by it (Day 118, 09:48:08 GMT)

solid or composed of an aggregate of finer particles. Because the scoop door closed with no observable difficulty, it was concluded that the lump was, in fact, an aggregate. As a check, that portion of the lump pinched off and enclosed in the scoop was transported to footpad 2 and dumped on the footpad for television observation. The material disaggregated on dumping, as seen in Figs. IV-7 and IV-8.

At another location (point H in Fig. IV-4), an object about 1 cm in diameter, with higher albedo than the lunar surface, was picked up and transported to footpad 2 to determine whether the object was solid. During the dumping operation on the footpad, more soil fell out of the scoop and buried the object, which was, however, later identified on the footpad. A third object, also of higher albedo and approximately 2.5 cm in diameter, was located embedded in the lunar soil adjacent to the head of the second trench. It was excavated and picked up in the left side of the scoop, as shown in Figs. IV-11 and IV-12. In clasping the object, the scoop door exerted a force of about 2.5×10^6 dynes (6 lb). The object was restrained by the edge of the scoop, which is 0.1 cm thick. If it is assumed that the bearing area on the object was 1.2 cm long by 0.1 cm wide, then the scoop door exerted a stress on the order of 2×10^7 dynes/cm^2. More of the lighter surface of the object was apparent after it was picked up than when it was embedded. The lower surface, as seen in Fig. IV-12, is darker. The scratch in this lower surface was probably made by the scoop in excavating the object and may indicate that the lower surface is covered with the darker soil.

6. Homogeneity of Lunar Soil

It can be seen from bearing test penetrations that, considering the probable variation in the force applied to the lunar surface, the lunar material appears relatively homogeneous over the test area of 1.9 m^2 (see Fig. IV-28).

However, with reference to the impact test data, it appears that somewhat less penetration occurred for impact tests 7 through 10 in the vicinity of the auxiliary battery than took place in impact tests 1 through 6 at similar drop heights in the area closer toward footpad 2 (see Fig. IV-29). It should be noted that this variation may result from changes in the drop heights caused by SMSS elevation motor changes and a result of the spacecraft attitude, rather than developing as a result of differing lunar surface properties. In addition, impact test 4 may have been too close to a previous test. However, if differences result from the soil properties, two factors which can effect changes are the strength or the density of the material.

No substantial differences were observed in the resistance of the soil encountered in the different trenching operations.

7. Depth Variation of Lunar Soil Properties

In the bearing tests, the SMSS was lowered by one 2-s command into the lunar soil. Then, the SMSS was given successive 2-s commands, which resulted in small additional penetrations. When the movement ceased, the bearing test was terminated. In the absence of motor current measurements, a detailed evaluation of the force vs depth relation is not possible. Characteristically, a penetration of 1.9 to 2.5 cm was achieved in a bearing test at the lunar surface. However, bearing test 4, conducted at the bottom of the third trench at a depth of approximately 5 to 7.5 cm below the lunar surface and probably in disturbed soil, gave a penetration of about 0.6 cm, as shown in Fig. IV-30. This fact, together with the difficulties observed in making the second and third passes through a trench (even considering the effect of trench confinement mentioned), appears to indicate that the lunar soil is firmer or denser below this depth. The comparison of the open-scoop impact tests 11 and 12 on the undisturbed surface with impact test 13, conducted on the material at a depth of 5 to 7.5 cm below the surface, confirms that the material is stronger or denser below a depth of from 5 to 7.5 cm.

When the scoop was rested on the lunar surface under a vertical force of an estimated 4.5×10^5 to 9×10^5 dynes (1 to 2 lb), little penetration was observed. Therefore, it appears that an extremely soft upper layer does not exist in the immediate vicinity of *Surveyor III*. Under the high sun at lunar noon, the detailed texture of the rough surface is no longer visible, and a clear picture of the distance to which the soil is disturbed by a bearing test can be obtained, as seen in Fig. IV-31. The cracks in the ground surface are the surface manifestations of the underground displacement caused by the test. The cracks are not the result of the presence of a surface crust of stronger or more brittle material.

The higher albedo of the undisturbed lunar surface compared to that of the disturbed material in trenches appears to be an extremely shallow effect, as seen in Fig. IV-10a and b.

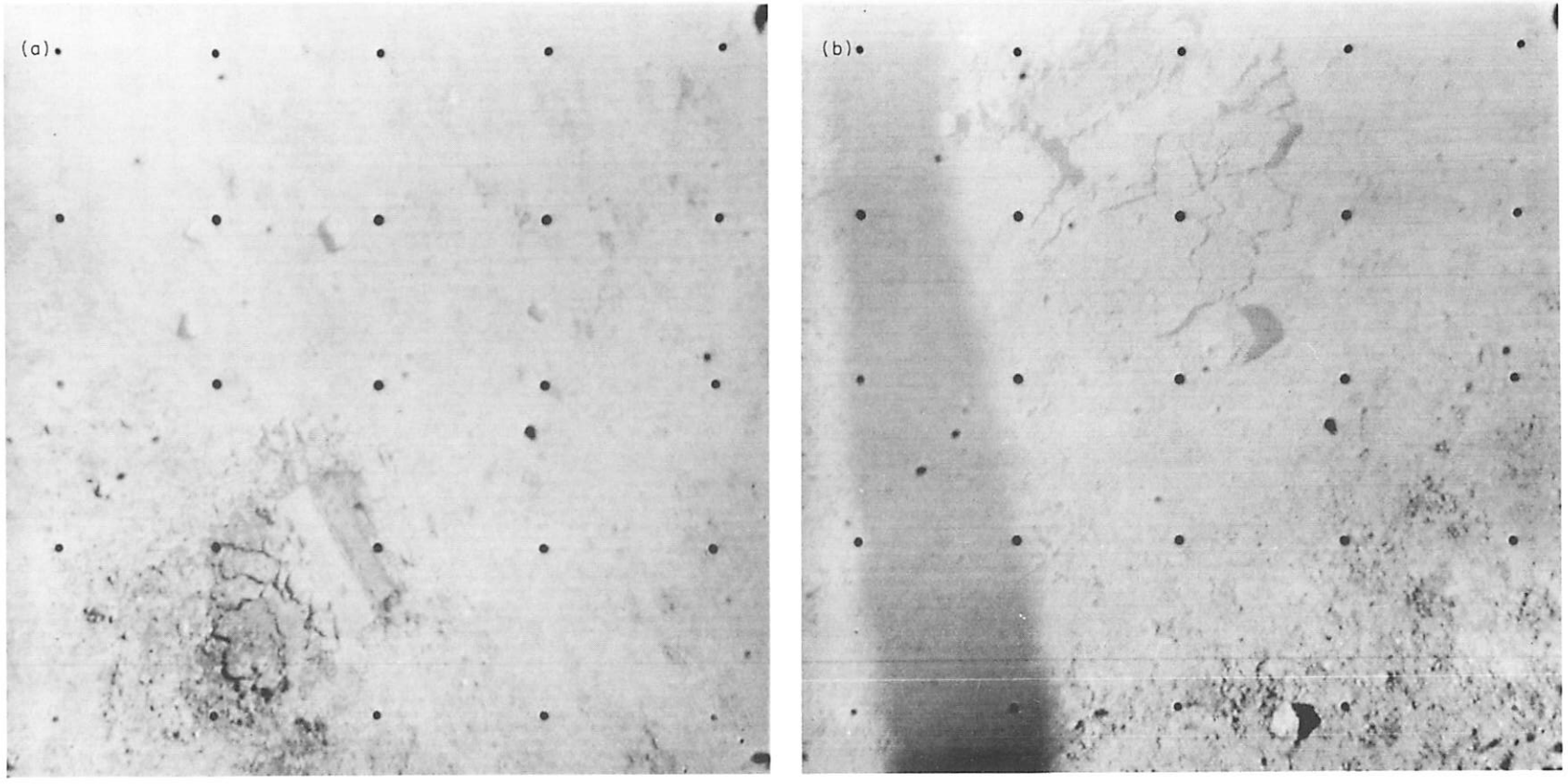

Fig. IV-28. (a) Bearing test 3 near footpad (Day 117, 09:30:12 GMT); (b) bearing test 5 near auxiliary battery (Day 120, 15:40:08 GMT). There is an obvious similarity in the imprints of these two tests, which are separated by a distance of several meters. Note small object below imprint in (b).

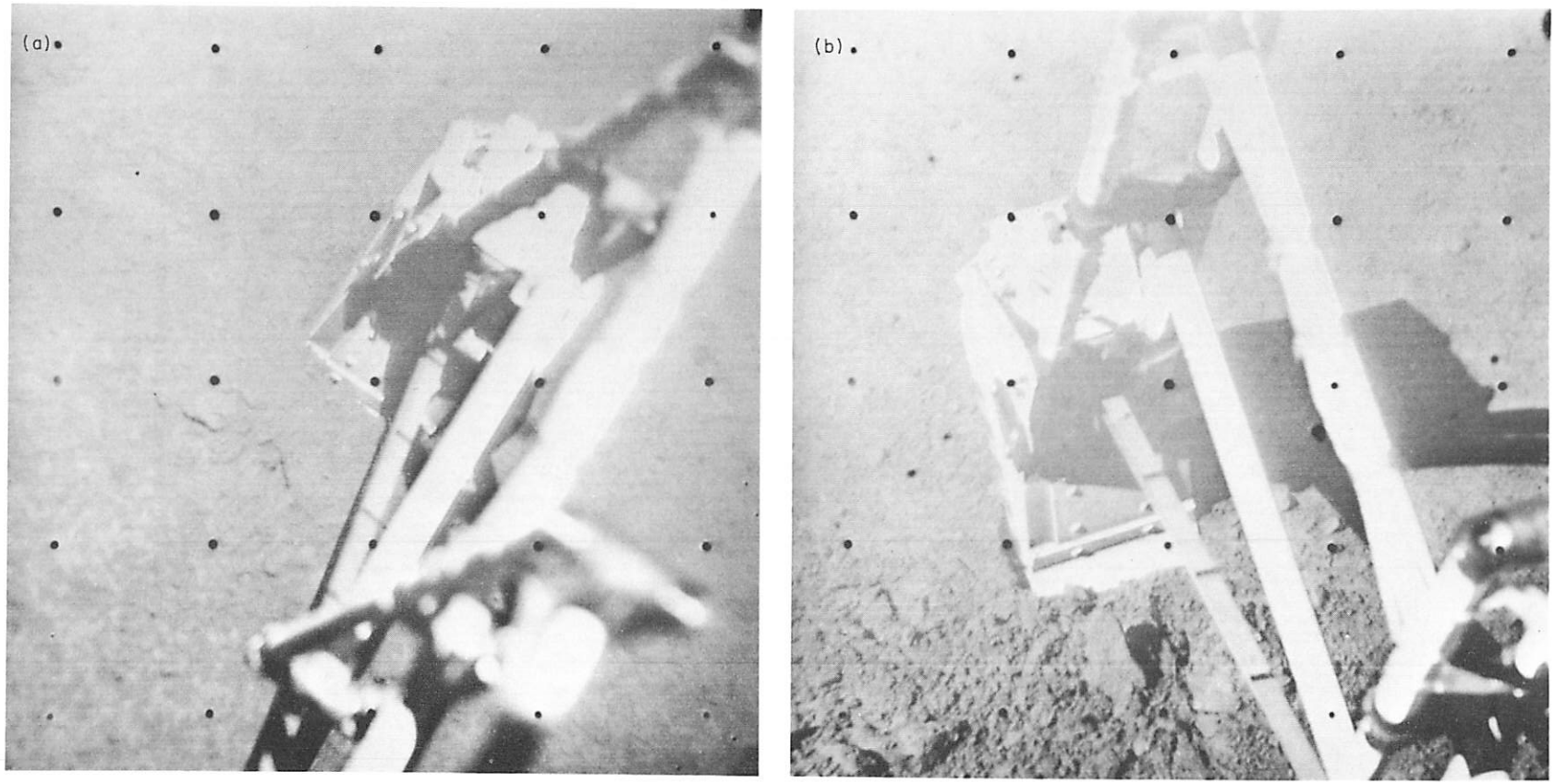

Fig. IV-29. (a) Impact 4 from a height of about 60.9 cm near footpad 2 (Day 119, 10:08:29 GMT); (b) impact 10 from a height of about 60.9 cm near auxiliary battery (Day 120, 16:41:30 GMT). There is a difference in the depths of penetration in these two tests

Fig. IV-30. Bearing test 4 impression in bottom of trench 3 at a depth of 5.1 to 7.6 cm below lunar surface. Depth of impression estimated from shadow. Broken-up soil from trenching operation is visible (Day 118, 13:35:22 GMT)

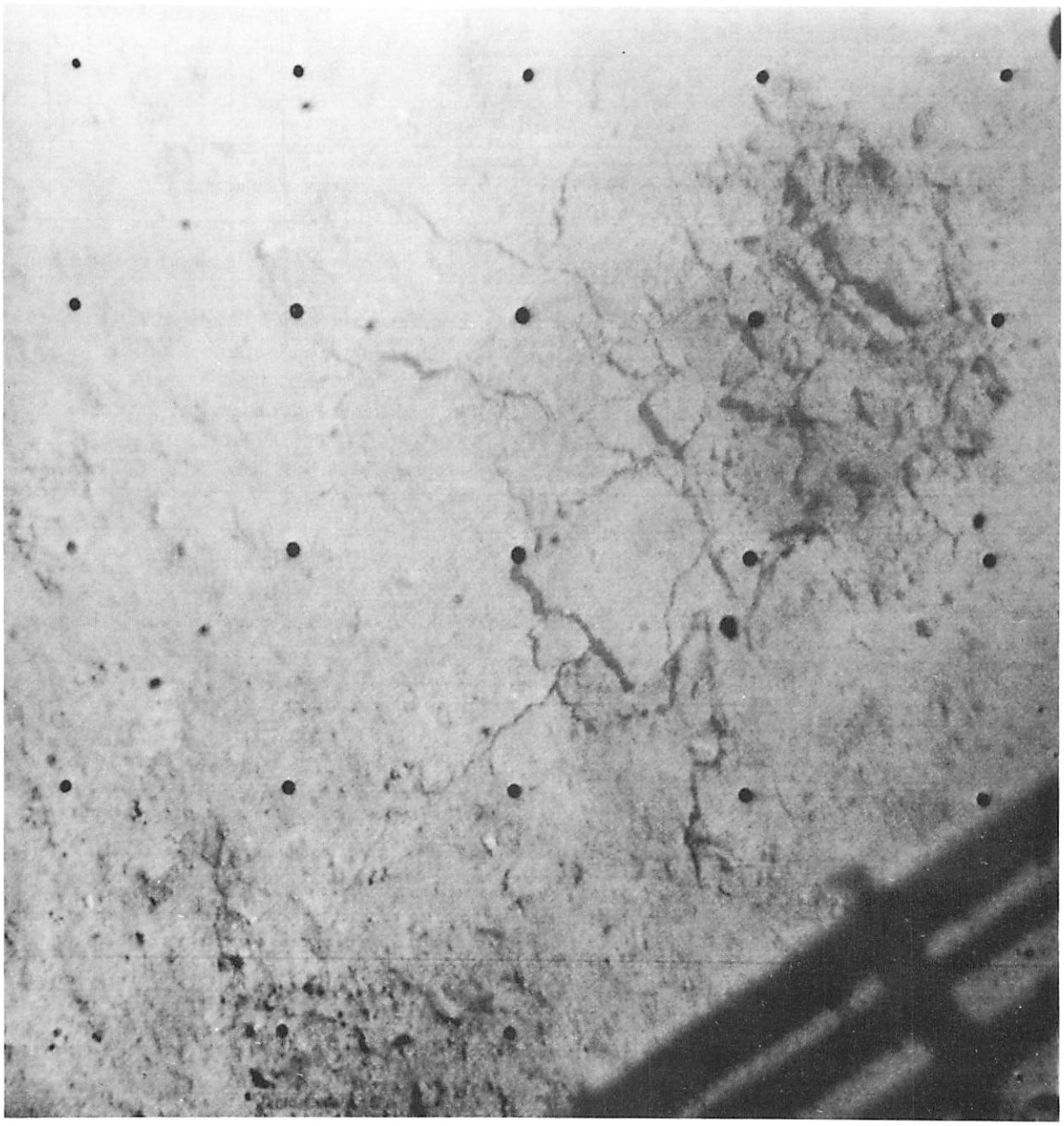

Fig. IV-31. Imprint of bearing test 2 observed at high sun. The cracks caused by the test and extending to the surface of the soil are clearly seen (Day 117, 08:56:45 GMT)

As far as can be determined from the SMSS operations, any change in the soil grain size with depth takes place below the resolution of the camera. There is no obvious albedo change with depth, once the lighter surface material has been disturbed. The albedo of the smoothed surface caused by bearing test 4 on the undisturbed surface in a trench floor will be studied.

E. Analysis

This section of this report discusses the analyses of the SMSS operations performed to date for the purpose of determining the lunar soil properties. The tests referred to are the bearing tests, because the uncertainty over the retraction motor torque leaves the trenching forces still uncertain at this time. Analysis of the impact tests is still incomplete.

1. Bearing Tests

Three bearing tests of different sizes of footing have, in effect, been conducted: the *Surveyor* footpads with a diameter of 20 to 30 cm (8 to 12 in.); the SMSS with the scoop closed; and the SMSS with the scoop open. The results of these tests are given in Table IV-4.

Table IV-4. Bearing test results

Test	Dimension, cm	Depth of penetration, cm	Pressure, dynes/cm^2
Footpad	20	5	4×10^5
SMSS closed	2.5	2.5	2×10^6
SMSS open	0.32	3.8 to 5	1×10^6

It is considered that failure or yielding of the soil by general shear (Ref. IV-1) occurred in all of these tests. Therefore, the pressure represents the static bearing capacity of the soil at the depth of penetration achieved. The value used for the bearing capacity for the footpad is deduced from the *Surveyor I* landing. It is compatible with the data obtained from the *Surveyor III* landing.

The bearing capacity, p, of a footing at a shallow depth, z, below the surface of soil is (Ref. IV-1) approximately given by the expression

$$p = G_c N_c c + G_\gamma N_\gamma \rho g b + N_q \rho g z$$

where

N_c, N_γ, N_q = dimensionless numbers depending only on the friction angle Φ of the soil

G_c, G_γ = dimensionless numbers depending on the shape of the loaded area; $G_c = G_\gamma = 1$ for a strip footing; $G_c = 1.3$ for a round footing; $G_\gamma = 0.6$ for a round footing

c = cohesion of the soil

ρ = density of the soil

g = local gravitational acceleration

b = half of the width of the footing

For the surface sampler base, G_c is taken as 1.1 and $G_\gamma = 0.9$. The equation given has been selected because the lunar soil seems to behave in general shear rather than local shear under a footing. Considering the *Surveyor* footpad at a 20-cm diameter and the SMSS with a 2.5-cm width as two bearing tests, two equations can be obtained from the above equation. For the present, ignoring the open-scoop test, there are three unknowns, ρ, c, and Φ (because N_c, N_γ, and N_q are functions of Φ only), to be determined – if it is assumed for the present that the lunar soil is homogeneous to a depth of several centimeters. There are many ways of determining the soil parameters. The method selected here is to choose values of ρ, the density, compatible with the observation that the material is granular, relatively incompressible, and has a deformational behavior qualitatively similar to that of terrestrial soils. For each density, values of cohesion, c, and internal friction, Φ, of the lunar soil may be calculated. The values obtained are discussed in terms of the observed behavior.

For the calculations, densities of 1.0, 1.5, and 2.0 g/cm^3 (approximately 2, 3, and 4 slugs/ft^3) have been selected. For a solid mineral component density of 3 g/cm^3, porosities have also been calculated. The results are shown in Table IV-5. To show the variation that may be expected in the results, the values of cohesion and friction angle, shown in parentheses, are those calculated for a *Surveyor I* footpad bearing capacity of 2.8×10^5 dynes/cm^2. This value may represent a lower limit of the bearing capacity at the footpad scale.

For a soil composed of solid mineral particles of ordinary terrestrial density (2.5 to 3 g/cm^3), a density of 1.0 g/cm^3 represents a material with a large proportion

Table IV-5. Soil property calculations

Density, g/cm³	Porosity	Cohesion, dynes/cm²	Angle of friction, deg
1.0	0.67	9×10^2 (5.5×10^3)	42 (33)
1.5	0.50	1.4×10^3 (8×10^3)	39 (30.0)
2.0	0.33	1.7×10^3 (1×10^4)	37 (27)

of void spaces, or high porosity. Such a soil does not exhibit the generally incompressible behavior shown by the lunar soil in the bearing tests. In addition, the friction angle of a particular soil increases as the density increases and is in the range of 25 to 45 deg for soils with low to high densities. It is seen from Table IV-5 that the lower the density of the material is assumed to be, the higher must be the friction angle, to explain the observations.

If the lunar soil were composed of porous mineral particles that did not break up during the bearing tests, the incompressible behavior could occur, and the material could have a friction angle of 40 deg and at the same time possess a low density. However, a large proportion of the lunar surface material is apparently composed of particles smaller than from 40 to 50 μm in diameter. These small particles would have to be porous for a lunar soil of low density to exhibit the observed mechanical behavior. Although this possibility is not excluded, it seems more reasonable to conclude from the calculations (see Table IV-5) that the lunar surface material has a density in the range of 1.5 g/cm³ with an accompanying cohesion of about 1.4×10^3 dynes/cm² and a friction angle of 39 deg.

In bearing tests of this type, the soil is typically uplifted and disturbed on the surface to a distance that depends on the angle of internal friction of the material. For the 2.5-cm width of the SMSS base, a material with an angle of friction of 30 deg would be disturbed to a distance of about 10 cm from the edge of the base, and a material with an angle of friction of 40 deg to a distance of about 17.5 cm. It is observed in the SMSS bearing tests under a high sun angle (Fig. IV-32) that soil disturbance takes place to a distance of at least 10 to 12.5 cm, indicating an angle of internal friction of at least 35 deg. The nature of the displacement phenomenon, observed in the bearing tests, indicates that the soil density does not change appreciably during the test.

For any of the discussed soils, a calculation using the given equation applied to the open-scoop SMSS bearing test indicates that a much greater depth of penetration should have been obtained under the vertical force employed. The indication is, therefore, that below a depth of about 5 cm (2 in.), the lunar soil is substantially firmer or denser. This confirms the soil behavior observed in the trenching tests.

This increase in strength affects the calculations of the soil properties based on the bearing tests, because the size and depth of penetration of the spacecraft footpads are such that the assumption of vertical homogeneity cannot be made. In this case, the equation cannot be used and the relative values in Table IV-5 are not correct because the firmer soil (assuming it existed also at the *Surveyor I* site) would affect the penetration of the spacecraft footpad. In a homogeneous material of the same average characteristics as the top 5 cm of the lunar soil, the spacecraft footpad would have penetrated deeper at the same applied pressure. If this consideration is used to re-evaluate the data, it appears that (for all the assumed densities) friction angles would be from 2 to 3 deg lower, and the cohesion perhaps 7×10^2 dynes/cm² higher. The small amount of cohesion apparently present in the lunar soil leads to the tentative conclusion that van der Waal forces, rather than primary bonding forces, are those causing the cohesion.

It is possible that the increase of strength with depth is a phenomenon associated with the *Surveyor III* landing position, because legs 2 and 3 of the spacecraft apparently rest on or near the rim of a small shallow crater and the SMSS tests were performed on the rim material. If this is not the case, and the increase in strength with depth is a general lunar feature, there is no obvious reason why there should be a sudden increase at the 5-cm depth. It is possible, therefore, that there is a gradual increase with depth. The lack of SMSS motor current data precludes any confirmation of this property assumption.

Because trenching was performed to depths greater than 5 cm, further analysis of the trenching information may yield quantitative results on the soil profile below that depth.

2. Trenching

The behavior of the retraction motor is still being analyzed to determine the reasons for its anomalous

reactions. The forces applied by the SMSS to the lunar soil during trenching operations remain unknown.

In an attempt to measure these forces, trench 4 was dug on Day 122, after turning on the strain gages on *Surveyor's* shock absorbers. A preliminary analysis of the static strain gage readings immediately following the landing indicates that a change in the force in a shock absorber of amount greater than 4.5×10^6 dynes (10 lb) could be discriminated in the strain gage record. The strain gage traces obtained during the trenching test show no indication of any load level change. It is tentatively concluded from further analysis, therefore, that the SMSS was exerting a retraction force of less than 4.5×10^6 dynes on the lunar surface during the formation of trench 4. Further reduction of the strain gage records is planned.

3. Impact Tests

A complete analysis of the impact tests cannot be given at this time. However, the velocity of the surface sampler at contact with the lunar surface from a drop height of 60 cm (corresponding approximately to four 2-s elevation steps) can be estimated to be about 2.1 to 2.5 m/s. Laboratory tests have been carried out on earth with a prototype SMSS striking various soils at a range of velocities. For a slightly higher impact velocity than that given for the SMSS moon impacts, laboratory tests on densely packed dry sand (density about 1.7 to 1.8 g/cm^3), with the scoop closed, have given penetration depths of 1.6 to 1.9 cm. Such a soil has a friction angle of about 40 deg and is essentially cohesionless. Comparison of the SMSS lunar impact tests with the terrestrial tests indicates that the material densities are comparable, although preliminary analyses indicate that penetration depths at these impact velocities are not very sensitive to density. The density of the terrestrial tests (about 1.5 g/cm^3) would be compatible with the value in the analysis of the static lunar test results. The effect of the stronger or denser lunar soil layer below a depth of from 5 to 7.5 cm on the impact test results remains to be investigated. It would tend to lessen the penetrations.

4. Material Handling

Because the disturbed lunar soil remained in the open SMSS scoop above the lunar surface, it can be calculated that it possesses a cohesion greater than about 3×10^2 dynes/cm^2 for an assumed density of about 1.5 g/cm^3. Since the walls of the trenches have not collapsed at a depth of 15 to 17.5 cm, it appears that the cohesion may be at least 10^3 dynes/cm^2. In one impact test, conducted with the scoop open, a quantity of soil was dumped on the lunar surface almost equal in volume to the capacity of the scoop, as best as can be estimated. In such an impact test, the maximum deceleration is in the range of from 5 to 10 earth g. Therefore, the upper limit of the adhesion of the disturbed soil to the scoop can be estimated as being about 10^4 dynes/cm^2.

In one bearing test, an object (see Fig. IV-28b) resting on the lunar surface was depressed and found to crumble under a relatively gentle pressure (contact 3, item T in Fig. IV-4). It is concluded that this object was an aggregate of smaller particles, as was the clod of material broken by the scoop door at the foot of trench 2. One of the objects of higher albedo that was picked up seemed to have a substantially greater strength than these clods, and may be termed a rock.

Reference

IV-1. Scott, R. F., *Principles of Soil Mechanics*, Addison Wesley, Reading, Mass., 1963.

Acknowledgment

Special appreciation is extended to M. C. Clary, JPL, for his analysis of the performance of the mechanism and auxiliary during the mission.

V. Lunar Surface Mechanical Properties

E. M. Christensen, S. A. Batterson, H. E. Benson, R. Choate, L. D. Jaffe, R. H. Jones, H. Y. Ko, R. L. Spencer, F. B. Sperling, and G. H. Sutton

Interpretation of the lunar surface mechanical properties, as discussed in this report, is based on observations associated with the landing impacts, telemetry data of *Surveyor III*, and a comparison with *Surveyor I* data. The data[1] consist primarily of:

(1) Loads in the landing gear shock absorbers recorded throughout the entire landing sequence.

(2) Pictures obtained by the spacecraft television camera of the spacecraft/lunar interactions, and the lunar surface disturbed by the landings.

(3) Results of various analytical and laboratory simulations.

The landing of *Surveyor III* was quite different from that of *Surveyor I*. *Surveyor I* made one landing on a relatively flat surface with its three landing legs contacting the surface about the same time (Ref. V-1). In contrast, *Surveyor III* made three distinct touchdowns on a sloping crater wall. The features of this crater, observed in pictures obtained from the *Surveyor III* camera and compared with those obtained from the *Lunar Orbiter III* camera, show that the spacecraft is now resting on the eastern slope of a crater about 200 m in diameter (see Section III of this report) with its landing leg 2 oriented in the uphill direction of the crater slope. During the first two landing events, the three vernier engines that controlled the spacecraft attitude and velocity during its final descent to the moon generated an upward force almost equal to the lunar weight of the spacecraft. Prior to the third landing, however, the vernier engines were shut down, and the spacecraft contacted the surface in a free-fall condition. Nominally, the spacecraft should have had a free fall from an altitude of 4 m after a normal shutdown of the vernier engines.[2]

Figure V-1 is a picture of a *Surveyor III* spacecraft model, showing the components and structures discussed in this report. The three legs are designed to rotate upward against the resistance of a shock absorber during a landing impact in order to limit the loads imposed on spacecraft components (Figs. V-2 and V-3).

[1]Data obtained from the soil mechanics surface sampler are, in general, not considered here; see Section IV of this report.

[2]Values are given in the centimeter-gram-second units. To convert to feet-pound-second units, the following factors may be used: 1 m = 3.28 ft; 1 cm = 0.39 in.; 1 N (newton) = 0.225 lb; 1 dyne/cm^2 = 1.46 × 10^{-5} lb/in.^{2}.

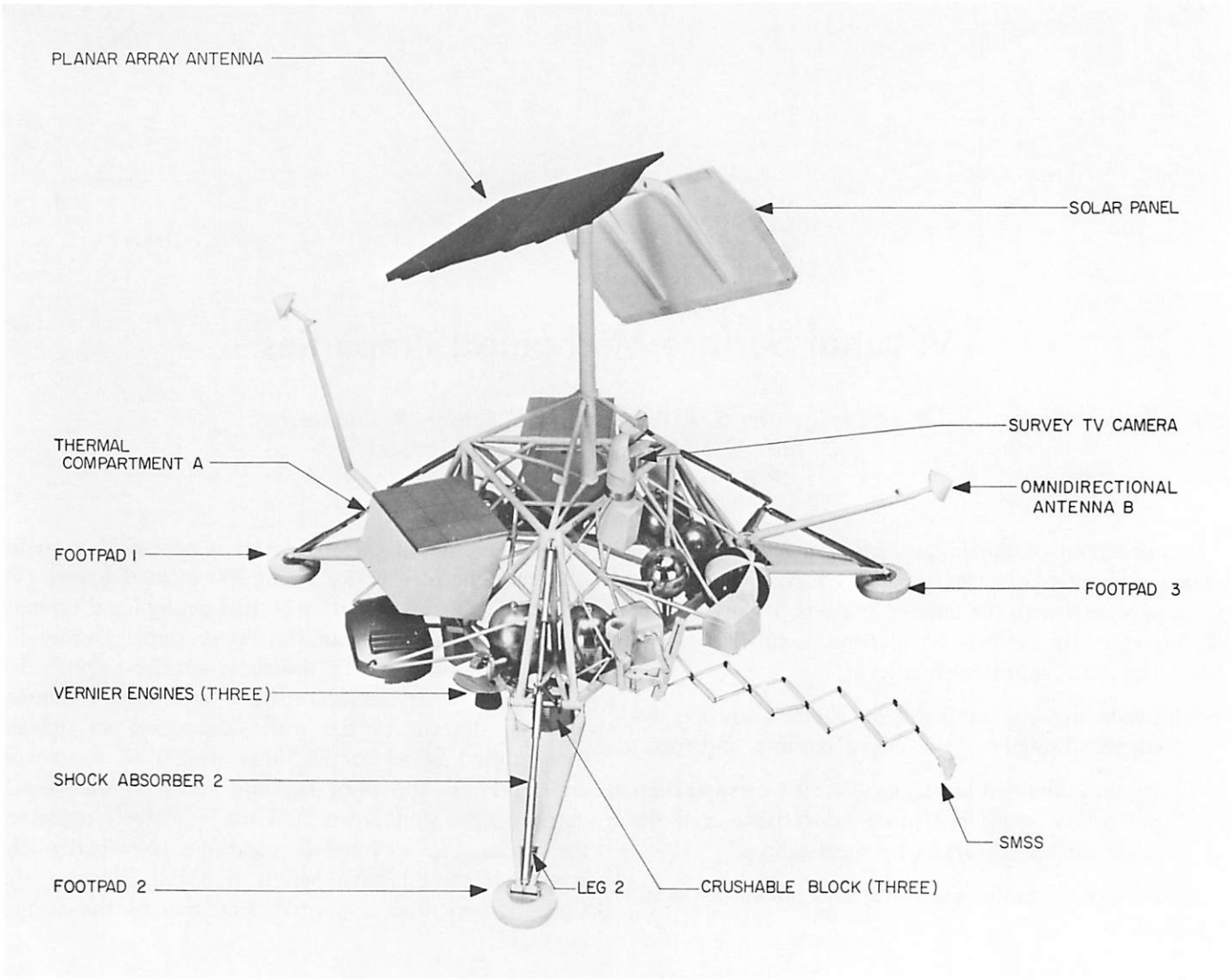

Fig. V-1. *Surveyor III* spacecraft model

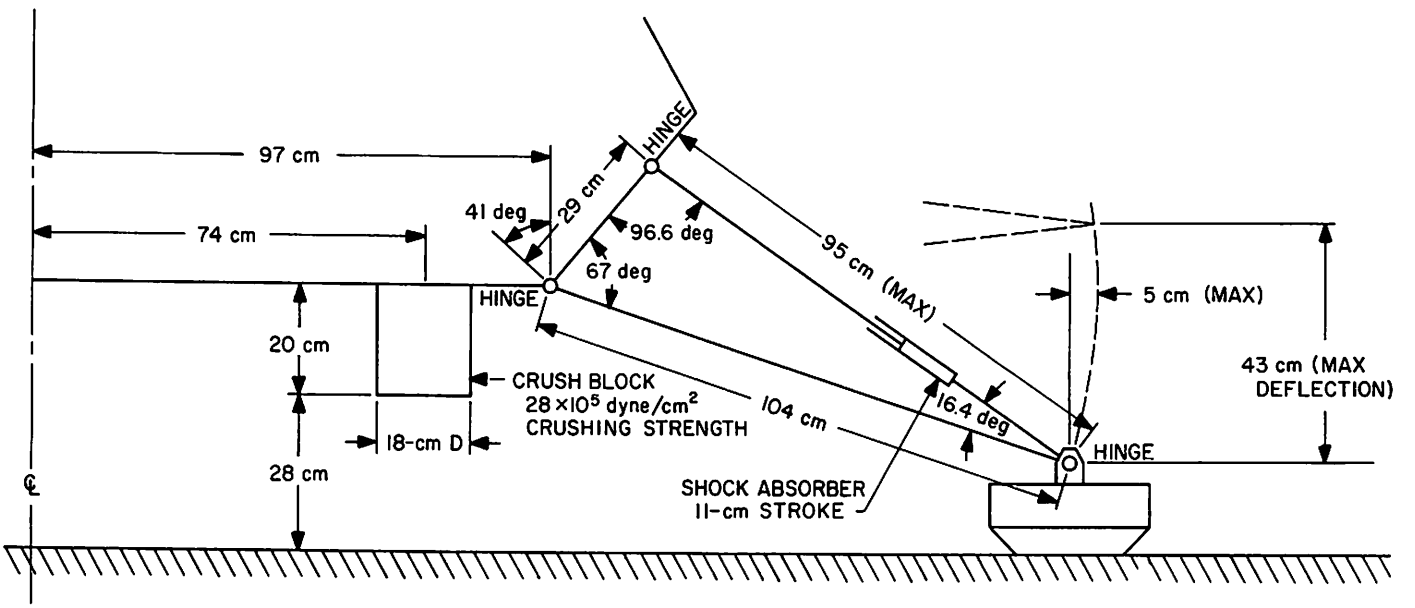

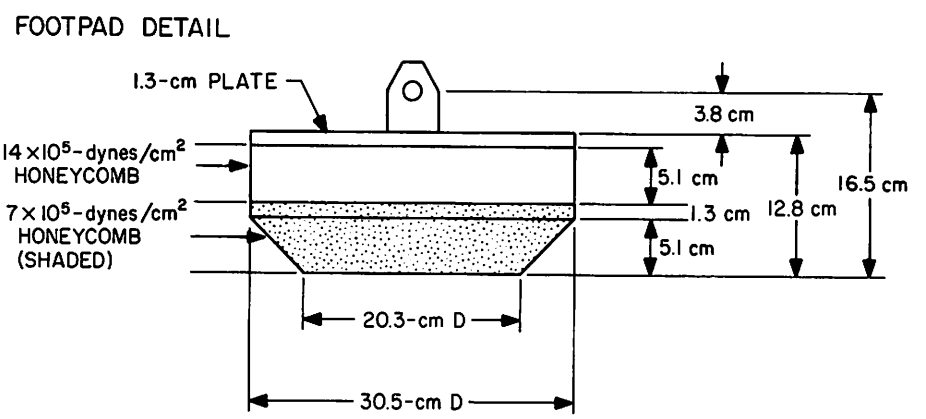

Fig. V-2. Dimensions of landing gear assembly

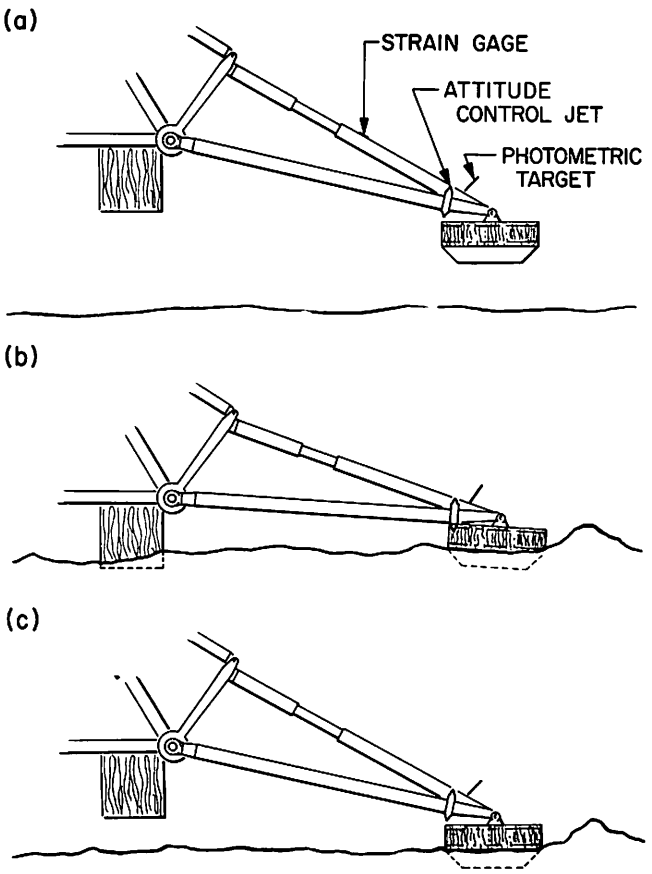

Figure V-3. Sequence of landing gear positions during a landing. Assembly is shown fully extended in (a); during landing, the shock absorber compresses and the footpad moves up and away from the spaceframe, as shown in (b); assembly is shown re-extended after landing in (c)

Following the landing impact, the shock absorbers return to their pre-touchdown position. For purposes of additional energy dissipation, the footpads are made of a crushable material (Figs. V-4 and V-5), and crushable honeycomb blocks are located on the underside of the spacecraft inboard of each of the legs.

A. Observations

1. Landing

The general reconstruction of the three major landing events was deduced primarily from the data obtained from strain gages, which measured the axial load in each of the three landing gear shock absorbers, and from television pictures of the disturbances of the lunar surface caused by the spacecraft touchdowns.

Figure V-6 shows the complete time records of the shock absorber axial loads from the time of initial surface contact until the time the spacecraft came to rest. This record indicates the three distinct landing events. During most of the time between the landings, the axial loads were zero, indicating that the spacecraft was not in contact with the lunar surface. Because of the continued thrusting of the vernier engines and the elasticity of the landing gear, the spacecraft rebounded after the first impact and was clear of the surface for about 24 s before landing the second time. The third, and final, landing took place following a second rebound that lasted about 12 s. After the final landing, the magnitude of the axial loads was consistent with the value required to support the static weight of the spacecraft. This indicated that the spacecraft came to rest on its three footpads after the third landing and that no thrust was being developed by the spacecraft's vernier engines.

As discussed later in this section, footpad 2 contacted the surface first in each of the landing events. This suggests that the initial touchdown during each landing event occurred on the sloping crater wall and that the spacecraft was essentially level with respect to the true lunar vertical. This would also suggest that, during the interval between landings, the spacecraft flight control system brought the spacecraft to essentially the same level attitude and prevented significant angular motions about the spacecraft vertical axis. The final angle between the spacecraft vertical axis and the true lunar vertical is from 12 to 15 deg, with the spacecraft tilted approximately in the direction of the downhill slope of the crater wall (Fig. V-7).

The direction of spacecraft travel during landing events was inferred from pictures of the third landing event imprints of footpads 2 and 3 and of the disturbed lunar material around the footpads (Figs. V-8 and V-9). A television search for surface marks of the first and second landing events was guided by these data. The suspected landing areas were to the east of the spacecraft. Unfortunately, the camera glare during the lunar morning precluded obtaining good pictures of these areas until Day 116, when the sun angle was 77 deg above the horizon. The pictures taken on Day 116, however, revealed no distinctive marks between the imprints shown in Fig. V-10 and the spacecraft; yet this area is a relatively uniform, uncratered slope on which spacecraft marks should be visible if they were there.

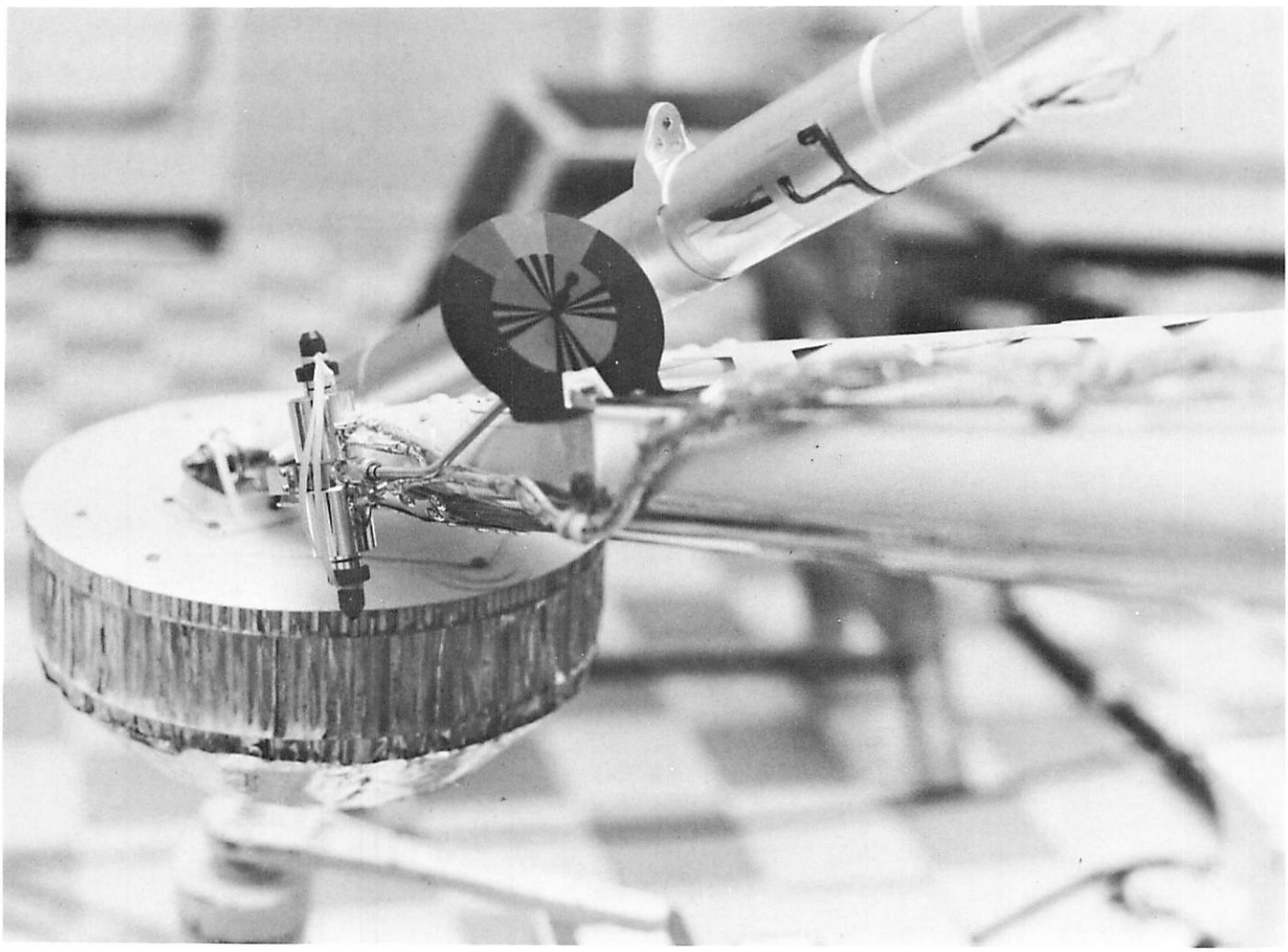

Fig. V-4. Picture, taken before launch, of footpad 2. Ballast weights are visible on top of footpad

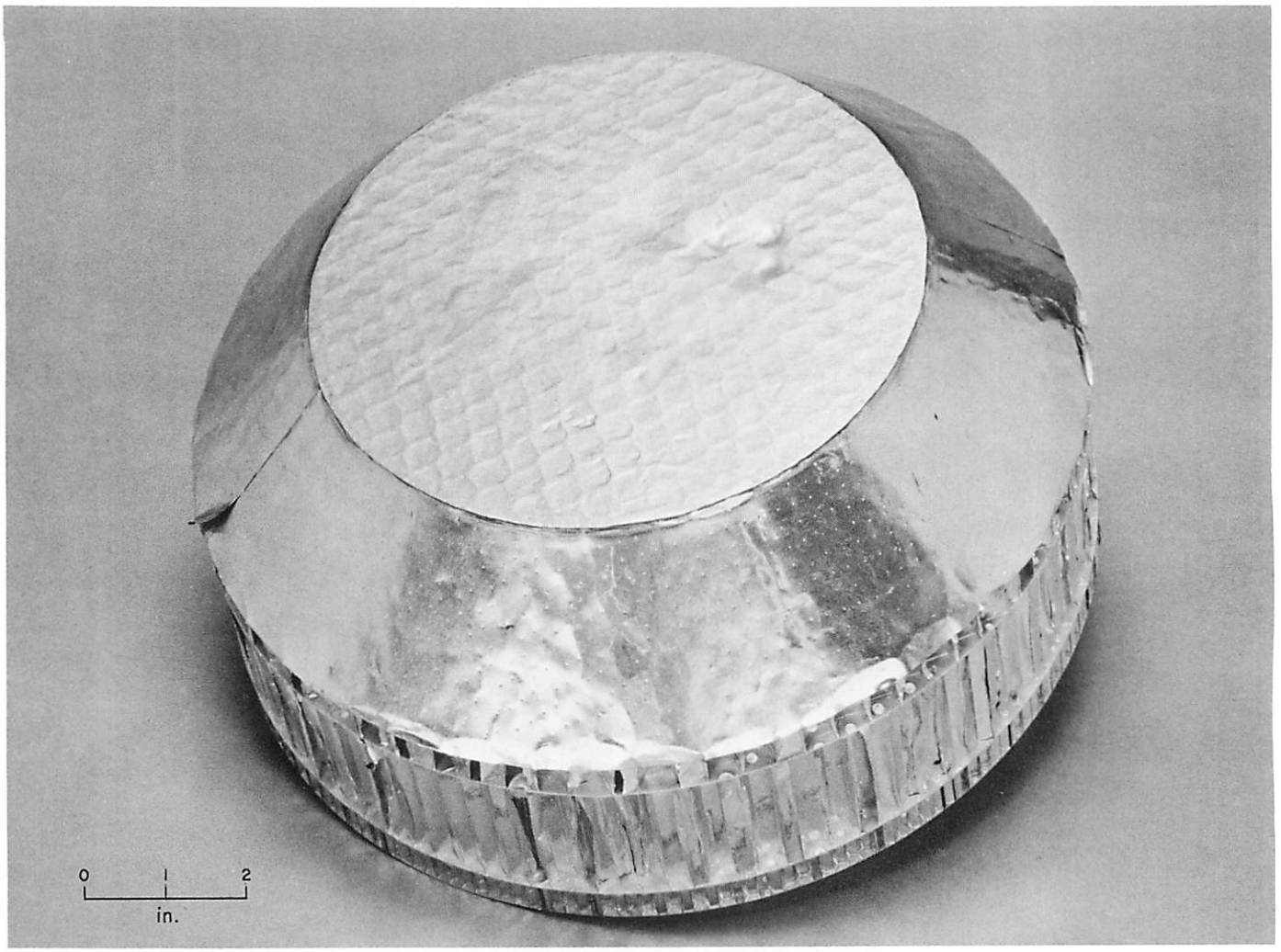

Fig. V-5. Picture of bottom of a *Surveyor* footpad. Footpad has been lightly loaded in vertical compression, thereby exposing the honeycomb pattern

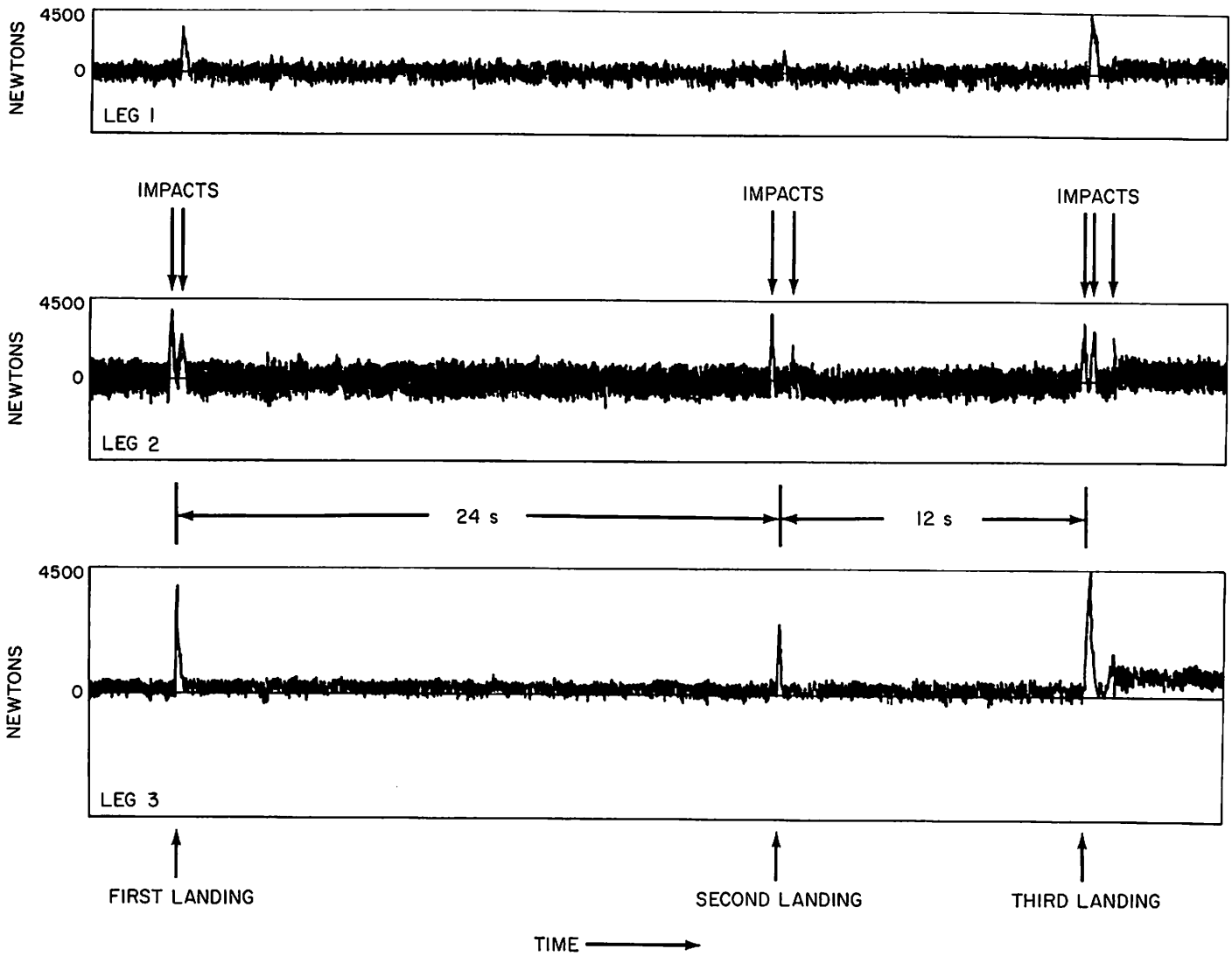

Fig. V-6. Histories of the axial forces in the shock absorbers of the three landing legs of *Surveyor III* during the entire landing sequence, touchdown to final position

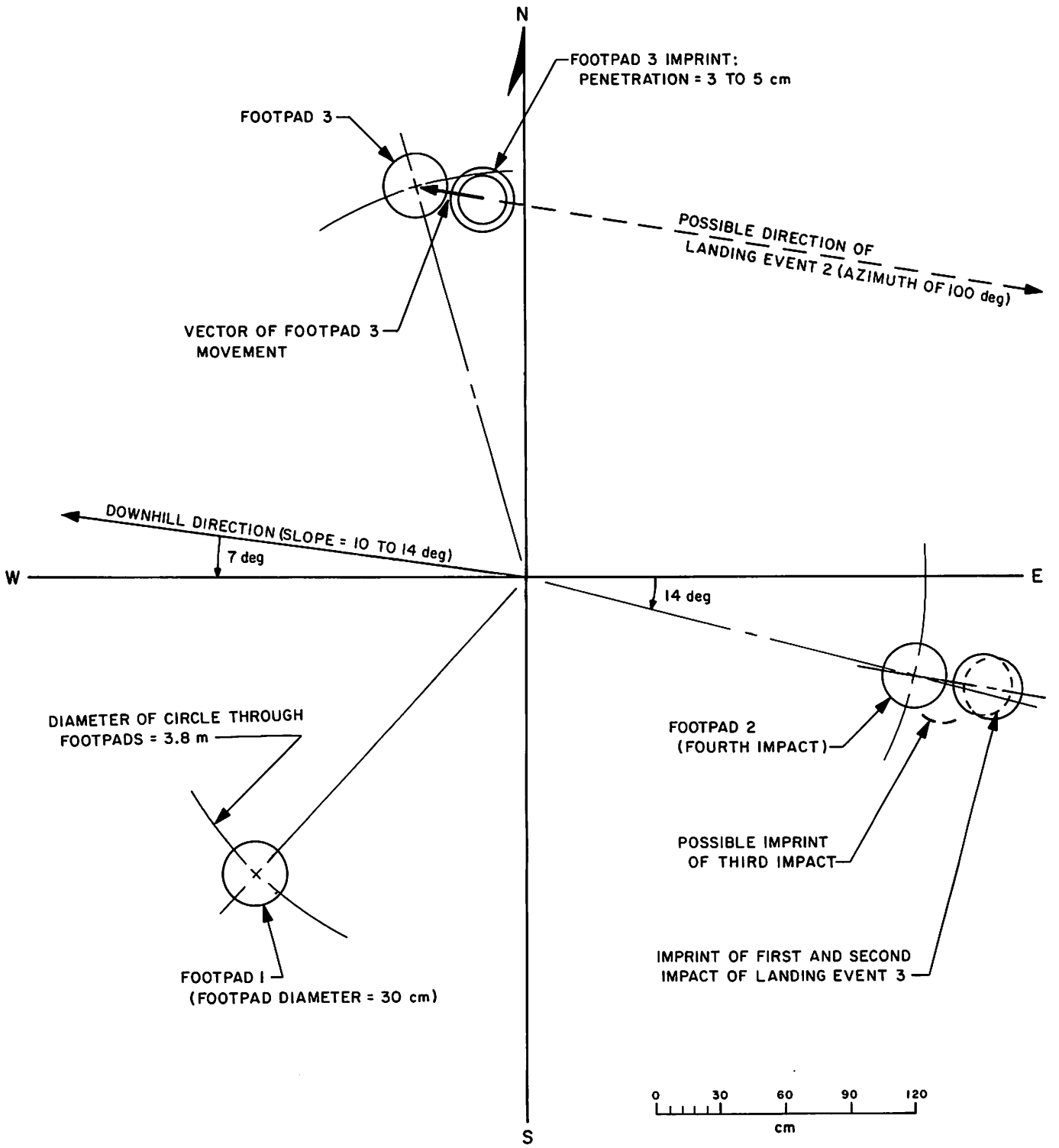

Fig. V-7. Preliminary evaluation of relationships during and after landing event 3

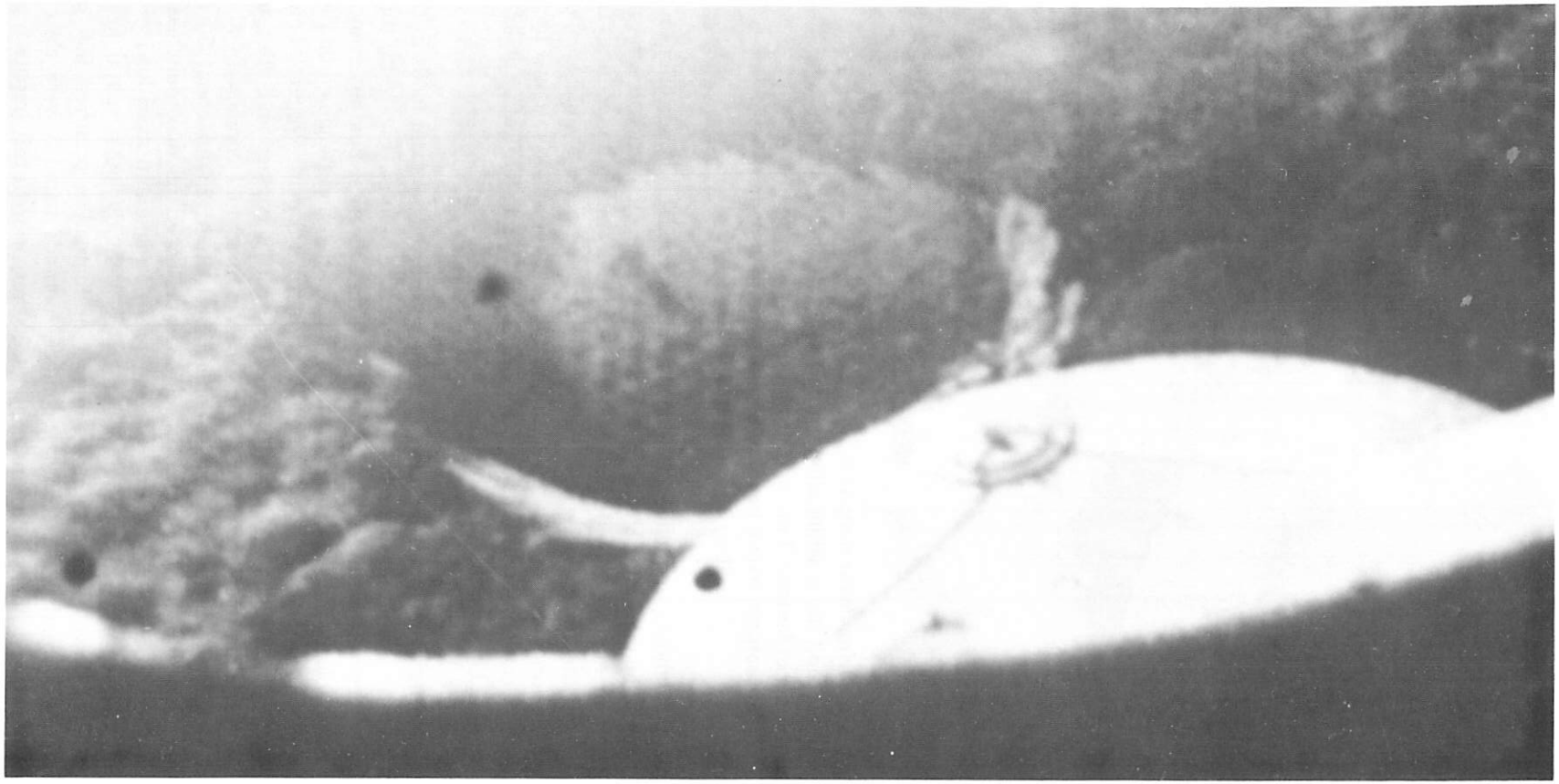

Fig. V-8. Imprint in lunar surface just outboard of footpad 2. Note honeycomb pattern on bottom. Imprint is attributed to first and second impacts of footpad 2 during third landing event. Note reflection off conical part of imprint. Black area in lower part of frame and white streak between this and imprint are images of camera housing. Sun angle was 14 deg (Day 110, 09:05:17 GMT)

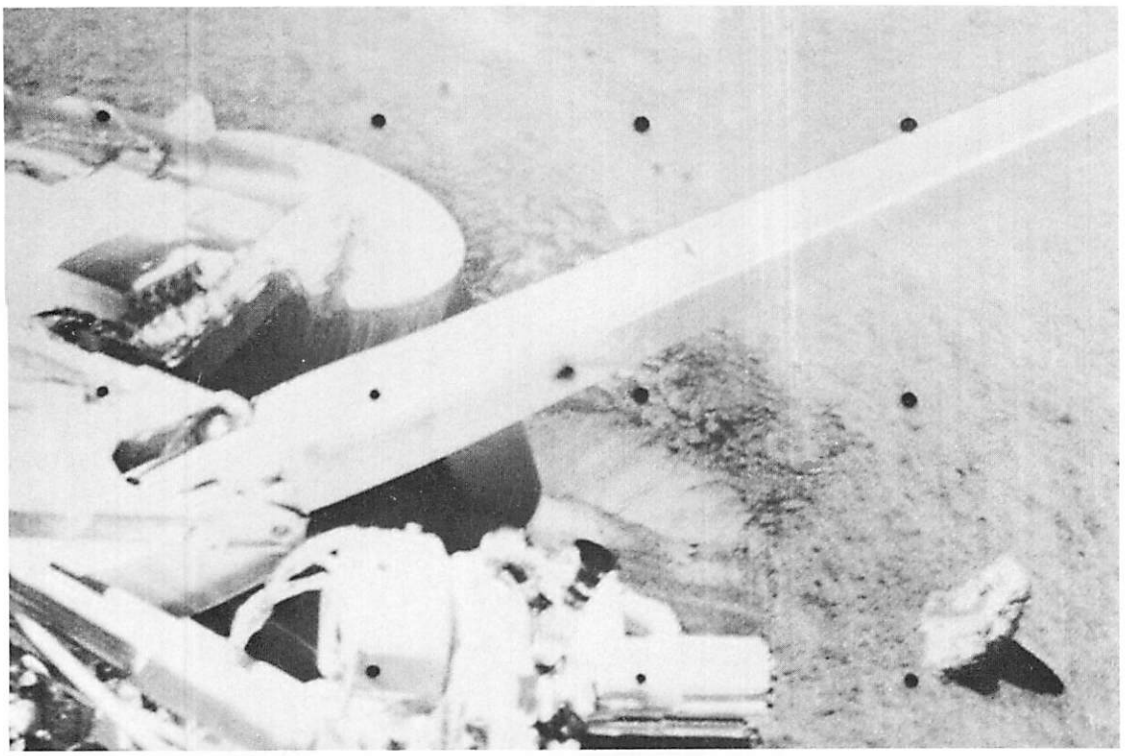

Fig. V-9. Lunar surface near footpad 3, with portions of *Surveyor III* spacecraft. Image of footpad top is white ellipse at left center. Imprint attributed to first impact of footpad 3 during third landing event is to lower right of footpad, below boom of omnidirectional antenna (Day 120, 13:42:24 GMT)

Figure V-11 is a sketch of the landing sequence of *Surveyor III* as interpreted from available data. During landing events 1 and 2, the vernier engines provided a thrust equivalent to about 0.9 of the lunar spacecraft weight. If the spacecraft had a horizontal velocity of 0.9 m/s, the distances covered between landing events 1 and 2 would have been 22 m, and 11 m between landing events 2 and 3. Estimates of the horizontal distance between the first and second landing events and the rebound heights are not firm because accurate values of the vernier engine thrust and spacecraft attitude, during the intervals in which it was clear of the surface, have not been established.

Figure V-12 shows an expanded time-scale record of the shock absorber axial loads developed during the first landing. It indicates that footpad 2 impacted first and then rebounded clear of the surface. Footpad 3 was next, with impact occurring about 260 ms after the initial impact of footpad 2; leg 1 touched down about 290 ms after initial impact. The load on footpad 2 was completely relieved for about 150 ms and then built up again. The second load indication of footpad 2 started at about the time the loads on the other two footpads were near their maximum values. Loads on all three footpads reached a zero value at about the same time, indicating that the spacecraft was approximately normal to the local slope at the instant it left the surface.

Time records of the axial loads in the shock absorbers during landing event 2 (Fig. V-12) differ from those obtained during the first landing event. Again, footpad 2 made contact first and remained on the surface for about 200 ms; footpad 3 made contact about 370 ms after the initial footpad 2 contact and after footpad 2 had left the surface. Footpad 1 contacted 440 ms after the initial contact of footpad 2 and about 50 ms before landing gear 3 experienced its maximum axial load. It can be seen that the maximum axial load in leg 1 was considerably less than the other initial loadings. The second impact of footpad 2 occurred 900 ms after its initial contact; footpads 1 and 3 were clear of the surface for about 300 ms prior to this impact.

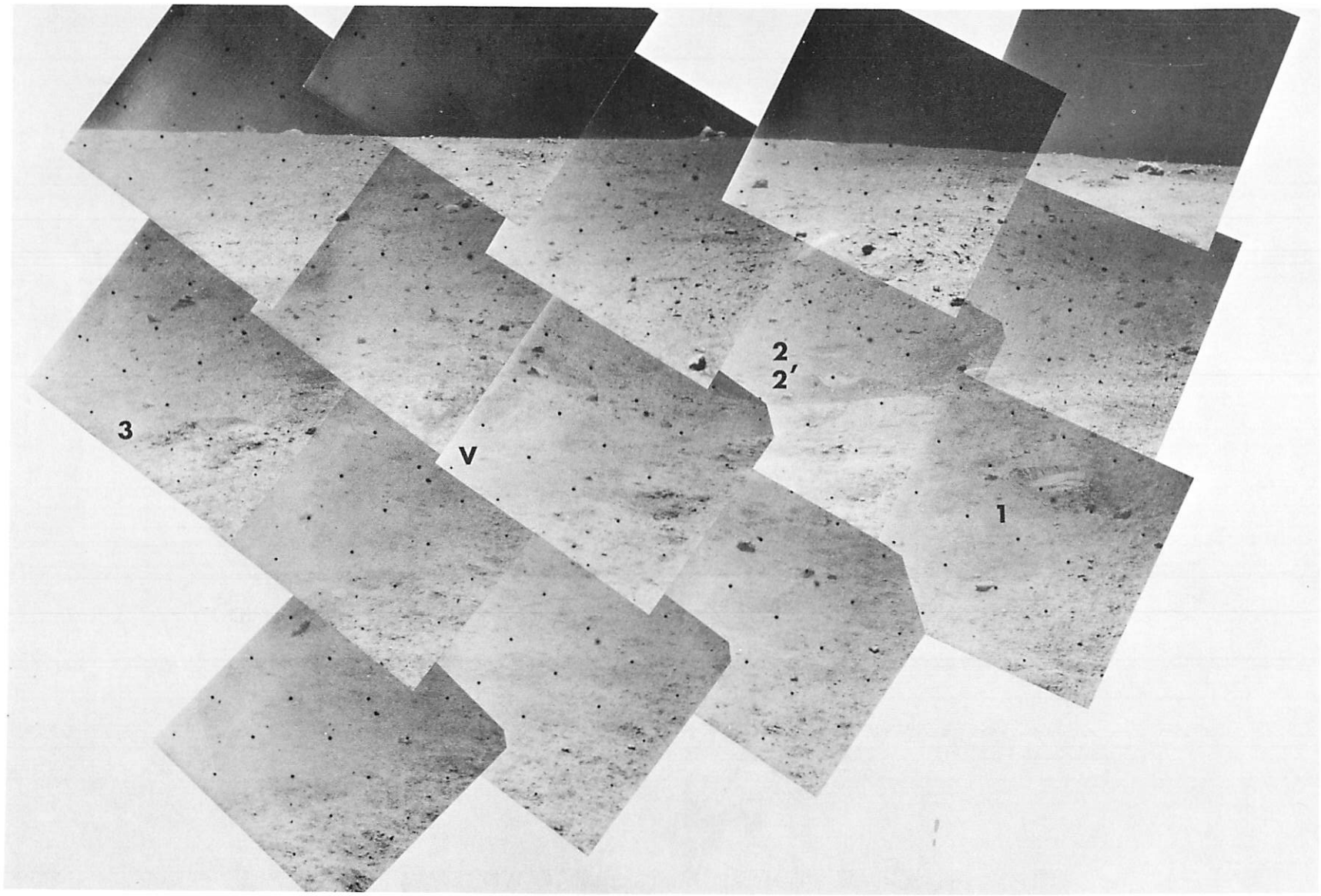

Fig. V-10. Narrow-angle mosaic of the second landing area to the east of the spacecraft. Imprints of the footpads are indicated by numerals (Catalog No. 3-MP-01, Day 116, between 07:06:46 and 09:27:06 GMT)

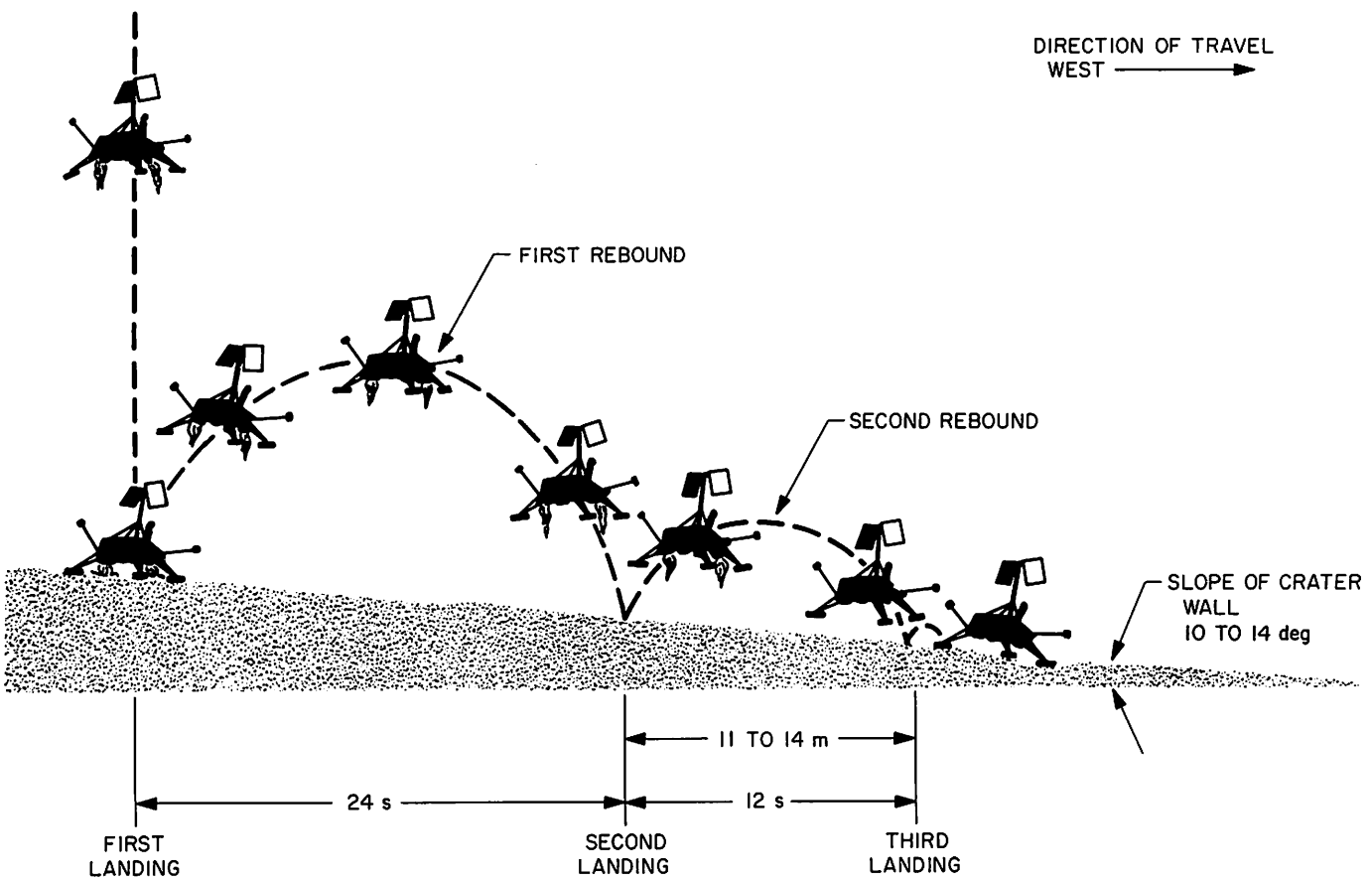

Fig. V-11. Sketch showing events during landing of *Surveyor III* on the moon

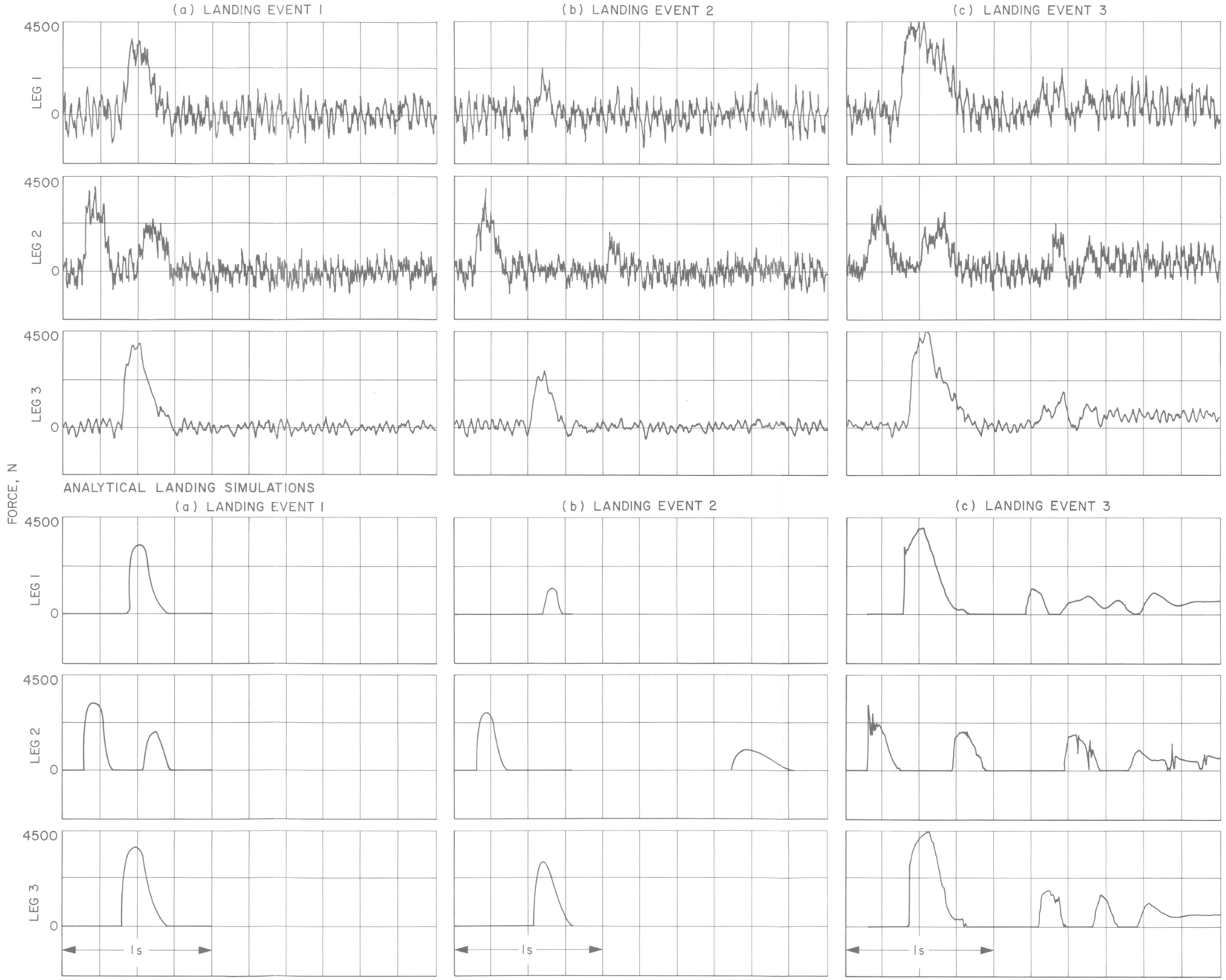

Fig. V-12. (a) Comparison of histories of axial forces in the three landing legs of *Surveyor III*, during the first landing event, with corresponding data obtained from an analytical simulation. Conditions for the simulated landing are: horizontal velocity, 0.3 m/s; vertical velocity, 1.8 m/s; surface slope, 11.5 deg. (b) Comparison of histories of axial forces in the three landing legs of *Surveyor III*, during the second landing event, with corresponding data obtained from an analytical simulation. Conditions for the simulated landing are: horizontal velocity, 0.6 m/s; vertical velocity, 1.5 m/s; surface slope, 14.0 deg. (c) Comparison of histories of axial forces in the three landing legs of *Surveyor III*, during the third landing event, with corresponding data obtained from an analytical simulation. Conditions for the simulated landing are: horizontal velocity, 0.9 m/s; vertical velocity, 1.2 m/s; surface slope, 9.2 deg

(Blank Page)

Axial loads, developed in the shock absorbers during the third landing event, are also shown in Fig. V-12. They are similar in character to those observed in the first landing, although the maximum loads are somewhat higher. Again, footpad 2 made initial surface contact, followed 240 ms later by the impact of footpad 1; footpad 3 contact occurred about 270 ms after the initial impact of footpad 2. The surface contacts of footpads 1 and 3 occurred during a short period in which there was no axial load measured in the shock absorber of leg 2. The second impact of footpad 2 occurred when the axial loads in legs 1 and 3 were at about their maximum value. All three footpads then left the surface at about the same time, and a much smaller impact was recorded from 400 to 500 ms later. This final rebound was caused by the landing gear elasticity, and corresponds to a similar rebound experienced by *Surveyor I*.

Table V-1 gives the maximum axial forces in each shock absorber for all three events, as well as the initial contact times, as reduced from data from the 210-ft antenna at the Goldstone, Calif., Tracking Station (DSS 14).

Following the last impact of landing event 3, a small amplitude oscillation, visible for about two cycles and with a frequency of 6.5 Hz, can be observed in the three strain gage records. The peak-to-peak amplitudes of these oscillations are on the order of 450 N. *Surveyor I* also developed a similar oscillation, but of larger magnitude. The greater magnitude (more than 1000 N) was a result of the higher impact velocity of *Surveyor I*. For both landings, these oscillations are interpreted as a vertical mode of oscillation of the spacecraft, which is related to the elastic properties of the spacecraft and is also influenced by the elastic properties of the lunar surface material. This is discussed further in Section V-B.

Table V-1. Maximum shock absorber axial forces for the three landing events

Leg	Axial force, N; time from initial contact, s		
	Landing event 1	Landing event 2	Landing event 3
1	2970 00.29	1420 24.44	3860 36.59
2	3060 (1820) 0	2800 (930) 24.00	2440 (1950) 36.35
3	3680 00.26	2350 24.37	4120 36.62

Values in parentheses are peak forces of the second impact of leg 2 within each landing event. Because of considerable noise in the data, the peak force readings are considered accurate within ±20%. Times are accurate within ±10 ms.

A narrow-angle mosaic of surface disturbances, believed to have been made by the spacecraft during the second landing event, is shown in Fig. V-10. The analysis presented in Section V-B indicates that imprint 1 was made by footpad 1, footpad 2 touched down at 2 and then at 2′, and imprint 3 was made by footpad 3. A disturbed area can be observed at V, which corresponds to the second landing event location of vernier engine 3.

2. Footpad/Surface Interactions

The direction and distance traveled by the spacecraft during the third touchdown event exposed to the television camera the area initially disturbed by the two footpads during this landing. The pictures of this area provided information related to the interaction between the footpads and the lunar surface material.

The imprint area in front of footpad 2, formed during the third touchdown, is shown in Fig. V-13. The imprint is composed of two truncated conical depressions superimposed one on another; the bottom of this imprint is quite flat. Dimensions of the imprint, as determined by simulations, are described in Section V-B.

In the imprint area, where pictures were taken in the afternoon (Fig. V-14), the edge of another imprint was observed to the right and just beyond the top of the footpad. This feature was not apparent in the pictures taken in the morning. This imprint, located in the ejecta of the first two imprints, is only a few centimeters away from the edge of the footpad itself. It appears from the strain gage data that footpad 2 made four distinct impacts with the lunar surface during the third landing event; thus, the imprint seen over the top of the footpad would be the one made by the third impact. The first two imprints, which are partially superimposed, and the fourth (the imprint underneath the footpad at its present position) are in an approximate straight line, whereas the third imprint appears to be offset a few centimeters from this line. The pattern of the disturbed soil is unsymmetrical, with more soil deposited to the right of the footpad and its imprints, indicating that footpad 2 was moving with some lateral velocity in the direction toward the right. This observation is further substantiated by the smoothness of the top edge of the first imprint at a position corresponding to the lagging

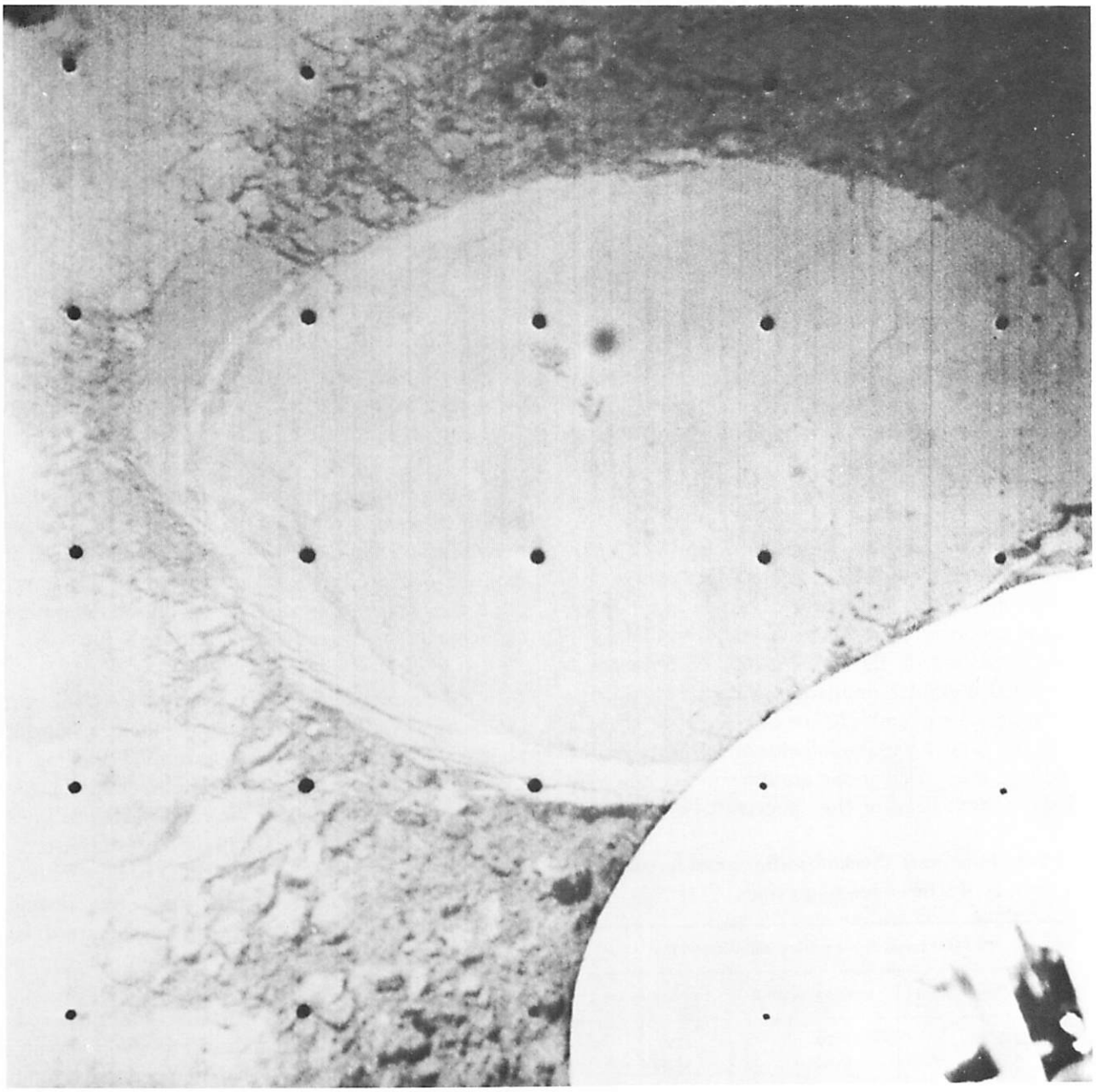

Fig. V-13. Narrow-angle view of the footpad 2 imprint, made during the third landing event (Day 116; 06:05:55 GMT)

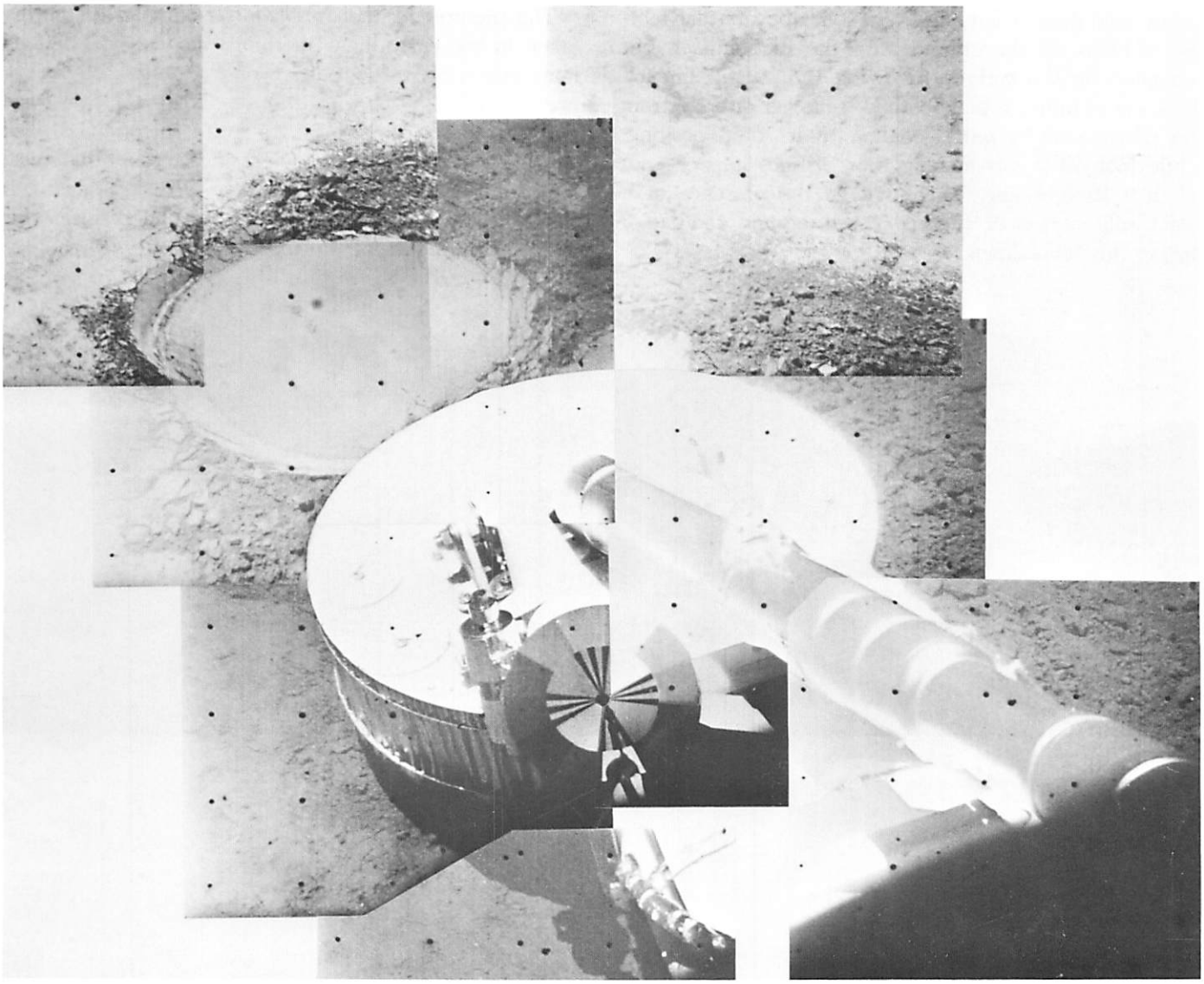

Fig. V-14. Narrow-angle mosaic of footpad 2 and imprints during third landing event (Day 116, 05:59:33 to 08:31:47)

edge of the footpad. The scalloped edges of the left side of the two first imprints are estimated to be 7 to 10 cm apart, but there is no distinction between these two imprints on the right side. The factors are evidence that leg 2 did not move along a straight line throughout the third landing event.

Figure V-15 shows that the ejected material displaced by footpad 2 during the third landing event has a darker appearance than the undisturbed material. This same characteristic was noted in the pictures obtained from *Surveyor I*; also, both the disturbed and undisturbed material have the same general appearance as that found near footpad 2 on *Surveyor I*. This disturbed soil consists of irregularly shaped clods of material, plus a spray of fine particles. The clods, however, appear to be more flat-sided than those in the *Surveyor I* pictures. The distribution of the ejected material extends for several feet and is believed to be the combined displacement from all of the impacts of footpad 2 during the third landing event.

A footpad imprint also appears near footpad 3, as shown in Fig. V-9, and in the narrow-angle mosaics in Figs. V-16 and V-17. The pattern of ejected material resulting from the impacts of footpad 3 is shown in Fig. V-18. The relative directional position of this imprint, with respect to the final position of footpad 3, is the same as that of the first imprint of footpad 2, with respect to the final position of footpad 2. From the leg 3

strain gage data of landing event 3, it appears that footpad 3 lifted off the ground after the first impact, but remained on the surface following the second impact. This would indicate that footpad 3 moved directly from the position of its initial contact to its final position, while footpad 2 was making four distinct impacts, not all in a straight line. This suggests the presence of a slight roll motion of the spacecraft around footpad 3 during this touchdown.

The pictures of the *Surveyor III* footpad 2 imprint, taken in the early lunar morning, show a well-defined honeycomb, or waffle, pattern on the bottom of the depression (Fig. V-8). This indicates that at least some particles in the lunar soil are quite fine-grained. The waffle pattern is an impression of the bottom of a typical footpad (Fig. V-5). The depressions between the ridges shown in Fig. V-5 were caused by small deformations of the bottom skin of the footpad, which was made of

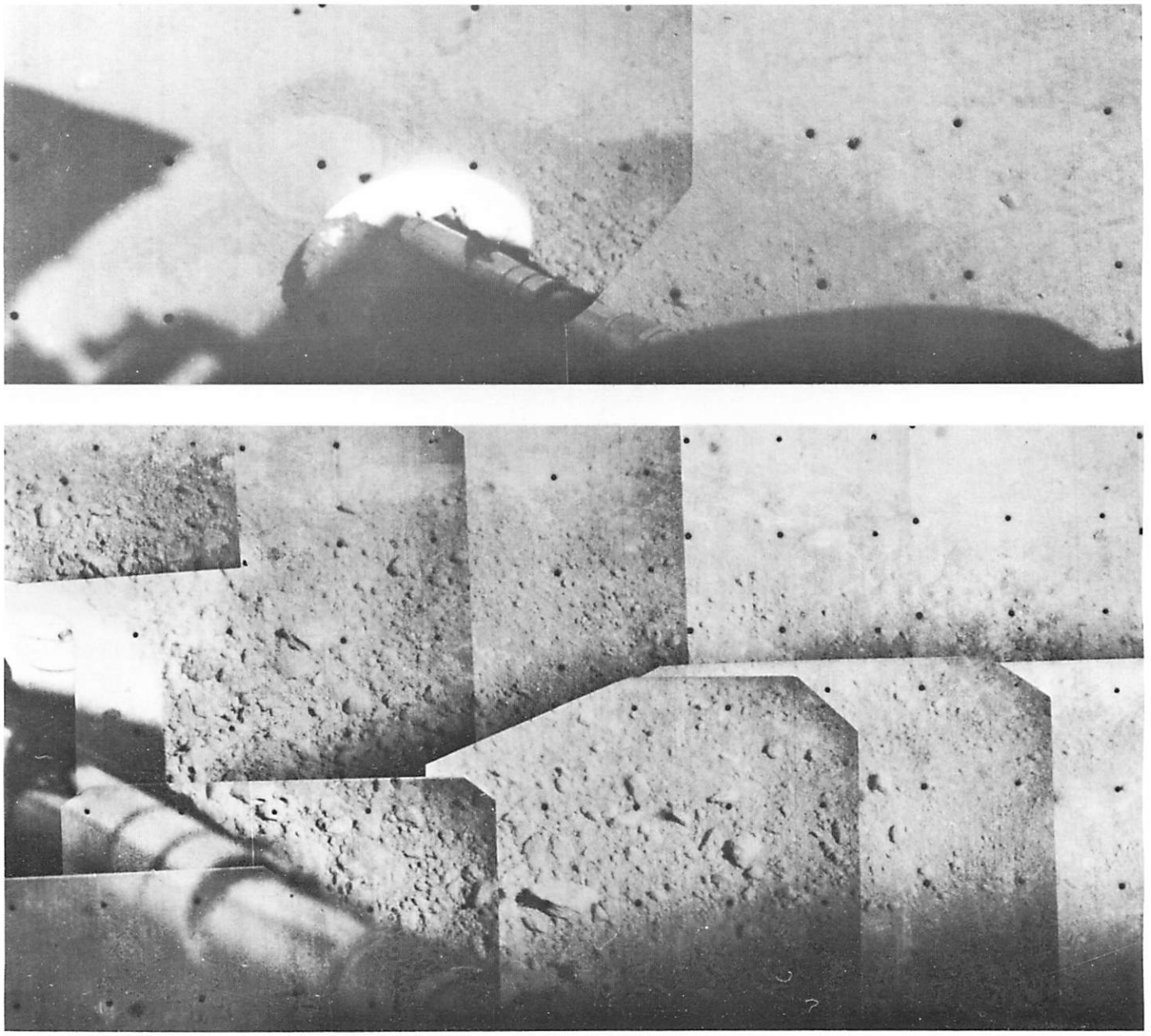

Fig. V-15. Mosaic of wide-angle (Catalog No. 3-MP-04, Day 120, 09:52:27 and 11:09:10 GMT) and narrow-angle (Catalog No. 3-MP-05, Day 120, 12:17:28 to 12:43:32) frames showing ejected material around footpad 2

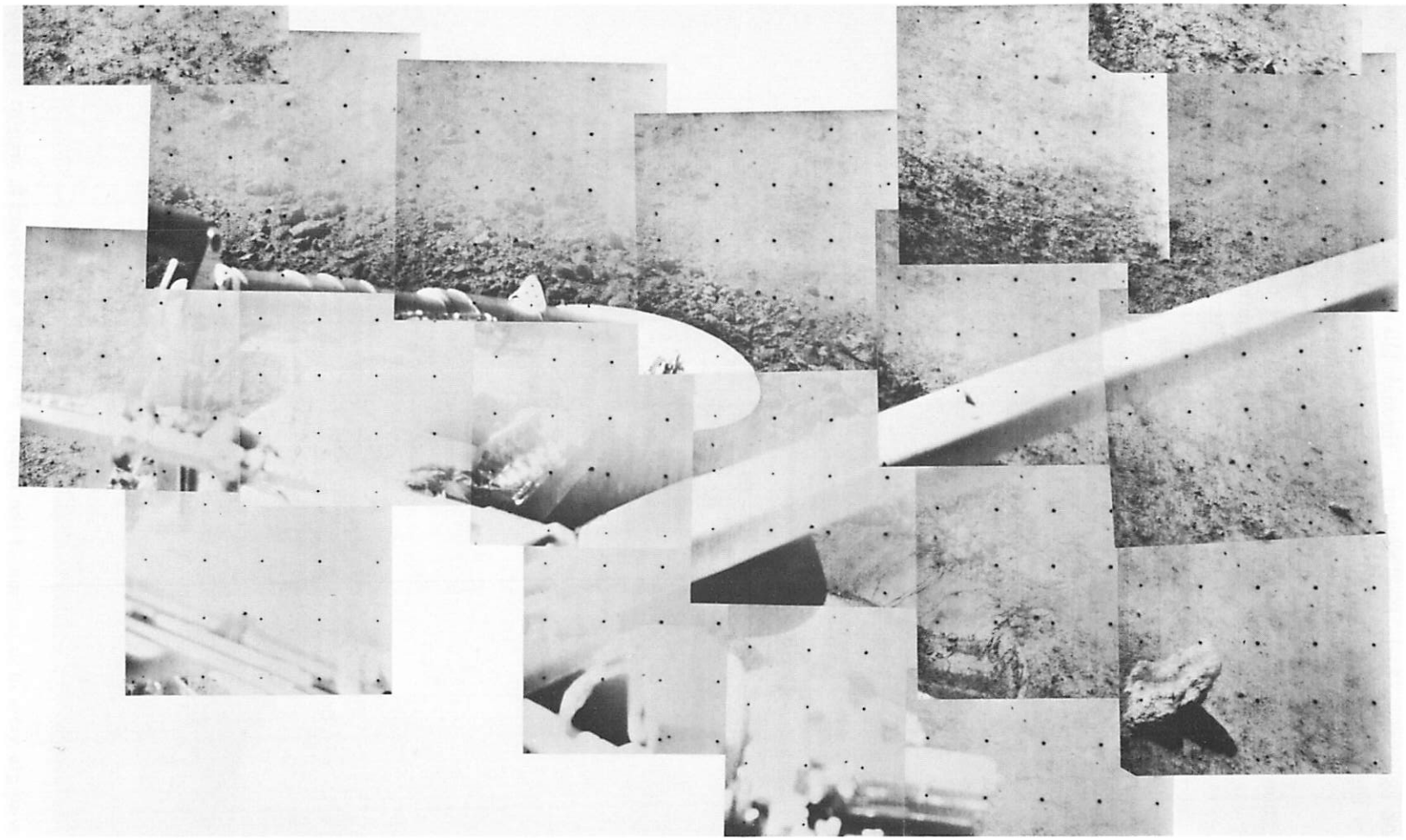

Fig. V-16. Narrow-angle mosaic of area around footpad 3 including the footpad imprint seen below antenna boom (Catalog No. 3-MP-06, Day 120, between 13:42 and 15:04 GMT)

0.025-mm-thick aluminum alloy sheet. The ridges are spaced about 1 cm apart, are 0.5 to 1 mm wide, and are estimated to be 0.04 to 0.8 mm high. (See Section V-B-3 for a discussion of the imprint simulation.)

The bottoms of the numerous imprints made by the footpads were brighter (as seen by the camera) than the surrounding surface, except when the phase angle was low (i.e., when the line from imprint to sun was near the line from imprint to camera). Under the latter condition, as observed in pictures taken on Days 117 through 119 for the footpad 2 imprint in landing event 3, and on Days 118 through 120 for all footpad imprints in landing event 2, there was little difference in brightness. The disturbed material outside the imprints was always darker than the undisturbed material. The walls of footpad imprints were intermediate in brightness between the imprint floors and the disturbed material outside the footpad imprints.

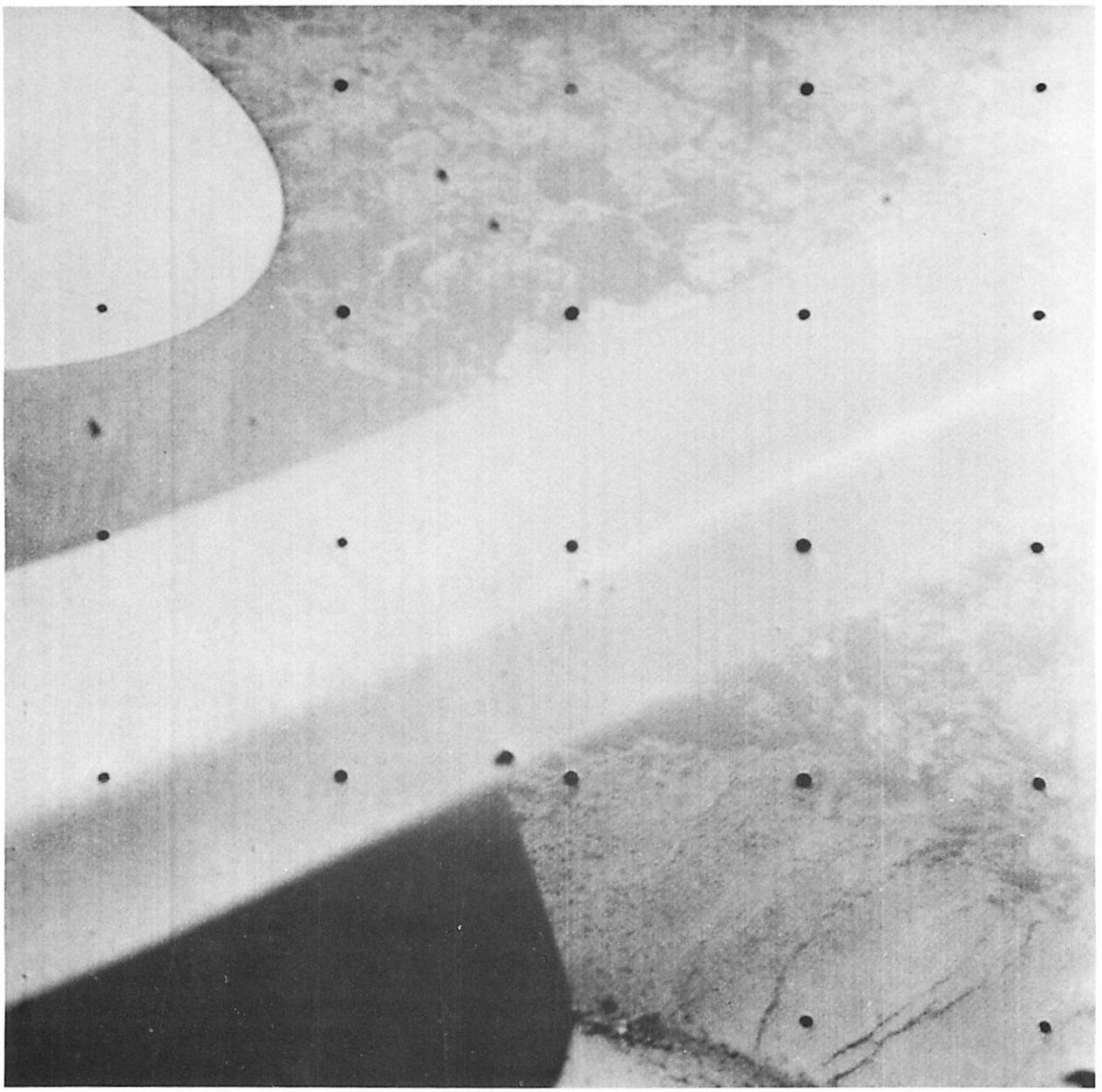

Fig. V-17. Narrow-angle view of a portion of the imprint attributed to footpad 3. Imprint is at lower right. This picture shows part of the area covered in wide angle by Fig. V-9 (Day 120, 14:56:04 GMT)

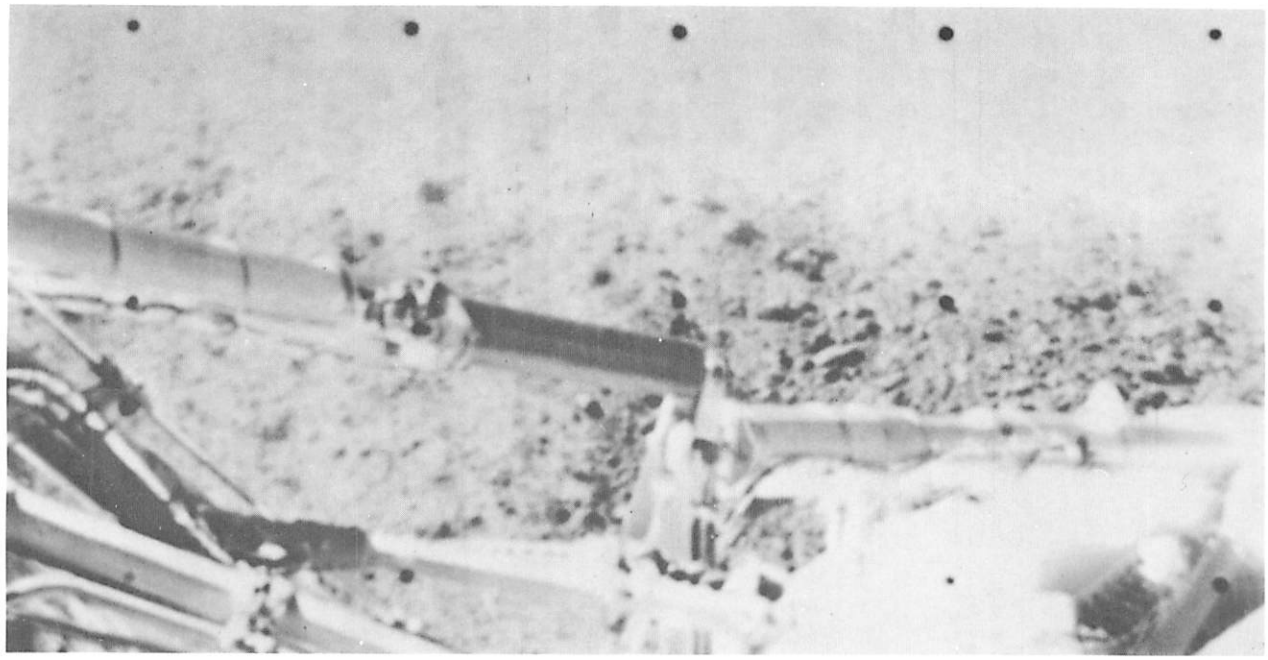

Fig. V-18. Wide-angle view of surface area looking over leg 3. The clumps and pattern of darker material indicate the extent of the ejecta around footpad 3, which can be seen at lower right (Day 121, 12:12:09 GMT)

There is no evidence that footpad 2 or 3 crushed during the landing sequence (Figs. V-8, V-9, and V-14). For the low-landing velocities, which were encountered during all three landing events, no crushing would be expected as long as the footpad loading was uniform, because the footpads are designed to crush at a loading greater than 6.9×10^5 dynes/cm^2. Analyses of footpad imprints are discussed in Sections V-B-4 and V-B-5.

3. Vernier Engine Effects

As indicated previously, the vernier engines were operating throughout the first and second landing events, and a lunar surface feature, possibly caused by vernier engine 3, was noted at the second landing site (item V in Fig. V-19). This is a shallow trench, elongated in the direction of the spacecraft motion during the second landing. The bottom of the trench is lighter or brighter in appearance than the surrounding material. This appearance could be analogous to that of the compressed or packed material in the bottom of the footpad imprints made during the third landing event. To the left, and slightly uphill from this feature, a somewhat darker area can be observed which resembles the typical darker ejected material seen around the spacecraft footpads. The trench and an uphill lighter area are estimated to be more than 1 m long.

Potential soil erosion marks under the spacecraft, created during the third landing event, have not been detected. Difficulty was experienced in searching for under-the-spacecraft lunar surface disturbances created during the third touchdown event by the television camera glare, limited camera operation, and high sun angles and associated spacecraft shadows when pictures were taken of those areas.

Some contamination or degradation of the spacecraft surface finishes occurred during the lunar landing. This is evidenced by the glare effect caused by a fogging of the television camera mirror, which was positioned facing footpad 3 during the landing; the particles of material observed on footpad 2 (Fig. V-20); and a fogging of the auxiliary mirrors (see Section V-A-4). Through comparison with pictures of a duplicate spacecraft on earth, suspected lunar material on the side of compartment A, near a vernier engine, proved to be a sunlight reflection from the specular finishes of nearby spacecraft components. There was no unusual number of particles on the *Surveyor III* thermally sensitive mirrors on top of compartments A and B.

Prior to the flight, it was anticipated that the firing of *Surveyor's* vernier engines as close to the lunar

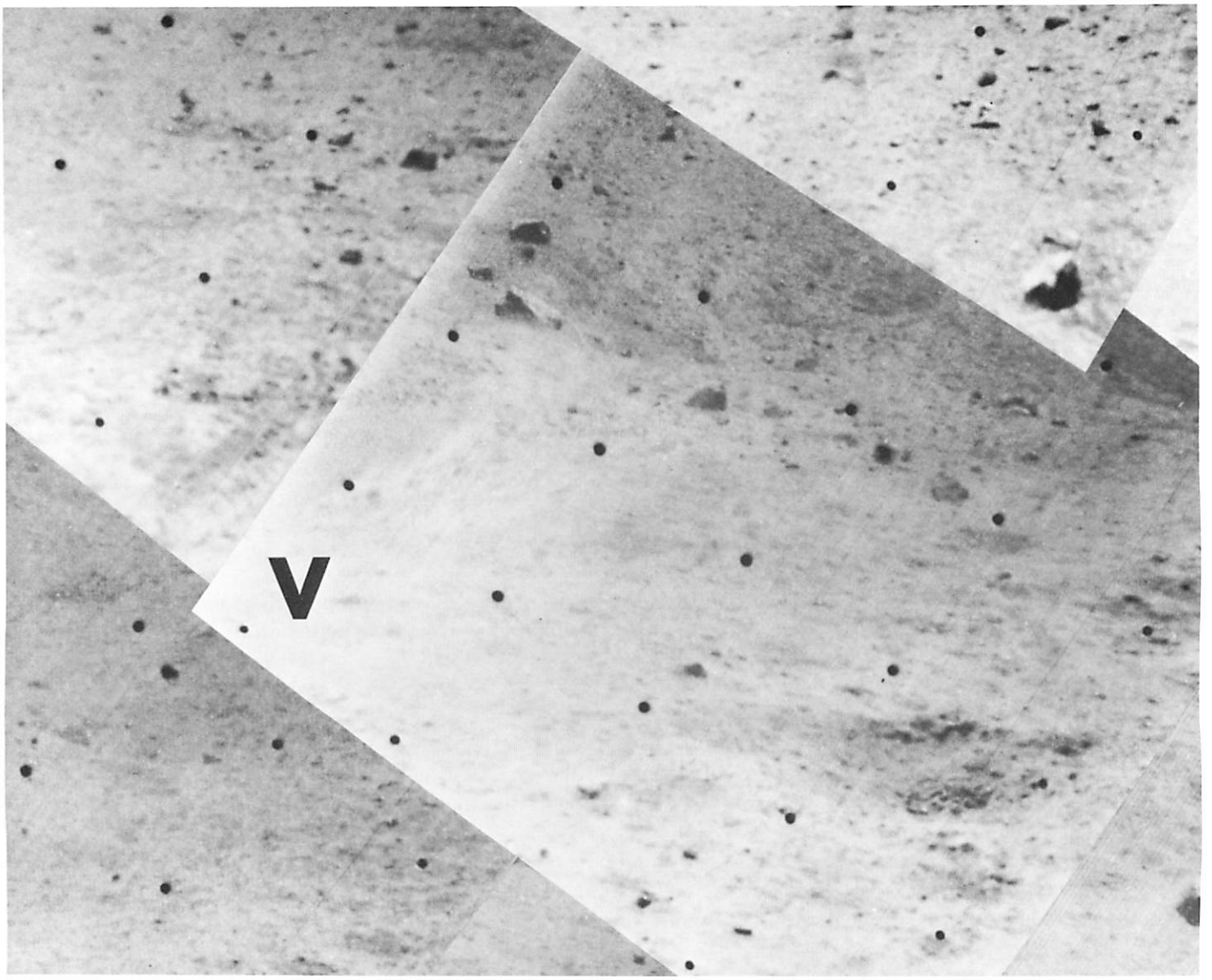

Fig. V-19. Narrow-angle mosaic of lunar surface that was eroded by vernier engine 3 during the second landing event. This is an enlargement of a portion of Fig. V-10 (Day 116, 08:37:36)

surface as occurred during the first and second touchdown events might deposit lunar material on the spacecraft and that the spacecraft operation could be jeopardized. The fact that *Surveyor III* survived suggests that the erosion hazard during a lunar landing of future spacecraft may not be as severe as had been anticipated.

4. Auxiliary Mirrors

Some of the lunar surface areas under the spacecraft that might have been disturbed by the crushable blocks, and/or by the operation of the vernier engines, cannot be seen directly by the television camera. To provide some visibility of these areas, two auxiliary mirrors were mounted inside the spaceframe on *Surveyor III* opposite to the camera mounting position. The large mirror provided a view of the bottom part of crushable block 3, the lunar surface area directly below block 3, and the surface area directly below vernier engine 3. The smaller mirror permitted a view of the surface area below vernier engine 2.

As part of the camera calibration and alignment testing performed at Cape Kennedy, Fla., before the launch of *Surveyor III*, both wide- and narrow-angle pictures of the mirrors were taken by the spacecraft camera.

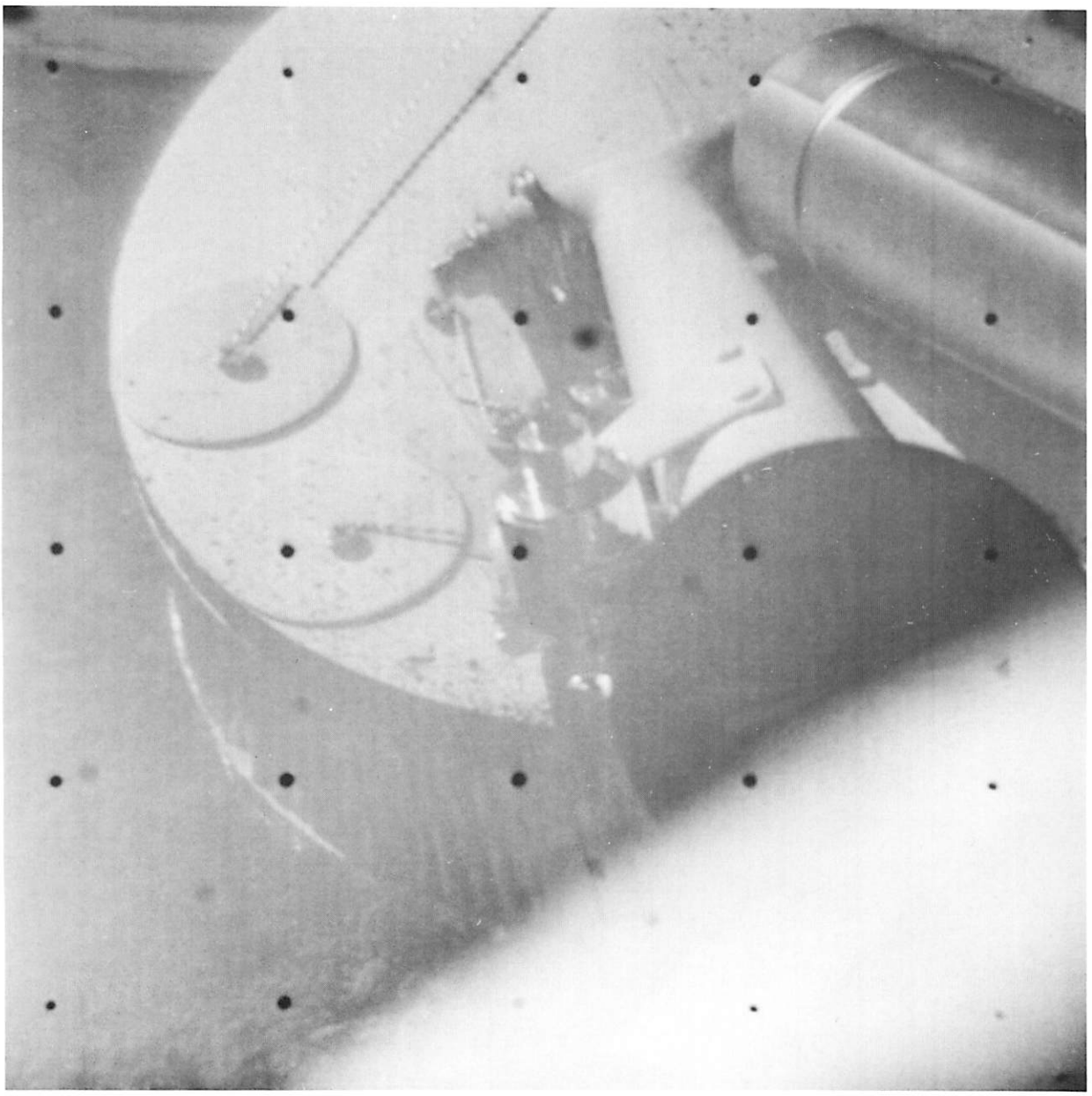

Fig. V-20. Narrow-angle view of footpad 2. Small particles of lunar material can be seen on the footpad top surface. The two disks and lockwires are part of the ballast weight assembly, attached to the footpad at Cape Kennedy before launch (Day 111, 07:39:59 GMT)

Figure V-21 is a wide-angle view of the mirrors on *Surveyor III*. The positions of the imprint areas and the scale on the surface are indicated by the bottom pattern of lines and circles. Figure V-22 is a wide-angle picture of the same area, taken by *Surveyor III* after landing on the moon; the glare problem present in many of the pictures is also noticeable. However, the various imprint areas can be located by comparing these two wide-angle pictures. A series of narrow-angle pictures was also taken to permit a more detailed study of the several potential imprint areas. Preliminary studies have not shown conclusive evidence of surface disturbance by the crushable

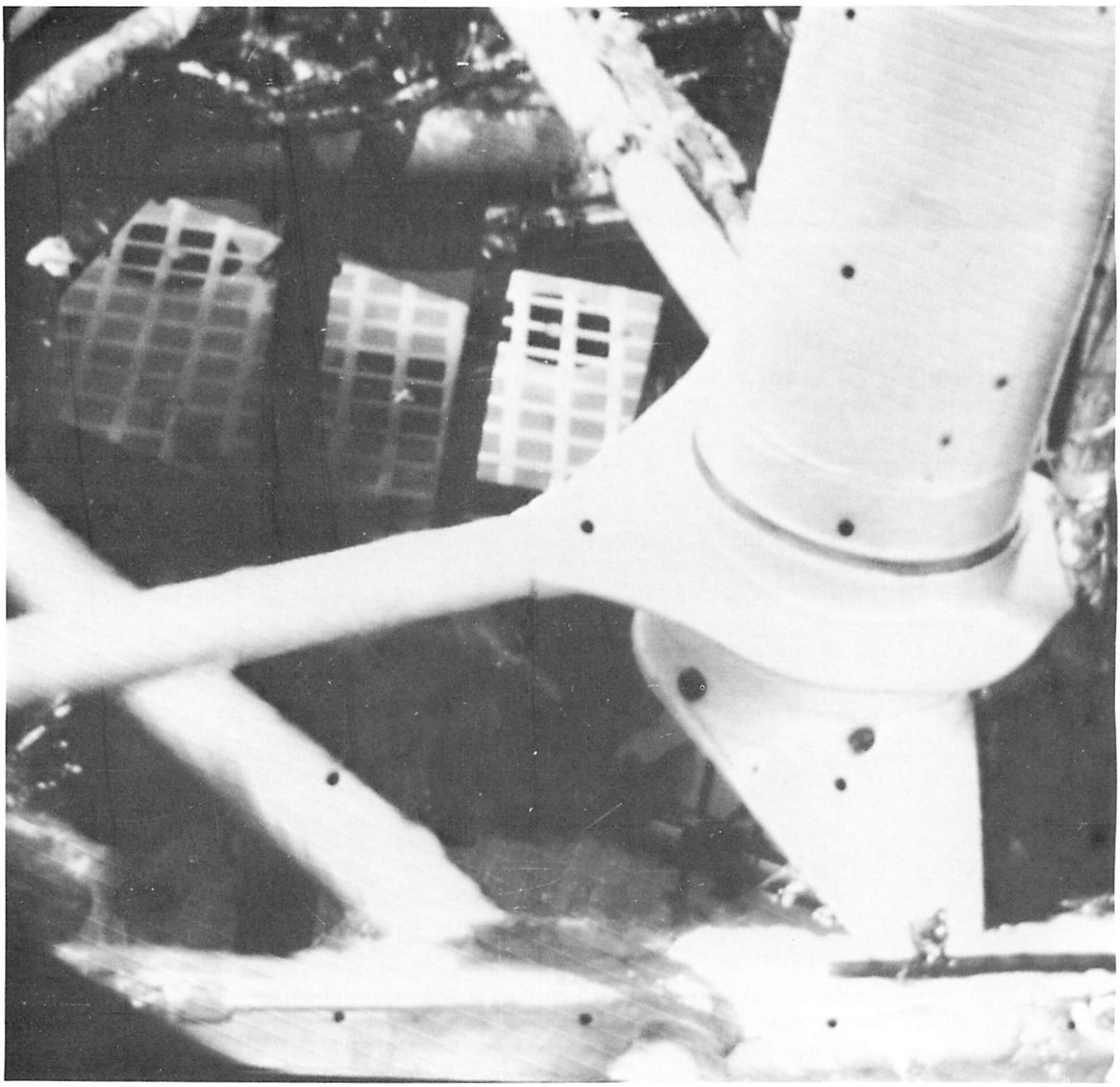

Fig. V-21. Wide-angle view of the two auxiliary mirrors mounted to the spaceframe of *Surveyor III*. The dark circles overlaid by grids indicate the surface areas directly below crushable block 3 and vernier engines 2 and 3. This picture was taken before launch using the spacecraft television camera

Fig. V-22. Wide-angle view of the auxiliary mirrors on *Surveyor III*. The shadowed areas under crushable block 3 and the vernier engines are visible in this frame (Day 117, 11:17:45 GMT)

blocks. However, there may be no block imprints under the spacecraft because the crushable blocks normally would not contact a flat, hard landing surface that is level during a landing at the estimated third event touchdown velocity of approximately 1.2 m/s.

5. Attitude Control Jet Experiment

Prior to launch, it was planned that an attitude control jet would be operated after the spacecraft was on the moon in an attempt to determine lunar soil erosion characteristics. This experiment was conducted with *Surveyor I* (Ref. V-2). The experiment requires good pictures (possibly at low sun angles) of the lunar surface area beneath the jet prior to and after operation of the jet, because the soil disturbance might be small. It was almost lunar noon before clear pictures (but with small contrast) were obtained of the potential impingement area under the *Surveyor III* attitude control jet on leg 2. At that time, the probability of detecting a jet-created soil disturbance was small because of the lack of surface shadows. Within 48 h, the shadow of leg 2 would cover the area for the remainder of the lunar day. Because of these reasons and the undesirability of firing the jets when the flight control electronics were overly hot, the jets were not fired during the first lunar day.

B. Analyses and Simulations

1. Simulated Landing Studies

Computer landing simulation studies are being conducted with the objective of estimating the mechanical properties of a surface material that would give surface penetrations and shock absorber axial loads similar to those obtained during the *Surveyor III* landings. Preliminary computer simulations have been made of all landing events, and reasonable comparisons between analysis and flight data have been achieved. Representative analytical shock absorber force/time histories for landings on a rigid surface are compared with *Surveyor III* flight data in Fig. V-12. To date, the best simulation correlations have been achieved using the following landing velocities:

Landing event	Landing velocities, m/s	
	Vertical	Horizontal
1	1.8	0.3
2	1.5	0.6
3	1.2	0.9

The 0.9-m/s horizontal velocity for landing event 3 is consistent with the estimate of 11-m distance between the second and third landing sites. The 0.6-m/s horizontal velocity for landing event 2 indicates that the distance between first and second landing sites is approximately 15 m.

From computer simulations, the maximum normal force exerted against the lunar surface by a spacecraft footpad has been determined to have been approximately 1450 N (footpad 3 during landing event 3). Based on a measured surface penetration of approximately 2.5 cm, this force would correspond to a pressure level of approximately 2.8×10^5 dynes/cm^2.

The landing simulation program also was used to establish the relative angle between the spacecraft XY plane (horizontal plane with respect to the spacecraft on a level surface) and the ground (plane established by the three footpad/ground contact points) for all three landings. The roll orientation of the spacecraft was determined with respect to the uphill direction of the ground slope. The spacecraft was nominally close to level at times of initial impact during each of the landing events, and the attitude control system retained this attitude throughout the landing sequence, except for transients during the actual touchdowns. Thus, these angles constitute approximations to the lunar surface slopes at the three landing sites. The numerical values obtained are:

Landing event	Surface slope, deg	Angle between leg 2 and uphill direction, deg
1	11.5	−3.0
2	14.0	+3.0
3	9.2	−7.8

With respect to the uphill direction, the angle is defined positive if leg 2 deviates in a clockwise direction, looking down at the spacecraft.

Landing simulations have indicated that the landing legs did not stroke sufficiently for the crushable blocks to make contact with a planar landing surface in all three landing events. It can, therefore, be assumed that the crushable blocks never touched the lunar surface, unless a local surface protuberance were encountered.

Most landing simulations performed so far assume a rigid surface, i.e., static bearing strength larger than 6.9×10^5 dynes/cm^2. It has been established that simulations are relatively insensitive to surface hardness. Therefore, to reduce the number of variables involved, it is preferable to consider hard surfaces for early simulations. Various bearing strength values and profiles, as well as various effective friction coefficients, will be investigated until an optimum match with the flight data is achieved, with respect to axial shock force histories and footpad penetrations. However, an evaluation of these data, thus far, indicates that the conclusions regarding mechanical properties of the lunar surface material probably will be similar to the conclusions obtained from the *Surveyor I* touchdown data (Refs. V-3 through V-6).

The time histories of thrust levels and surface proximities of the vernier engines for landing event 2, corresponding to the simulation shown in Fig. V-12, are shown in Fig. V-23. (Implications of the data are discussed in Section V-B-8.)

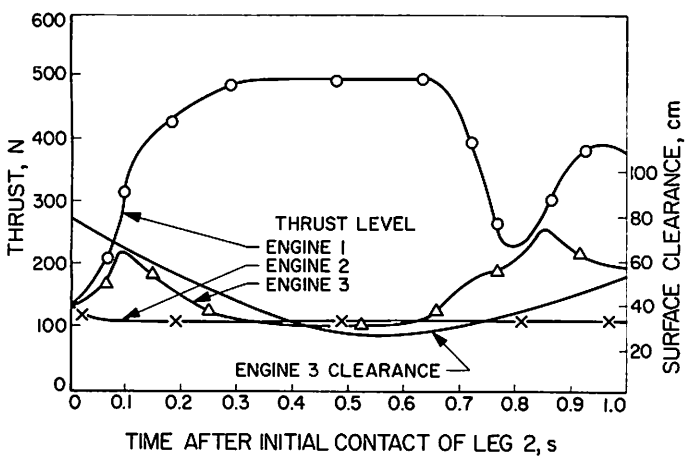

Fig. V-23. Time histories, from analytical simulations, of vernier engine thrusts and surface proximity of vernier engine 3 during landing event 2. Conditions for the simulated landing are as listed for Fig. V-12(b)

2. Second Landing Site

The narrow-angle mosaic (Fig. V-10) shows footpad imprints made during one of the landings. The following analysis indicates that they were made by the spacecraft during the second landing. Figure V-24 shows the disturbed area mosaic with the addition of an overlay sketch that indicates a probable position of the footpads and vernier engine 3 during the second landing event. The angle values for the television camera elevation and azimuth angles appearing in the mosaic were derived from the telemetered television camera angular information. The camera view angles between the several surface features were measured directly from the picture. The sketch presented in Fig. V-25 was constructed by using the angle information obtained from the mosaic. The lower spacecraft image represents the final position of *Surveyor III* after the third landing event. Lines were drawn, radiating from the television camera position, at the angles determined from the overlay of Fig. V-24. A second spacecraft image, positioned so that each footpad rested on its respective view line, represents the relative position of *Surveyor III* during the second landing. The strain gage record of this landing indicated that footpad 2 was not in contact with the surface at the instant that imprints of footpads 1 and 3 were being made. Therefore, in this sketch, footpad 2 can be assumed to be free of the surface and is shown in line with, but between, its two imprints.

Using the same linear scaling as for the spacecraft sketches, the separation between these spacecraft positions is 10.7 m. This distance is consistent with the average horizontal velocity of 0.9 m/s between landing events 2 and 3 previously stated.

The distance between points 2 and 2′ (Fig. V-26) also seems to verify the assumption that these imprints were made during the second landing event. This distance is estimated to be 0.6 to 1.0 m. During the first landing event, the time between the two contacts of footpad 2 was approximately 0.15 s. To travel 0.6 m, a horizontal velocity of about 4 m/s would have been necessary during landing event 1 and it is unlikely that the horizontal velocity was this high. The time between the two contacts of footpad 2 during the second landing event, however, was 0.7 s; the resulting horizontal velocity for this time period would have been between 0.9 and 1.2 m/s, which correlates with values given previously.

The angular position of the vernier engines, and crushable blocks relative to the footpad, can be determined from the sketches in Fig. V-25. Transposing these angles back to the overlay in Fig. V-24, it is possible to make a close approximation of the surface area that would be below the vernier engines and crushable blocks during this touchdown event. Vernier engine 3 and crushable block 3 were found to be over the disturbed area V shown in the mosaic. This area can be seen more clearly in Fig. V-19.

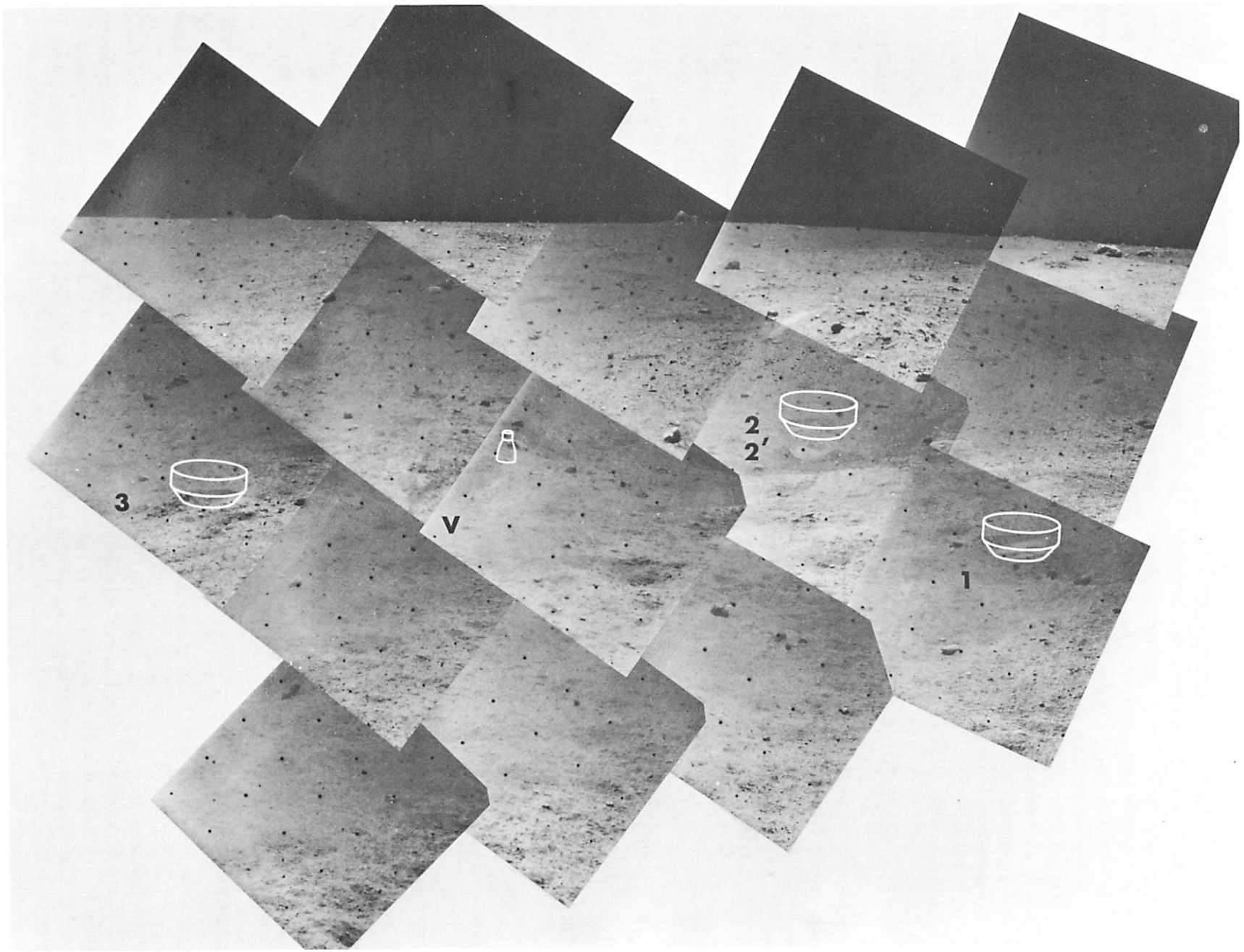

Fig. V-24. The outlines of the *Surveyor* footpads indicate the probable position of the spacecraft during the second landing event. The camera angles were based on picture information from the landing site mosaic (Fig. V-10)

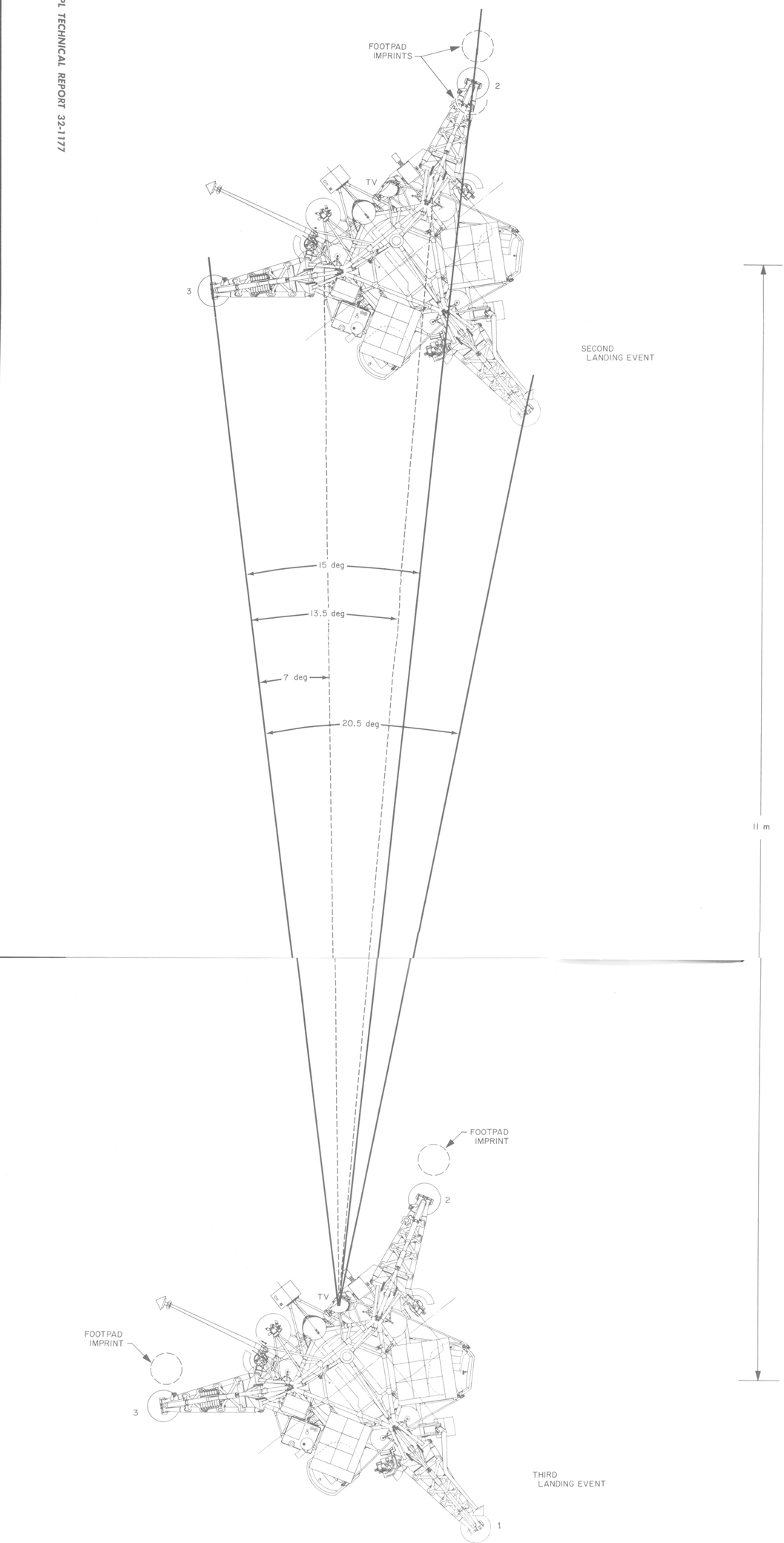

Fig. V-25. Relative positions of the second and third landing sites. The viewing angles of features in the second landing site were based on the mosaic as shown in Fig. V-24

(Blank Page)

Fig. V-26. Narrow-angle picture of landing event 2 imprints of footpads 1 and 2. This figure is an enlargement of portion of Fig. V-10 (Day 116, 08:37:36 GMT)

The small force observed in the leg 1 shock absorber during the second landing event can be explained by the fact that the inner edge of the footpad hit on the inner slope of a small crater (Fig. V-10), which resulted in a smaller horizontal constraint than for a flat surface. Note that the imprint (item I in Fig. V-26) is flat with no ridge on the edge away from the spacecraft centerline.

3. Footpad Imprint Simulations

Preliminary measurements of the depth, attitude, and position of the landing imprints of footpads 2 and 3 during landing event 3 have been performed with the aid of a full-scale *Surveyor* model. This spacecraft model, located at the Jet Propulsion Laboratory's *Surveyor* Experiment Test Laboratory (SETL), was operated in conjunction with a collimated light source simulating the sun. Television pictures that reasonably duplicate the shadow patterns and footpad imprints seen in *Surveyor III* pictures have been made by use of this equipment. Figures V-27 through V-29 are pictures of footpad 2 imprints simulated in three soils with different ranges of particle size. The simulated imprints of footpad 2 best duplicate *Surveyor III* pictures at a location 35 cm out from the present position of footpad 2, along the centerline of leg 2; and 2 to 3 cm perpendicular to the leg 2 centerline (toward footpad 3). Because small variations in imprint locations ($\pm$0.5 cm) can be observed in the television pictures, the above dimensions are considered accurate within $\pm$3 cm.

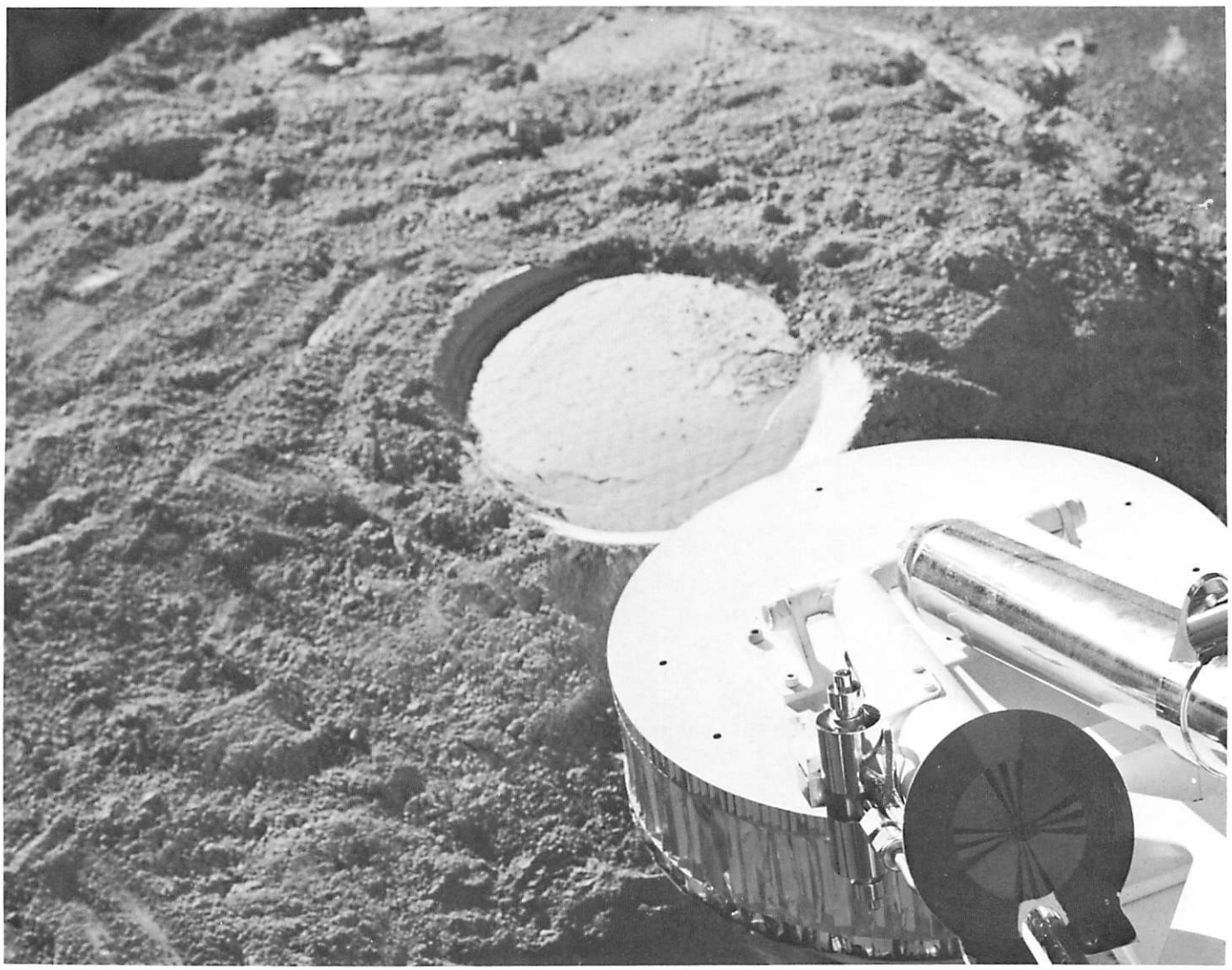

Fig. V-27. Laboratory simulation of footpad and imprint, made on earth with full-scale model of *Surveyor*. Surface material: finely crushed basalt, particle size in clay range. Lighting angle similar to that in Fig. V-8

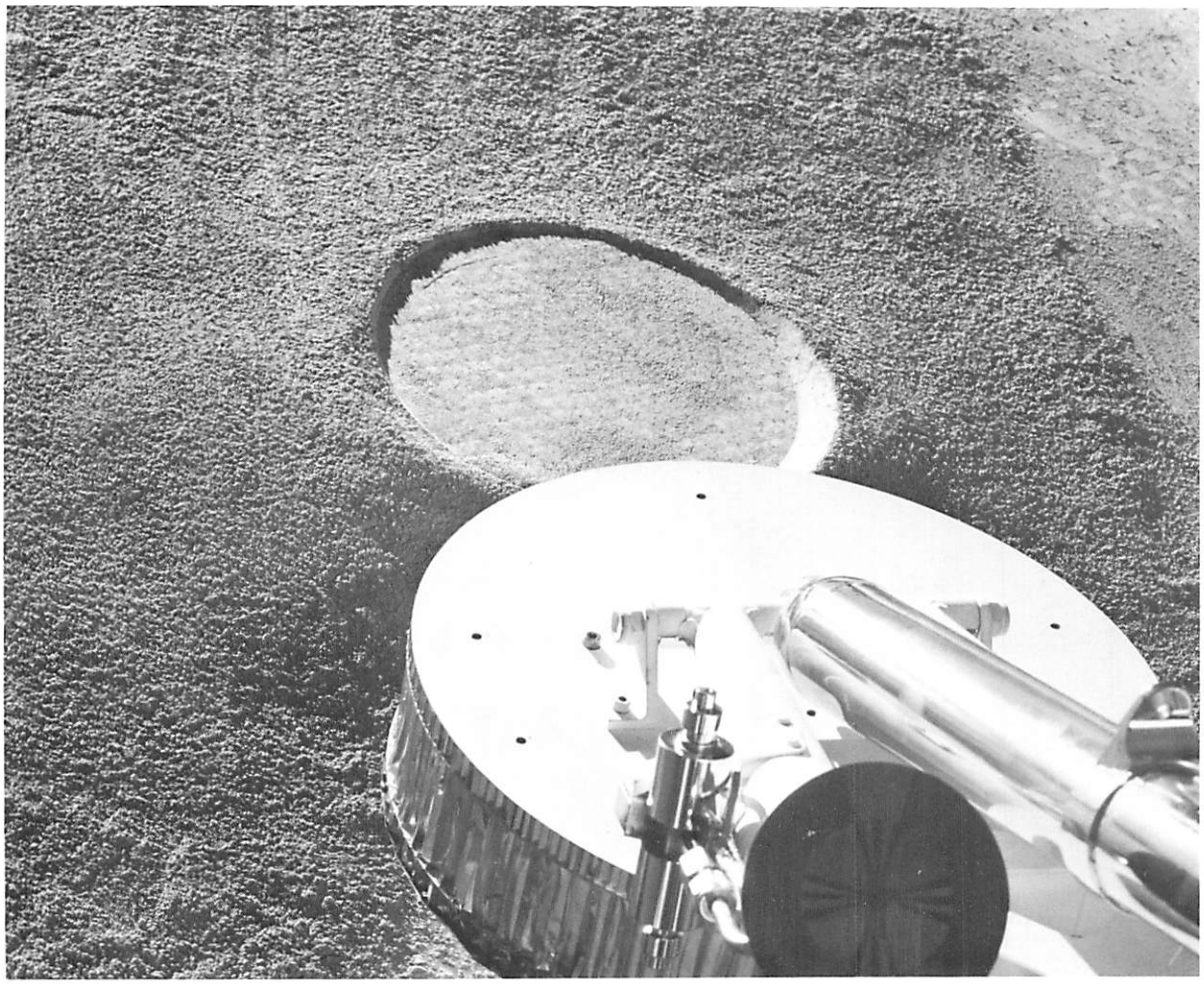

Fig. V-28. Laboratory simulation of footpad and imprint, made on earth with full-scale model of *Surveyor*. Surface material: crushed basalt, 50% fine particles (in clay range) and 50% coarse (in sand range). Lighting angle similar to that in Fig. V-8

Simulated imprints of footpad 2 in Figs. V-27 through V-29 are made with crushed basalt. Soil particle size ranges in the soil models are: Fig. V-27, clay-size particles; Fig. V-28, a mixture of 50% clay-size particles and 50% sand-size particles; and Fig. V-29, sand-size particles.[3] The 14-deg illumination angle in Figs. V-27 through V-29 duplicates the lunar morning sun/*Surveyor III* landing site conditions at 08:00 on Day 110. All three simulations reproduce the honeycomb texture of the bottom of the footpad as seen in Fig. V-8; however, at a 14-deg light source elevation angle, this pattern shows up clearly only in the pictures of the clay-size and sand/clay-size models. Of these two models at that sun angle, the mixed-particle-size soil best reproduces the light-reflecting characteristics seen in *Surveyor III* pictures. In these pictures, the observed brightness of the bottom surface of the footpad imprint is greater than that of the undisturbed lunar surface at this lighting angle. In the simulated models (Figs. V-27 and V-28), the observed brightness of the imprint in the sand/clay mixture is slightly greater than that of the undisturbed surface, whereas the brightness of the imprint in the clay-size soil is much greater than that of the undisturbed surface at the same lighting angle. It is recognized that other phenomena besides grain-size variation may explain the described brightness effects on the moon.

The imprint of footpad 3 from landing event 3 is shown in Fig. V-9. Television pictures of simulated footpad imprints indicate that the centerpoints of the present location of footpads 2 and 3 are 30 to 40 cm from the

[3]In the MIT system of grain-size classification, clay-size particles are <0.002 mm; silt-size particles have diameters >0.002 and <0.06 mm; and sand-size particles have diameters >0.06 and <2.0 mm.

Fig. V-29. Laboratory simulation of footpad and imprint, made on earth with full-scale model of *Surveyor*. Surface material: crushed basalt, particle size in sand range only. Lighting angle similar to that of Fig. V-8

first imprints of landing event 3 and in the same direction. Lines connecting the centers of the initial impacts and those of the final positions of footpads 2 and 3 point along an azimuth of 280 deg from north. This azimuth should represent the general direction of spacecraft movement during landing event 3. If so, then landing event 2, and possibly landing event 1, should have occurred along an azimuth of 100 deg from the present position of *Surveyor III*. This value compares well with the estimated direction of due east obtained from the pictures of the second landing event.

Depths of footpad 2 and 3 penetrations during landing event 3 have been obtained from measurements of the model imprints at SETL that best duplicate *Surveyor III* pictures, as well as from measurements on *Surveyor III* pictures. The most accurate measurement of penetration could be made for footpad 2 because of better picture quality and photographic coverage of the imprint area. Model imprint simulations indicate that the depth of penetration across each imprint was not uniform. This may be partially due to the fact that the footpads can rotate during the landing about a horizontal axis perpendicular to the spacecraft leg. Pictures indicate that the at-rest orientation of the footpads, relative to the spacecraft XY plane, are:

(1) Footpad 2: outer edge tilted downward 12 $\pm$2 deg.

(2) Footpad 3: outer edge tilted downward 10 $\pm$2 deg.

From simulation studies, a preliminary estimate of the average depth of penetration of footpad 2 in making the dual imprint is from 1 to 3 cm; the imprint for footpad 3 is approximately 3 to 5 cm deep.

4. Analysis of Footpad Imprint Pictures

Analysis of pictures of footpad imprints has included a study of the spacecraft shadows on the lunar surface. Using the size and location of spacecraft features and the direction of the sun, calculations can be made as to the footpad penetrations and the topography of the disturbed material around the footpads. Preliminary results indicated that the average footpad penetration for footpads 2 and 3 in their final resting positions is less than 2.5 cm. From this analysis, both footpads appear to be tilted, outward edge down, to an angle of 8 to 12 deg.

The imprint produced by the first two impacts of footpad 2 during landing event 3 has an estimated average depth of 2.5 cm. The deeper imprint caused by footpad 3 is surrounded by some of the ejected material that forms a sloping wall several centimeters high. The depth below the original level is estimated to be about 5 cm. The extent of the area over which the material was ejected indicates that much of the material was removed from the impact hole. The relative height of footpad 3 in its final position indicates that possibly it is resting on a patch of the ejected material. Some clumps of soil beyond the footpad form a ridge a few centimeters lower than the top of the footpad.

Figure V-26 shows a narrow-angle view of the imprint formed by footpad 1 during landing event 2. The depth of penetration at the left edge is 4 cm; the angle of the left imprint edge to the horizontal is about 60 deg.

5. Reflective Properties of Lunar Soil

The bottom of the footpad imprints was brighter than the nearby undisturbed surface, except at small phase angles. It appears that the photometric characteristics of the imprint bottoms are more Lambertian than those of the undisturbed material. No such strong difference in photometric function was obvious for disturbed material outside the footpad imprints. The fine structure, which gives the undisturbed lunar surface strong backscattering characteristics, was apparently substantially destroyed, possibly by the macroscopic compressional deformation under the footpads. On the other hand, the macroscopic deformation of the exposed surfaces of material ejected by the footpads was not caused by simple compression. This apparently left these surfaces with a different fine structure than for the imprints.

6. Estimations of Soil Parameters

Because of the horizontal velocity and surface slope associated with the landing of *Surveyor III*, the vertical loads on the surface during landing are more difficult to estimate than for *Surveyor I*, which landed nearly vertically on a near-horizontal surface. However, it is certain that the vertical dynamic loads developed during landing event 3 were lower than those for *Surveyor I*. Preliminary estimates of the vertical landing loads (when compared with estimated footpad penetrations) indicate that, at least as far as dynamic penetration of the material is concerned, the soils at the two *Surveyor* landing sites are similar.

The imprint in front of footpad 2 (Figs. V-13 and V-8) is estimated to be 2.5 cm deep. If the material were completely frictionless, then the cohesion required to support the 45-deg slope edge of the imprint would be at least 30 dynes/cm^2. If the material were cohesionless, its angle of internal friction would be at least 45 deg. The left rim of the impression attributed to footpad 1 during landing event 2 (Fig. V-26) is estimated to have a slope of about 60 deg to the horizontal with a height of about 4 cm. If the material were frictionless, the cohesion would be at least 100 dynes/cm^2 to support this slope under lunar gravity; if the material were cohesionless, then its angle of internal friction would be at least 60 deg.

An upper bound for the cohesion can be obtained from the bearing strength. For a frictionless material, the contribution of cohesion to bearing strength is approximately six times the cohesion if soil failure is by general shear, and four times the cohesion if failure is by local shear. Thus, with a maximum dynamic bearing capacity of 3×10^5 dynes/cm^2, as estimated from preliminary landing simulations, the cohesion cannot exceed 5×10^4 dynes/cm^2 if failure is by general shear, or 7×10^4 dynes/cm^2 if failure is by local shear.

Some information concerning the density and the mode of failure of the top layer of the surface material can be obtained by examining the magnitude of the inertial contribution to the bearing capacity. Considering landing event 3, footpad 2 (with a vertical velocity at impact of 150 cm/s and a penetration of 2.5 cm), the penetration time with no deceleration would be 17 ms. With uniform deceleration, the penetration time would be 33 ms. The observed time to peak load for this and other impacts was about 80 ms. Landing dynamic analyses indicate that the peak load usually is reached essentially at full penetration, i.e., near zero velocity. During

the initial stages of penetration, up to 0.5 cm or so, the resistance of the soil was small (not over 7×10^4 dynes/cm^2), as compared to the peak bearing pressure of 3×10^5 dynes/cm^2.

For general shear failure during low-velocity penetration of a soil by a circular plate, Scott (Ref. V-6) gives the resistance resulting from soil inertia

$$p_i = 1.2\,\rho(\dot{h}^2 + h\ddot{h}) + 2.1\,\rho b\ddot{h} \qquad (1)$$

where ρ is the density of undisturbed soil, h is the depth of penetration, and b is the radius of the plate. Assuming uniform deceleration, $\ddot{h}$ would be 3.5×10^3 cm/sec^2. Then at initial contact, with $h = 0$ and $b = 10$ cm, p_i must be at least $1.2 \times 10^5\ \rho$. Because the total pressure at this time is less than 7×10^4 dynes/cm^2, either $\rho < 0.6$ g/cm^3 or soil deformation at this state is not caused by general shear (or both). On the basis of experience with earth soils, general shear would not be expected at $\rho < 0.6$ g/cm^3. Thus, during the initial stages of soil movements, local shear should have occurred.

For local shear, Scott (Ref. V-6) and Chandaysson[4] give

$$p_i = \frac{\rho_2\rho}{\rho_2 - \rho}(\dot{h}^2 + h\ddot{h}) \qquad (2)$$

where ρ_2 is the soil density after local shear. During the initial stages, with an assumed initial velocity of 150 cm/s, then $p_i < 7 \times 10^4$ dynes/cm^2, $h = 0$, and $\dot{h}^2 = 2.25 \times 10^4$ cm^2/s^2, so

$$\frac{\rho_2\rho}{\rho_2 - \rho} < \frac{7 \times 10^4}{2.25 \times 10^4} = 3.1\ \text{g/cm}^3 \qquad (3)$$

If it is assumed that the density of the compressed soil after failure is 2 g/cm^3, the density of the undisturbed material at the surface is 1.2 g/cm^3 or less. Or, if it is assumed that the density of the compressed soil after failure is 1.7 g/cm^3, the density of the undisturbed material at the surface is 1.1 g/cm^3 or less. This analysis applies only to the top 0.5 cm of the lunar surface material, and is sensitive to the assumed initial velocity. Lower limits were estimated earlier for the *Surveyor I* site (Ref. V-7).

[4]Unpublished work, 1966.

Particle size of most of the lunar soil beneath and close to the spacecraft is less than the resolution of the television camera (approximately 1.0 mm at footpad distance). For rock particles larger than 1.0 mm seen throughout the entire field of view of the television camera, particles appear to be relatively well-graded (poorly sorted); that is, the particles have a continuous size gradation from the 1.0-mm minimum resolution up to the maximum size present. Because there is no reason to suspect that grain-size distribution has a discontinuity at the 1.0-mm resolution of the camera, it can be predicted that grain-size distribution extends smoothly into the sand-size range well below 1.0-mm. Also, it can be predicted from comminution studies that some significant fraction of the soil (probably $> 10\%$, at the least) should lie within the silt-size range (Ref. V-8).

As with *Surveyor I*, the appearance of the disturbed lunar material in the vicinity of the footpads is suggestive of material similar in mechanical properties to a moist terrestrial soil containing a fair amount ($> 10\%$) of fine silt or clay-size particles (less than about 10 μm).

7. Elastic Properties of Lunar Soil

Oscillations on the strain gage records following the final impact were observed on *Surveyors I* and *III*. In both cases, the observed frequency was near 6.5 Hz. An approximate analysis of the effective spring constant for the unstroked *Surveyor* landing legs indicates that the spacecraft oscillates at a frequency of 8.0 Hz (with an uncertainty of about ± 0.8 Hz) in a vertical translational mode when supported by its landing legs on a rigid surface. The fact that the frequency observed on the moon is lower indicates that the elastic properties of the lunar surface material are affecting the oscillations. Assuming that the equivalent springs of the spacecraft and of the lunar surface are acting in series and using 8 Hz and the observed 6.5 Hz, the effective spring constant of the lunar surface material averaged over a depth of the order of the footpad diameter is $K \approx 4.9 \times 10^8$ dynes/cm. From Timoshenko and Goodier (Ref. V-9), the effective stiffness K for an isotropic medium uniformly loaded over a circular area is

$$K = \pi^2 Er/4(1 - \nu^2)$$

where E is Young's modulus, r is the radius of the loaded area (12.7 cm), and ν = Poisson's ratio. From the preceding equation and relations among elastic constants

$$4K/\pi^2 r = E/(1 - \nu^2) = 2\mu/(1 - \nu)$$

where μ is the rigidity modulus. Using the value obtained for K and taking various values for ν, a range of values for μ can be determined. Further taking a range of values for the bulk density ρ of the lunar surface material, a range of values for the shear wave velocity, V_s, and the compressional wave velocity, V_p, can be obtained. Table V-2 is a summary of results of these calculations. It should be noted that the uncertainty in the spacecraft resonant frequency produces uncertainties of the rigidity moduli and of the velocities of about a factor of 2 and 1.4, respectively.

From Table V-2, it may be seen that this type of observation provides a narrow range of rigidity modulus and, for a given density, a narrow range of shear wave velocities and a lower bound for the compressional wave velocity. The shear wave velocities are about one order of magnitude lower than those obtained on earth in loose sand; they are near the values found for fine ocean bottom sediments near the water/sediment interface. It is planned to obtain more precise estimates of the resonant frequencies of the spacecraft and to obtain more reliable estimates of the possible ranges of average shear and compressional wave velocities of the upper 20 cm or so of the lunar surface material. The above estimates are for a lunar surface loaded by the approximate 3.4×10^4-dyne/cm^2 static pressure exerted by the *Surveyor* footpads.

8. Camera Mirror Contamination vs Vernier Erosion

If the camera mirror contamination were caused by lunar material kicked up by the vernier exhaust gases, the material probably came from the general area under the crushable block and the vernier engine located near leg 3. To demonstrate the possibility that this could have occurred during the second landing event, the following experiment was performed. In the SETL, simulation tests were conducted in which a light source was moved around on the ground (assuming *zero* footpad penetrations) to determine the positions required for its light to shine on the camera mirror positioned as it was during the landing. Figure V-30 shows some of these positions, together with the lighting pattern on the mirror at each position (A or B) of the light source. Thus, the vicinity of A or B possibly could have been original positions of lunar soil particles that could have hit the mirror, assuming that they traveled in a straight line and that the spacecraft was not moving. The first assumption probably is not far from being realistic, because of the reduced gravity on the moon as well as the high velocity that the vernier exhaust gases might have imparted on these particles. Particles originating from other surface locations within the region around A and B (Fig. V-30) could have produced similar results.

Two important parameters in the study of soil erosion created by exhaust gas impingement are the engine thrust levels and the height of the nozzle above the soil. Computer simulation of the landing dynamics has provided estimates of the vernier engine thrust levels and the vernier engine 3 height above the surface during the second landing (Fig. V-23).

Logically, vernier engine 2 thrust level should go down to a minimum (as shown) as footpad 2 touches down, because of the turning moment exerted on the spacecraft by leg 2. It is also logical that, simultaneously, vernier engine 1 should go to a maximum thrust level (as shown). However, the quick dropoff after a short rise of vernier engine 3 was unexpected. It is surmised that the thrust level should have been higher, although probably not as high as vernier engine 1. From these simulations, studies of the second landing site terrain, and the geometric relationships of the spacecraft, the height of the spacecraft above the lunar surface was estimated.

Table V-2. Preliminary estimates of μ, V_p, and V_s for assumed values of ν and ρ

ν	ρ	ρ = 0.5 g/cm^3		ρ = 1.0 g/cm^3		ρ = 1.5 g/cm^3		ρ = 2.0 g/cm^3	
	μ, dynes/cm^2 × 10^6	V_s, m/s	V_p, m/s	V_s, m/s	V_p, m/s	V_s, m/s	V_p, m/s	V_s, m/s	V_p, m/s
0	7.8	39	55	28	40	23	33	20.0	28
0.4	4.7	31	76	22	56	18	46	15.0	38
0.45	4.3	30	100	21	70	17	56	14.5	48
0.5	3.9	28	∞	20	∞	16	∞	14.0	∞

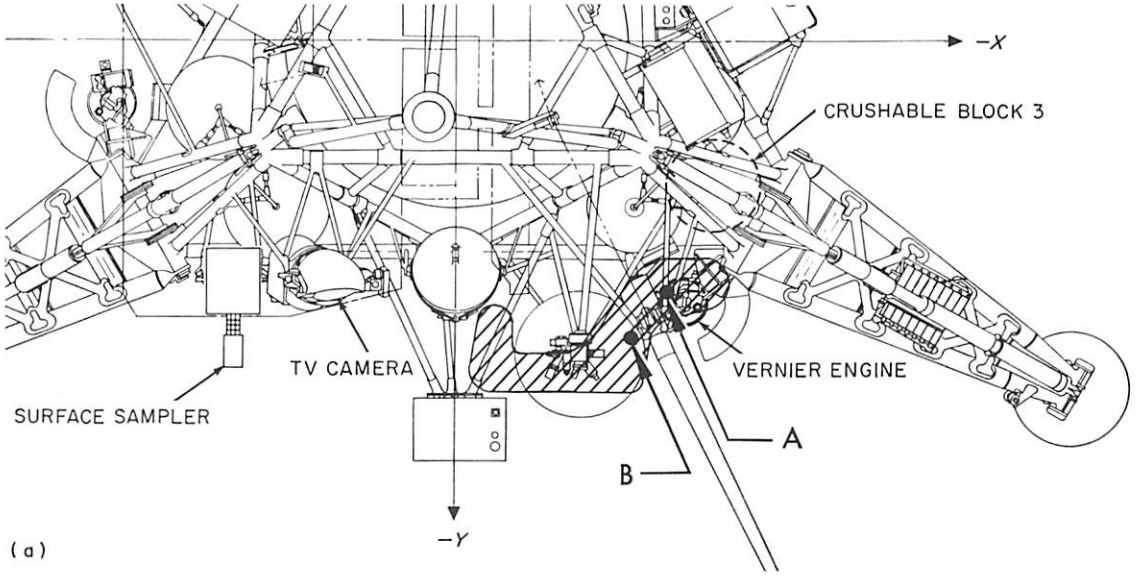

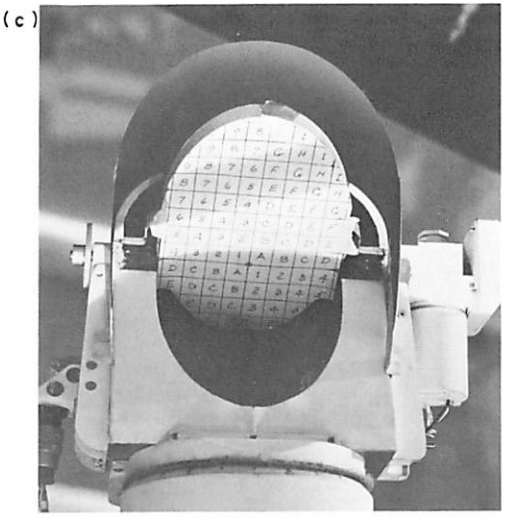

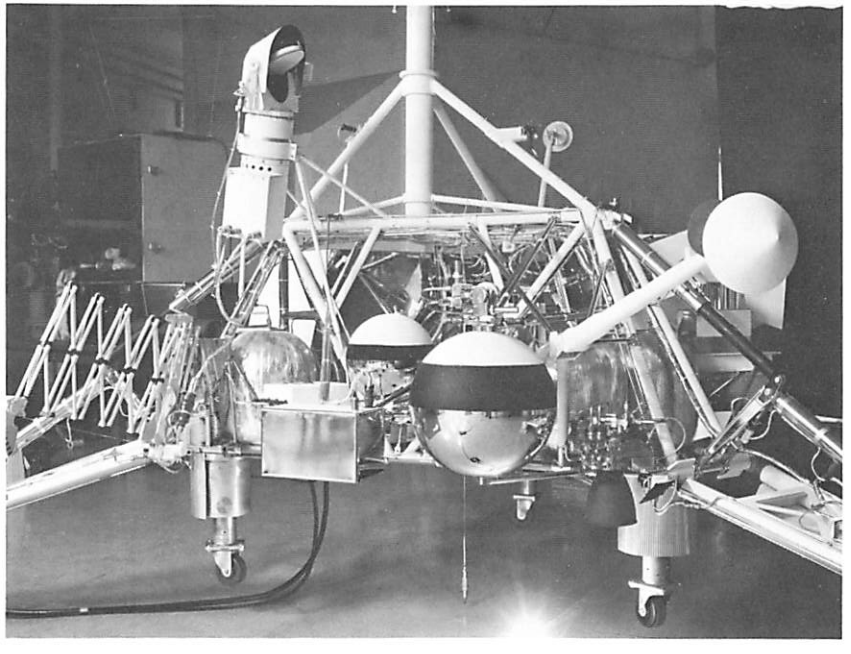

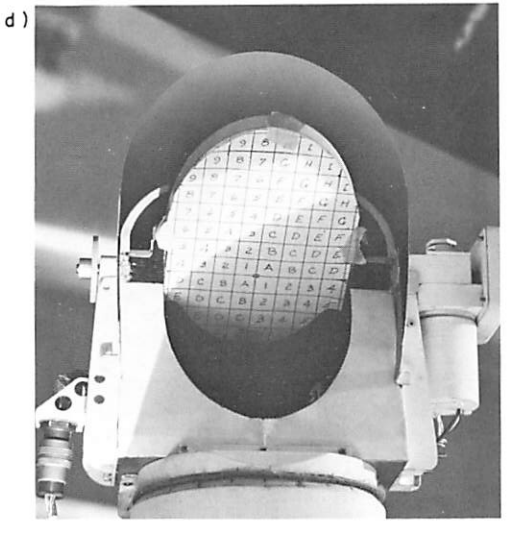

Fig. V-30. Potential camera mirror contamination vs vernier engine erosion: (a) plan view of spacecraft; (b) light source on ground level with spacecraft footpads; (c) light pattern on mirror with source at A; and (d) light pattern on mirror with source at B

The height of the vernier engine 3 nozzle exit plane was from an estimated 25 to 120 cm during the estimated 2-s time interval that the engine was over the erosion mark shown in Fig. V-19. If the nozzle heights are correct, crushable block 3 did not contact the lunar surface, and the lunar markings were created solely by the vernier engine erosion. Thus, the eroded particles possibly traveled along a trajectory that eventually caused them to hit the mirror, causing deposition on, and/or abrasion of, the mirror surface.

The depth of the erosion mark is unknown and is difficult to predict because of the unknown shape of the original surface.

9. Strength Estimate of Lunar Rock

Figure V-31 shows a rock fragment, about 1.2 cm in diameter, held in the jaws of the SMSS. Dimensions and applied forces for the rock fragment are given in detail

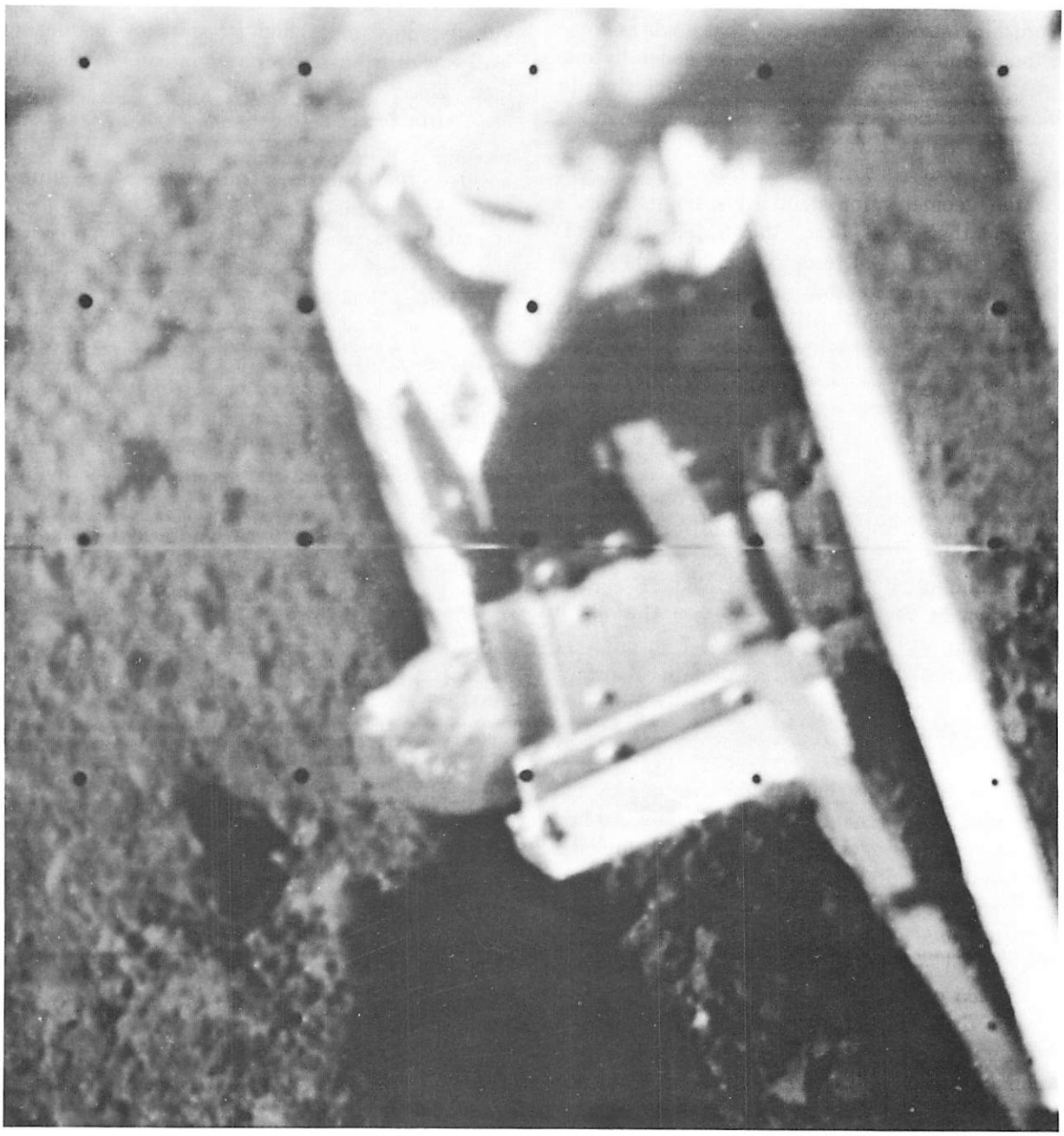

Fig. V-31. Narrow-angle picture of lunar rock in jaws of SMSS (Day 121, 15:21:05 GMT)

in Section IV of this report. The maximum force available (30 N) was applied to this rock fragment for 10 to 15 min in an attempt to determine its strength. After this time interval, the rock fragment apparently popped out of the jaws of the SMSS between television picture frames and was not subsequently located; therefore, the breaking strength was equal to or greater than the stress applied. Maximum pressure was applied to this rock fragment along the edge of the sampler scoop (0.10 cm). Assuming a contact length of 1.2 cm, a pressure of about 2×10^7 dynes/cm^2 was estimated. This value is in the range of crushing strength for weak rocks such as some tuffs, siltstones, and claystones. Rocks are generally one order of magnitude (or more) weaker in tension than in compression. Their shear strength is also generally much lower than their compressive strength.

Because the geometry for standard strength tests is different from that used here, the SMSS at SETL was used in a brief series of tests to determine the types of rocks or dry, coherent soil masses that could be broken by the *Surveyor* SMSS. Although the SETL surface sampler does not exactly duplicate flight versions of the SMSS, any differences present are negligibly small compared to differences expected from variations in rock strengths and areas of loading for specific rock specimens.

Some specimens of weak rocks and dry, coherent soils were selected from collections at JPL; most of the specimens were selected from the weakest rocks contained in the Wards Technological Collection, MC 460. Specimens tested are shown in Fig. V-32. Specimens 1 through 6 did not fail during the testing; specimens 7 through 14 failed. The approximate area of stress or failure surface is given for each specimen; the stress plane is indicated by arrows (Fig. V-32).

In general, the specimens that failed were porous, had low density, and were weakly cemented (grains rubbed off easily between the fingers). This description includes the friable sandstone of the Sespe formation. In contrast, the specimens that did not fail were dense and fairly well cemented. For the specimens that did not fail, the cross-sectional area of the potential failure plane ranged from 0.35 cm^2 to 0.90 cm^2; tensile stress ranged from 7.6×10^5 dynes/cm^2 to 3×10^6 dynes/cm^2, respectively. For the naturally occurring specimens that failed, cross-sectional area of the failure plane ranged from 0.35 cm^2 for the Sespe sandstone to 3 cm^2 for the Pasadena arkosic clay; average stress ranged from 7.7×10^6 dynes/cm^2 to 1.2×10^6 dynes/cm^2.

Initial bearing area was substantially different for different specimens, depending on their shape. Thickness of the sampler blade is 0.10 cm; thus, if length of contact of the blade along a specimen is less than the 1.8-cm blade length, the cross-sectional bearing area (in contrast to area of fracture) will be less than 0.18 cm^2, and the pressure will be greater than 2×10^7 dynes/cm^2. For most rock specimens, the initial bearing area will be substantially below the above value.

Generally, failure progressed with crumbling of individual grains under high-stress point loading, until the load was distributed over a significant width of the specimen. Once the blade had cut into a specimen until one-fourth to three-fourths of the specimen's width was in contact with the blade, little additional visible strain occurred until the specimen failed entirely. In all cases, in the SETL tests, when a rock was broken, a part of the specimen was retained in the scoop as the jaws snapped shut; the part of the specimen outside of the jaws, in some cases, flew out of view of the camera.

The sugar cube was a better test specimen than expected. The cube failed in the same manner as did the natural specimens. Failure of a sugar cube (1.5 cm on a side) is just within the force range of the SMSS under maximum torque; therefore, any individual could demonstrate for himself the approximate strength of a rock that can be broken by the *Surveyor* SMSS. The individual need only press on a sugar cube with the back edge of a jack knife or dinner knife until the cube fails.

C. Summary

An analysis of the data obtained from the landings of *Surveyor III*, which occurred inside a crater, indicates that the mechanical properties of the lunar surface material at this site are generally similar to those of the lunar mare site on which *Surveyor I* landed. The three landings made by *Surveyor III* were progressively farther down into the crater. Footpad imprints were detected at a distance of from 11 to 14 m from the spacecraft. Application of various techniques has verified that these imprints were made during the second landing event.

The preliminary estimate of the lunar soil static bearing capability, as determined by the *Surveyor III* spacecraft landing interactions with the moon, appears to be in the same range as that of *Surveyor I*, i.e., 2×10^5 to 5.6×10^5 dynes/cm^2 (3 to 8 psi) for a depth of penetration

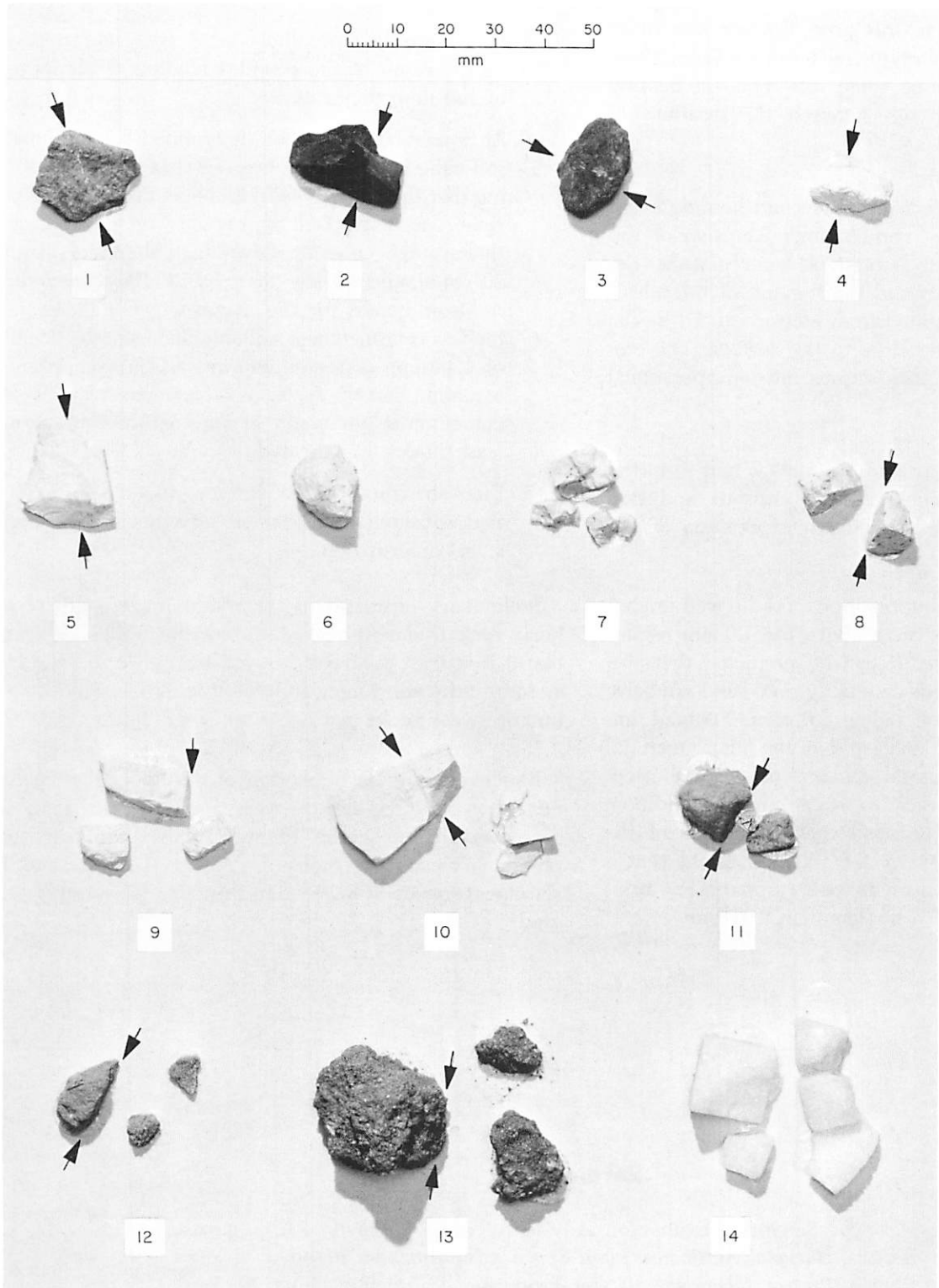

(1) Illite bearing shale
Fithian, Ill.
Wards No. 51
Specimen failure: no
Area stressed: 0.8 cm^2

(2) Fire clay
Golden, Colo.
Wards No. 50
Specimen failure: no
Area stressed: 0.6 cm^2

(3) Illite bearing shale
Fithian, Ill.
Wards No. 51
Specimen failure: no
Area stressed: 0.6 cm^2

(4) Magnesite
Riverside, Calif.
Wards No. 375
Specimen failure: no
Area stressed: 0.35 cm^2

(5) Halloysite
Eureka, Utah
Wards No. 61
Specimen failure: no
Area stressed: 0.8 cm^2

(6) Monmorillonite (Bentonite)
Chambers, Ariz.
Wards No. 58
Specimen failure: no
Area stressed: 0.9 cm^2

(7) Monmorillonite (Bentonite)
Chambers, Ariz.
Wards No. 58
Specimen failure: yes
Fracture area: 0.7 cm^2

(8) Monmorillonite (Bentonite)
Chambers, Ariz.
Wards No. 58
Specimen failure: yes
Fracture area: 0.65 cm^2

(9) Argillaceous limestone
Trenton Falls, N. Y.
Wards No. 69
Specimen failure: yes
Fracture area: 0.65 cm^2

(10) Argillaceous limestone
Trenton Falls, N. Y.
Wards No. 69
Specimen failure: partial
Fracture area: 1.0 cm^2
(Initial stress area: 1.1 cm^2)

(11) Jarosite
Chihuahua, Mexico
Wards No. 327
Specimen failure: yes
Fracture area: 0.6 cm^2

(12) Friable sandstone
Sespe Formation
(Oligocene age)
Santa Ynez Range
Santa Barbara area, Calif.
Specimen failure: yes
Fracture area: 0.35 cm^2

(13) Arkosic clay, porous, dry
Alluvial fan
San Gabriel Mountains,
Pasadena, Calif.
Specimen failure: yes
Fracture area: 3.0 cm^2

(14) Sugar cube (15 × 15 × 15 mm)
C&H Co.
Density: 1.12 g/cm^3
Specimen failure: yes
Failure area: 2.25 cm^2

Fig. V-32. *Surveyor* SMSS rock fracture tests: specimen identification

of from 2.5 to 5 cm and for an area equivalent to that of a footpad. This range of values is based on computer simulations carried out to this time. Further simulation work will be conducted with a view toward refining these values. There seems to be some difference in bearing capability of the lunar soil between the locations of *Surveyor III* footpads 2 and 3.

A trench-like disturbance in the second landing event area is attributed to the vernier engine erosion of the lunar surface. The small amount of lunar material deposited on the spacecraft and the fogging of the television camera possibly resulted from erosion caused by the vernier engines operating close to the surface. The erosion effects did not result in serious mission operational limitations or failure.

Pictures of the areas around footpads 2 and 3, in the final resting position, show several imprints and skid marks which afford the following interpretation of soil properties:

(1) Particle-size distribution appears to be well graded (poorly sorted) for sizes above the 1.0-mm resolution of the camera. It can be predicted that size distribution extends smoothly into the sand-size particle range well below 1.0 mm. Footpad imprint simulations suggest that the lunar material contains a substantial amount of particles finer than the size of sand (< 0.06 mm). In addition, comminution studies and the appearance of the disturbed material on the moon indicate that a significant fraction of the soil (probably $> 10\%$) consists of particles smaller than 0.01 mm.

(2) Imprints and soil ejecta patterns suggest a low compressibility of the lunar surface material.

(3) Difference in footpad 2 and 3 penetrations may be the result of the complex landing dynamics or of soil inhomogeneity.

(4) An upper bound can be determined for the lunar soil cohesion from the bearing strength by assuming that the material is frictionless. For a 5.6×10^5 dyne/cm^2 static bearing capacity on the surface, the average cohesion down to a depth of about 20 cm should be less than 1.4×10^5 dynes/cm^2. A lower bound for the average cohesion for the top few centimeters of soil obtained from the height of standing slopes of imprints is 100 dynes/cm^2, assuming that the material is frictionless. If it were cohesionless, an angle of internal friction of at least 60 deg is indicated.

(5) Fine structure of the surface material is modified substantially by small amounts of compressional deformation.

Preliminary estimates of the minimum strength of a lunar rock fragment picked up by the SMSS indicate that it is at least as strong as weak terrestrial rocks, such as some tuffs, siltstones, and claystones. The SMSS can fracture weak rocks that occur on earth.

Ranges for the elastic moduli of the upper few centimeters of the lunar surface were obtained from analysis of spacecraft oscillations following the landing. These preliminary estimates indicate a rigidity modulus and a shear wave velocity lower than those for loose terrestrial sand.

References

V-1. *Surveyor* Scientific Evaluation Advisory Team, *Surveyor I Preliminary Results, National Aeronautics and Space Administration Five-Day Science Report*, Project Document 97, Jet Propulsion Laboratory, June 30, 1966, also in *Science*, Vol. 152, No. 3730, pp. 1737–1750, 1966.

V-2. *Surveyor I Mission Report. Part II: Scientific Data and Results*, Technical Report 32-1023, Jet Propulsion Laboratory, Pasadena, Calif., Sept. 10, 1966.

References (contd)

V-3. Sperling, F., and Garba, J., *A Description of the Surveyor Lunar Landing Dynamics and an Evaluation of Pertinent Telemetry Data Returned by Surveyor I*, Technical Report 32-1035, Jet Propulsion Laboratory, Pasadena, Calif., 1967.

V-4. Alderson, R. G., and Wells, D. A., *Final Report on Surveyor Lunar Touchdown Stability Study*, Report MM-66-19, Analytical Mechanics Department, Bendix Corp., South Bend, Indiana, 1966.

V-5. Deitrick, R. E., and Jones, R. H., *Surveyor Spacecraft System. Touchdown Dynamics Study*, SSD-3030R, Hughes Aircraft Co., Culver City, Calif., 1964.

V-6. Scott, R. F., *Problem of the Penetration of a Projectile into Soil or Soil-like Medium, or Compressible Rock*, four reports to Space-General Corporation, El Monte, Calif., 1962 (copies available from author).

V-7. Jaffe, L. D., "Surface Structure and Mechanical Properties of the Lunar Maria," *J. Geophys. Res.*, Vol. 72, pp. 1727–1731, 1967.

V-8. Meloy, T. P., and Faust, L. H., *Lunar Surface Roughness Comminution Study*, Final Report, Space and Defense Sciences Department, Allis-Chalmers Manufacturing Co., Milwaukee, Wis., April 1965.

V-9. Timoshenko, S., and Goodier, D., *Theory of Elasticity*, Second Edition. McGraw-Hill Book Co., Inc., New York, p. 367, 1951.

Acknowledgment

Appreciation is extended to Ronald Scott, California Institute of Technology, for reading the article and offering suggestions; Charles Goldsmith, Alex Irving, William Peer, and Robert Steinbacher, JPL, for assisting in the simulations of the footpad imprints and performing spacecraft shadow predictions; Daniel Bookstein, JPL, David Conaway, Margaret Dove, and John Hinchey, Hughes Aircraft Company, for assisting in the landing dynamic simulations; and E. N. Shipley, Bellcomm, Inc., for participating in the early portion of the first lunar day operations.

(Blank Page)

VI. Lunar Temperatures and Thermal Characteristics

J. W. Lucas, J. E. Conel, R. R. Garipay, W. A. Hagemeyer, C. B. Jones, J. M. Saari, G. Vitkus, and J. T. Wang

Surveyor III provided data on lunar surface temperatures, thermophysical characteristics, and spacecraft thermal performance on the lunar surface. The spacecraft carried no specific instrumentation to measure lunar surface temperature and was (similar to *Surveyor I*) designed to be thermally independent of its flight and post-landing environments. Following the *Surveyor I* analysis, outer canister temperatures of electronic compartments A and B were used to estimate average brightness temperatures of parts of the surface.

The spacecraft landed at selenographic coordinates 2.94°S latitude, 23.34°W longitude. Temperature data for compartments A and B and also for the solar panel and planar array antenna were obtained until 00:04 GMT on Day 124 (May 4) or about 2 h after sunset. Temperature records during the eclipse of Day 114 (April 24), which occurred between 09:48 and 14:06 GMT, were also obtained.

A. Thermophysical Properties of *Surveyor III* Site, as Determined From Earth-Based Data

Thermal measurements on the lunar surface were made from *Surveyor III* under three conditions: (1) during the day, (2) during the total eclipse of Day 114, and (3) until shortly after sunset. For comparison, results from earth-based measurements are available for conditions (1) and (2) for the *Surveyor III* site.

During the lunar day, the observed lunar surface temperature depends on sun angle, surface albedo, and directional effects in infrared emission. The sun angle can be calculated exactly for a level surface. Because *Surveyor III* rests in a shallow crater, however, the temperature may be expected to vary from place to place in the depression as a result of variations in topography. The total solar albedo, i.e., the fraction of solar insolation reflected into space, is required for calculating daytime temperatures. In principle, this quantity may be obtained by integration of the photometric function (scaled by the normal albedo) over a hemisphere, and with wavelength throughout the solar spectrum. A simpler method is to use the simultaneous infrared and photometric scan data of Shorthill and Saari (Refs. VI-1 and VI-2). Of particular interest is the scan made over the full moon (phase angle of -2 deg) just prior to the December 19, 1964, eclipse. For this scan, the change in brightness temperature with change in photometric brightness, B, has been studied. One can write

$$\sigma T_{L}^{4} = (1 - A)\, S \sin \psi \qquad (1)$$

where

σ = Stefan-Boltzmann constant

T_L = Lambertian temperature of the surface

A = total solar albedo

S = solar insolation

ψ = elevation angle of the sun to the surface

For a full-moon scan, the observed brightness temperature, T_b, differs from the Lambertian temperature because of directional effects (discussed later) so that

$$T_b(\psi) = D(\psi)\, T_L \tag{2}$$

where $D(\psi)$, the directional factor, is defined by this equation. Assuming that the total solar albedo of a small element of surface is proportional to the full-moon brightness of the same element, it can be written that

$$A = KB \tag{3}$$

where K is a constant to be determined. If measurements are made on two areas, 1 and 2, of differing albedo at the same ψ

$$\left.\begin{aligned} \left[\frac{T_{b,1}}{D(\psi)}\right]^4 &= (1 - KB_1)\, S \sin\psi \\ \text{and} \\ \left[\frac{T_{b,2}}{D(\psi)}\right]^4 &= (1 - KB_2)\, S \sin\psi \end{aligned}\right\} \tag{4}$$

Eliminating $D(\psi)$ between these two equations and solving for K,

$$K = \frac{T_{b,2}^4 - T_{b,1}^4}{B_1 T_{b,2}^4 - B_2 T_{b,1}^4} \tag{5}$$

Because K could possibly be a function of ψ, many pairs of points of different brightness were measured over the disk; the results showed that K was independent of ψ. The photometric brightness of the *Surveyor III* site was measured on this full-moon scan; multiplying by the constant K, determined as above, gave a value of 7.6% for the total solar albedo. Because the telescope measurements were made to a resolution of 10 s of arc (18 km at the center of the lunar disk), the local albedo of the *Surveyor III* site may depart considerably from this value.

Predicted lunar surface (Lambertian) brightness temperatures (Fig. VI-1) were computed, using the program described in Ref. VI-3 for an equatorial site and several different values of the thermal parameter. The thermal parameter, γ, equals $(k\rho c)^{-1/2}$ where k is thermal conductivity, ρ is density, and c is specific heat. The total solar albedo was taken equal to 0.076. Note that, during the day, surfaces with a γ greater than 500 (cgs units) have essentially the same temperatures.

Thermal measurements were made with *Surveyor III* during the Day 114 total eclipse. Figure VI-2 shows a predicted cooling curve for the site based on measurements obtained by Saari and Shorthill (Refs. VI-4 and VI-5) during the December 19, 1964, eclipse. By assuming that directional effects persist during totality to the same degree as observed just prior to the start of the eclipse, it was possible to infer from the telescopic data a value for γ of 1420, using the theoretical eclipse cooling curves for a homogeneous model (Ref. VI-6). This is close to a value of 1350 obtained in the same manner for the *Surveyor I* site. Values of γ in this range are representative of the insulating material that characterizes much of the lunar surface. The warming curve in Fig. VI-2 represents calculated equilibrium surface temperatures corresponding to the insolation at each time.

Infrared measurements made during the December 19, 1964, eclipse showed that the lunar surface exhibits a great deal of thermal inhomogeneity (Ref. VI-4). Because extensive spatial temperature fluctuations were found on features as small as 4 km, they could exist to a scale comparable to that of the *Surveyor III* site. Thus, the thermal characteristics of this site may be considerably different than observed from earth with a resolution of 18 km. Isothermal contours of the *Surveyor III* site obtained during totality of that eclipse are shown in Fig. VI-3. The region is relatively bland; the nearest hot spot is associated with Fra Mauro C at about 21.6°W, 5.4°S. A very mild enhancement is noted closer to the site at 24.0°W, 3.5°S.

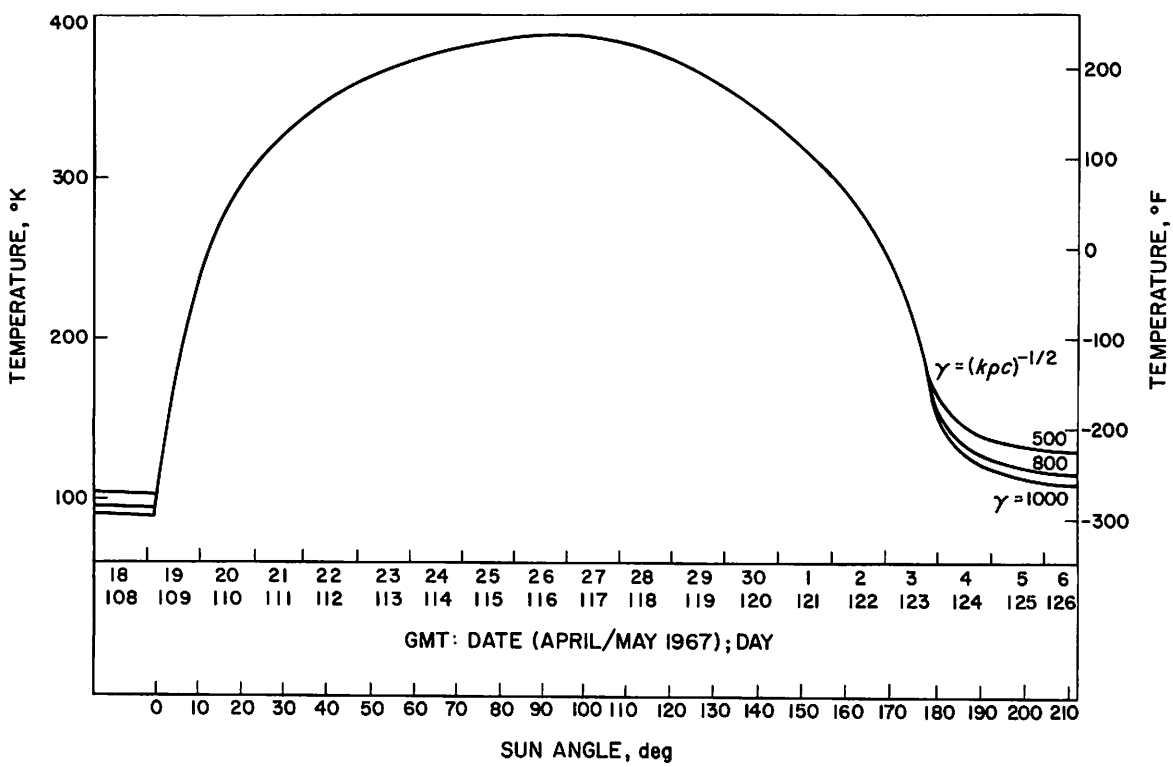

Fig. VI-1. Predicted lunar surface brightness temperatures on lunar equator

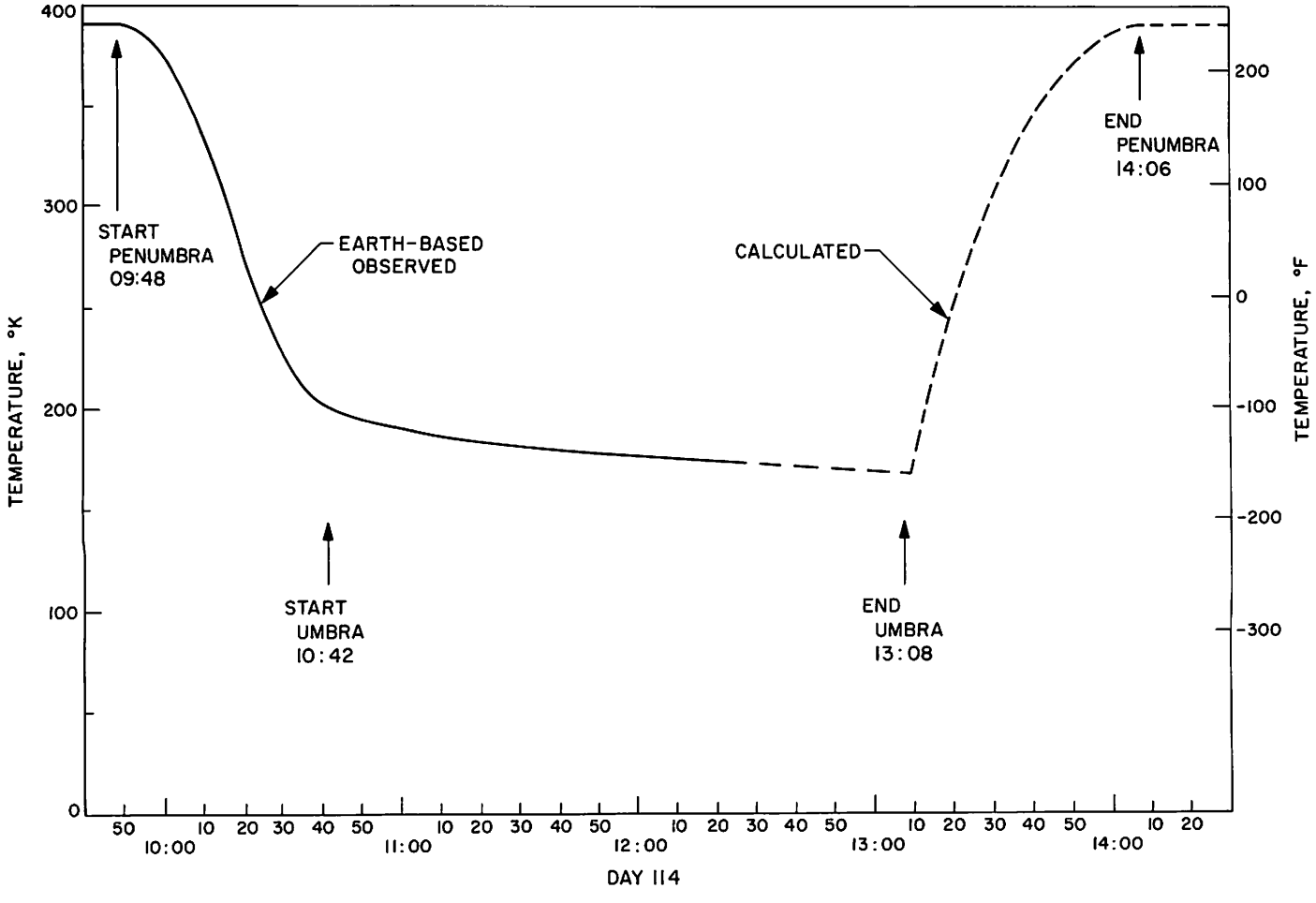

Fig. VI-2. Lunar surface brightness temperature at nominal *Surveyor* landing site, during eclipse (data from December 1964 eclipse adjusted for time of April 1967 eclipse)

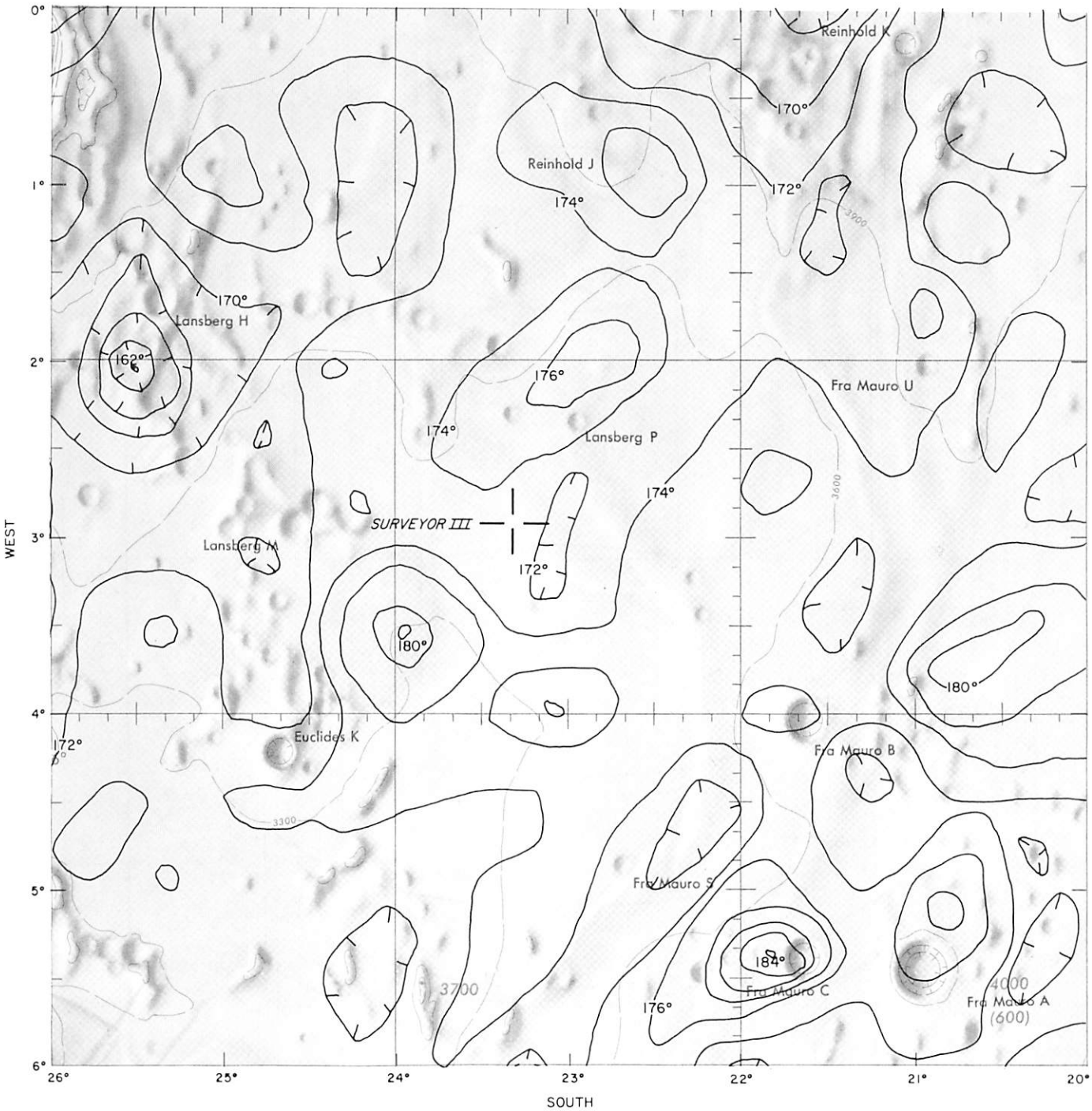

Fig. VI-3. Isothermal contours in *Surveyor* landing site region obtained during totality of lunar eclipse

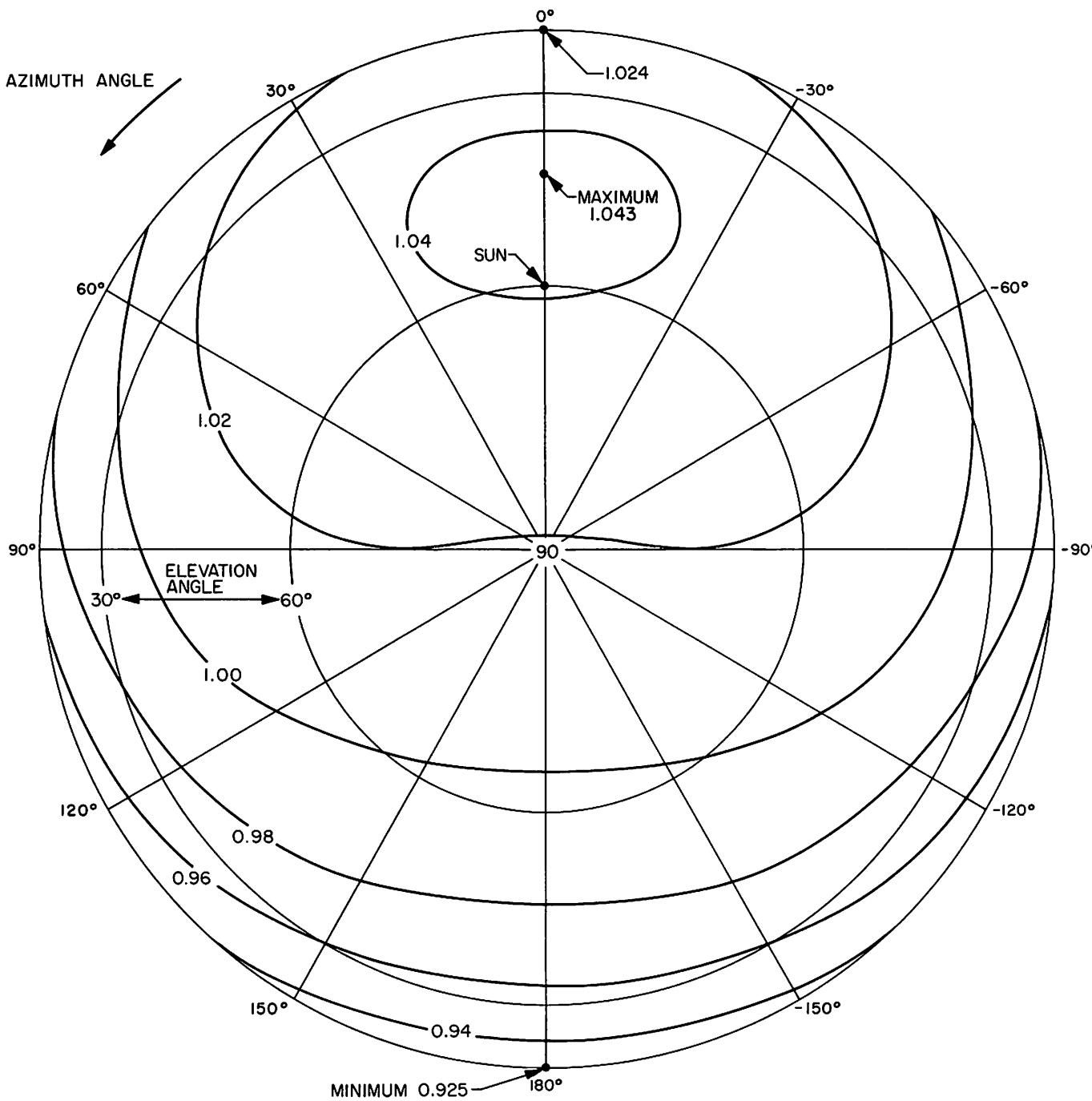

Fig. VI-4. Contours of directional factor for sun elevation angle of 60 deg

B. Directional Effects of Lunar Infrared Emission

It has been determined (Ref. VI-7) that, when the lunar surface is illuminated by the sun, the observed brightness temperature is not constant for different angles of observation, i.e., the surface does not behave like a Lambertian surface. This effect, ascribed to surface roughness, causes the brightness temperature to be higher when the phase angle is small (i.e., when the sun/surface/observer angle is small) than when it is large. Qualitatively, the emission is greater in the direction of the sun. It is clear that such directionality will have an effect on the radiation received by the compartments on *Surveyor*.

To correct for directional effects, measurements from all over the lunar disk for three sun angles were used. For a sun elevation angle of 90 deg, we take the measurements of Sinton (Ref. VI-8), which give the variation in radiance from the subsolar point as a function of the elevation angle of the compartment.

For the other two sun angles of 30 and 60 deg, the infrared scan data for different phases made by Shorthill and Saari were used. For these scans, each made at a different phase angle, the brightness temperatures were determined at points where the sun elevation angles were 30 and 60 deg (Ref. VI-7) and every 10 deg in thermal longitude. (With reference to a latitude/longitude system where the subsolar point is the north pole and the terminator the equator, thermal longitude is measured from the great circle passing through the subsolar point and the disk center.) Albedo corrections for each point were made from the full-moon photometric data. The directional factor was calculated from Eq. (2) using calculated values of Lambertian temperatures at each point.

Directional factors obtained in this manner were referenced to a local coordinate system with azimuth and elevation angles for the direction of observation defined as follows. Azimuth angles are measured from the normal projection of the sun direction onto the surface. Elevation angles are measured from the surface in the plane of observation. Directional factors obtained over the globe were referenced to this azimuth/elevation angle system. A least-squares spherical harmonic fit, symmetrical with respect to plus and minus azimuth angles, was then computed for the data. A contour plot of the directional factor for a sun elevation angle of 60 deg is shown in Fig. VI-4. The spherical harmonic fit was then used to compute the directional factor for elements of the scene viewed by the compartments for the calculation of an effective Lambertian temperature. Directional factors were, of necessity, obtained from global measurements made on a variety of features. It is possible, therefore, that a small area such as the *Surveyor III* site could have different directional effects than the *average surface* if local roughness or surface configuration differed significantly from the average.

C. Spacecraft View of Lunar Scene

The assumed orientation of *Surveyor III*, with respect to lunar coordinates, is given in Fig. VI-5. The azimuth of leg 1, the Y axis, is given as 46.1 deg southwest (S46.1°W); the $-Z$ axis is taken to be tilted 12.4 deg from the vertical in an azimuth direction of 6.4 deg northwest (N83.6°W). The normal to the compartment A outer canister face lies in a vertical plane of azimuth 9 deg southeast (S9°E) and is inclined at an angle of 65 deg to the local vertical. The normal to the compartment B outer canister face has an azimuth 16 deg northwest (N74°W) and is inclined at an angle of 81 deg to the local vertical. If the spacecraft $-Z$ axis approximates the direction of the local surface normal, both compartment normals are inclined at 69 deg to this direction.

Surveyor's landing site (about 45 m southeast of the crater center) is shown in Fig. VI-6. The general sectors of lunar surface viewed by each compartment are indicated. Compartment A views a scene to the southeast of the spacecraft where the horizon is from -5 to $+12$ deg (with an approximate average of 0 deg) above a flat moon from a level spacecraft (Fig. VI-7). Generally, compartment B looks to the northwest, where the horizon is $+2$ to $+12$ deg (with an approximate average of 11 deg) above the horizontal. The portions of surface viewed by both compartments overlap in a 65-deg sector looking southwest.

The surface area viewed by each compartment is limited by the canister face orientation and crater rim. On this basis, compartment A views a maximum projected surface area of 1.3×10^4 m^2, and compartment B an area of 2.6×10^4 m^2.

In Fig. VI-6, the region enclosed by a dotted line is either totally or partially obscured by the spacecraft structure in television coverage of the surface. Detailed descriptions of the observable portions are given in Section III of this report.

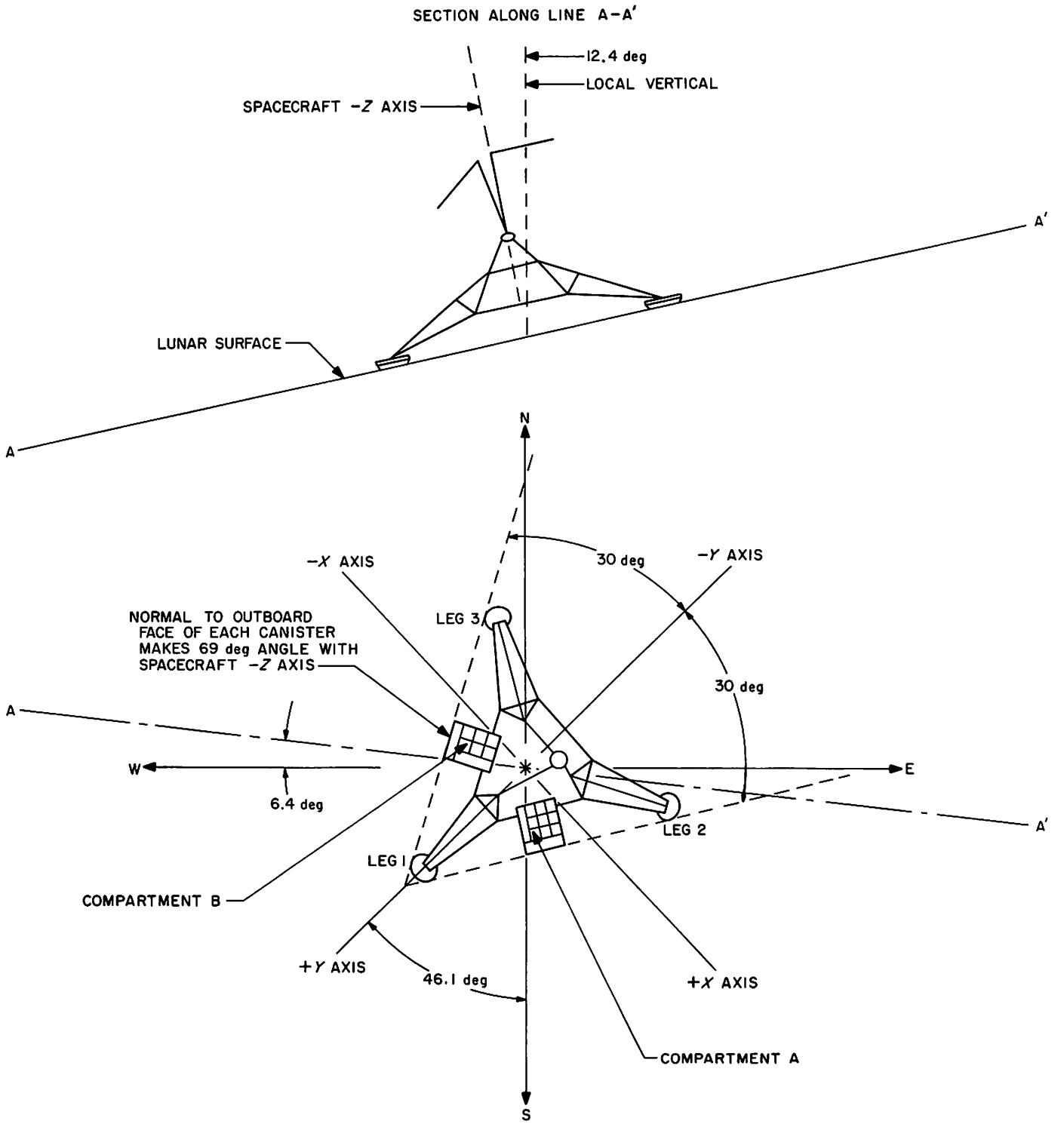

Fig. VI-5. *Surveyor III* landed orientation

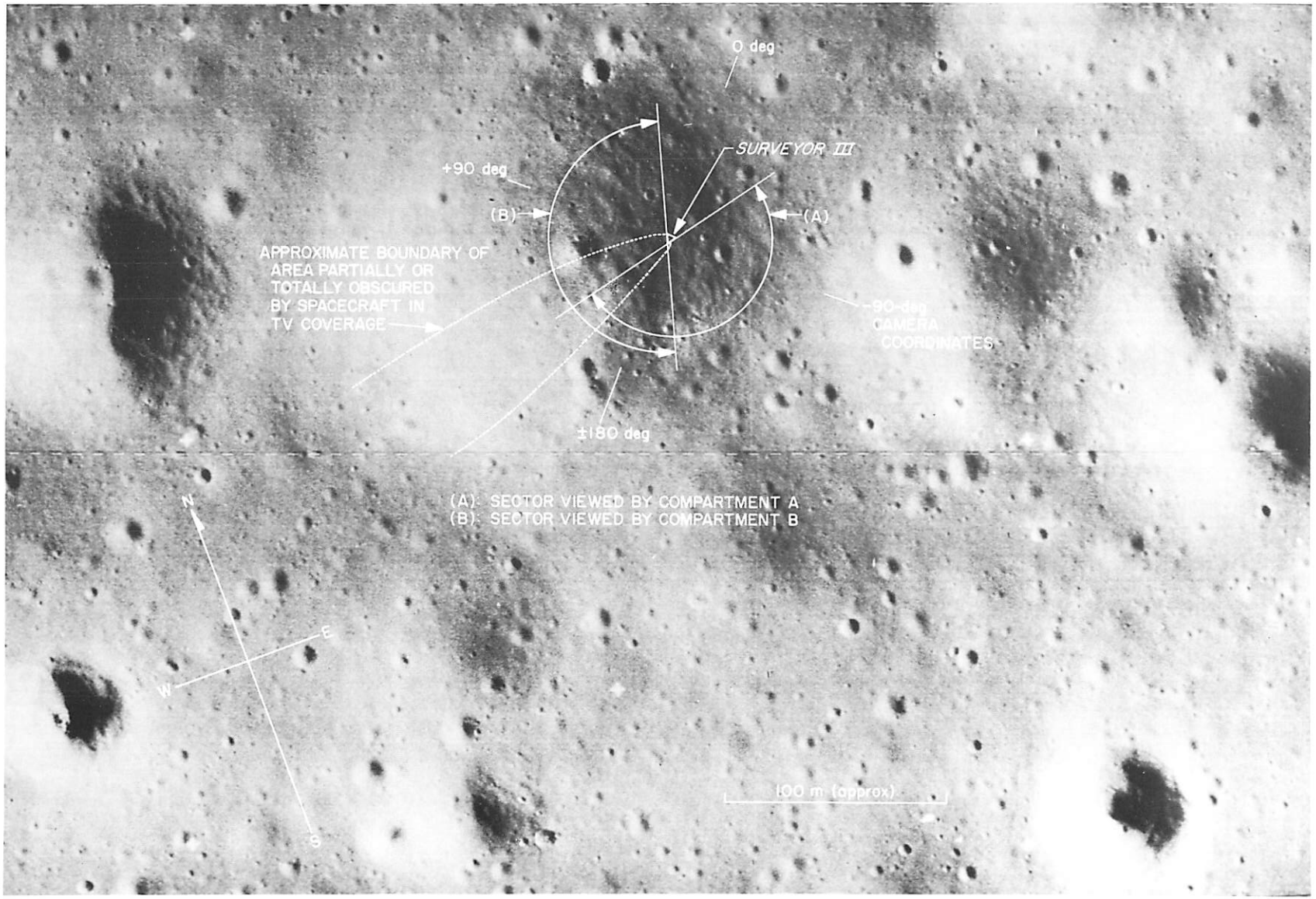

Fig. VI-6. *Surveyor III* landing site (photograph taken by *Lunar Orbiter III*), showing sectors viewed by compartments A and B

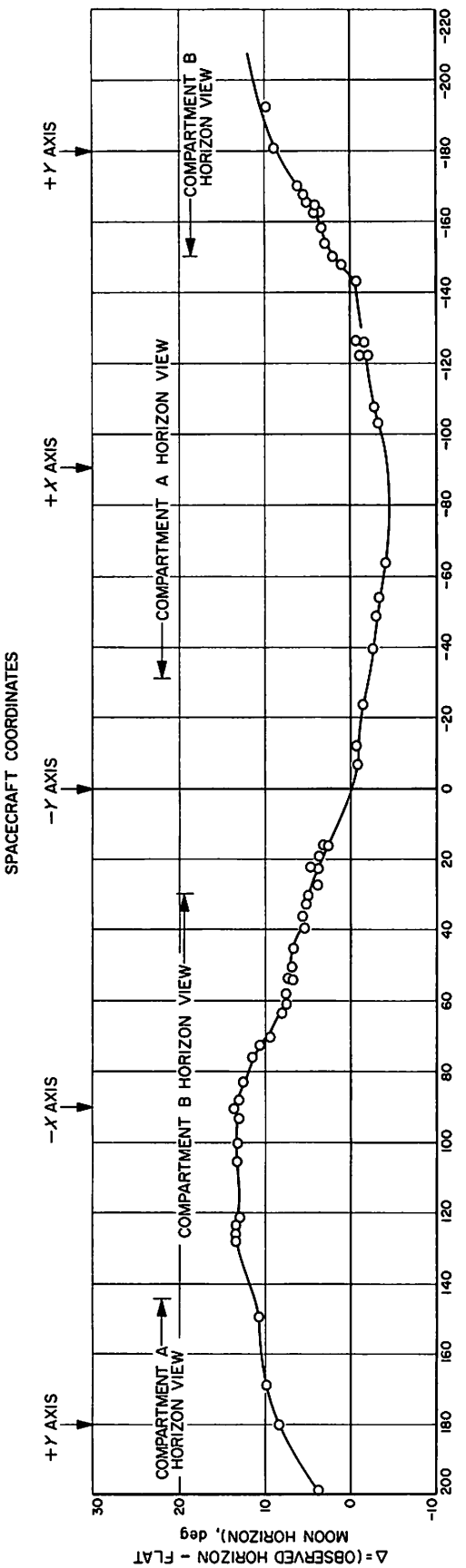

Fig. VI-7. Lunar horizon viewed from *Surveyor III* (data of E. A. Whitaker)

D. Spacecraft Raw Data

1. Spacecraft Description

The basic structure of the *Surveyor* spacecraft (Fig. VI-8) is made up of tubular aluminum, which serves as a tetrahedral mounting structure for the electronic gear and propulsion subsystems. The three spacecraft legs are attached at the three corners of the structure's base. The planar array antenna and solar panel, which are mounted on a mast that protrudes approximately 1 m above the apex of the structure, cast varying shadow patterns on the structural members and spacecraft subsystems throughout the lunar day. Changes in shadow patterns result from repositioning of the antenna and solar panel, as well as from the normal movement of the sun at about 0.5 deg/h.

The thermal finish of the structural members is a combination of inorganic white paint and polished aluminum. Generally, the white paint is applied to all top and visible-side surfaces of the structure; the underside of the surface is polished metal. This thermal finish distribution provides a low-solar-absorptance white paint surface in the sun-illuminated areas with a high-emittance coupling to space in the infrared regions. The polished aluminum underside of the structure acts to isolate the spacecraft from the hot lunar surface.

The telemetered temperatures of the center of the outer faces of compartments A and B (Fig. VI-9) are used to compute lunar surface temperatures. Also, data are provided for the solar panel and planar array antenna.

a. Compartment canister and environment description. The compartment A and B canisters (see Figs. IV-4 and IV-5 of Ref. VI-9) are thin aluminum shells; their purpose is to contain a 75-layer blanket of superinsulation that surrounds each compartment. The largest part of the top surface of each compartment is covered with Vycor glass second-surface mirrors. The mirrors are part of the bimetallic-actuated thermal switches used to reject heat from the temperature-controlled compartments. The selected temperature sensors are mounted approximately in the geometric center of the outboard face. (It should be noted that this face contains corrugations.) The sensors are bonded to the polished aluminum inner surface of the canister (i.e., the surface facing the superinsulation).

The canisters are reasonably well isolated from the remainder of the compartment and spacecraft structure; therefore, they are in thermal equilibrium with their environment, which is made up primarily of the lunar surface, space, and a variable amount of solar energy input. The superinsulation isolates the surfaces from the inside of the compartment so that the heat input from that boundary is negligible during the lunar day. This assumption is not valid when an attempt is made to calculate lunar surface temperatures during a lunar eclipse or during the lunar night.

These parameters are needed to compute lunar surface temperatures by the methods described in this report:

(1) Angle between normal to compartment outboard face and spacecraft $-Z$ axis.

  (a) Compartment A: 68°30′ ±30′.

  (b) Compartment B: 68°40′ ±30′.

(2) Compartment canister properties.

  (a) Infrared hemispherical emittance: $\epsilon_H = 0.87 \pm 0.02$.

  (b) Solar normal absorptance: $\alpha_S = 0.20 \pm 0.02$.

  (c) Material: 2024 aluminum, 0.4 mm (0.016 in.) thick, coated with inorganic white paint.

Lunar day outer compartment face temperatures are presented in Fig. VI-9. The angle between a normal to the compartment outboard faces and the sun vector is presented in Fig. VI-10. The extent of shading on the compartment B face is shown in Fig. VI-11; sunlight could not fall on it before Day 115 and full sunlight was on it after Day 117. Compartment A was shaded during Day 119 only (Fig. VI-9); the percentage of shading during this interval is unknown. Figures VI-12 through VI-14 show the compartment face temperature data for the solar eclipse and lunar sunset periods.

b. Solar panel and planar array antenna description. The solar panel and planar array antenna (Fig. VI-15) are relatively low-heat-capacity planar surfaces. The data derived from these two surfaces may be useful in removing some of the uncertainties associated with lunar surface temperatures that are based on compartment outer face data during intervals in which the outer face temperature is appreciably lower than the inner compartment temperature. As discussed in Ref. VI-9, this temperature difference results in heat flow from inside to outside, the exact value of which is uncertain.

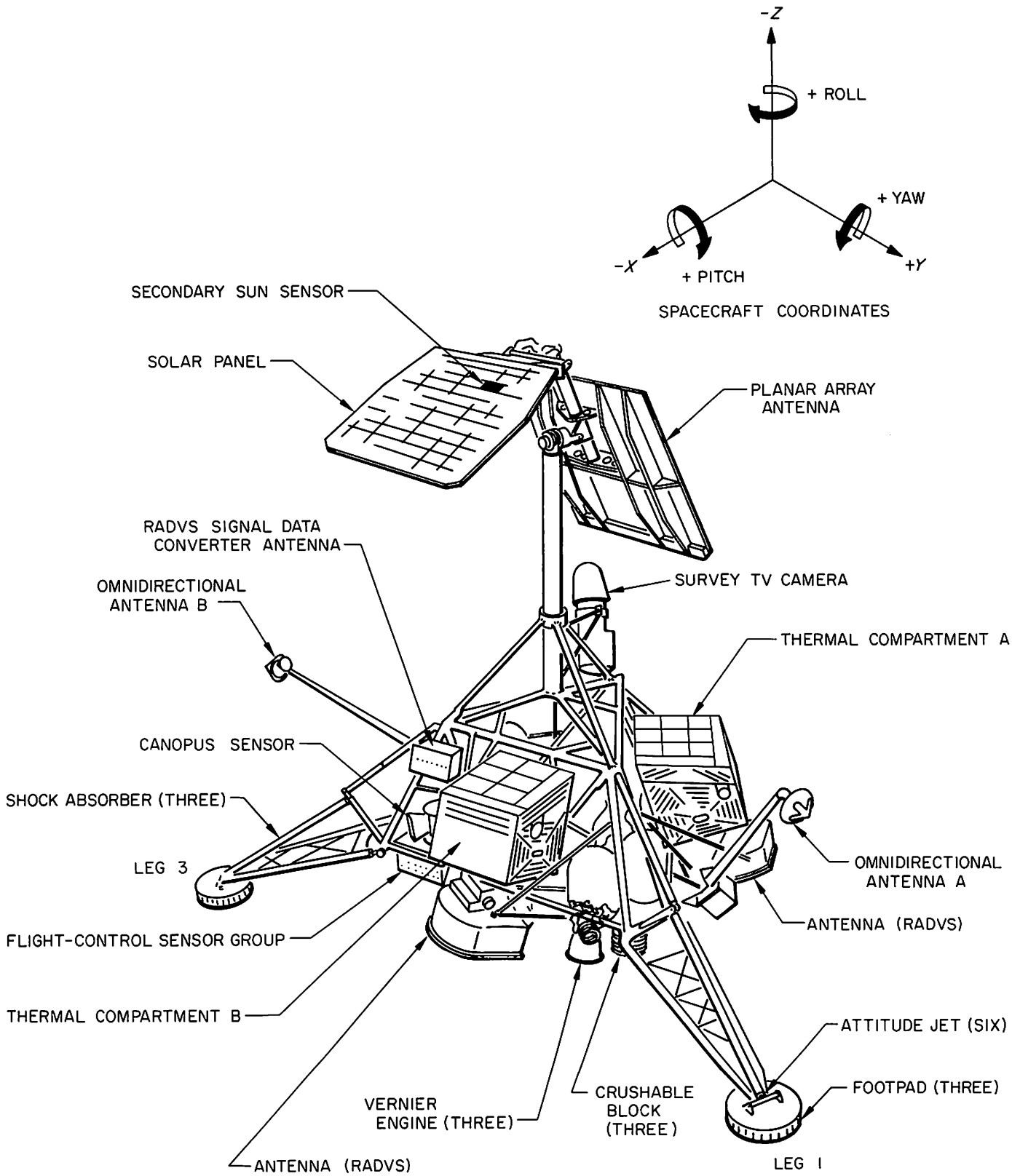

Fig. VI-8. *Surveyor* spacecraft configuration

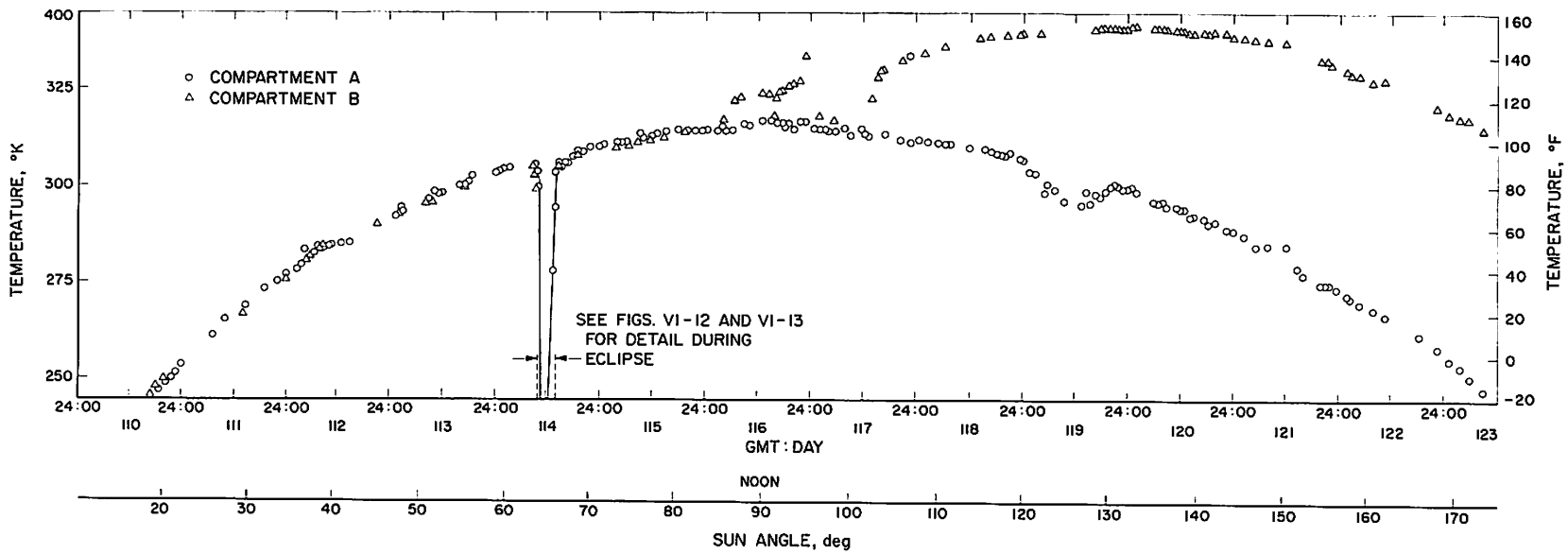

Fig. VI-9. Temperatures of outboard faces of compartments A and B during lunation

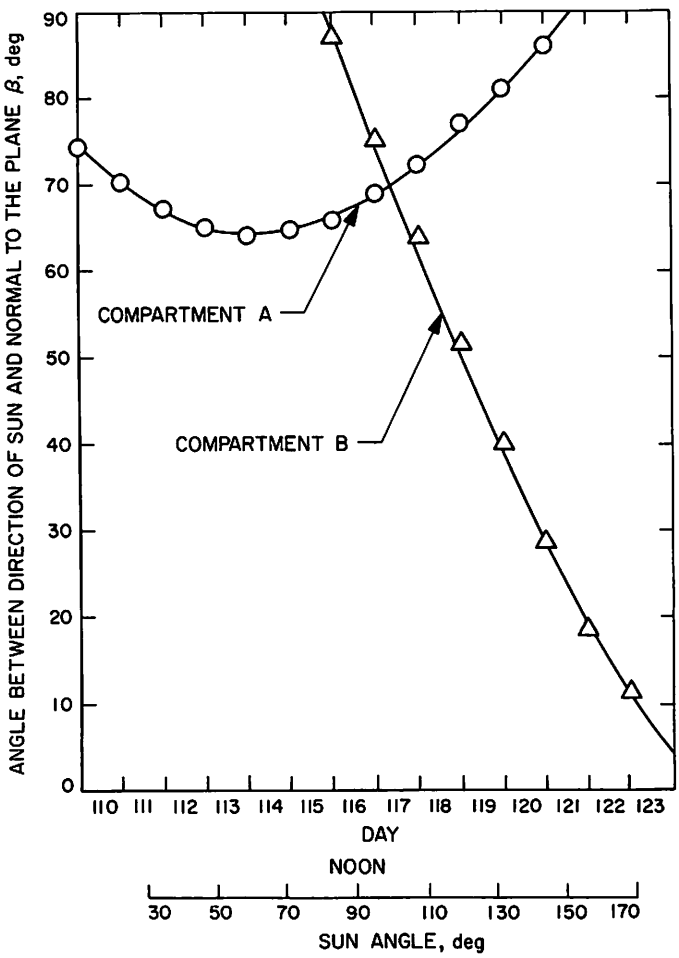

Fig. VI-10. Angle between direction of sun and normal to outboard plane of compartments A and B during first lunar day

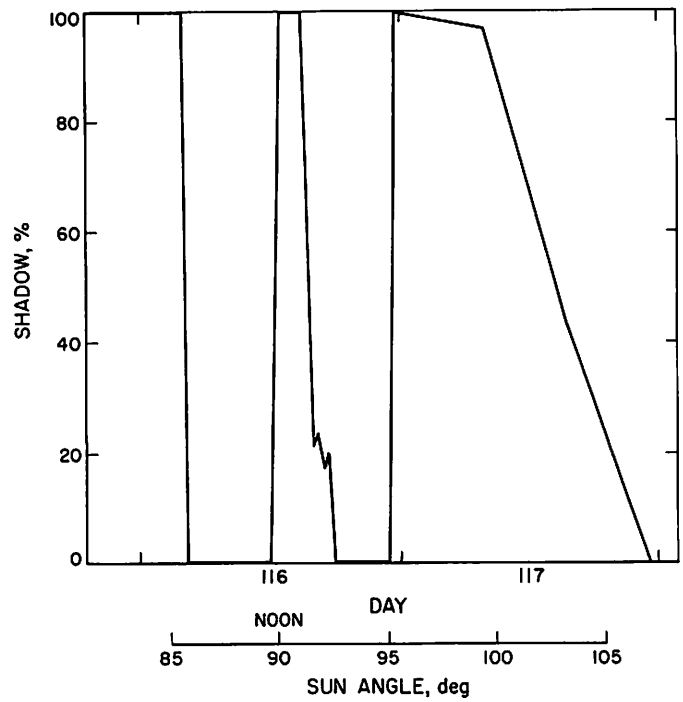

Fig. VI-11. Percent of shadow on outboard face of compartment B

Fig. VI-12. Temperatures of outboard face of compartment A during eclipse ⟶

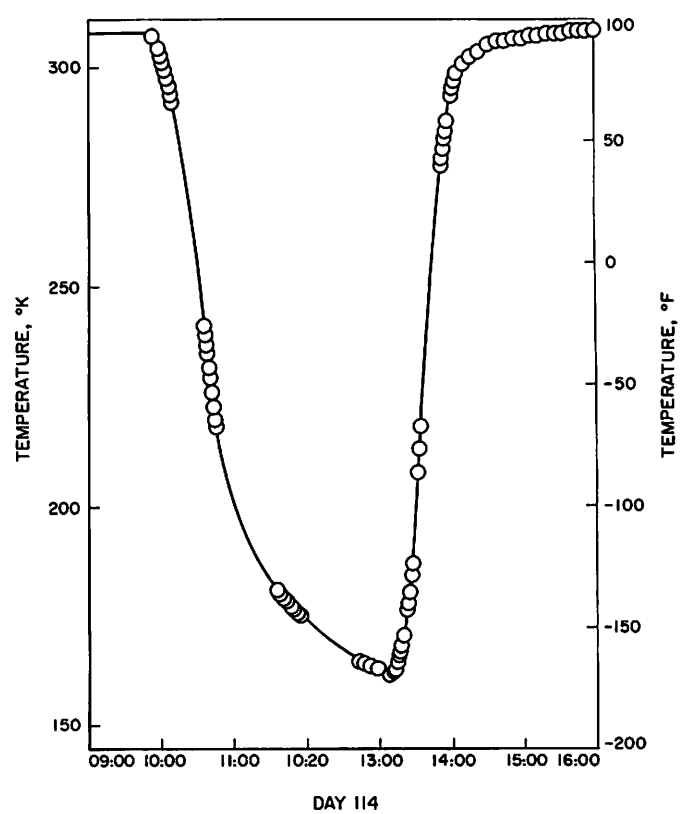

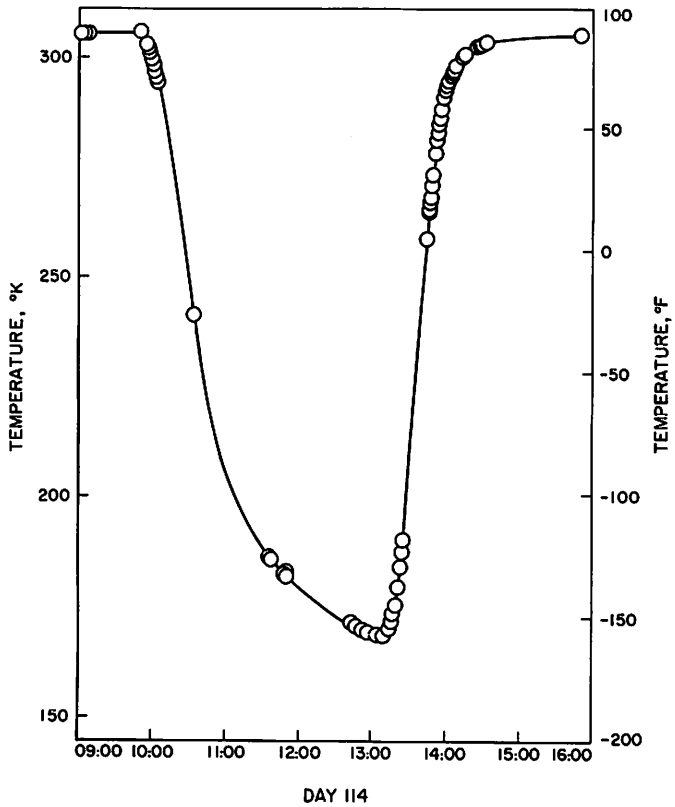

Fig. VI-13. Temperatures of outboard face of compartment B during eclipse

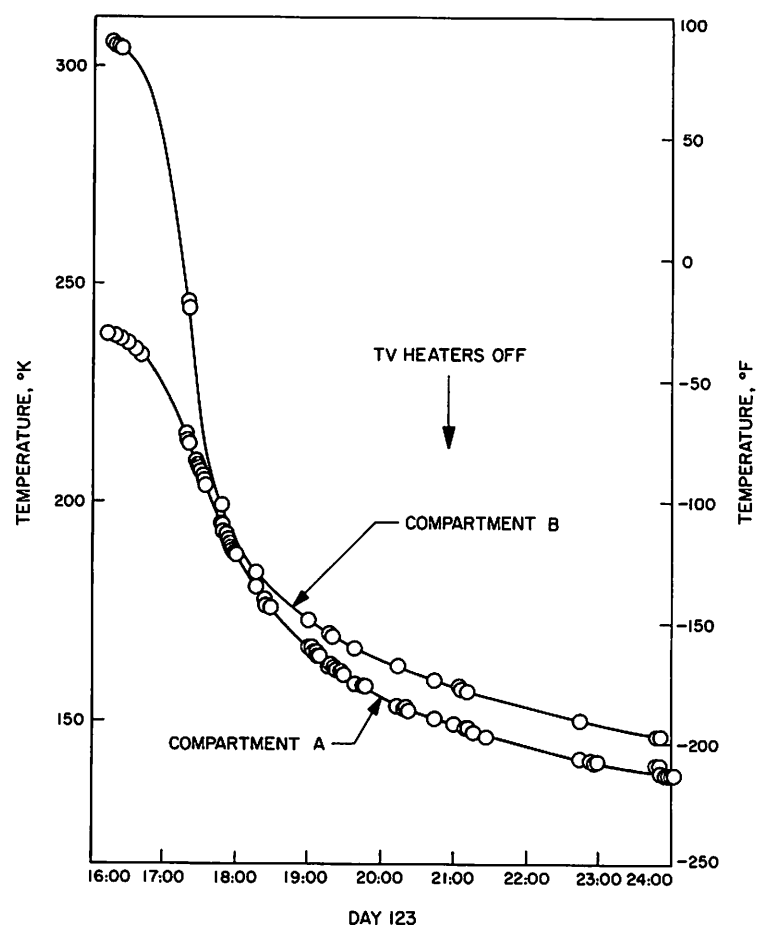

Fig. VI-14. Temperatures of outboard faces of compartments A and B during sunset

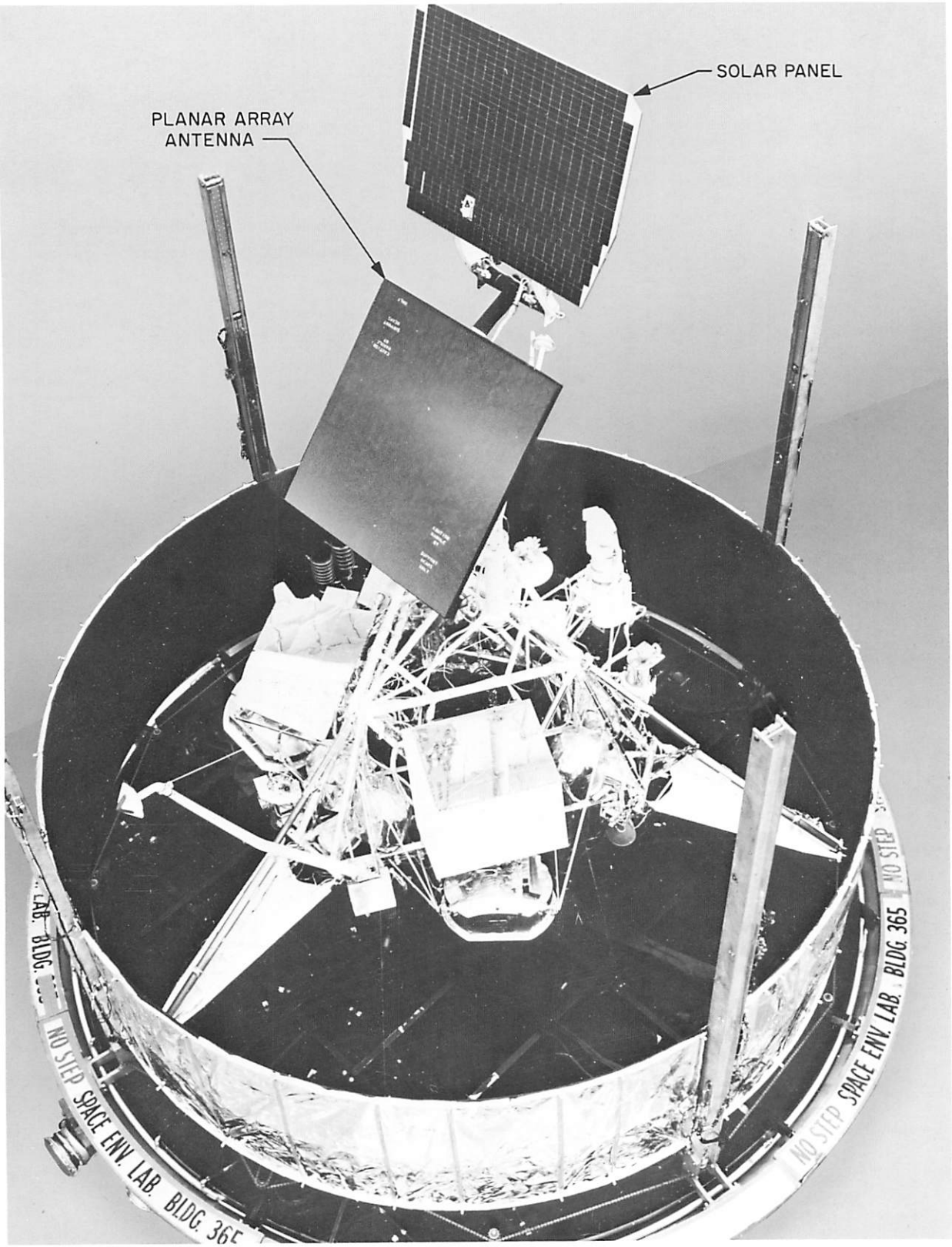

Fig. VI-15. *Surveyor* spacecraft model, showing solar panel and planar array antenna

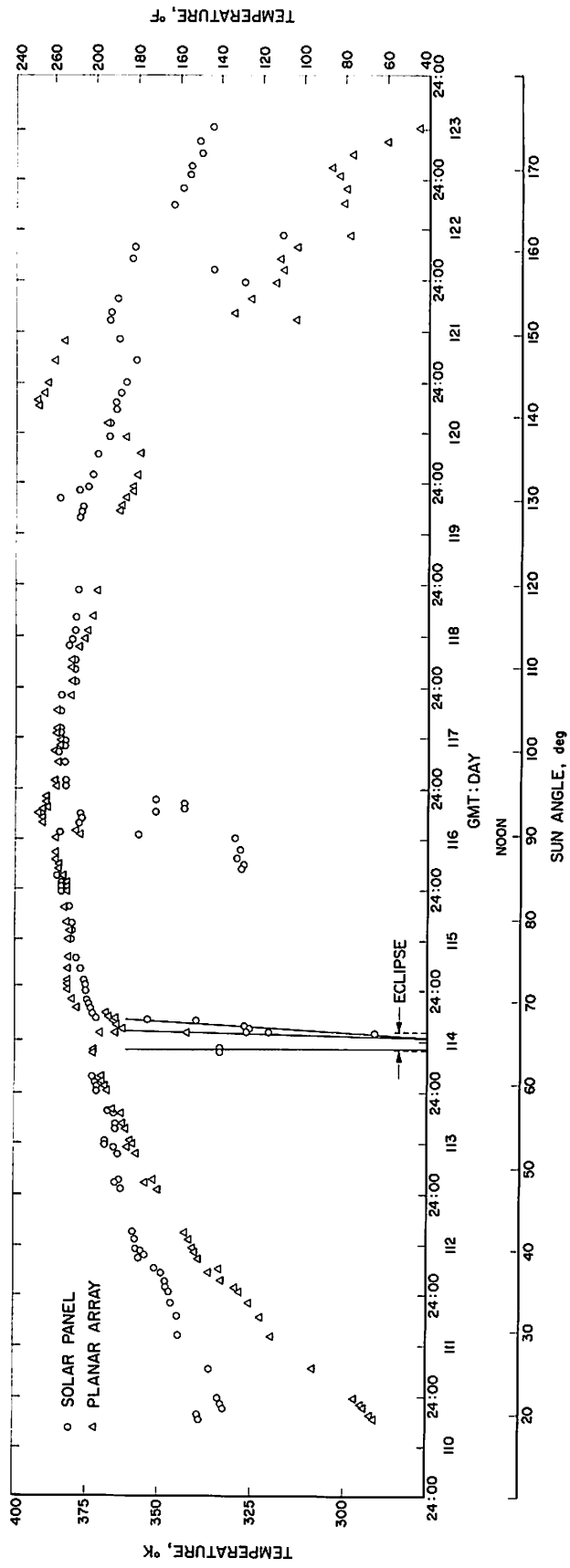

Fig. VI-16. Temperatures of solar panel and planar array antenna during lunation

The parameters needed to compute lunar surface temperatures by the methods described in this report are:

(1) Solar panel properties.

(a) Surface area.

Front: 0.85 m^2.

Back: 0.91 m^2.

(b) Total heat capacity: 0.76 kg-cal/h°C.

(c) Conductance (front to back): 50 kg-cal/h°C.

(d) Solar normal absorptance.

Front surface: 0.76 ±0.02.

Back surface: 0.30 ±0.02.

(e) Infrared hemispherical emittance.

Front surface: 0.80 ±0.02.

Back surface: 0.84 ±0.02.

(f) Angle between normal to solar panel and spacecraft −Z axis.

Eclipse (Day 114): 117 deg.

Lunar night (Day 123): 44.5 deg.

(g) Angle between −X axis and projection of normal into XY plane (measured toward −Y axis).

Eclipse: 140.4 deg.

Lunar night: 306.0 deg.

(2) Planar array antenna properties.

(a) Surface area.

Front (projected): 0.97 m^2.

Back (total): 1.40 m^2.

(b) Total heat capacity: 1.04 kg-cal/h°C.

(c) Conductance (front to back): 16.8 kg-cal/h°C.

(d) Solar normal absorptance: 0.80 ±0.02.

(e) Infrared hemispherical emittance: 0.88 ±0.02.

(f) Angle between normal to planar array antenna and spacecraft −Z axis.

Eclipse: 31.0 deg.

Lunar night: 34.5 deg.

(g) Angle between −X axis and projection of normal into XY plane (measured toward −Y axis).

Eclipse: 140.4 deg.

Lunar night: 126.0 deg.

Solar panel and planar array antenna temperature data are presented in Figs. VI-16 through VI-19. The angles between the normal to the solar panel and the sun vector, and to the spacecraft −Z axis are shown in Fig. VI-20. Figure VI-21 shows the angles between the normal to the planar array antenna and the sun vector, and to the spacecraft −Z axis.

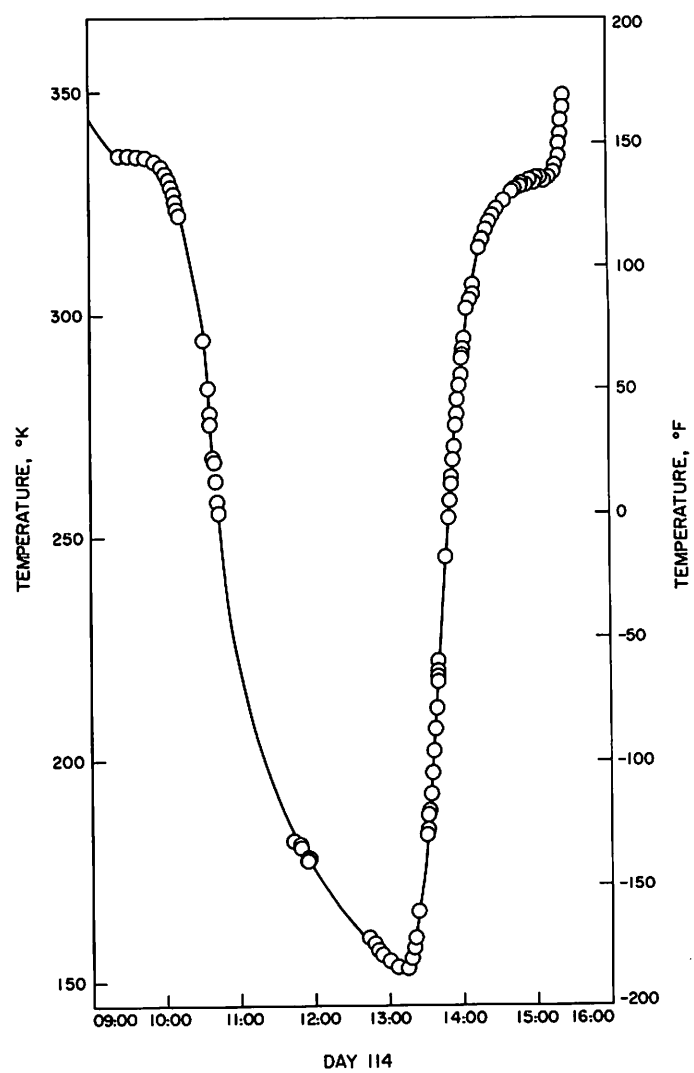

Fig. VI-17. Temperatures of solar panel during eclipse

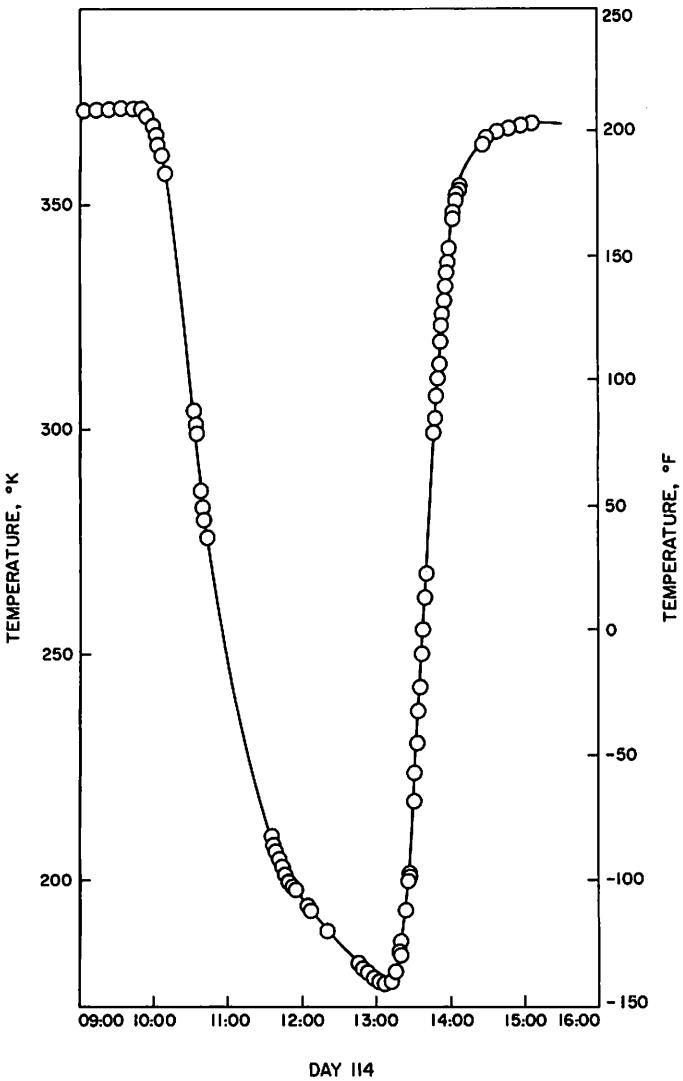

Fig. VI-18. Temperatures of planar array antenna during eclipse

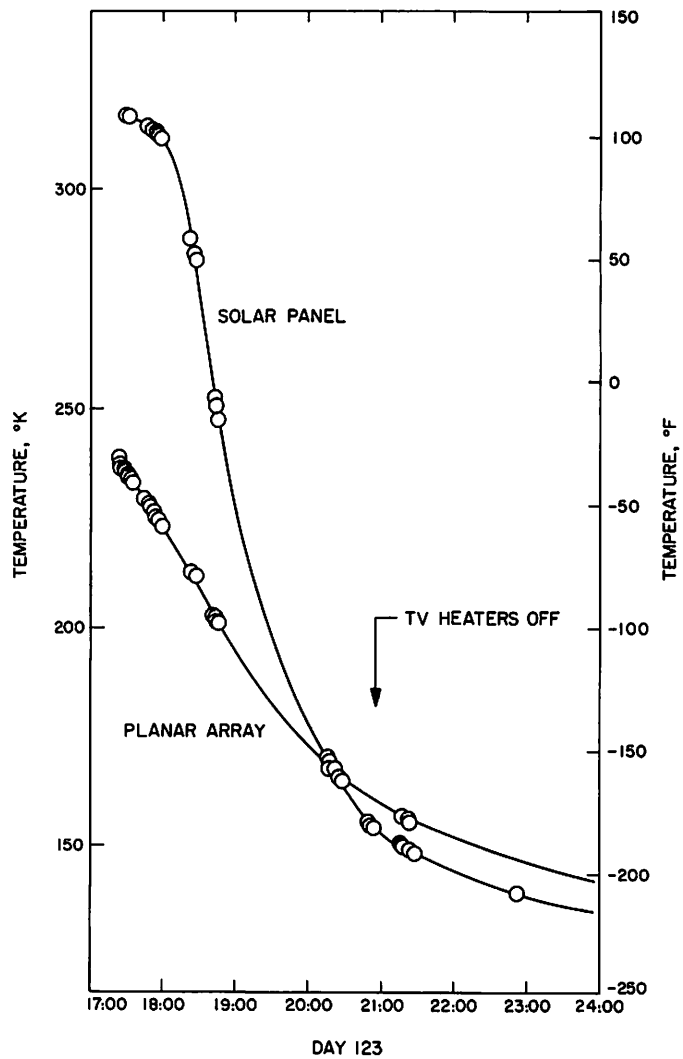

Fig. VI-19. Temperatures of solar panel and planar array antenna during sunset

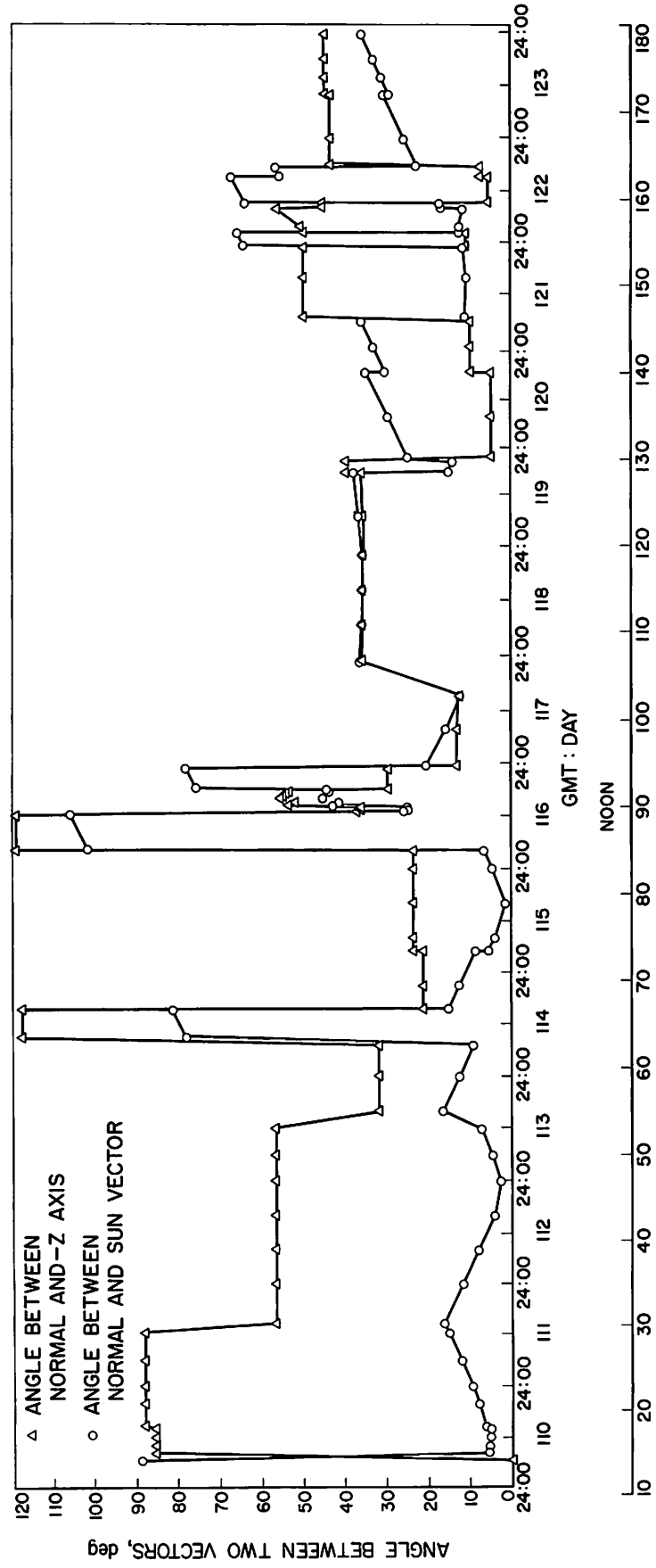

Fig. VI-20. Angle that normal to solar panel makes with sun vector and −Z axis

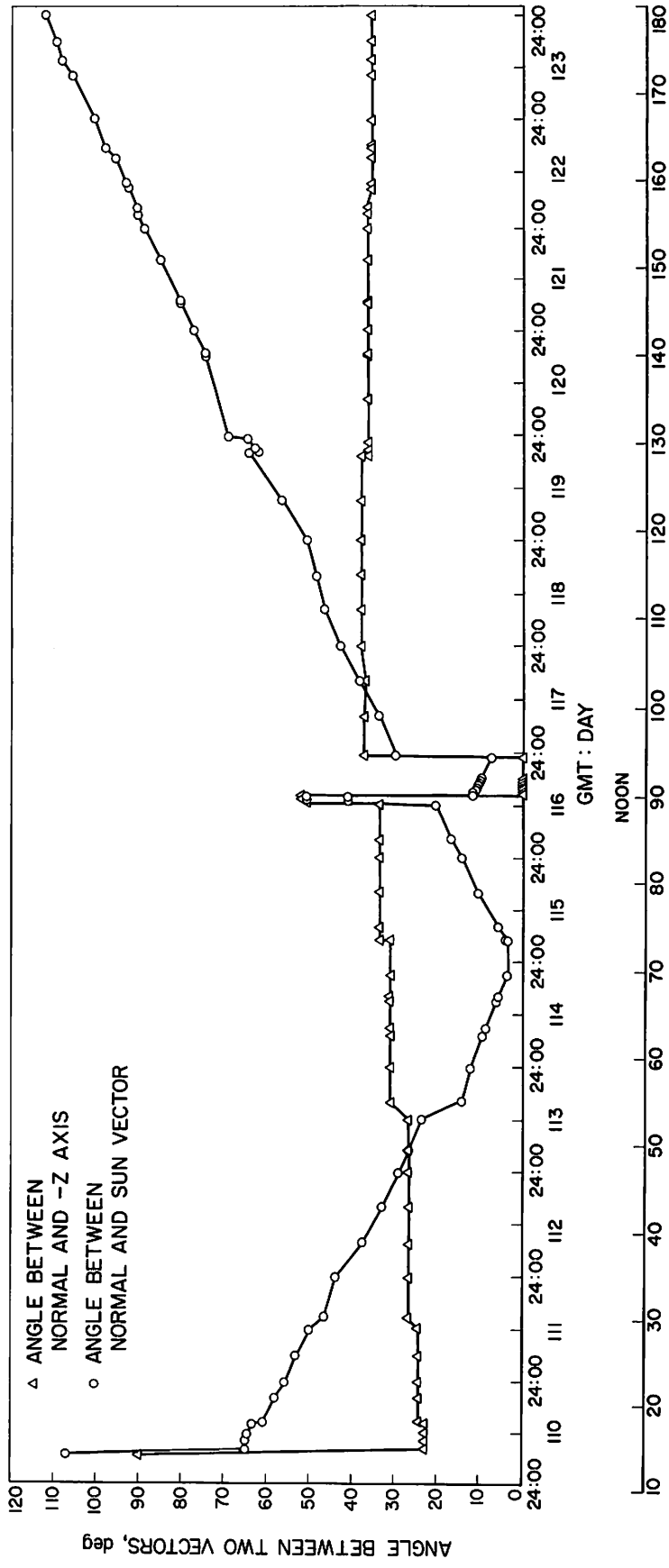

Fig. VI-21. Angle that normal to planar array antenna makes with sun vector and −Z axis

c. Thermal instrumentation. Surveyor carries 75 platinum resistance temperature sensors, which are located at various points in the spacecraft; primary consideration was given to operational hardware and key thermal interfaces. Each sensor is calibrated individually to ±1°C; other nominal-system inaccuracies degrade the system to ±3°C.

During the three landing events, the engineering measurements telemetry system experienced damage that resulted in an abrupt downward shift of all temperature data. Post-mission studies by telemetry and signal processing experts have produced a set of correction factors felt to be accurate to ±3°C for the sensor data presented in this report. Thus, the over-all accuracy of telemetered temperatures from *Surveyor III* is ±6°C.

E. Shading Effects on Compartments

On Day 116 (April 26), stepwise solar panel and planar array antenna positioning maneuvers were conducted to determine the effects of shading on compartment B temperature measurements (Fig. VI-22). Conduction heat-transfer effects between elements of the compartment canister, as well as radiation heat transfer between the canister and the RADVS antenna, were obtained by differentially shading these elements.

The following solar panel and planar array antenna positioning sequence was performed on Day 116:

Phase	Time, GMT	Experiment
I	04:03 to 04:23	Unshade RADVS, face and top of compartment B
	04:23 to 12:18	Hold
II	12:18 to 12:55	Shade RADVS, face and top of compartment B (Fig. VI-22a)
	12:55 to 14:00	Hold
III	14:00 to 14:30	Unshade RADVS (Fig. VI-22b)
	14:30 to 16:00	Hold
IV	16:00 to 16:10	Unshade face of compartment B (Fig. VI-22c)
	16:10 to 18:00	Hold
V	18:00 to 18:07	Unshade top of compartment B
	18:07 to 20:00	Hold

Results of the thermal experiment are shown in Fig. VI-23. Initial temperature, with compartment B and RADVS antennas unshaded (phase I), was found to be 324°K (124°F). Shading compartment B and RADVS antennas (phase II) introduced a ΔT of −6.7°K (−12°F). Unshading the RADVS (phase III) raised the compartment B temperature 0.6°K (1°F). The rise in the curve

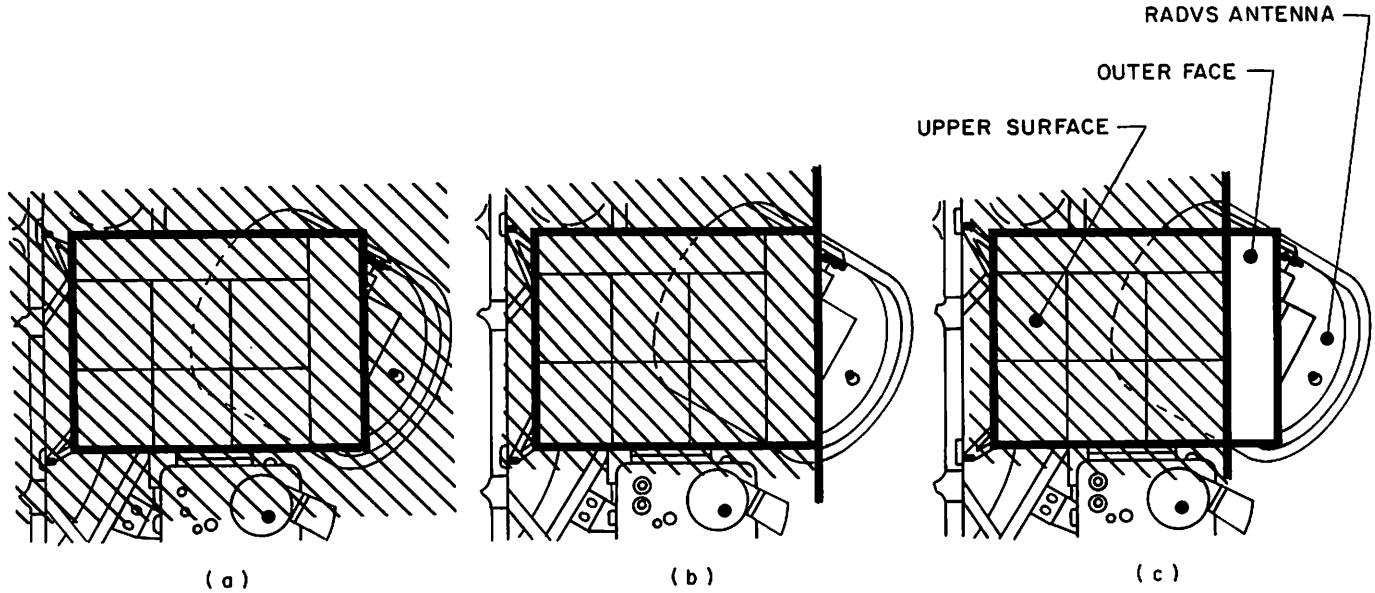

Fig. VI-22. Shading configuration for compartment B during shading experiment

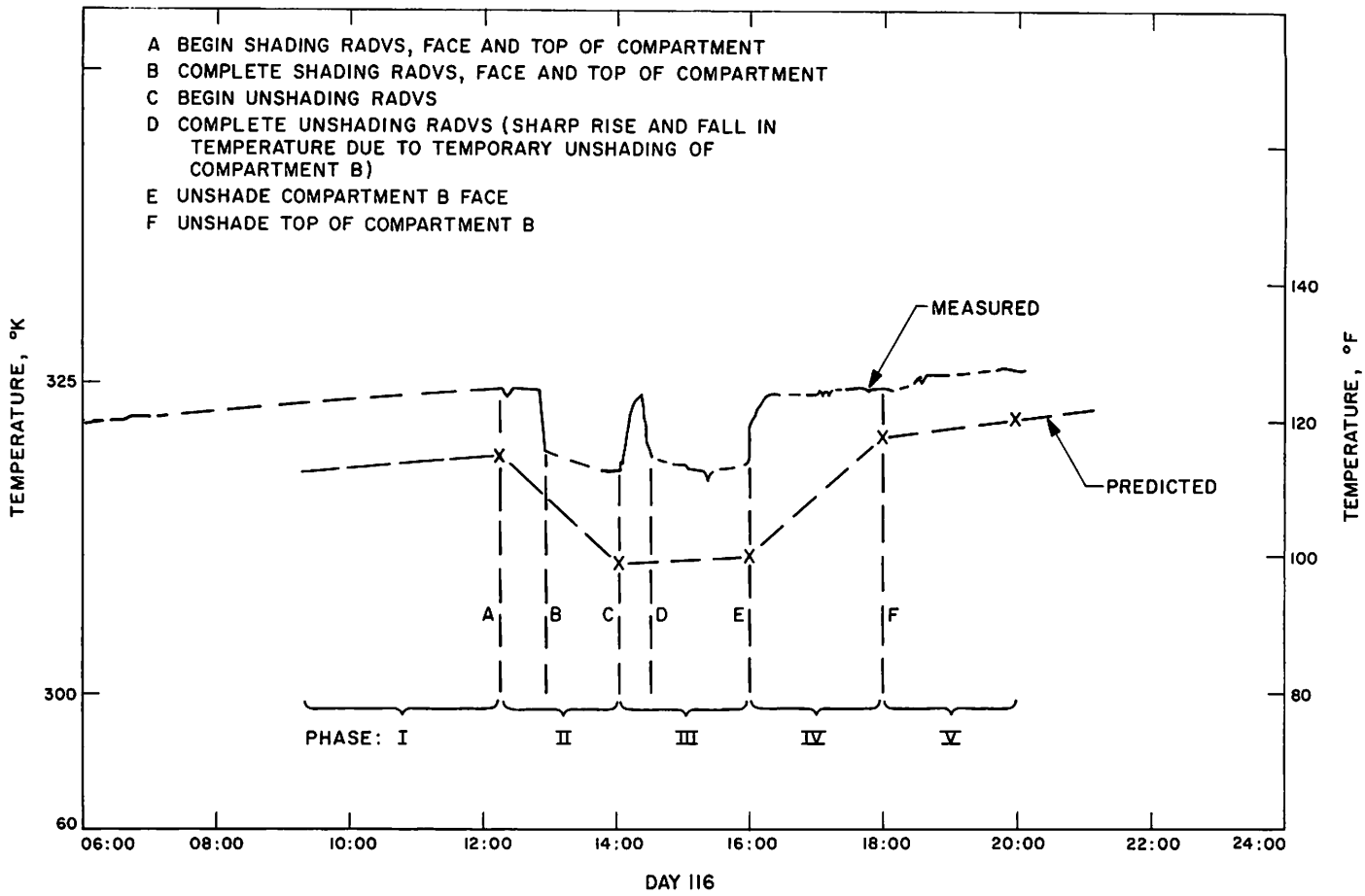

Fig. VI-23. Temperatures of compartment B during shading experiment

between C and D is accounted for by a temporary unshading of the compartment B outboard face during the positioning maneuvers necessary to unshade only the RADVS antennas. Unshading the compartment outboard face (phase IV) introduced a ΔT of 6.1°K (11°F). Unshading the top of compartment B (phase V) resulted in a ΔT of 0.8°K (1.5°F) in the canister sensor temperature. The 1.7°K (3°F) increase in base temperature (unshaded) from point A, beginning of shading, to 20:00 GMT (end of experiment) resulted from the greater sun angle incident to the canister outboard face at the end of the experiment.

The thermal experiment provided excellent data for evaluating shading effects on the spacecraft thermal compartments. Measured temperatures indicate that radiation heat-transfer effects between the center of the outer face of the compartments and other elements of the spacecraft are negligible. Observed changes in temperature agreed well with predictions, although the absolute temperatures predicted were slightly lower (Fig. VI-23). The predictions were based on preliminary calculations as to spacecraft orientation; therefore, these differences in absolute temperatures are not considered significant. Because of the excellent data received for compartment B, it was decided not to duplicate the experiment with compartment A.

F. Lambertian Lunar Surface Temperature Calculations

Calculations were performed using the following equation [taken from Ref. VI-9, Eq. (VI-2)]:

$$\sigma T_2^4 = \frac{\sigma T_1^4}{\varepsilon_2 (F_{12} - F_{13})} - \frac{F_{13}}{F_{12} - F_{13}} \sigma T_3^4 - \frac{\alpha_{1s} S}{\varepsilon_1 \varepsilon_2 (F_{12} - F_{13})} \left[(F_{12} - F_{13}) \rho_2 \sin \phi + \cos \beta \right] - \frac{\dot{q}}{\varepsilon_1 \varepsilon_2 (F_{12} - F_{13})} \quad (6)$$

where

T_1 = compartment surface temperature

T_2 = lunar surface brightness temperature

T_3 = lunar surface brightness temperature in shadow, $T_3^4 << T_2^4$ is assumed.

S = 1386 W/m²

F_{12} = geometric view factor from 1 to 2

= 0.31 for compartment A for 0-deg horizon (Section VI-C of this report)

= 0.41 for compartment B for 11-deg horizon (Section VI-C of this report)

F_{13} = geometric view factor from 1 to 3

$\dot{q}$ = conduction heat flux between inside and outside of compartment wall

= 3.5 W/m²

σ = Stefan-Boltzmann constant

= 5.675×10^{-8} W/m² °K⁴

ε_1 = compartment surface emittance

= 0.87 ±0.02

ε_2 = lunar surface emittance

= 1.0

α_{1S} = compartment surface solar absorptance

= 0.20 ±0.02

β = angle between direction of sun and normal to compartment surface, from Fig. VI-10

ϕ = sun angle (between lunar surface and direction of sun)

$\rho_2 \equiv A$ = 0.076 = lunar reflectivity to solar irradiation

The view factor F_{13} from compartment B is plotted in Fig. VI-24; F_{13} from compartment A is negligible.

1. Lunation

Figure VI-25 represents the lunar surface brightness temperature for the lunar day as calculated from compartment A and B telemetered temperatures using Eq. (6). It is suggested that compartment B indicates a higher lunar surface temperature early in the day than does compartment A because compartment B senses (1) a higher lunar surface temperature on the western part of the crater due to the relatively greater sun elevation angle there and (2) a higher directional lunar surface temperature at that time, because compartment B views the lunar surface more directly along the sun line direction. In the afternoon, the reverse is true.

In Figs. VI-26 and VI-27, lunar surface temperatures indicated by compartments A and B are shown separately. Also shown are the computed curves previously given in Fig. VI-1, but shifted 10 deg to the right in sun angle to account for local lunar surface tilt toward the west at the *Surveyor III* landing site (see Section III of this report). There is fair agreement in the morning, good agreement at noon, and fair agreement in the afternoon with predicted Lambertian temperatures.

Lunar surface brightness temperatures derived from compartment B data on *Surveyors I* and *III* are compared in Fig. VI-28. The curves are plotted for corresponding sun angles, but with the *Surveyor I* curve shifted 10 deg to the right. The strong correspondence between the two curves shows that essentially identical lunar surface brightness temperatures were observed for sun elevation angles above 30 deg. This is not surprising because a wide range of γ values yield the same day temperatures.

2. Eclipse

Figure VI-29 shows the lunar surface temperature data indicated by compartments A and B during the eclipse. Except for the initial portion of the first penumbral stage and the final portion of the second penumbral stage, both compartments sensed essentially the same lunar surface temperatures during the eclipse. This indicates that (differing) directional lunar surface temperatures, which are sensed by the two compartments when under full illumination, are not present at low insolation. Note also that both components sensed the same lunar surface temperature when communication with the spacecraft was terminated shortly after sunset (Fig. VI-25).

Also included in Fig. VI-29 is the predicted lunar surface temperature during the eclipse (given in Fig. VI-2). The spacecraft sensed a lunar surface temperature that lagged and did not fall as low as predicted. Using eclipse cooling curves of Jaeger (Ref. VI-6), it is estimated that a lunar surface with an effective γ of about 400

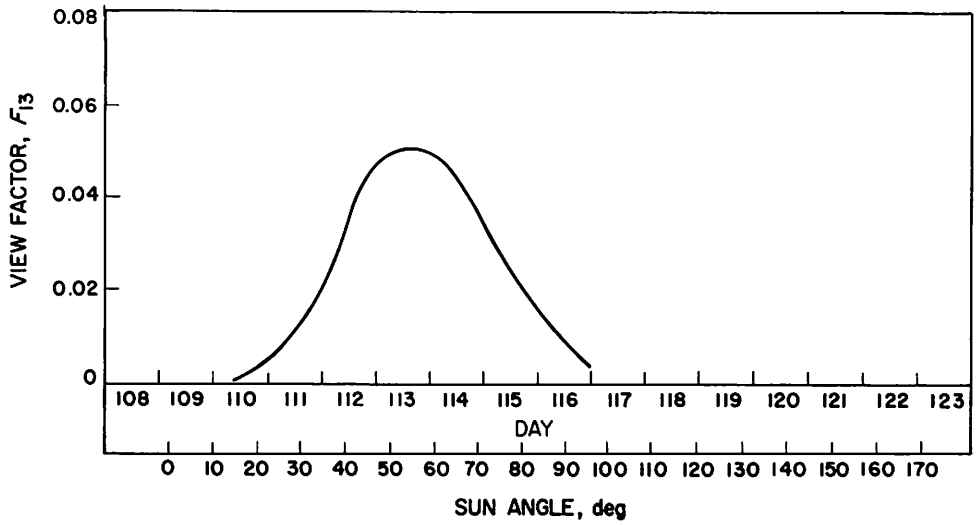

Fig. VI-24. F_{13} for compartment B (view factor between compartment B and shaded part of lunar surface)

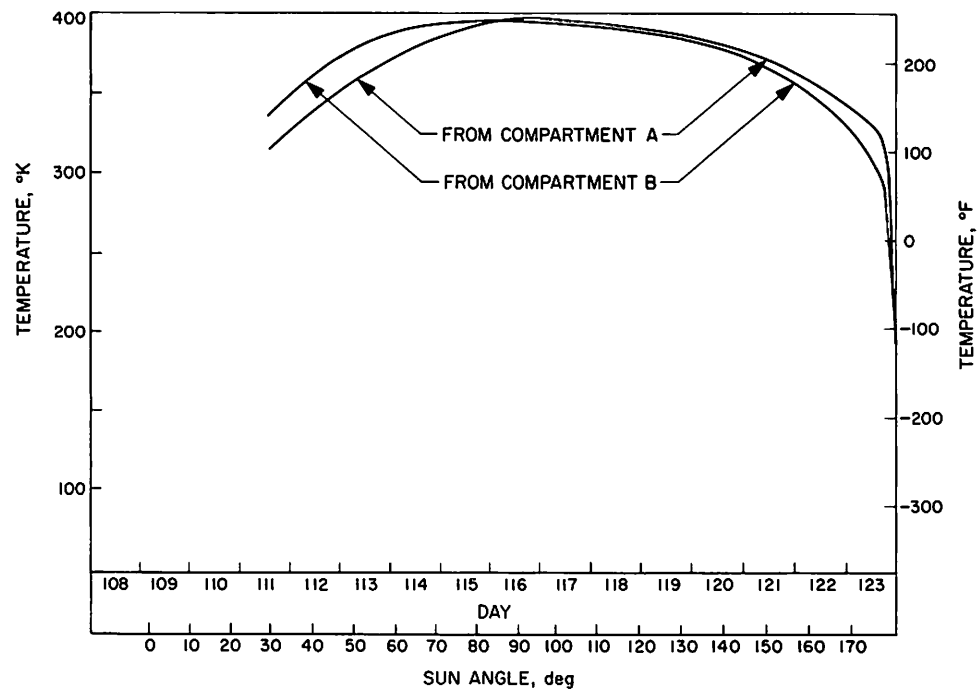

Fig. VI-25. Lunar surface temperatures, as calculated from telemetry data

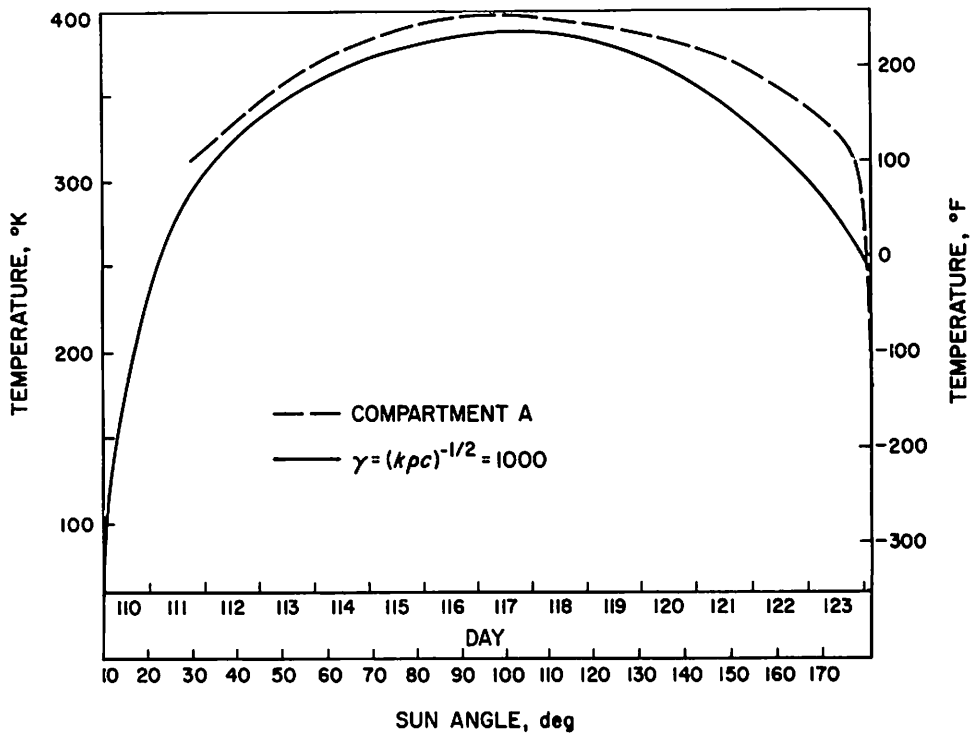

Fig. VI-26. Lunar surface brightness temperatures during lunation from compartment A data compared with predicted temperatures

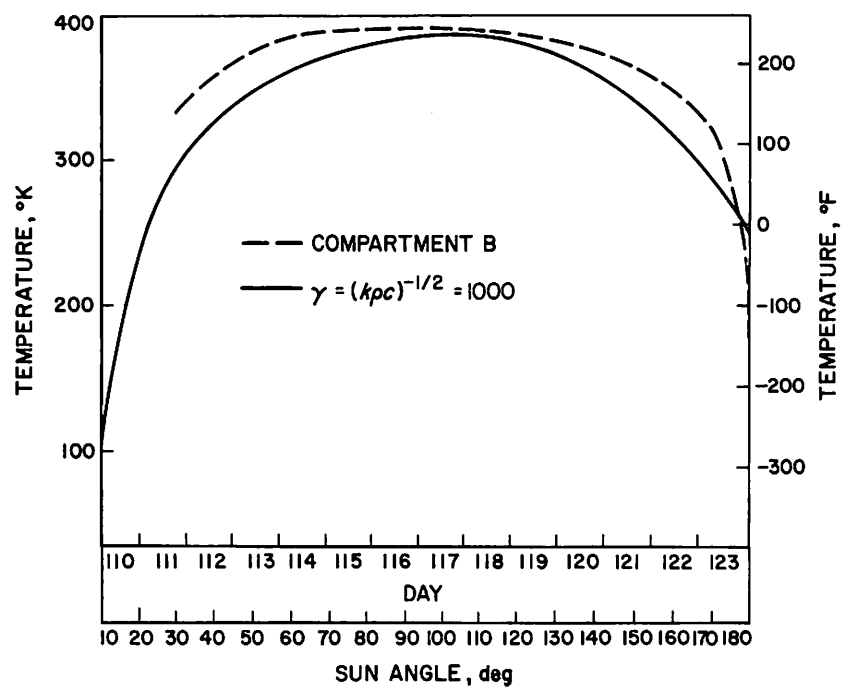

Fig. VI-27. Lunar surface brightness temperatures during lunation from compartment B data compared with predicted temperatures

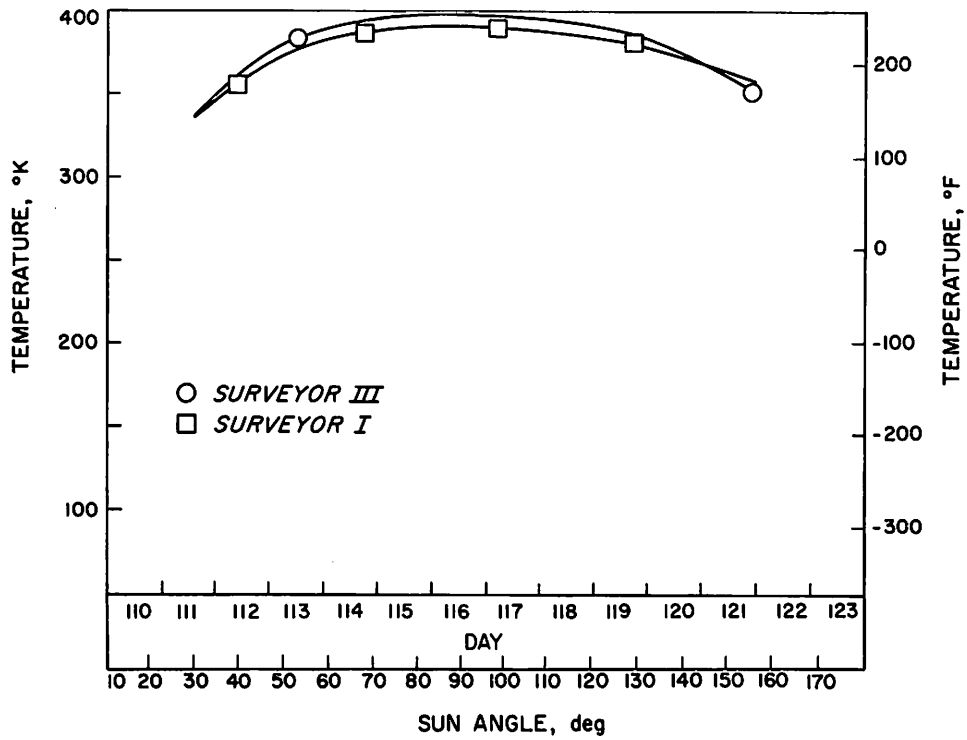

Fig. VI-28. Lunar surface brightness temperatures from compartment B data on *Surveyors I* and *III* (*Surveyor I* curve adjusted in time to *Surveyor III*)

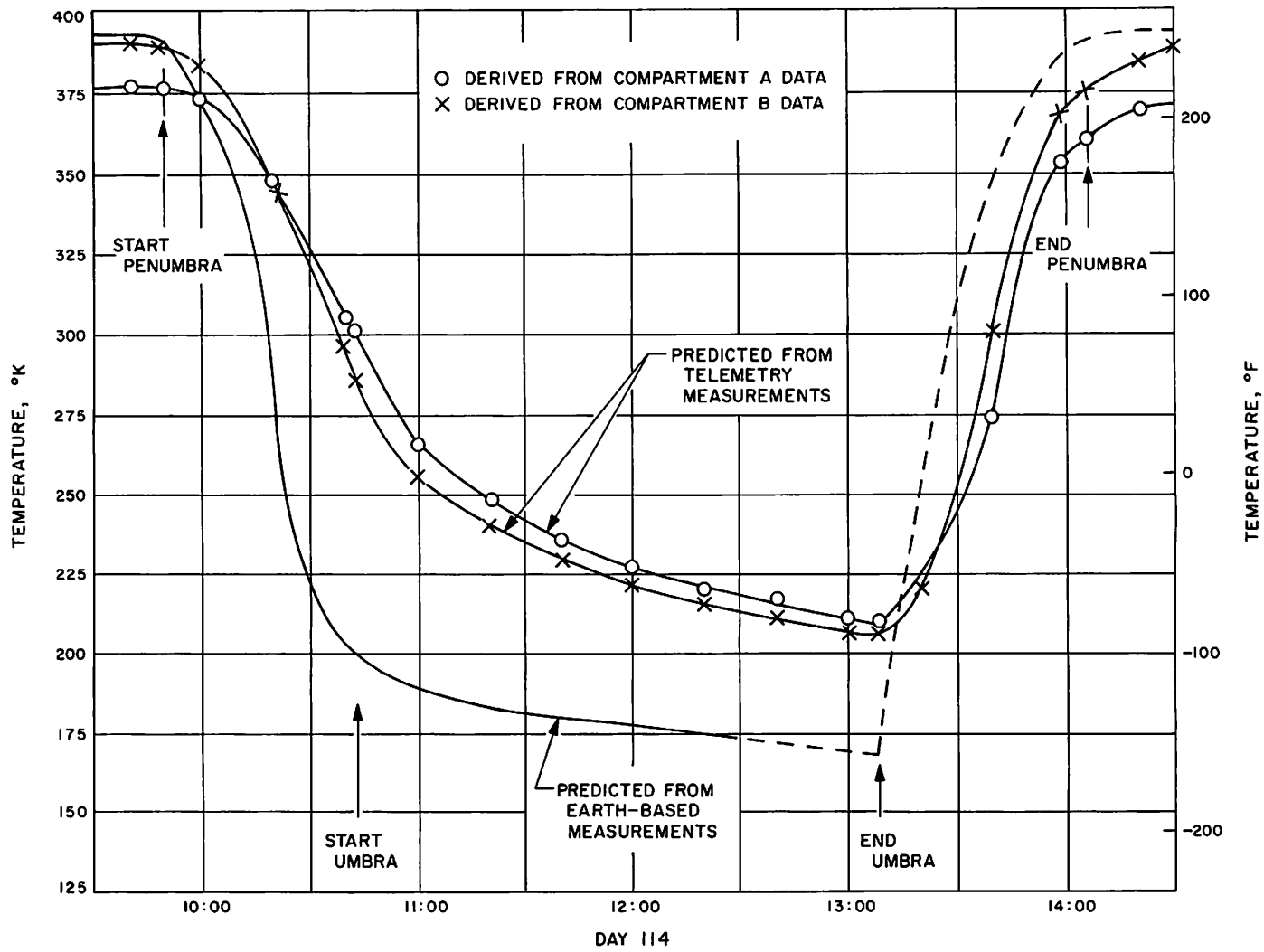

Fig. VI-29. Lunar surface brightness temperatures during eclipse

would exhibit the observed cooling curve. It was determined that the heat capacity of the compartment cover could contribute a negligible portion of the observed lag between compartment temperatures and expected lunar surface temperatures.

It should be noted that the cause of the elevated cooling curve cannot be accounted for by a heat-transfer cavity effect in the crater. A possible cavity effect was assessed, using the curves in Ref. VI-10, and found to be negligible. If the crater were flattened, the observed cooling curve would remain.

The heat capacity of lunar surface blocks was considered. From television observation, 1% of the lunar surface, as viewed from directly overhead, is covered with blocks 2 cm and larger (see Section III). Since most of the lunar surface seen by the compartment A and B faces is viewed at a low incidence angle, it is estimated that 10% of the lunar surface, as viewed from the compartment faces, consists of blocks 2 cm and larger.

Applying calculated cooling curves for postulated 3-cm rock cubes resting on top of the surface[1] failed to appreciably increase the expected lunar surface temperature. The postulated 3-cm rock cooled down approximately 50% at the end of the umbral phase from the pre-eclipse lunar surface temperature. This compares with a 43% drop of the lunar surface temperature as calculated from the compartment temperatures. Taking into consideration a 10-cm rock, but assuming that one-half of the rock is exposed and the other half is buried below the surface, the rocks still failed to increase the lunar surface temperature appreciably, considering that only 10% of the view consists of blocks.

G. Directional Lunar Surface Temperature Calculations

Surveyor III compartment A and B outboard surface temperature profiles during the lunar day were predicted on the basis of the earth-based observed directional lunar surface temperature data described previously. The observed temperature of a specific area on the lunar surface is dependent on the sun and elevation and azimuth angles of the compartment (Fig. VI-30). When the azimuth angle is small, the compartment (looking with the sun) sees higher temperatures; when the compartment looks against the sun, lower temperatures are seen.

[1]J. M. Saari, private communication.

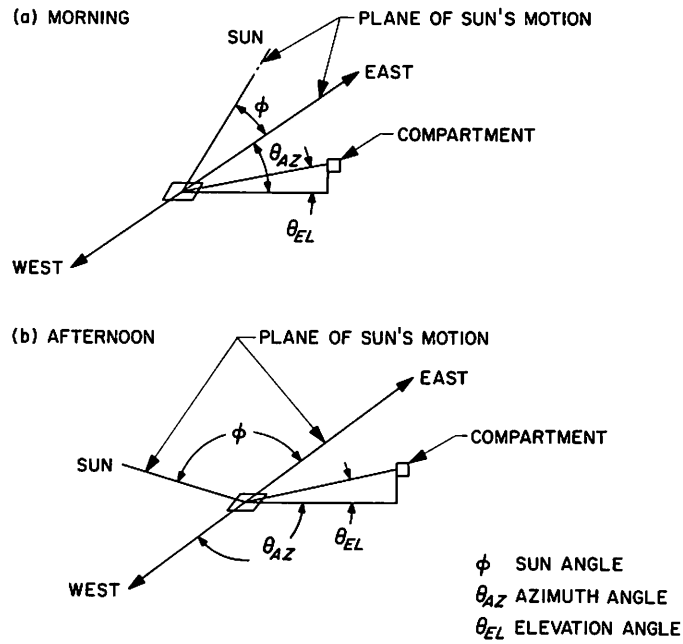

Fig. VI-30. Definition angles

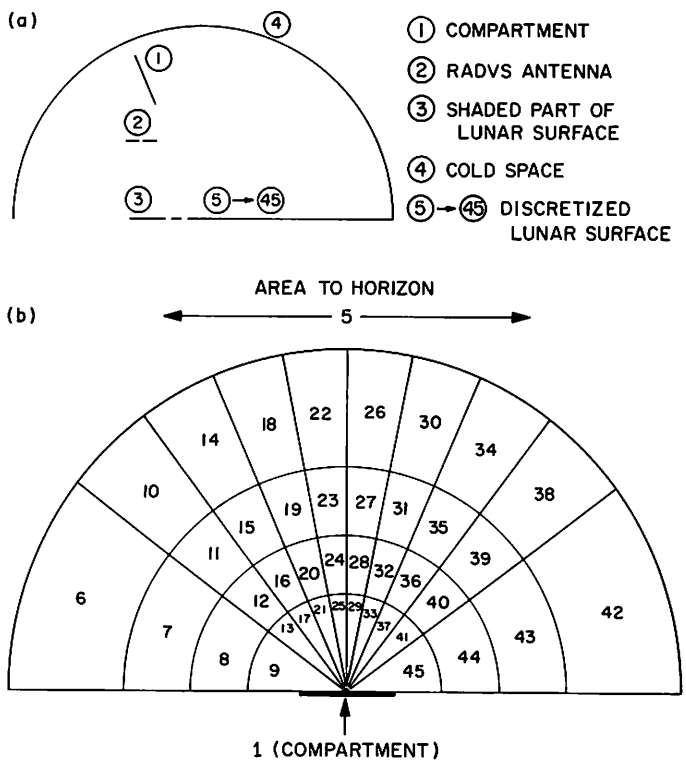

Fig. VI-31. (a) Mathematical model; (b) discretized lunar surface

Forty-five nodes were used in the mathematical model: the compartment, the RADVS antennas, the cold space, the spacecraft shadow on the lunar surface, and the sunlit lunar surface (Fig. VI-31a). The lunar surface

was divided into 41 nodes, each assumed to be flat and isothermal (Fig. VI-31b). The JPL Thermal Analysis System Computer Program (Ref. VI-11) was used for the calculation. The spacecraft shadow on the lunar surface was neglected in this directional analysis.

The lunar surface form factors and associated directional temperatures (Tables VI-1 and VI-2) were computed for a horizontal, flat lunar surface with the spacecraft $-Z$ axis tilted 0 deg toward the lunar surface for compartment A and 11 deg toward the lunar surface for compartment B.

Predicted compartment temperature profiles for sun angles from 30 to 150 deg are plotted in Figs. VI-32 and VI-33. Comparison with the telemetered compartment

Table VI-1. Compartment A directional temperatures

Node	$F_{(1,x)}$ x(5 to 45)	Directional temperature, °F				
		ϕ=30 deg	ϕ=60 deg	ϕ=90 deg[a]	ϕ=120 deg	ϕ=150 deg
5	0.012	116	186	189	186	116
6	0.005	38	161	199	226	201
7	0.005	40	163	224	227	200
8	0.010	48	168	246	230	195
9	0.010	80	191	256	238	170
10	0.005	60	168	194	219	183
11	0.005	62	170	207	219	182
12	0.010	67	175	223	223	178
13	0.010	90	196	249	233	158
14	0.005	75	173	193	211	166
15	0.005	76	174	203	212	166
16	0.010	80	179	217	216	163
17	0.010	97	200	247	229	148
18	0.005	88	176	193	203	151
19	0.005	89	177	202	204	150
20	0.010	92	183	216	208	148
21	0.010	103	203	244	224	139
22	0.005	101	180	193	194	133
23	0.005	102	182	201	195	133
24	0.010	103	187	214	200	133
25	0.010	111	207	244	218	129
26	0.005	114	185	193	187	119
27	0.005	114	186	201	189	119
28	0.010	115	191	214	191	120
29	0.010	118	211	244	213	121
30	0.005	126	190	193	182	108
31	0.005	126	192	202	184	108
32	0.010	126	197	216	189	109
33	0.010	125	216	244	209	114
34	0.005	143	199	193	178	94
35	0.005	143	200	203	179	94
36	0.010	142	205	217	184	97
37	0.010	135	221	247	205	106
38	0.005	164	210	194	173	77
39	0.005	163	211	207	175	77
40	0.010	160	214	223	180	82
41	0.010	147	228	249	200	98
42	0.005	192	223	199	165	50
43	0.005	191	223	224	167	52
44	0.010	186	226	246	172	58
45	0.010	164	236	256	194	85

[a]Based on Ref. VI-8.

temperatures indicates good agreement for both compartments from 30- to 90-deg sun angles. During the lunar afternoon, *both* compartment temperatures are higher than predicted.

Also plotted in Figs. VI-32 and VI-33 are predicted compartment temperatures assuming increased solar absorptance, α_{1S}, values of 0.3 and 0.4. A value of approximately 0.35 brings predicted and observed temperatures of compartment B into reasonable agreement. However, this is not the case for compartment A, which sees little sun in the afternoon. This indicates that changing α_{1S} is not the explanation for the higher afternoon temperatures observed by both compartments.

Table VI-2. Compartment B directional temperatures

Node	$F_{(1,e)}$ x(5 to 45)	Directional temperature, °F				
		ϕ=30 deg	ϕ=60 deg	ϕ=90 deg[a]	ϕ=120 deg	ϕ=150 deg
5	0.005	116	186	180	186	116
6	0.005	143	199	194	178	94
7	0.000	142	202	210	182	96
8	0.001	139	212	233	193	101
9	0.003	129	228	251	216	113
10	0.005	163	209	194	173	78
11	0.005	161	212	210	177	81
12	0.004	151	220	233	189	89
13	0.003	135	232	255	212	109
14	0.010	186	220	194	167	57
15	0.010	183	222	210	171	61
16	0.011	173	229	233	183	74
17	0.010	143	236	255	208	104
18	0.014	200	226	194	162	40
19	0.016	196	228	210	166	46
20	0.016	185	233	233	178	62
21	0.015	148	238	255	205	101
22	0.015	202	226	194	161	37
23	0.018	198	228	210	165	43
24	0.019	186	234	233	177	60
25	0.019	149	239	255	205	100
26	0.015	193	223	194	165	49
27	0.018	189	225	210	169	54
28	0.019	179	231	233	180	68
29	0.019	145	237	255	207	102
30	0.014	173	214	194	171	70
31	0.016	170	217	210	175	73
32	0.016	162	224	233	186	83
33	0.015	138	233	255	210	107
34	0.001	147	201	194	177	91
35	0.010	145	204	210	181	93
36	0.011	142	213	233	192	99
37	0.010	130	228	255	215	112
38	0.000	121	188	194	184	112
39	0.005	121	192	210	188	113
40	0.000	122	203	233	199	115
41	0.003	122	223	255	220	119
42	0.005	99	179	194	195	136
43	0.000	101	183	210	199	135
44	0.001	105	195	233	209	133
45	0.003	114	217	255	226	126

[a]Based on Ref. VI-8.

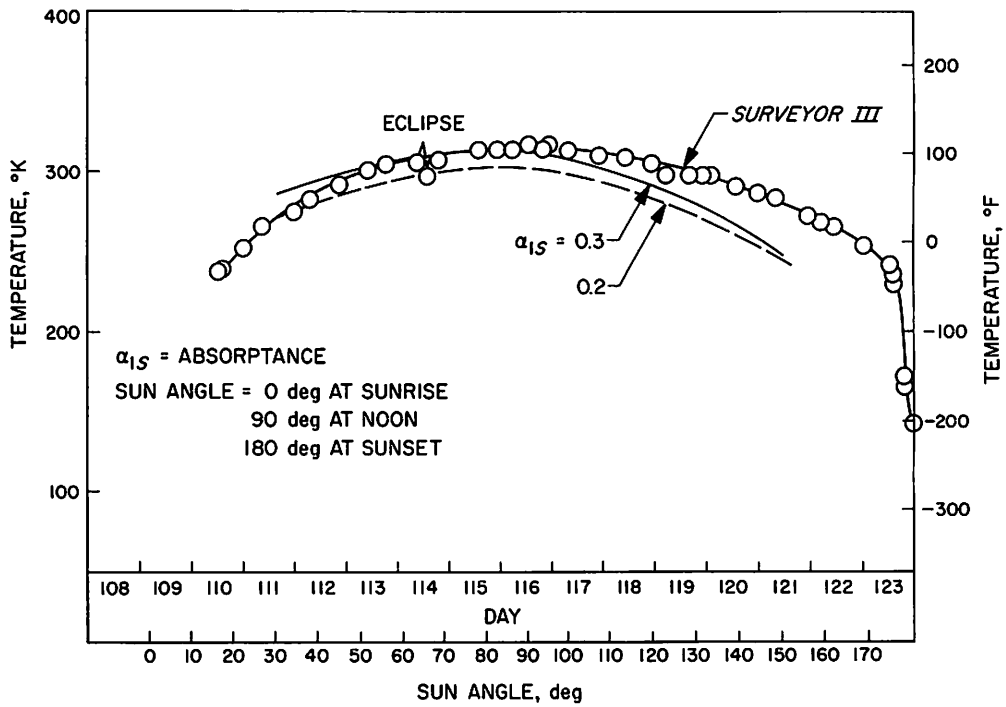

Fig. VI-32. Directional predicted and measured temperatures of outboard face of compartment A

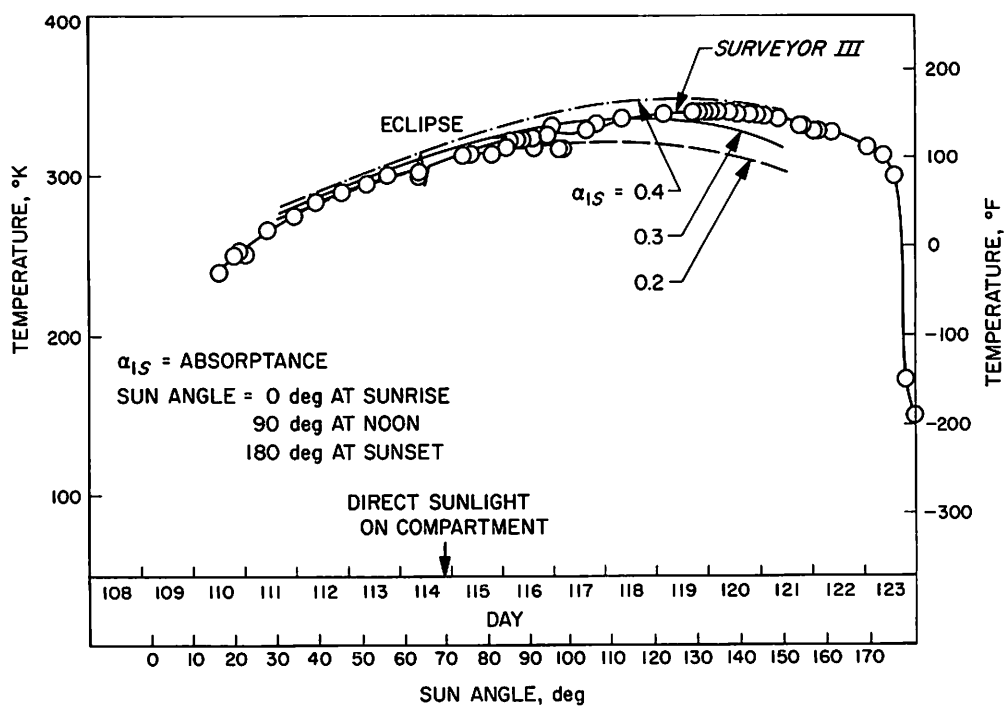

Fig. VI-33. Directional predicted and measured temperatures of outboard face of compartment B

H. Summary

From the analysis, the following tentative conclusions may be drawn:

1. Lunation Data

(1) Predicted and observed lunar surface temperatures from both compartments are in good agreement around noon and are compatible with the homogeneous surface model with thermal inertia, γ, greater than 400. Sunset data are not inconsistent.

(2) Differences in compartment A and B temperatures during the morning may be explained by different local lunar surface sun phase angles and by directional (non-Lambertian) thermal emission from the lunar surface.

(3) Correspondence in lunar surface brightness temperatures measured by *Surveyors I* and *III* indicates lack of any thermally significant dust on compartment faces.

(4) During the afternoon, compartment temperatures are higher than expected from earth-based data. Increased solar absorptance of the compartments does not account for the discrepancy. This is consistent with no thermal indication of dust on the compartment faces.

2. Eclipse Data

(1) Compartments A and B saw essentially the same lunar surface temperature throughout all of the umbral and almost all of both penumbral phases. This indicates Lambertian (i.e., nondirectional) lunar surface emission at low insolation.

(2) During both penumbral phases, observed lunar surface temperatures lagged those predicted from earth-based data; umbral lunar surface temperatures were 40°K above those predicted. Both suggest an effective γ near 400.

References

VI-1. Shorthill, R. W., and Saari, J. M., "Radiometric and Photometric Mapping of the Moon Through a Lunation," *Ann. N. Y. Acad. Sci.*, Vol. 123, Article 2, pp. 722–739, 1965.

VI-2. Shorthill, R. W., and Saari, J. M., *Isothermal and Isophotic Atlas of the Moon: Contours Through a Lunation*, to be published as a NASA publication, 1967.

VI-3. Jones, B. P., "Diurnal Lunar Temperatures," Paper 67-289 presented at AIAA Thermophysics Specialist Conference in New Orleans, La., April 17–20, 1967.

VI-4. Saari, J. M., and Shorthill, R. W., "Thermal Anomalies on the Totally Eclipsed Moon of December 19, 1964," *Nature*, Vol. 205, pp. 964–965, 1965.

VI-5. Shorthill, R. W., and Saari, J. M., "Non-uniform Cooling of the Eclipsed Moon: A Listing of Thirty Prominent Anomalies," *Science*, Vol. 150, No. 210, 1965.

VI-6. Jaeger, J. L., "Surface Temperature of the Moon," *Aust. J. Phys.*, Vol. 6, No. 10, 1953.

References (contd)

VI-7. Six, F., Montgomery, C., Saari, J. M., and Shorthill, R. W., paper presented at AIAA Thermophysics Specialist Conference, New Orleans, La., April 17-19, 1967.

VI-8. Sinton, W. M., "Temperatures of the Lunar Surface," *Physics and Astronomy of the Moon*, (Z. Kopal, ed.), Chapter 11, Academic Press, New York, 1962.

VI-9. Lucas, J. W., Conel, J. E., Hagemeyer, W. A., Garipay, R. R., and Saari, J. M., "Lunar Surface Thermal Characteristics From Surveyor I," *J. Geo. Res.*, Vol. 72, No. 2, pp. 779–789, Jan. 15, 1967. Also in *Surveyor I Mission Report. Part II: Scientific Data and Results*, Technical Report 32-1023, Jet Propulsion Laboratory, Pasadena, Calif., Sept. 10, 1966.

VI-10. Kelly, F. J., and Moore, D. G., *A Test of Analytical Expression for the Thermal Emittance of Shallow Cylindrical Cavities*, NASA SP-55, 1965.

VI-11. Hultberg, J. A., Porter, C. D., and O'Brien, P. F., *Thermal Analysis System I*, JPL Space Programs Summary 37-43, Vol. IV, pp. 140–142, Feb. 28, 1967.

Acknowledgment

Appreciation is extended to all JPL and Hughes Aircraft Company *Surveyor III* development and flight operations engineers for obtaining raw data used. Special thanks are given to K. Y. Eng, Hughes, for providing raw data plots, and to W. Heathcote, Hughes, for special positioning of solar panel during the shading experiment. Thanks are also extended to P. F. O'Brien, the University of California at Los Angeles, for analysis consultations.

VII. Lunar Surface Electrical Properties

W. E. Brown, Jr., R. A. Dibos, G. B. Gibson, D. O. Muhleman, W. H. Peake, and V. J. Poehls

Radar (radar altimeter and doppler velocity sensor, RADVS) preliminary results for *Surveyor III* indicate that the radar cross sections (*rxs*)[1] for the 25-deg off-normal and vertical beams were approximately the same as those obtained by the *Surveyor I* data (Ref. VII-1) and earth-based measurements (Ref. VII-2). The *rxs* values of −12 dB for a 25-deg angle and −8 to −4 dB for the vertical beam yield an estimate[2] of the relative dielectric constant as $\epsilon = 3.5 \pm 0.7$. These values apply to regions external to the crater in which *Surveyor III* landed. The echo data from within the crater have not yet been related to surface slope variations and gain switching transient conditions.

The values of −12 dB and −4 dB for the 25-deg *rxs* and 0-deg *rxs*, the computed value of ϵ, coupled with earth-based measurements of the microwave phase lag angle (40 deg), thermal parameter[3] ($\gamma = 1420$), and specific heat ($c = 0.2$) allow a value for the ratio of electrical loss tangent to density to be computed as

$$\frac{\tan \phi}{\rho} = 2.5 \times 10^{-2} \pm 20\%$$

This ratio tends to be invariant with packing factor and could possibly aid in the identification of the surface material. Quartz-like minerals found on the surface of the earth have a value of approximately 1.5×10^{-2} for this ratio (Ref. VII-3).

The *rxs* for each of the four beams vs altitude is shown in Figs. VII-1 through VII-4. The equations used for converting the signal strength and the geometry of the beams are given in Ref. VII-1. Corrections for the off-normal approach angle at altitudes above 8500 m have not been made; thus, the values for *rxs* on beams 1, 2, and 3 are slightly in error for altitudes above 8500 m. The relatively low values of *rxs* on beam 4 may be a consequence of processing or systematic error. In all beams, there are *rxs* inaccuracies below 1000 m which are apparently caused by gain switching.

[1]The symbol σ is used throughout the literature for radar cross section, but it is also used for conductivity, which will be discussed in subsequent reports. In addition, radar cross section is often confused with reflectivity; therefore, it is considered worthwhile to designate a separate and less ambiguous symbol, *rxs*, for radar cross section.

[2]The estimate of dielectric constant may be determined by many different methods. The wide uncertainties (± a factor of 2) in the published values of *rxs* lead to a wide range of values for dielectric constant as calculated by any single method. Thus, the significance of any estimate of dielectric constant (permittivity) from the *rxs* is somewhat questionable. This estimate would agree with Ref. VII-4 if the backscatter gain were about 0.7, rather than unity. Evidence for backscatter gain less than unity for a dielectric sphere is given in Ref. VII-5.

[3]Please refer to Section VI of this report for additional definition of this parameter.

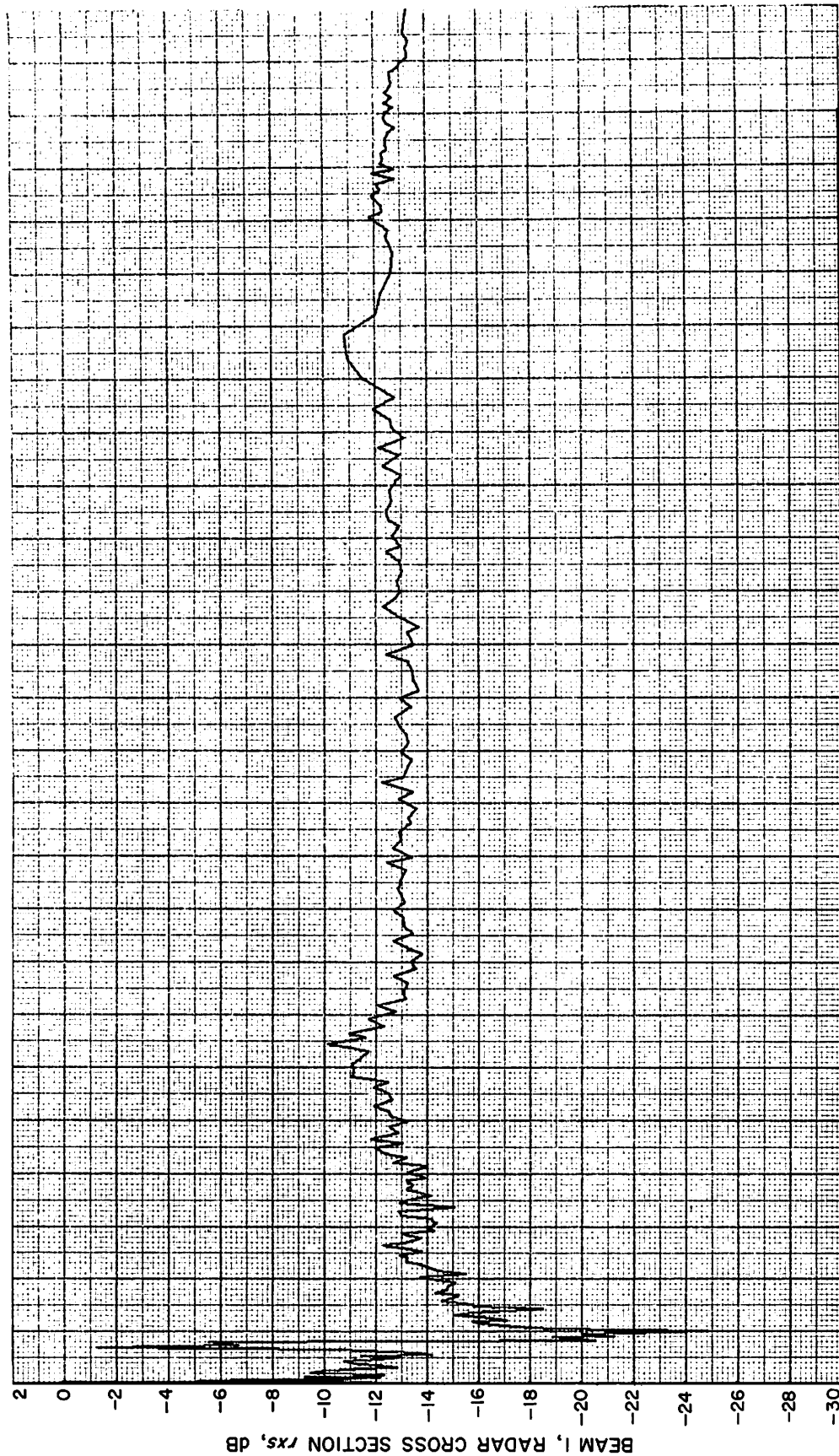

Fig. VII-1. Radar cross section vs altitude, beam 1

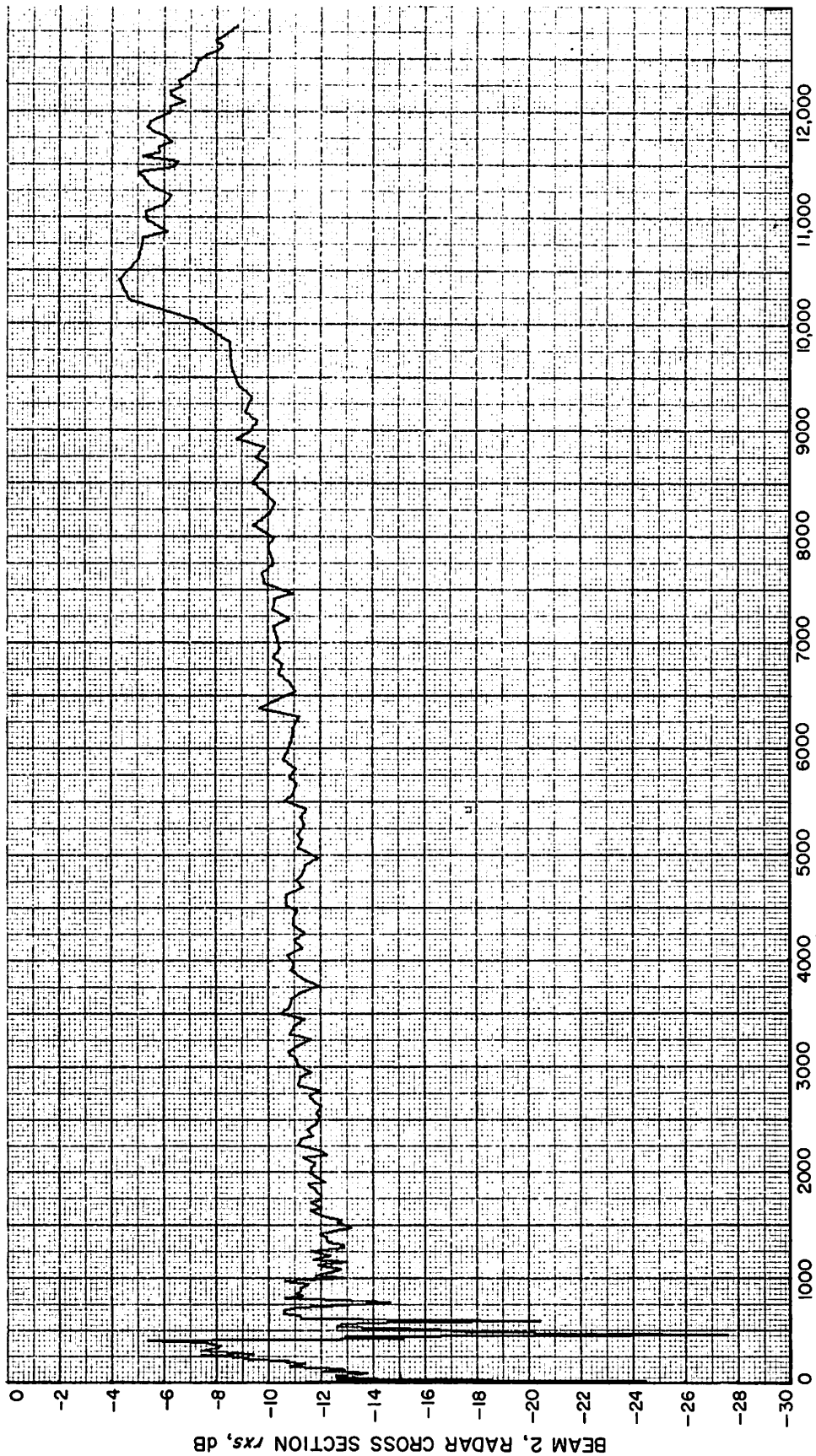

Fig. VII-2. Radar cross section vs altitude, beam 2

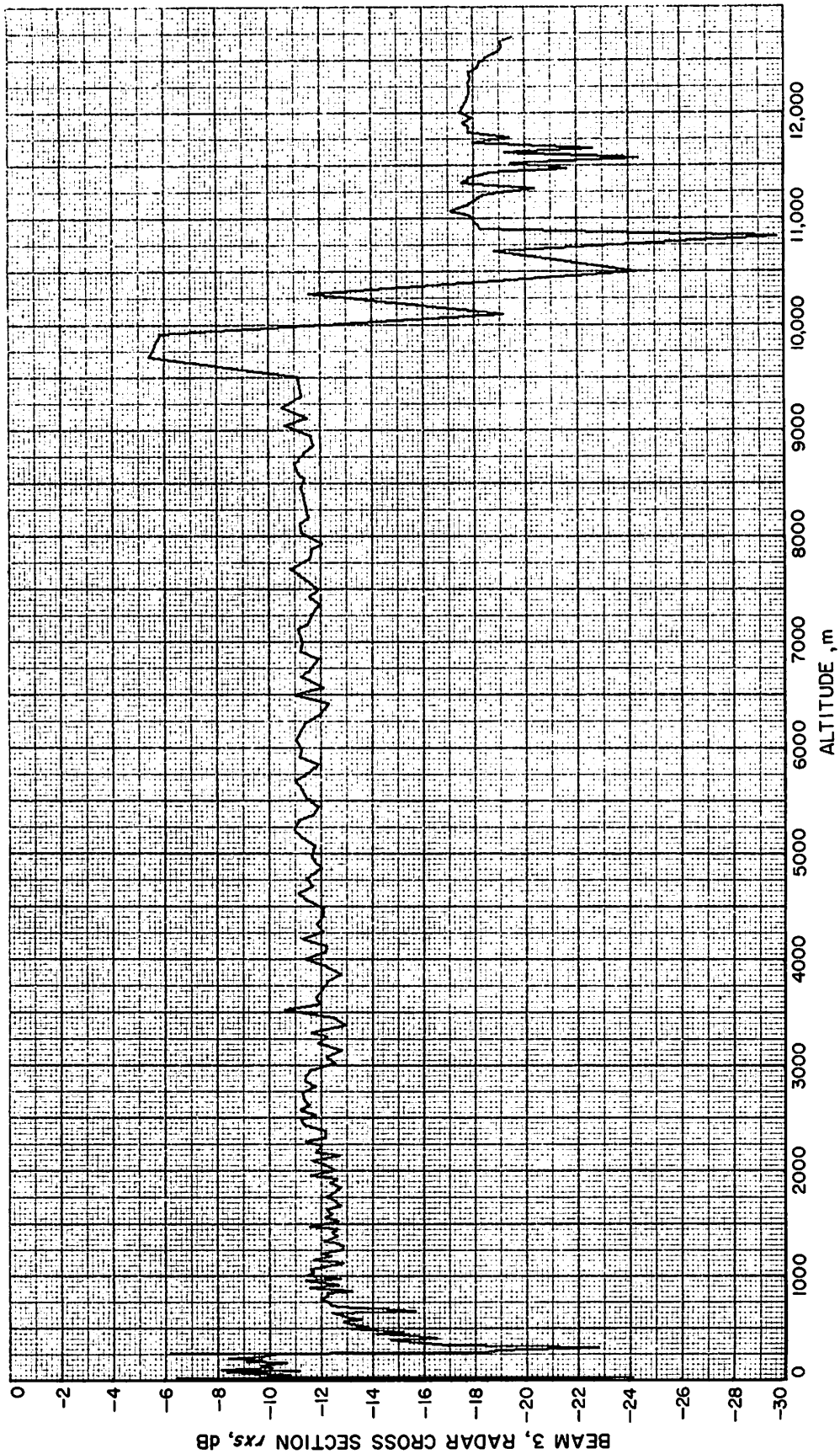

Fig. VII-3. Radar cross section vs altitude, beam 3

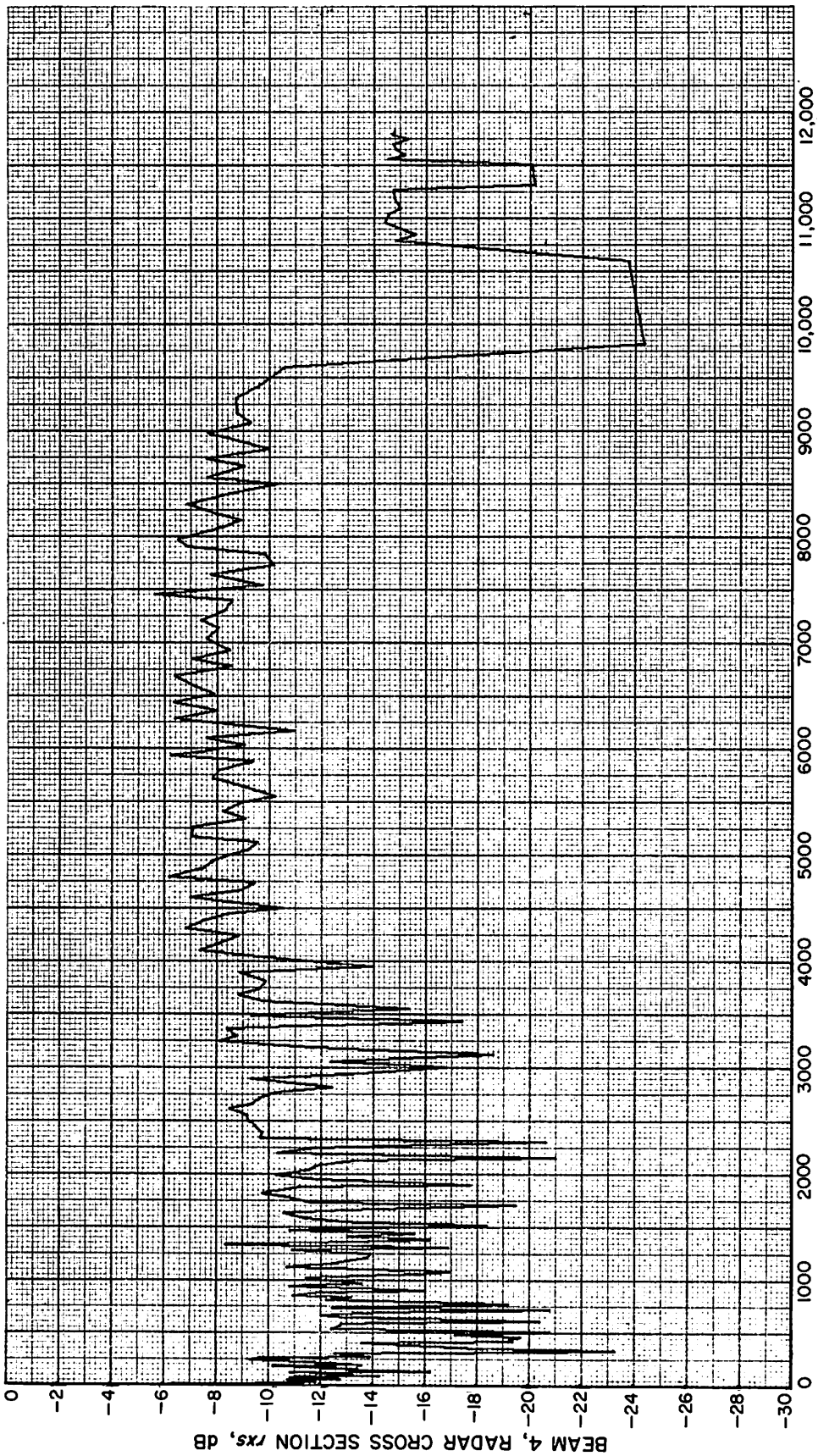

Fig. VII-4. Radar cross section vs altitude, beam 4

References

VII-1. Brown, W. E., Jr., "Lunar Surface Surveyor Radar Response," *J. Geophys. Res.*, Vol. 72, No. 2, p. 791, Jan. 15, 1967.

VII-2. Evans, J. V., *Radio-Echo Observations of the Moon at 3.6 cm Wavelength*, Lincoln Laboratory Technical Report 256, Lincoln Laboratories, Lexington, Mass., Feb. 19, 1962.

VII-3. Troitsky, V. S., "Radio Emission of the Moon, Its Physical State and the Nature of Its Surface," *The Moon*, p. 475, Academic Press, 1962.

VII-4. Evans, J. V., and Pettengill, G. H., "The Scattering Behavior of the Moon at Wavelengths of 3.6, 68, and 784 Centimeters," *J. Geophys. Res.*, Vol. 68, No. 2, p. 439, Jan. 15, 1963.

VII-5. Kerr, D. E., *Propagation of Short Radio Waves*, Vol. 13, Rad Lab Series, McGraw-Hill Book Co., Inc., New York, p. 613, 1951.

VIII. Lunar Theory and Processes

D. Gault, R. Collins, T. Gold, J. Green, G. P. Kuiper, H. Masursky, J. O'Keefe, R. Phinney, and E. M. Shoemaker

Much valuable new information has been provided by *Surveyor III*; some of the most significant and interesting events are presented here. Only a limited interpretive discussion is included at this time, pending completion of data reduction and more detailed analysis of information available from the *Surveyor* mission.

A. Position on Lunar Surface

The location of the spacecraft is shown in Fig. VIII-1, and discussed in detail in Section III of this report. Features are indicated in this figure for reference in the following discussion. Approximate crater profiles, based on photometry of *Lunar Orbiter III* records, are shown in Fig. VIII-2; approximate spacecraft position is indicated on the profile BB'. Figure VIII-3 is a stereoscopic view of the crater composed of two convergent, high-resolution frames from *Lunar Orbiter III*. The right-hand frame is a near-vertical photograph; the other is rectified from a 37-deg tilted photograph.

The crater profiles, determined photometrically, indicate that the depth of the crater is from 22 to 25 m deep and that the slope component in the phase plane at the position of the spacecraft touchdown point is about 13 deg. The latter value corrects to a true slope of about 14 deg. Preliminary photogrammetric reduction of the *Lunar Orbiter III* photographs (Fig. VIII-3), however, indicates, consistent with results presented in Section III, that the photometric technique has overestimated the crater depth, perhaps by a factor of approximately two. Additional analysis will be required to resolve the differences between the two methods. Nevertheless, the results indicate that the eye of the spacecraft (the rotating mirror on the television camera system) is well below the rim crest of the crater.

It is important to emphasize that the rim of the crater is everywhere higher than the television camera on the spacecraft. Thus, the only lunar terrain visible to the *Surveyor III* camera system is restricted to the interior walls of the crater. Differences between the *Surveyor III* site and locations photographed by *Surveyor I*, *Luna IX*, and *Luna XIII* may be attributed to the landing location of *Surveyor III*. Both differences and similarities have fundamental implications in lunar theory and processes.

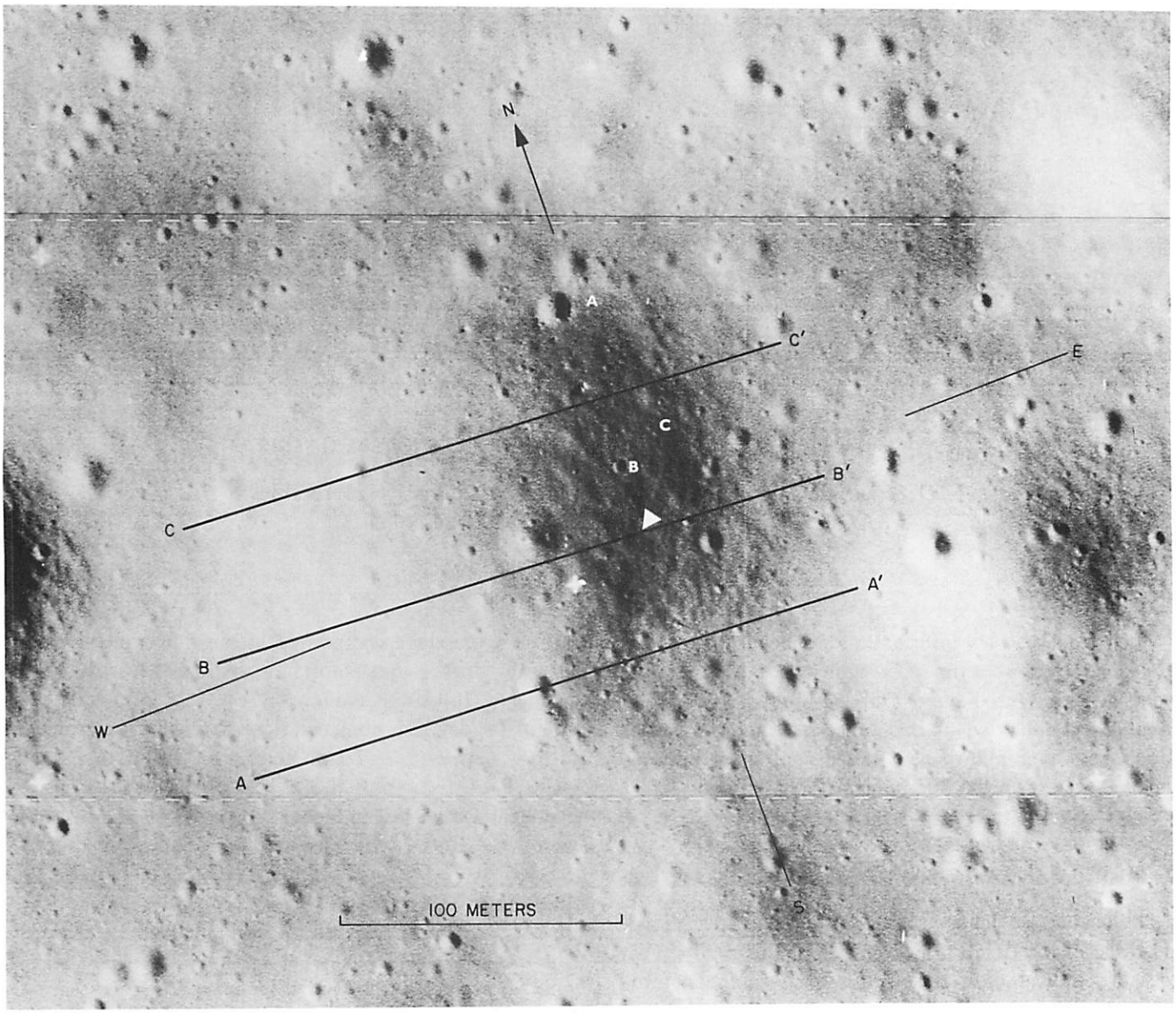

Fig. VIII-1. Portion of *Lunar Orbiter III*, P9, frame H154, showing the crater in which *Surveyor III* landed. The approximate position of the spacecraft is indicated by the triangular spot, and features mentioned in the text are identified with letters and numbers. The lines AA′, BB′, and CC′ define the traces for the photometric determinations used to estimate crater profiles shown in Fig. VIII-2

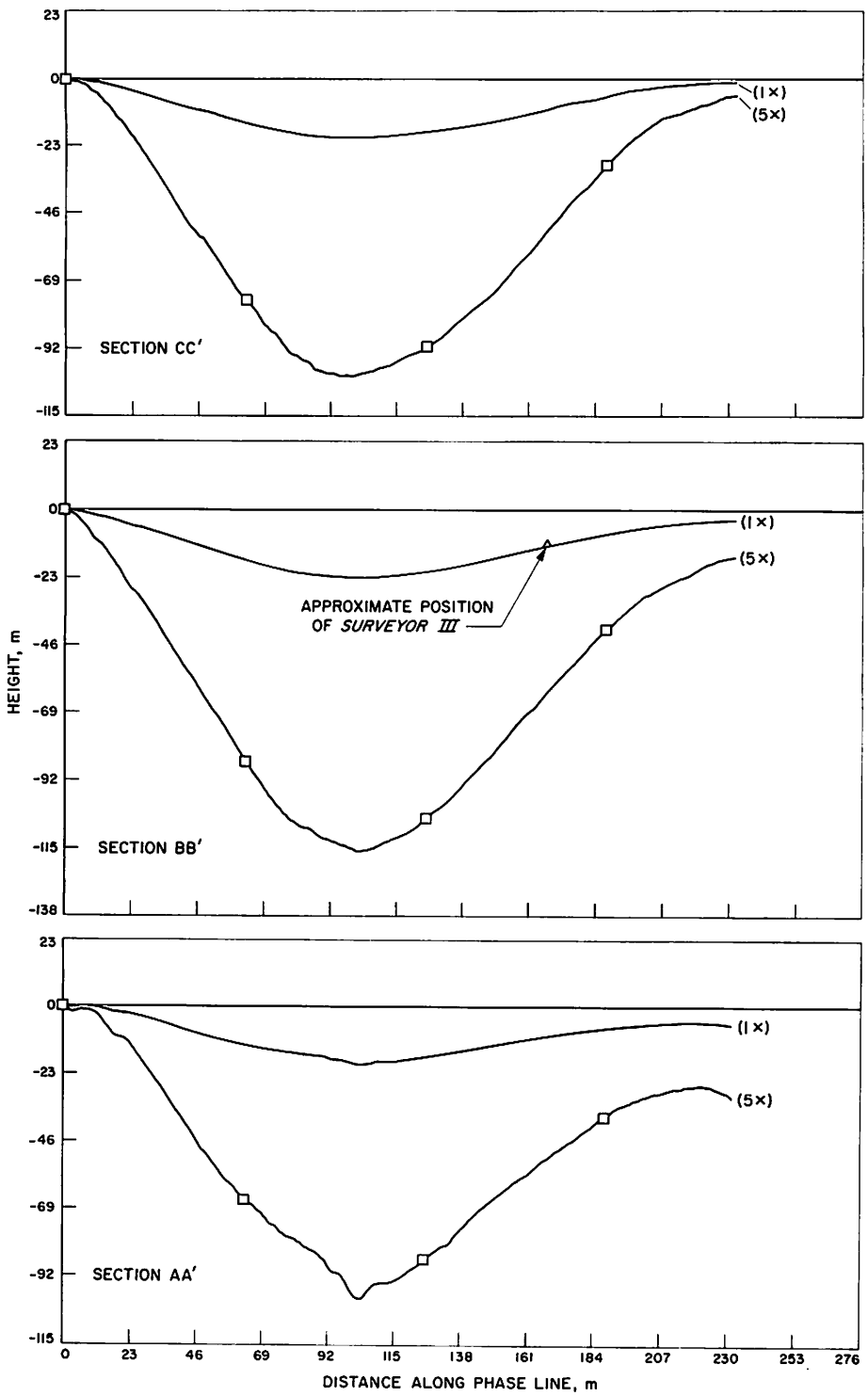

Fig. VIII-2. Topographic profiles of *Surveyor III* crater drawn by photometric methods from *Lunar Orbiter III*, P9, frame H154 (profiles obtained by G. R. Taylor and J. J. Lambiotte, NASA, Langley Research Center)

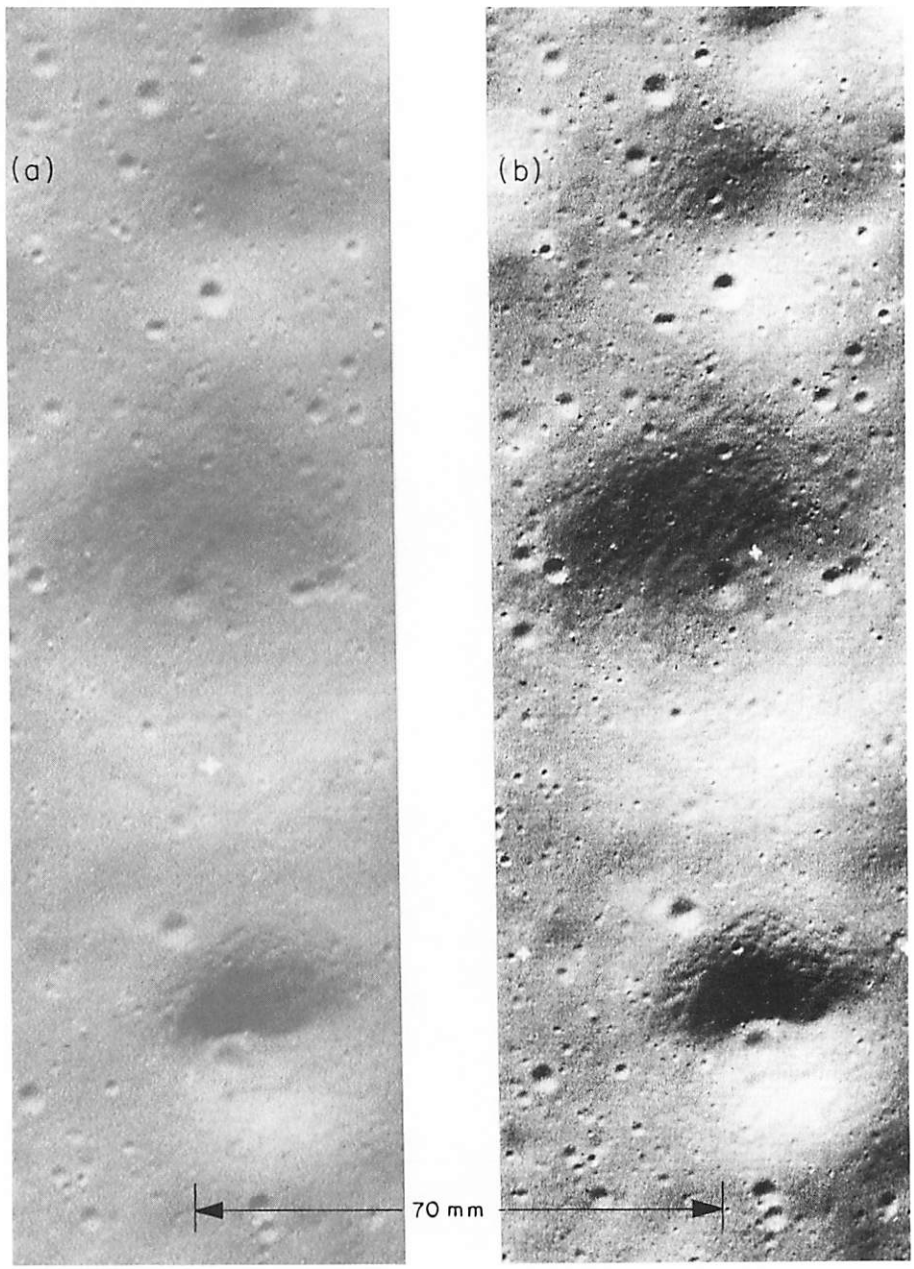

Fig. VIII-3. Stereoscopic pair of *Lunar Orbiter III* photographs of the crater in which *Surveyor III* landed: (a) site 9A, frame H137, rectified by R. A. Altenhofen, USGS; (b) site 9C, frame H154

B. Degradation of Pictures

Quality of some pictures, and thus information obtained during the mission, has been seriously decreased as a result of the degradation of the pictures resulting from scattered light in the optical system. In all cases in which the mirror was not exposed to sunlight, the pictures improve in quality, but still suffer from a general glare, which results in a severe loss of contrast in detail.

Regions of maximum degradation observed in the pictures appear to rotate about the center of the frame as the camera is moved in azimuth. In each case, this degradation is oriented on the frame in such a way that it corresponds to a direction from the camera lens associated with light scattered from the upper half of the mirror. The direction of the sun affects the degree of the degradation, but not its position. The effect is readily apparent in most of the pictures, but is demonstrated

most clearly in Fig. VIII-4,[1] which is a time exposure of the crescent earth obtained as part of observations conducted to determine spacecraft orientation. Figure VIII-4 was taken looking approximately due east with the sun setting directly behind at an angle of approximately 40 deg above the western horizon. The approximate 6-deg field of view is centered about 60 deg above the horizon; the only strong source of light incident on the mirror is that reflected from the lunar surface and from earth. The dark stripe in the upper right-hand

[1]This was brought to our attention by R. H. Steinbacher, JPL.

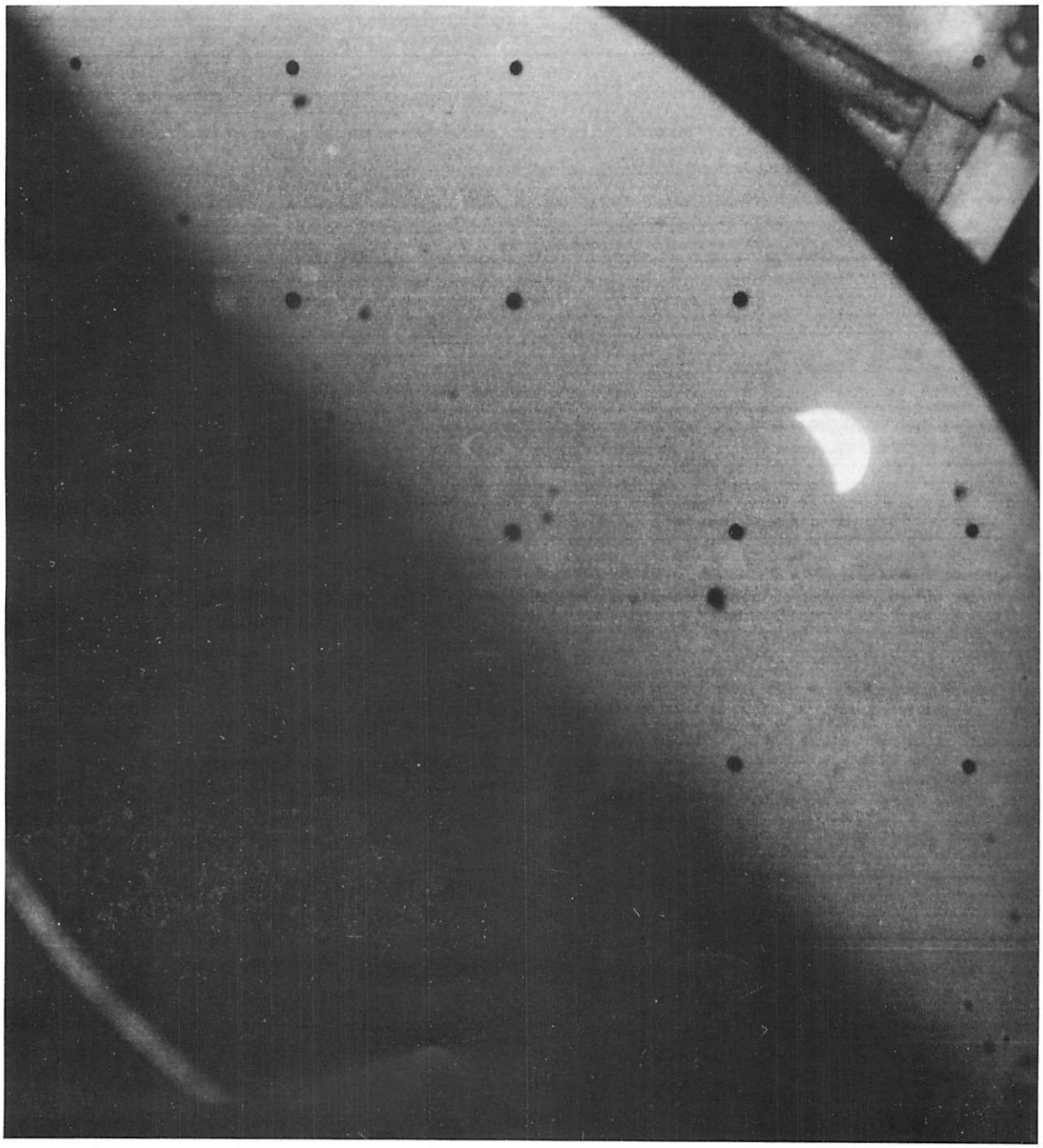

Fig. VIII-4. Time exposure of earth. The broad diffuse band of light extending from the lower right to the upper left is attributed to scattered light from fine particles adhering to the surface of the mirror (Day 120, 10:47:02 GMT)

corner and the bright stripe in the lower left-hand corner define the upper and lower edges of the mirror, respectively. The entire field of view should be dark except for the crescent earth. The broad diffuse white band over the upper half of the mirror appears to be consistent with the glare observed in the photographic images, and is apparently the result of either surface abrasion caused by the impact of fine particulate material that became entrained in the vernier exhaust or a deposit of fine particles and/or effluent from the vernier engines on the surface of the mirror. No such effect was observed in the case of *Surveyor I.*

It seems reasonable to assume that those effects were caused by some difference between *Surveyor I* and *III* missions. In both cases, the mirror was open, and thus exposed to the ambient environment during cislunar flight and touchdown. Exhaust gases from midcourse guidance and main retro maneuvers are not a likely source of contaminant, because the conditions there seem to have been the same as in the case of *Surveyor I.* The principal difference between the two missions occurred during the landing maneuver, when the bipropellant vernier engines (using nitrogen tetroxide and hydrazine derivative as fuel) continued to fire after landing and throughout the time of the first two contacts of the vehicle with the lunar surface. The relatively sharp boundary of the degraded region on the mirror does not seem consistent with the deposition of effluent from the vernier engines. The most likely cause of degradation, therefore, seems to be fine particulate material from the lunar surface sprayed up by the vernier engines. Particles dislodged from the surface by the vernier engine blast either could pit the surface of the mirror or adhere to it, if they were small enough. In fact, the most exposed part of the mirror was the upper half during touchdown; the glare pattern shown in Fig. VIII-4 is entirely consistent with such an orientation of the mirror.

It is possible to estimate the fraction of the surface of the mirror that must be covered with small particles in order to produce the observed degradation. Under the assumption that the particles on the surface of the mirror have the same albedo as the particles on the lunar surface, preliminary estimates suggest that more than 30% of the surface of the upper half of the mirror is covered with small particles. More detailed studies of the photometric properties of the diffused light and the amount of obscuration (when the mirror was in the shade) are required before more detailed conclusions can be drawn. It is significant, however, that if fine particles have adhered to the mirror, it is corroborating evidence for the existence of fine particulate material in the upper surface layers of the moon.

C. Properties of Lunar Surface Layer

Important new data on the physical and mechanical properties of the surficial layer of the lunar surface were obtained from two different sources. The principal source of new information was the soil mechanics surface sampler (SMSS) experiment, described in Section IV of this report. Valuable information was also obtained as a result of the unprogrammed multiple-landing sequence.

Despite the moderate cohesion exhibited by the material of the lunar surface to a depth greater than 15 cm, there is no conclusive evidence that lunar material adhered to the SMSS. The material that spilled involuntarily from the SMSS subsequent to trenching operations may have been "jammed" in the scoop, rather than physically adhering to the interior surfaces. Indeed, within the limits of resolution (1 mm) of the television camera system, it appears that the external surface of the SMSS remained clean throughout its digging operation. This fact seems at first difficult to reconcile with the adhesion of small particles to the mirror of the television camera. It is possible that a layer of fine material, such as that believed to exist on the mirror, also existed on the SMSS. It is significant, however, that no clots or clumps of surface material adhered to the external surface of the SMSS, although brought into intimate contact during the digging operation. The absence of adhesion forces was also displayed by the failure of the darker fine-grained lunar surface material to adhere to the small white-colored rock excavated by the SMSS (Fig. VIII-5a).

An additional observation of potential significance in spite of the limited area observed and photographed is the apparent absence of a raisin-bread texture in the fine particulate material, which was exposed by the SMSS as it first penetrated into the surface. The resultant smooth-textured surface (Fig. VIII-5b) gives no evidence for inclusions of rocks or hard grains large enough to be resolved by the television system.

As described previously, the final landing of the spacecraft was preceded by two other touchdowns (landing events 1 and 2), which preceded the final landing by about 36 and 12 s, respectively. The imprints of landing

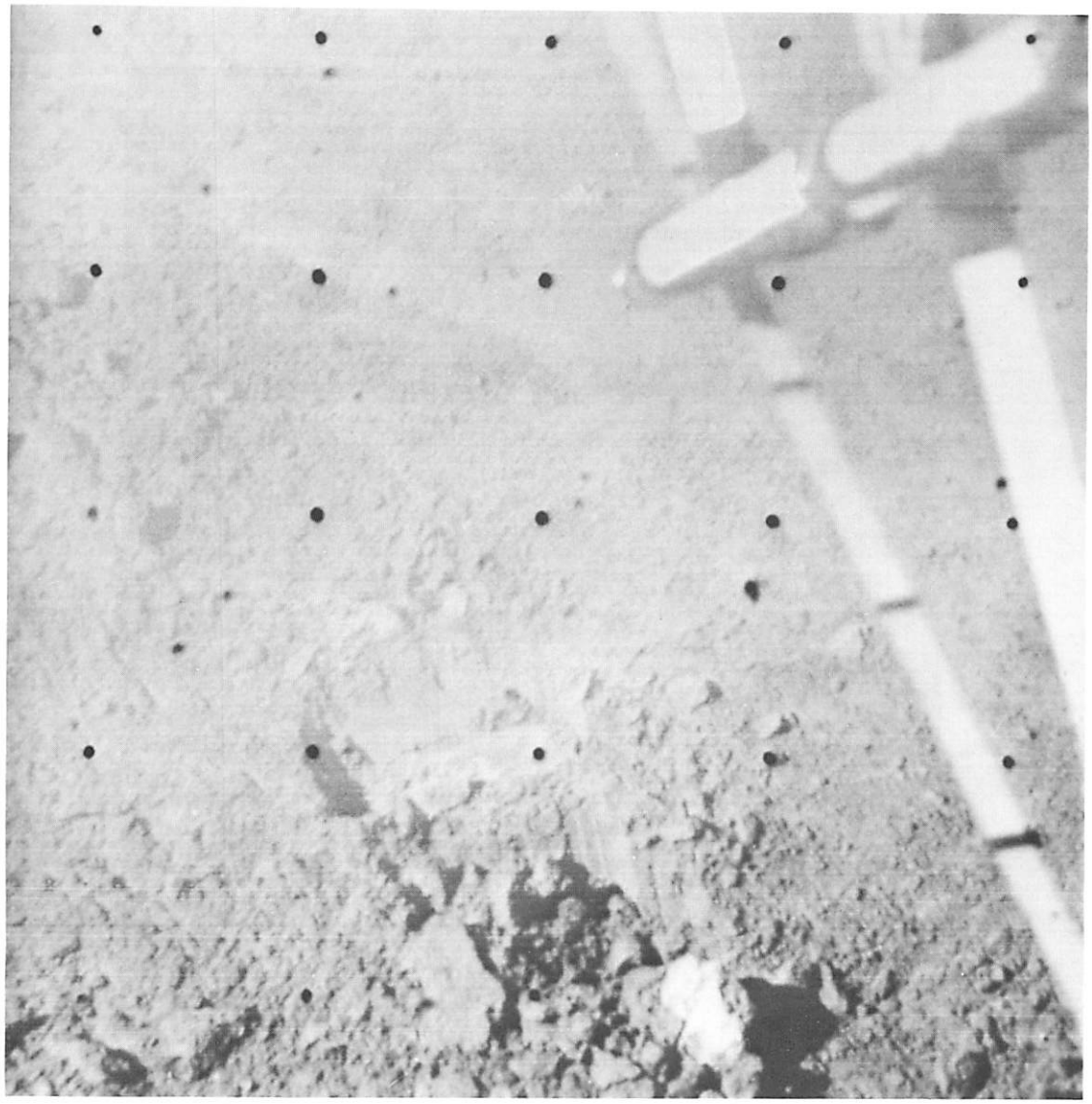

Fig. VIII-5(a). View of the small rock-like object that was excavated from the lunar surface during the SMSS experiment (Day 120, 16:54:48 GMT)

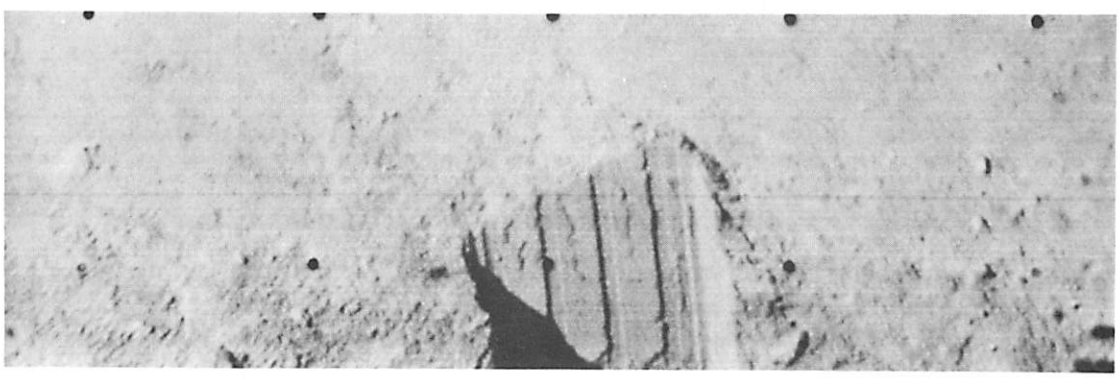

Fig. VIII-5(b). Smooth surface that resulted from an initial penetration of the SMSS scoop into the lunar surface (Day 120, 14:28:03 GMT)

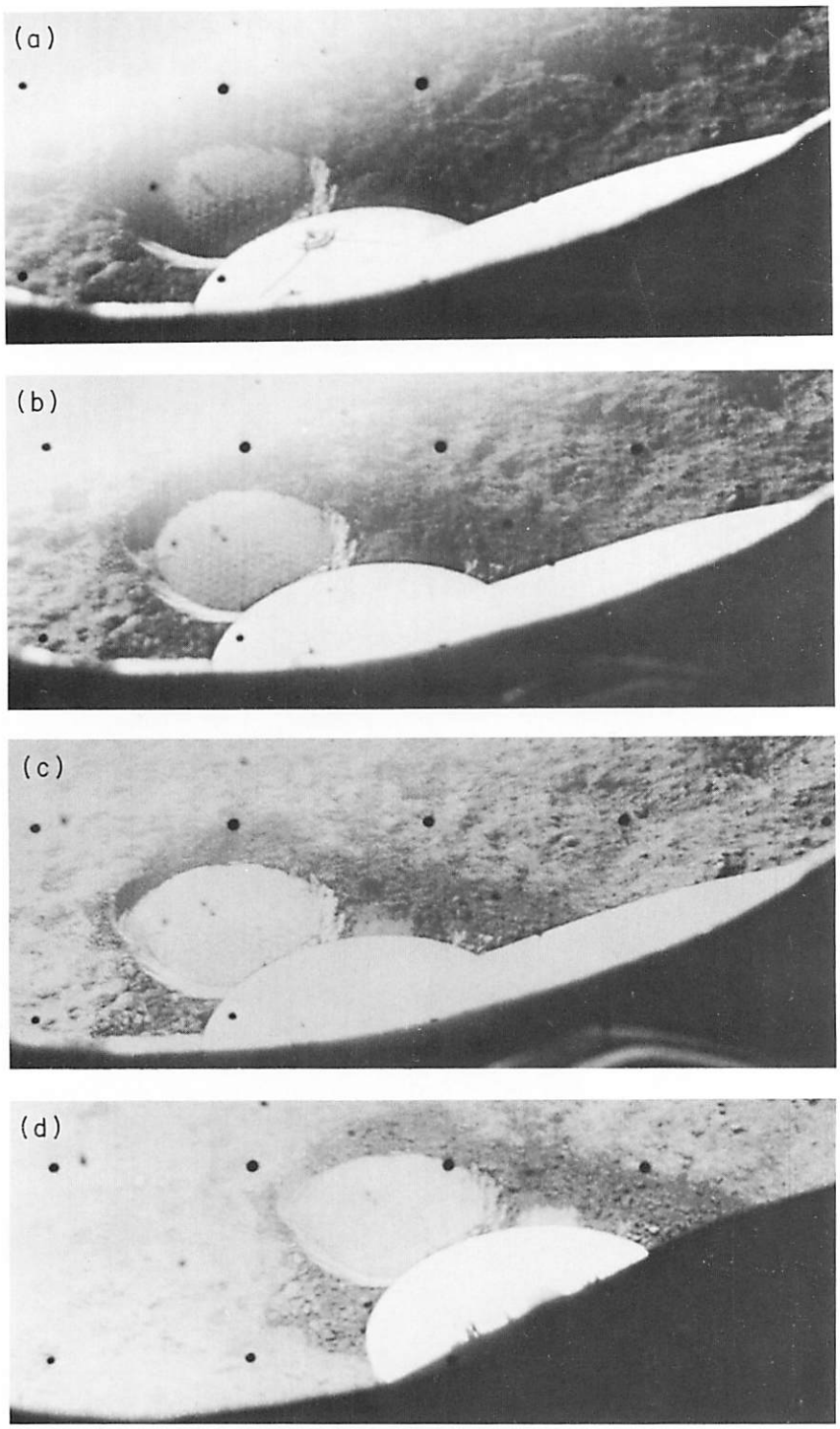

Fig. VIII-6. Pictures of the imprint formed by footpad 2: (a) Day 110, 09:05:17 GMT; phase angle approximately 134 deg; (b) Day 111, 02:39:32 GMT; phase angle approximately 126 deg; (c) Day 112, 00:49:30 GMT; phase angle approximately 114 deg; (d) Day 116, 05:54:53 GMT; phase angle approximately 66 deg

pads belonging to landing event 2 have been identified in the pictures.

In addition to providing information on the particle size of the material comprising the lunar surface layer, as discussed in Section IV, the footpad imprints provide further information on the photometric properties of the lunar surface. The bright conical rim seen under some lighting conditions on the imprint of footpad 2 demonstrates that the photometric properties of the disturbed surface material differ from those of the undisturbed surface. Pictures of the imprint formed by footpad 2 for Days 110 through 112 and Day 116 (Fig. VIII-6) show the variation of imprint brightness relative to the background of the undisturbed surface over a large range of phase angles. Photometric measurements are not yet available, and photographic records for Days 113 through 115 were not obtained because of operational limitations of the spacecraft. However, examination of the pictures in Fig. VIII-6 gives a strong impression that the surface became markedly brighter as the solar phase angle approached the angle near that for specular reflection and, thereafter, the brightness decreased after passing through the zero phase angle. A change in the photometric properties of the footpad area suggests that an important change has occurred in the state of the material. The usual photometric law for the moon has been attributed to intricate surface structure, which casts many shadows. This structure has to be at the millimeter (or smaller) scale. The destruction of the usual photometric properties of the moon makes it clear that the complex open structure has been crushed and the particles packed more densely. The range of scales between the resolvable millimeter and the wavelength of light (0.5 μm), therefore, has to have contained the intricate shadow-casting structure on the lunar surface. In practice, this cannot be accomplished with particles much larger than the order of 10 μm.

D. General Morphology of Landing Site

Although footpad landing imprints and SMSS experiments suggest that the lunar surface layer is composed of very fine particulate material, an inspection of the entire 200-m-diameter crater bowl shows the presence of many scattered rocks. Despite the fact that *Surveyor III* landed in a crater, the general appearance of the surrounding terrain in the vicinity of the spacecraft is not unlike that revealed by the *Surveyor I* pictures. The general area for both landing sites was selected for the apparent smoothness and suitability as a landing site for *Apollo*. Judging from the similarity of the appearance of the mare surfaces in *Lunar Orbiter* photographs, it now appears that most of the upper layers of the mare surfaces of the moon have the general character noted at the *Surveyor I* and *III* landing sites.

The area surrounding the spacecraft is shown in Figs. VIII-1, VIII-7, and VIII-8. In Fig. VIII-1, the *Lunar Orbiter* high-resolution frame is displayed at *normal gain*; that is, a nominal amplifier gain setting was used to convert the magnetic tape record to film. In contrast, Fig. VIII-7 shows the same scene at low gain to show detail in the shadows and high gain to show detail in the highlighted areas.

Figure VIII-8 is a mosaic of the region to the north of the spacecraft and illustrates the general types of rocky debris observable inside the crater. Small craters, as well as a scattering of rock fragments not obviously associated with them, may also be seen in this figure. The slopes and rims of these small craters suggest that they were formed in essentially homogeneous material, presumably similar in nature to that disturbed by the SMSS and the spacecraft's footpads. Crater B of intermediate size (diameter, 5 m; depth, 1 to 1.5 m) appears also to have been formed in the fine-grained surface material. Two craters, 16 m north-northeast of crater B (craters C in Figs. VIII-1 and VIII-8), each 2 m (6 ft) in diameter, have no rocks directly associated with them. Thus, it would appear that the fine particulate surface material extends below the approximately 15 cm (5 in.) excavated by the soil-sampling experiment to a depth of as much as 1.5 m (5 ft). Below this depth, it would seem the consistency of the lunar material changes to one not unlike terrestrial rock that fractures into angular pieces. This result is essentially the same as that observed at the *Surveyor I* landing site.

A crater 12 to 13 m in diameter (A in Fig. VIII-1) may be seen 80 m due north of the spacecraft. This crater is surrounded by angular rocks, the largest of which are visible at the scale of the *Lunar Orbiter* photographs. *Surveyor* images of examples of these rocks are reproduced in greater detail in Figs. VIII-9 and VIII-10. Figure VIII-9 is a mosaic of three adjacent frames showing crater A and surrounding area. This small crater is approximately 2 to 2.5 m deep, based on estimates from the *Lunar Orbiter* photograph. The blocky rocks on its rim are, by their distribution, clearly ejecta from the crater.

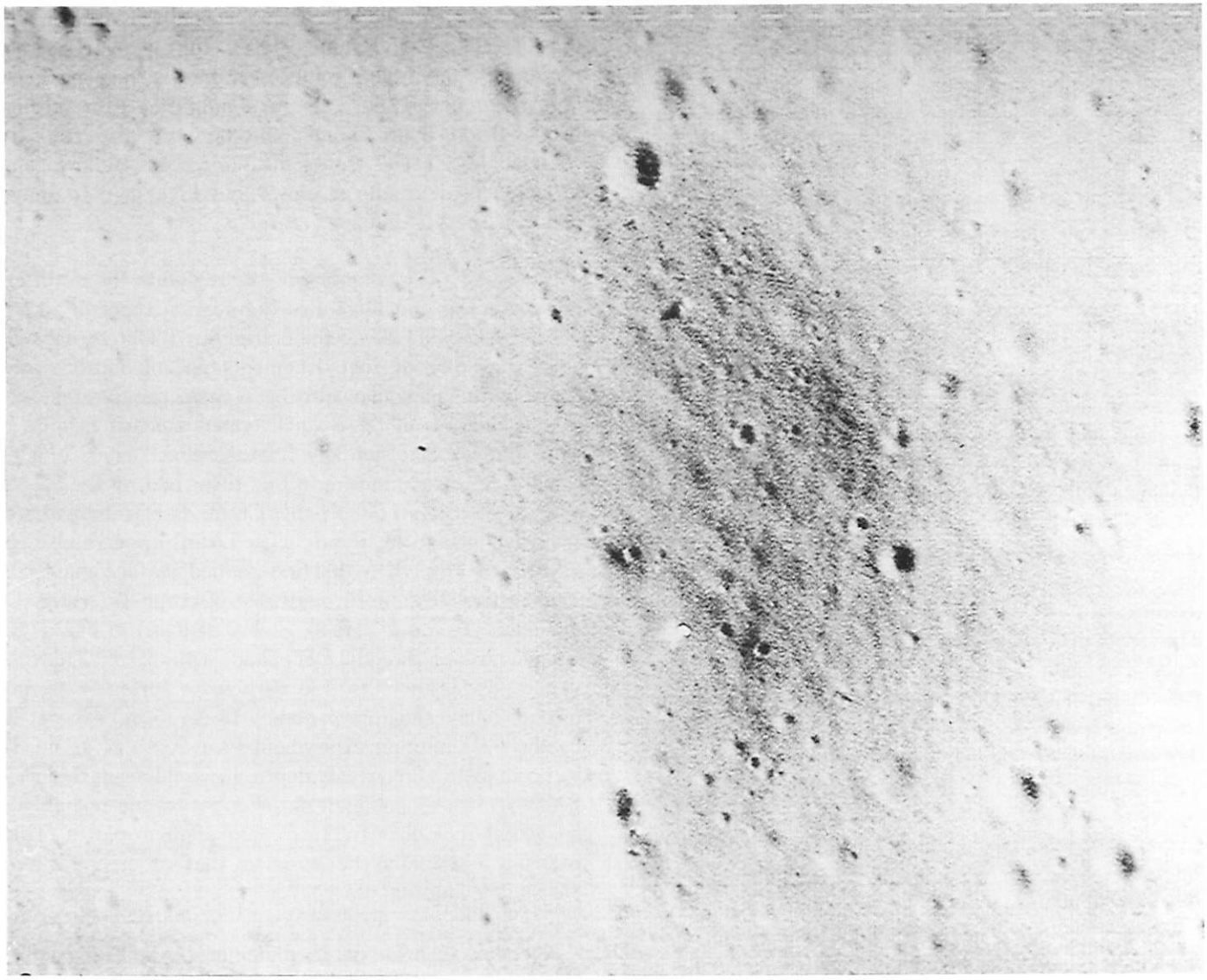

Fig. VIII-7(a). Portion of photograph from *Lunar Orbiter III*, site 9C, frame H154, framelet 27. In contrast to Fig. VIII-1, a low amplifier gain setting was employed to convert the magnetic tape record to film (photography courtesy of I. G. Recant, NASA, Langley Research Center)

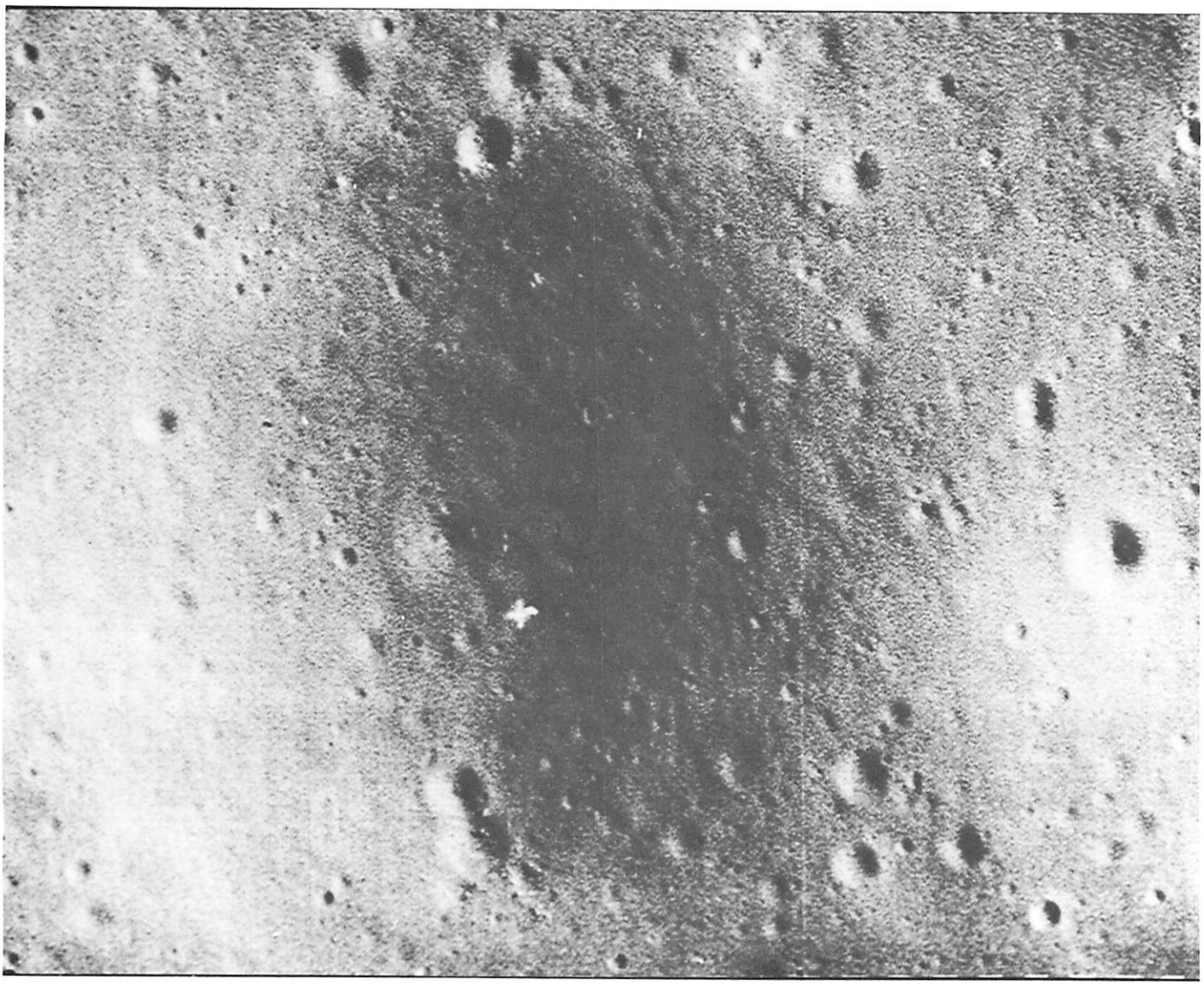

Fig. VIII-7(b). Portion of photograph from *Lunar Orbiter III*, site 9C, frame H154, framelet 27. In contrast to Fig. VIII-1, a high amplifier gain setting was employed to convert the magnetic tape record to film (photograph courtesy of I. G. Recant, NASA, Langley Research Center)

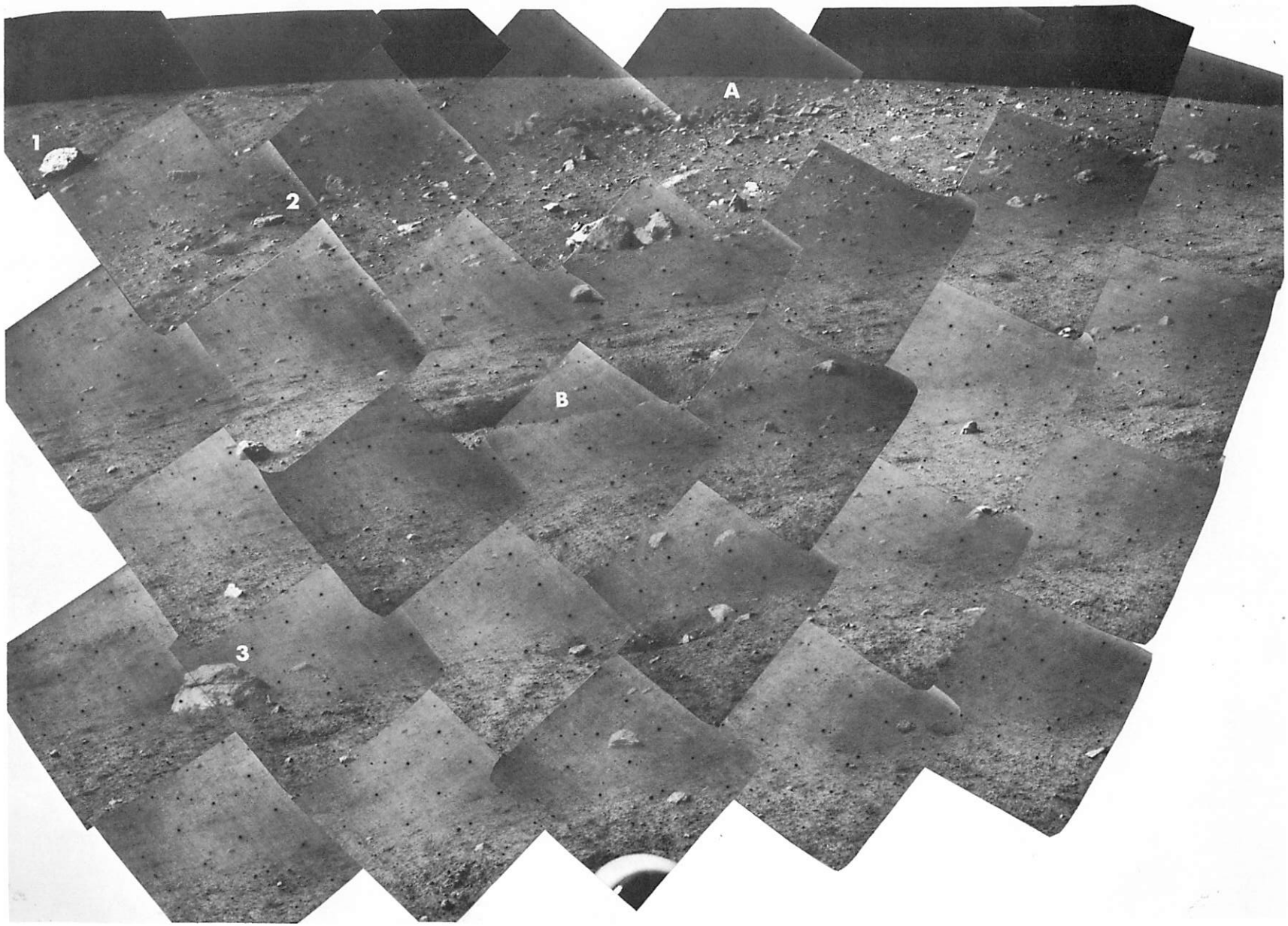

Fig. VIII-8. Mosaic of the crater wall to the north of the spacecraft (Catalog No. 90SI, Day 120, 14:38:57 to 15:07:45 GMT)

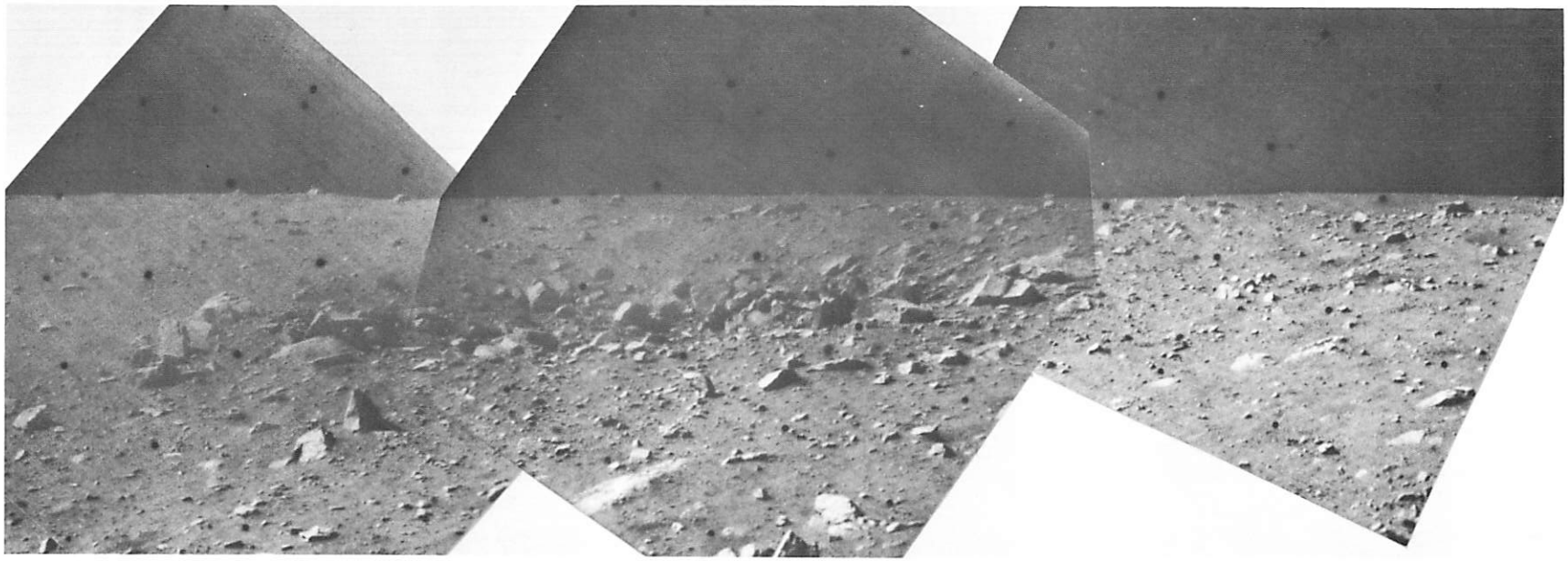

Fig. VIII-9. Mosaic of three narrow-angle frames, showing details of crater A and surrounding area (Day 120: left to right, 14:47:09, 14:45:05, and 14:41:04 GMT)

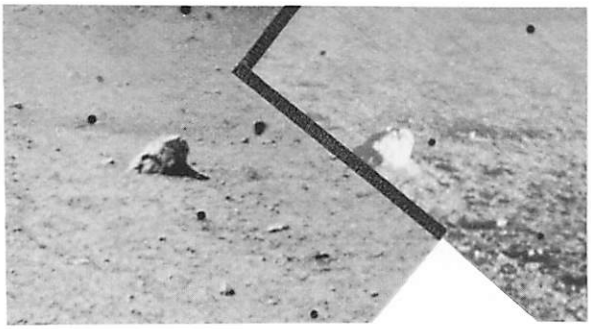

(a)

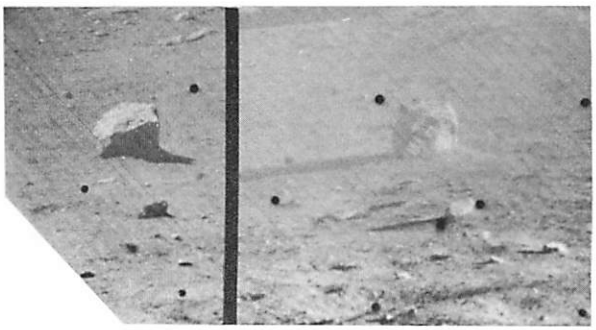

(b)

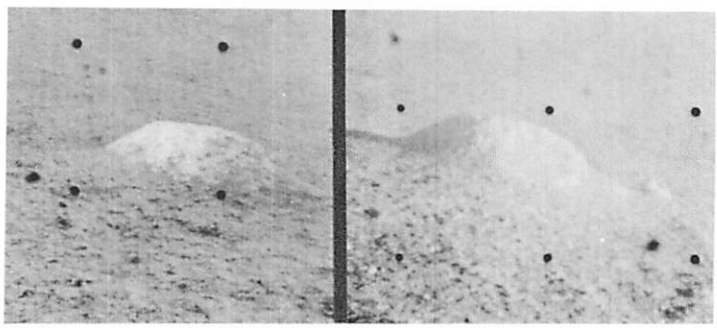

(c)

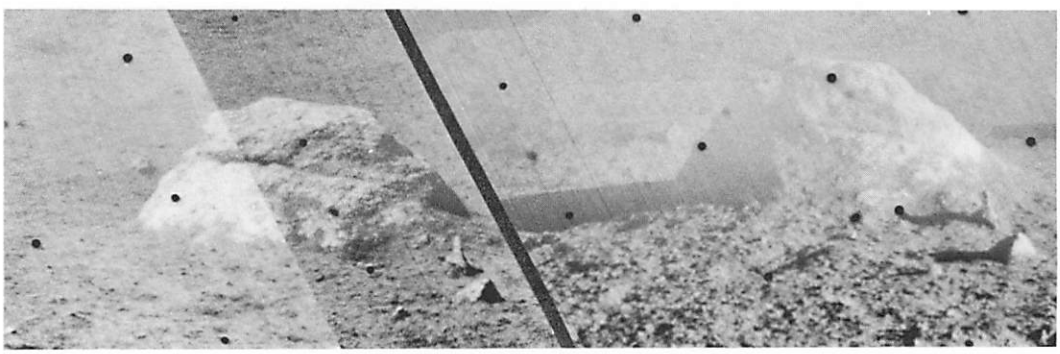

(d)

Fig. VIII-10. Selected rocks on wall of crater with lunar afternoon and early morning illumination (left and right views, respectively). Note absence of a fillet or accumulation of material on downhill (left) side of objects: (a) Day 120, 14:41:09 GMT; Day 111, 05:59:07 GMT; (b) Day 120, 14:47:03 GMT; Day 111, 05:59:25 GMT; (c) Day 120, 15:00:51 GMT; Day 111, 05:15:03 GMT; (d) Day 120, 14:54:23 and 14:52:22 GMT; Day 111, 05:14:55 GMT

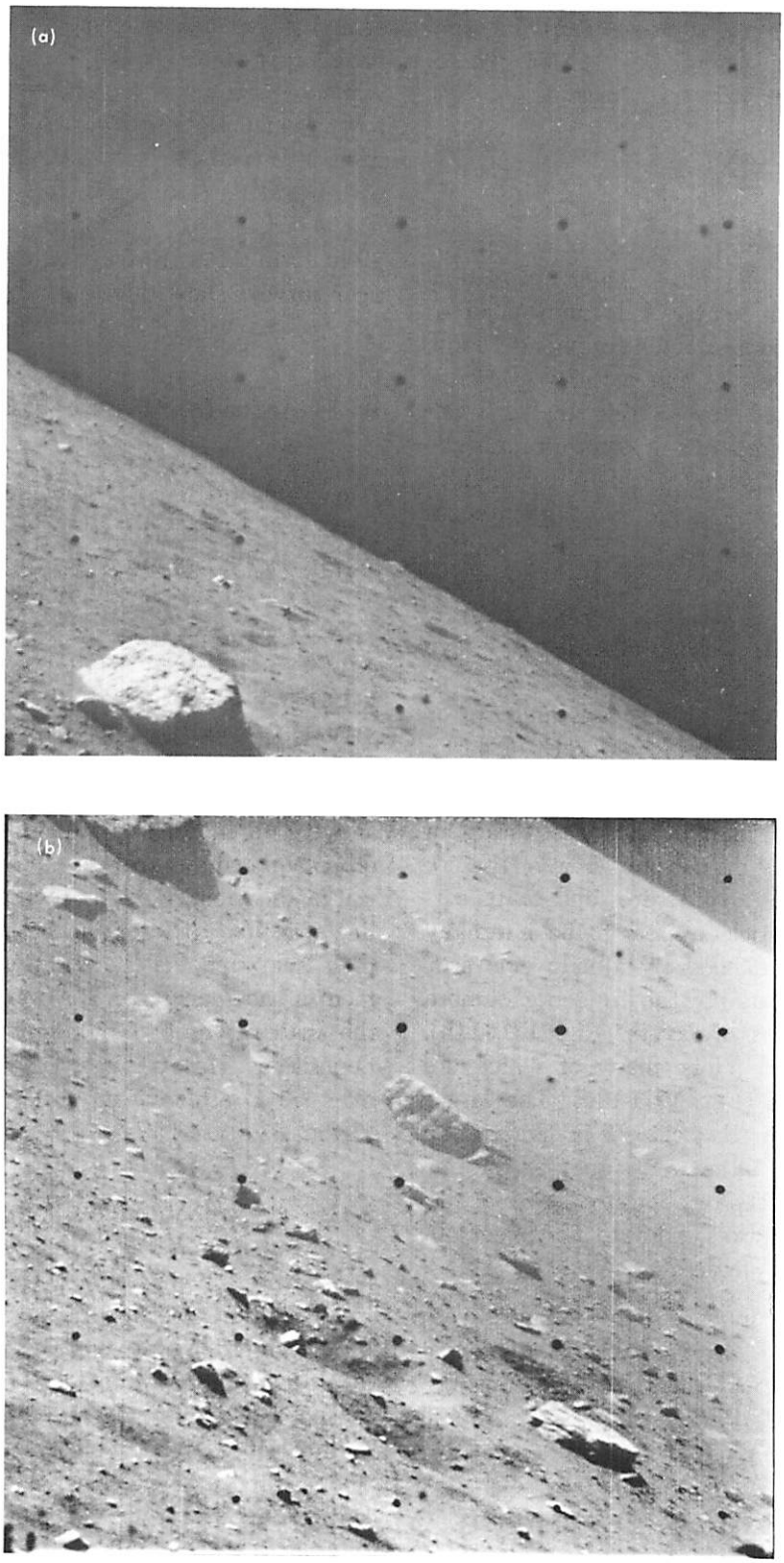

Fig. VIII-11. Details of (a) rock 1 (Day 120, 15:07:16 GMT) and (b) rock 2 (Day 120, 14:52:35 GMT)

Surveyor pictures show that positions of rocks on the lunar surface vary from lying almost completely on the surface to being almost completely buried. These rocks appear to belong to at least three classes:

(1) Sharp, jointed, or fractured or angular blocks found principally north of the spacecraft in the sector containing crater A. These are distinguished from class 2 objects by the presence of sharp corners and distinctly planar faces. Their association with, and origin from, crater A is unmistakable, although the more widely strewn fragments found in the area to the west of the crater may come from another source. Many of the smaller fragments found in this north quadrant are unmistakably sharp-edged and belong to this population of rocks. The small fragments are typically tabular with irregular outlines and lie flat on the surface, although the few exceptions are spectacular (a sharp, tabular stone at least half-buried, protruding upward, Fig. VIII-10d). Among the larger blocks, several appear to be partially buried in this position. Where visible, the walls and rim of crater A are composed almost entirely of large angular blocks in a random jumble.

(2) Large, subrounded to subangular blocks resting on the surface or partially buried only (Fig. VIII-11a). Despite the lack of clean fractures and sharp corners, many of these rocks appear to be internally heterogeneous as evidenced by albedo contrasts, parallel layering indicated by the projection of more or less resistant edges of layers (Fig. VIII-11b), and poorly developed joints, many of which are parallel to the layers (Fig. VIII-10d). The larger (nonvesicular) rock in *Surveyor I* is, perhaps, a member of this class. Other rocks such as the one illustrated in Fig. VIII-11a show evidence of pitting or vesiculation, also similar to an object observed in *Surveyor I* pictures.

(3) Low, rounded rocks appearing to be partially to almost totally buried. Many have a blanket of apparently very fine material built along the uphill side (Fig. VIII-10c). These rocks have a rough, mottled texture not unlike that of the lunar surface material and give the distinct impression of being the eroded remnants of blocks (say, population 1 and 2) partially mottled with fine particulate material from the lunar surface.

Type 2 blocks seem to make up nearly all those visible in the survey, but are a minority in the area to the north near crater A, since they are outnumbered there by the type 1 sharp blocks. Type 2 rocks may be rather uniformly distributed over the surface on all quadrants, while the type 1 rocks show association with crater A and a concentration toward it. The more widely strewn material may have another local source. There is a lack of this angular blanket to the northeast and east of the spacecraft; it apparently terminates toward the north at 10 to 15 m (30 to 50 ft) from the spacecraft, because the near surveys show only dark lunar material.

E. Evidence for Material Transport

The fine-grained material of the lunar surface shows a remarkable tendency to develop and maintain a smooth surface. In the case of *Surveyor I*, the mean surface was essentially horizontal; for *Surveyor III*, the mean surface level is inclined at an angle of approximately 14 to 15 deg. Most rocks seen in *Surveyor I* and *III* pictures appear to be partly submerged with the contact line between the rock and the lunar surface, nearly in the same plane as the lunar surface. Thus, if trenches or craters were made by the rocks as they fell into their observed positions, subsequent processes must have been at work to fill in and smooth over such scars. On the other hand, these processes have not piled up the material in the vicinity of the rock so as to produce a raised line of contact. There is at most a small fillet, centimeters high, that smooths the transition from the general surface to the rock face. The transportation mechanism of the material must be one that works toward smooth deposition. This transportation mechanism must, however, be as effective on a sloping surface as on a level surface.

Camera azimuths looking north-northeast and south-southwest from *Surveyor III* view the wall of the crater across the downhill slope. Thus, rocks viewed in these two directions permit one to examine and compare the uphill and downhill ends of the rocks (Fig. VIII-10). There is a definite indication of the downhill movement of material comprising the fine material of the lunar surface layer. A fillet of material encompasses the base of most rocks at the contact line with the fine-grained surface material; this fillet tends to be higher on the uphill end than on the downhill end. On some large rocks a well-developed fillet is observed that laps several centimeters up onto the uphill face of the rock. This enhanced fillet can be explained, regardless of the mechanism which sets the particles in motion, only as the

accumulation of fragments arrested in place during downhill motion.

F. Lunar Dielectric Constant

The dielectric constant of the lunar surface materials derived from terrestrial observations, k_{obs}, lies in the range 1.8 to 2.8 (Ref. VIII-1). This figure refers to the bulk dielectric constant, including the effects of porosity. To obtain the dielectric constant, k, of the individual grains, use may be made of the formulas of Twersky (Ref. VIII-1), Böttcher (Ref. VIII-2), and Odelevskii and Levin (Ref. VIII-2). To give an idea of the relative values these formulas provide, we find the following for $k_{obs} = 2.4$ and a porosity of 0.5: Twersky, $k = 5.8$; Böttcher (Ref. VIII-2), $k = 4.7$; and Odelevskii and Levin, $k = 4.4$.

Twersky's formula is stated to apply to granular material in which the grains are well separated; that of Böttcher to granular material; that of Odelevskii and Levin applies to vesicular material. Data presented in Ref. VIII-1 support the formula of Odelevskii and Levin. Data presented by Krotikov (Ref. VIII-2) support an interpolation formula between the Böttcher formula and that of Odelevskii and Levin. The Böttcher formula was adopted for this paper; it appears to give conservative values (i.e., high values) of the grain dielectric constant.

The formula of Böttcher is:

$$\frac{k_{obs} - 1}{3k_{obs}} = \frac{k - 1}{k + 2k_{obs}} (1 - \eta)$$

where η is the porosity, i.e., the ratio of intergranular void space to total volume. The formula is shown in Fig. VIII-12.

The data presented in Ref. VIII-3 were used to check Fig. VIII-12; the only points falling on this plot, and corresponding to known values of the solid dielectric constant, are:

(1) Sand, true dielectric constant of solid material probably 4.2 (handbook value for crystalline quartz) rather than 3.8, as quoted in Ref. VIII-3; the latter value is for fused silica.

k_{obs}	η	k of grains (Fig. VIII-12)
2.92	0.343	4.5
2.68	0.400	4.5
2.36	0.503	4.5
2.19	0.560	4.5
1.94	0.645	5.2
1.90	0.637	4.8

(2) Plate glass, true dielectric constant of solid material 7.3.

k_{obs}	η	k of grains (Fig. VIII-12)
3.01	0.559	8.4
2.27	0.680	8.2
1.96	0.739	8.1

It appears that Fig. VIII-12 is conservative.

The minimum value of the dielectric constant for plausible lunar materials in the solid form is that for clear silica glass, namely 3.8.[2]

At this writing, data on the porosity are not available from *Surveyor III* measurements of the lunar soil. It is possible to sketch the lines of constant bulk density on Fig. VIII-12, using the porosities shown and the accepted values of the bulk densities of the rocks. These values are indicated by dashed lines. When reliable values of the porosity and/or density become available, it may be possible to draw some conclusions about the nature of the lunar surface. It must be kept in mind, however, that the grains, themselves, may be vesicular; in this case they may appear to be more acid than they are. This is more important for basalts than for chondritic materials. To date, no cases of vesicular chondritic material have been pointed out.

[2]Handbook of Chemistry and Physics, Chemical Rubber Co., Cleveland, Ohio, 44th edition, p. 2626, 1962.

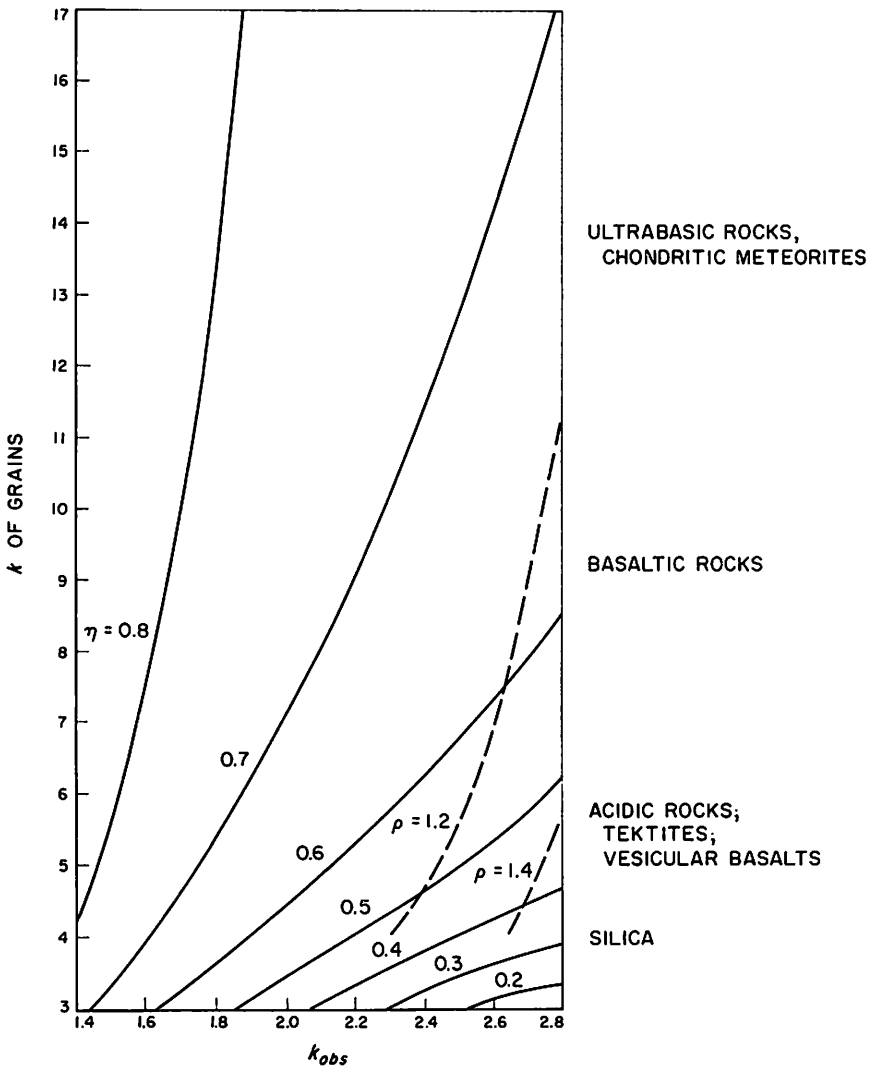

Fig. VIII-12. Relation between the bulk dielectric constant, k_{obs}, and the dielectric constant of the grains, k, according to the Böttcher formula; η is the porosity, ρ is the density

G. Concluding Remarks

Surveyor III results at this preliminary data evaluation give valuable information about the relation between the surface material responsible for the photometric properties and the deeper layers of material in which properties resemble those of ordinary terrestrial soils. In addition, they provide new insight into the relation between the general lunar surface as seen by *Surveyor I* and the interior of a large subdued crater. The new results have also contributed to an understanding of the mechanism of downhill transport. Many critical questions cannot, however, be answered until final reduction of experimental data.

References

VIII-1. *Radar Studies of the Moon*, Quarterly Report, Lincoln Laboratories, Lexington, Mass.

VIII-2. Krotikov, V. L., "Some Electrical Properties of Earth Rocks and Their Comparison With Those of the Lunar Surface Layer," proceedings of the High Scientific Institute, *Radiophysics Series*, Vol. 5, pp. 1057–1061, 1962.

VIII-3. Fensler, W. E., Knott, E. F., Olte, A., and Siegel, K. M., "The Electromagnetic Parameters of Selected Terrestrial and Extraterrestrial Rocks and Glasses," from *The Moon*, pp. 545–565, edited by Z. Kopal and Z. K. Mikhailov, Academic Press, New York, 1962.

(Blank Page)

Appendix

Surveyor Scientific Teams

For the *Surveyor III* mission, the analysis of the scientific data has been carried out by Investigator Teams, the *Surveyor* Scientific Evaluation Advisory Team, and associated working groups. Their composition was:

A. Investigator Teams

1. Television

E. M. Shoemaker, Principal Investigator	U. S. Geological Survey
R. A. Altenhofen	U. S. Geological Survey
R. M. Batson	U. S. Geological Survey
H. E. Holt	U. S. Geological Survey
G. P. Kuiper	University of Arizona
E. C. Morris	U. S. Geological Survey
J. J. Rennilson	Jet Propulsion Laboratory
E. A. Whitaker	University of Arizona

2. Soil Mechanics Surface Sampler

R. F. Scott, Principal Investigator	California Institute of Technology
R. Haythornwaite	University of Michigan
R. Liston	Detroit Arsenal

B. *Surveyor* Scientific Evaluation Advisory Team

L. D. Jaffe, Chairman	Jet Propulsion Laboratory
S. A. Batterson	Langley Research Center
W. E. Brown, Jr.	Jet Propulsion Laboratory
E. M. Christensen	Jet Propulsion Laboratory
S. E. Dwornik	NASA Headquarters
D. E. Gault	Ames Research Center
J. W. Lucas	Jet Propulsion Laboratory
R. H. Norton	Jet Propulsion Laboratory
R. F. Scott	California Institute of Technology
E. M. Shoemaker	U. S. Geological Survey
G. H. Sutton	University of Hawaii
A. Turkevich	University of Chicago

C. Working Groups

1. Lunar Surface Thermal Properties

J. W. Lucas, Chairman	Jet Propulsion Laboratory
J. E. Conel	Jet Propulsion Laboratory
R. B. Erb	Manned Spacecraft Center
R. R. Garipay	Hughes Aircraft Company
W. A. Hagemeyer	Jet Propulsion Laboratory
H. C. Ingrao	Harvard College Observatory
B. P. Jones	Marshall Space Flight Center
J. M. Saari	The Boeing Company

2. Lunar Surface Electrical Properties

W. E. Brown, Jr., Chairman	Jet Propulsion Laboratory
R. A. Dibos	Hughes Aircraft Company
G. B. Gibson	Manned Spacecraft Center
D. O. Muhleman	Cornell University
W. H. Peake	Ohio State University
V. J. Poehls	Ryan Aeronautical Company

3. Lunar Surface Mechanical Properties

E. M. Christensen, Chairman	Jet Propulsion Laboratory
S. A. Batterson	Langley Research Center
H. E. Benson	Manned Spacecraft Center
L. D. Jaffe	Jet Propulsion Laboratory
R. H. Jones	Hughes Aircraft Company
R. F. Scott	California Institute of Technology
E. N. Shipley	Bellcomm, Inc.
R. L. Spencer	Jet Propulsion Laboratory
F. B. Sperling	Jet Propulsion Laboratory
G. H. Sutton	University of Hawaii

4. Lunar Theory and Processes

D. E. Gault, Chairman	Ames Research Center
R. J. Collins	University of Minnesota
T. Gold	Cornell University
J. Green	McDonnell-Douglas Corporation
G. P. Kuiper	University of Arizona
H. Masursky	U. S. Geological Survey
J. A. O'Keefe	Goddard Space Flight Center
R. A. Phinney	Princeton University
E. M. Shoemaker	U. S. Geological Survey

5. Astronomy

R. H. Norton, Chairman	Jet Propulsion Laboratory
J. E. Gunn	Jet Propulsion Laboratory
W. C. Livingston	Kitt Peak National Observatory
G. A. Newkirk	High Altitude Observatory
H. Zirin	Mt. Wilson and Palomar Observatories